

**A Search for Starting Tracks in Icecube: A New Window for Detecting Astrophysical  
Neutrinos**

By  
Kyle Zachary Jero

A dissertation submitted in partial fulfillment of  
the requirements for the degree of

Doctor of Philosophy

(Physics)

at the  
UNIVERSITY OF WISCONSIN–MADISON  
2017

Date of final oral examination: October 31st 2017

The dissertation was reviewed by the following members of the Final Oral Committee:

Albrecht Karle, Professor, Physics

Jay Gallagher, Professor, Astronomy

Francis Halzen, Professor, Physics

Justin Vandenbroucke, Assistant Professor, Physics

Kimberly Palladino, Assistant Professor, Physics

## ABSTRACT

Neutrinos are a unique cosmic messenger which are in the early stages of opening a new window to the universe. Unlike their cosmic brethren, neutrinos are undeflected and unattenuated as they travel cosmic distances to reach the Earth.

In recent years IceCube has pioneered the search for astrophysical neutrinos with discoveries of a diffuse astrophysical neutrino flux in two different channels of neutrino detection; upward-going muon neutrinos which use the Earth as a shield against background and neutrinos which leave a cascade-like deposit which take advantage of correlations in air showers to remove background.

This thesis focuses on the underutilized detection topology of starting tracks, muon tracks from neutrinos whose interaction vertex is contained inside the detector, to access the astrophysical flux and observed new astrophysical neutrinos in archival data that would have otherwise remained unidentified. These starting tracks, when treated properly, can take advantage of a very strong effect called the direct self-veto to remove background events and open a nearly background free window for astrophysical neutrino detection in the southern sky.

Newly developed methods, techniques, and simulations are vital to the success of this work and are presented along the way to the final result.

## ACKNOWLEDGMENTS

I'd like to thank a number of people who helped me complete the work for this thesis.

First, I'd like to thank Dr. Albrecht Karle. You've taught me how to embody the university's ideals of sifting and winnowing for the truth. I know that the discerning eye I've acquired through your guidance will be irreplaceable as I move forward in my career and life.

Second, I'd like to thank Dr. James Madsen. If not for your support and encouragement through connections and opportunities when we worked together in River Falls, I don't think I would have had the chance to attend graduate school at UW-Madison. Thanks for believing in me and letting me gain so many life experiences while doing research with you.

Third, I'd like to thank the graduate students I've worked with for their time and assistance. In particular Jakob Van Santen, Christopher Weaver, and Jake Feintzeig, who taught me about IceCube, its software, and culture, and Sarah Mancina, who has helped me with some of the results of this thesis.

Finally, I'd like to thank my wife, Julia. You believed in me and supported me the whole way. I know it wasn't easy for you all the time. You kept me focused and let me take what I needed to be successful, sometimes at personal expense. Your contribution to this thesis is more important than any words in a paragraph or lines on a plot.

# TABLE OF CONTENTS

	Page
<b>ABSTRACT</b> . . . . .	i
<b>LIST OF TABLES</b> . . . . .	vi
<b>LIST OF FIGURES</b> . . . . .	vii
<b>1 Preface</b> . . . . .	1
<b>2 High Energy Cosmic Rays</b> . . . . .	3
<b>3 Physics Background</b> . . . . .	9
3.1 Cosmic Rays . . . . .	9
3.1.1 Charged Particle Acceleration . . . . .	13
3.2 Neutrino Physics . . . . .	15
3.3 Atmospheric Neutrino Production . . . . .	17
3.3.1 Conventional Neutrino Flux . . . . .	18
3.3.2 Prompt Neutrino Flux . . . . .	18
3.4 Astrophysical Neutrino Production . . . . .	20
3.4.1 Diffuse Neutrinos from the Galactic Plane . . . . .	20
3.4.2 Possible Astrophysical Sources of Neutrinos . . . . .	20
3.4.3 Cosmogenic Neutrinos . . . . .	23
3.5 Muon Physics . . . . .	23
3.6 Cherenkov Radiation . . . . .	25
3.7 Light Emission Topologies . . . . .	28
3.7.1 Muon Tracks Below 300 GeV . . . . .	28
3.7.2 Cascades . . . . .	29
3.7.3 Muon Tracks Above 300 GeV . . . . .	30
<b>4 Vetoing Atmospheric Neutrinos</b> . . . . .	31
4.1 Theory . . . . .	31
4.2 Implementation . . . . .	34
4.2.1 In Ice . . . . .	34
4.2.2 Surface . . . . .	36
<b>5 Astrophysical Neutrino Flux Measurements</b> . . . . .	37
5.1 Starting Event Analyses . . . . .	37
5.1.1 High Energy Starting Event Selection . . . . .	37
5.1.2 Medium Energy Starting Cascade Selection . . . . .	43

	Page
5.2 Upward-Going Muon Neutrinos . . . . .	50
5.3 Discussion of Astrophysical Flux Measurements . . . . .	61
<b>6 IceCube Detector . . . . .</b>	<b>64</b>
6.1 DOMs . . . . .	66
6.1.1 Hardware . . . . .	66
6.1.2 Operation . . . . .	69
6.2 Design of a String . . . . .	70
6.3 Calibration . . . . .	72
6.3.1 Calibrating a DOM . . . . .	72
6.3.2 Time Calibration . . . . .	75
6.4 Modernization of the IceCube DAQ . . . . .	75
6.5 Data Acquisition . . . . .	76
6.6 Data Filtering . . . . .	76
6.7 Ice . . . . .	77
6.7.1 Scattering . . . . .	79
6.7.2 Absorption . . . . .	82
6.7.3 Depth Dependence and Layer Tilt . . . . .	82
6.7.4 Anisotropy . . . . .	83
6.7.5 Local Effects . . . . .	86
<b>7 Event Simulation . . . . .</b>	<b>90</b>
7.1 Particle Generation . . . . .	90
7.1.1 Atmospheric Muons . . . . .	90
7.1.2 Neutrinos . . . . .	92
7.1.3 Weighting . . . . .	93
7.2 Particle Propagation . . . . .	96
7.2.1 Track-Like Particle Propagation . . . . .	96
7.2.2 Cascade-Like Particle Propagation . . . . .	97
7.3 Photon Propagation . . . . .	97
7.4 Detector Simulation . . . . .	98
<b>8 Event Reconstruction . . . . .</b>	<b>101</b>
8.1 Cascade Reconstruction . . . . .	101
8.2 Track Reconstruction . . . . .	102
8.2.1 Direction . . . . .	102
8.3 Millipede . . . . .	108
8.3.1 Introduction . . . . .	108
8.3.2 Underlying Algorithm . . . . .	110
8.3.3 Performance . . . . .	111
8.3.4 Use With an Angular Minimizer . . . . .	115
8.3.5 Issues . . . . .	115
8.3.6 Ideas about Resolving the Issues . . . . .	122

	Page
<b>9 Data Selection</b> . . . . .	124
9.1 Incoming Muon Veto . . . . .	125
9.1.1 Defining The Muon and Veto Regions . . . . .	128
9.1.2 Setting The Photon Table Scale . . . . .	130
9.1.3 Calculating The Veto Probability . . . . .	134
9.2 Cuts . . . . .	137
9.2.1 Pre-Cuts . . . . .	138
9.2.2 Coarse Grid Search . . . . .	140
9.2.3 Fine Grid Search . . . . .	152
9.3 High Level Reconstruction . . . . .	156
9.4 Final Cuts . . . . .	156
9.4.1 Down-going Selection . . . . .	156
9.4.2 Up-going Selection . . . . .	165
9.5 Event Rate At Different Cut Levels . . . . .	165
9.6 Neutrino Energy Estimate . . . . .	166
9.7 ESTReS Filter . . . . .	171
9.8 Effective Area . . . . .	171
<b>10 Analysis, Results, Outlook, and Conclusions</b> . . . . .	176
10.1 Expectation From Simulation . . . . .	176
10.1.1 Angular Resolution . . . . .	176
10.1.2 Energy Resolution . . . . .	177
10.2 Events in the Burn Sample . . . . .	181
10.3 Outlook for the Full Sample . . . . .	189
10.3.1 Events From Astrophysical Fluxes . . . . .	190
10.3.2 Events From Atmospheric Flux Models . . . . .	196
10.3.3 Point Source Potential . . . . .	202
10.4 Conclusions . . . . .	205
<b>APPENDIX Interesting Observed Events</b> . . . . .	207
<b>APPENDIX CORSIKA Modification For Faster Background Generation</b> . . . . .	209
<b>APPENDIX The pDOM DAQ</b> . . . . .	215
<b>LIST OF REFERENCES</b> . . . . .	224

## LIST OF TABLES

Table	Page
4.1 Parameters for the elbert formula . . . . .	34
5.1 Values for defining the charge dependent distance to edge cut . . . . .	48
5.2 Variables of the upward-going muon neutrino selection's BDT . . . . .	54
9.1 Table of the variables used in ESTES's BDT . . . . .	158
9.2 Table of the variables used to construct the classifier variable . . . . .	159
9.3 The weighted and unweighted separation gained by using cuts involving each variable in the BDT	160
9.4 The effect of cuts in the selection . . . . .	166
10.1 The number of events per year of burn sample which enter the ESTES selection . . . . .	181
10.2 The number of astrophysical events expected in 5 years with an astrophysical probability greater than 50% . . . . .	194
A.1 Table of the events which are likely to be astrophysical . . . . .	208

## LIST OF FIGURES

Figure	Page
2.1 Results from Victor Hess' and Werner Kolhörster's ballon flights . . . . .	4
2.2 The cosmic ray spectrum from 100 MeV to 1000 EeV . . . . .	5
2.3 Cosmic ray spectrum as measured by direct detection experiemnts . . . . .	6
2.4 Ultra high energy cosmic ray spectrum . . . . .	7
3.1 Hillas Plot . . . . .	11
3.2 Mean free path of gamma rays in interstellar space . . . . .	12
3.3 Neutrino interactions . . . . .	16
3.4 Neutrino-nucleon cross section . . . . .	17
3.5 Atmospheric neutrino fluxes . . . . .	19
3.6 Muon energy loss rate . . . . .	24
3.7 Cherenkov radiation . . . . .	26
3.8 Muon and electron speed as a function of energy . . . . .	27
3.9 Simulation of a 24 GeV electron in iron . . . . .	29
3.10 Angular emission profile of Cherenkov photons from electromagnetic cascades . . . . .	30
4.1 Diagram of two body decay . . . . .	32
4.2 Atmospheric self-veto probabilities . . . . .	35
5.1 The veto layer definition for the high energy starting event selection . . . . .	38
5.2 The veto time vs charge definition for the highe energy starting event selection . . . . .	39
5.3 The charge of events which pass the HESE veto definition . . . . .	40
5.4 The effective area for muon neutrinos for the through-going muon neutrino analysis . . . . .	41
5.5 Expected rates for HESE . . . . .	42



Figure	Page
5.6 Nested layer veto used to estimate the penetrating muon background rate . . . . .	43
5.7 Estimated background contamination rates coming from CORSIKA and the nested veto calculation	44
5.8 Penetrating muon background in MESE . . . . .	46
5.9 Penetrating atmospheric muon and neutrino background before and after the incoming track veto	47
5.10 Scaling veto for fixed charges from the top and side views . . . . .	48
5.11 Monte Carlo distributions after applying the scaling veto cut . . . . .	49
5.12 Effective areas for the MESC event selection . . . . .	50
5.13 Results of the MESC selection on two years of data . . . . .	51
5.14 Side(top) and top(bottom) views of two coincident down-going muons . . . . .	53
5.15 BDT score vs. $\cos$ of the zenith angle for upward-going muon neutrino event selection . . . . .	55
5.16 The effective area of the upward-going muon neutrino event selection . . . . .	56
5.17 The energy mapping and resolution of Truncated Energy . . . . .	57
5.18 The zenith resolution of the muon direction reconstruction used in the upward-going muon neutrino event selection . . . . .	58
5.19 Best fit of the upward-going muon neutrino selection . . . . .	59
5.20 Constraint on the astrophysical normalization and spectral index from the upward-going muon neutrino selection . . . . .	60
5.21 Contours of different analyses measuring the astrophysical spectrum with IceCube . . . . .	62
6.1 The IceCube Neutrino Observatory . . . . .	65
6.2 The efficiency of the DOM . . . . .	67
6.3 IceCube R7081 PMT . . . . .	68
6.4 A schematic of the IceCube DOM . . . . .	69
6.5 A waveform recorded in the ATWD(top) and fADC(bottom) . . . . .	71
6.6 The mechanical and electrical connection of the DOM to the cable . . . . .	73
6.7 Cross-section of the in-ice cable . . . . .	74
6.8 The cuts applied to obtain events for the muon filter . . . . .	78
6.9 Comparisons of the Henyey-Greenstein, simplified Liu, and Mie functions . . . . .	80

Figure	Page
6.10 Comparisons of the arrival time distributions for various $g$ and $f_{SL}$ values . . . . .	81
6.11 The effective absorption and scattering lengths as a function of depth centered on IceCube . . . . .	82
6.12 Tilt of the Ice near hole 50 in IceCube . . . . .	83
6.13 Diagram of the x-y position of strings used in the original study of ice anisotropy . . . . .	84
6.14 Evidence of anisotropy from the DOM's flashers . . . . .	85
6.15 Relative charge per angular bin for simulation and data . . . . .	87
6.16 Evidence of anisotropy from atmospheric muons . . . . .	88
7.1 The angular sensitivity of the DOM . . . . .	99
8.1 Depiction of the fastest travel time from a muon track to a DOM along the Cherenkov angle . . . . .	104
8.2 $\frac{dP(t d)}{dt}$ distributions for IceCube's version of the Pandel distributions . . . . .	105
8.3 $\frac{dP(t d)}{dt}$ distributions for IceCube's spline fits to the ice . . . . .	107
8.4 A depiction of the physics situation being modeled by the Millipede algorithm . . . . .	109
8.5 The convergence of different methods are compared against each other . . . . .	112
8.6 Reconstructed images from various algorithms . . . . .	113
8.7 Profiles of intensity from the brains in Figure 8.6 . . . . .	114
8.8 Point spread distributions for various track fits . . . . .	116
8.9 Distribution comparing the time residual of the best fit to the time residual from geometry . . . . .	117
8.10 The negative log likelihood value(logl) of a fit track as a function of time shift along the true direction . . . . .	118
8.11 Millipede results in original binning. . . . .	119
8.12 Millipede results regrouped into 10 meter bins. . . . .	119
8.13 Millipede results regrouped into 20 meter bins. . . . .	120
8.14 Millipede results regrouped into 40 meter bins. . . . .	120
8.15 Millipede results regrouped into 75 meter bins. . . . .	121
9.1 The effective livetime of the CORSIKA simulation used in this analysis as a function of primary energy . . . . .	126
9.2 The livetime of single muons as a function of muon energy created by MuonGun . . . . .	127

Figure	Page
9.3	A depiction of how the incoming muon veto works on a simulated event . . . . . 129
9.4	Figures showing the different earliest hit mapping assuming a definition using IMIM tables . . . 131
9.5	Figures showing the collection of hits which are in the muon and veto regions . . . . . 132
9.6	A set of figures depicting the cuts made on an incoming muon event . . . . . 135
9.7	A set of figures depicting the cuts made on a starting track event . . . . . 136
9.8	Contours of atmospheric to astrophysical ratios . . . . . 137
9.9	Flow chart of the cuts made in the ESTES selection . . . . . 139
9.10	Side view of the holes in the edge of the detector . . . . . 141
9.11	Top view of the holes along the edges of the detector . . . . . 142
9.12	A zoomed out view of the holes in the detector . . . . . 143
9.13	Figure 1 of 3 depicting how the tracks in the coarse veto are constructed to move through the holes in the detector . . . . . 144
9.14	Figure 2 of 3 depicting how the tracks in the coarse veto are constructed to move through the holes in the detector . . . . . 145
9.15	Figure 3 of 3 depicting how the tracks in the coarse veto are constructed to move through the holes in the detector . . . . . 146
9.16	Figure 1 of 2 showing the side view of the tested tracks used in a different starting track event . 147
9.17	Figure 2 of 2 showing the side view of the tested tracks used in a different starting track event . 148
9.18	Figure showing the side view of the tested tracks used in a different incoming track event . . . . 149
9.19	Figure showing the event view of the tracks found from testing used on a different incoming track event . . . . . 150
9.20	Event view of a starting track to be tested with the fine grid scan . . . . . 153
9.21	Depiction of the x, y, z axis cross for position variations of the fine grid scan . . . . . 154
9.22	Depiction of the set of tested tracks in the fine grid scan . . . . . 155
9.23	A plot of the fraction of astrophysical signal that is lost for different cut values of the BDT . . . 162
9.24	A validation of the training of the BDT . . . . . 163
9.25	The differential(left) and cumulative(right) distribution of the decision scores from the BDT . . 164
9.26	Probability distribution for the first loss reconstructed by Millipede . . . . . 168

Figure	Page
9.27 Probability distribution for the the losses after the first as reconstructed by Millipede . . . . .	169
9.28 Probability distribution for the first loss reconstructed by Millipede after conditioning . . . . .	169
9.29 Probability distribution after conditioning for the the losses after the first as reconstructed by Millipede . . . . .	170
9.30 The negative log-likelihood distribution for an example event . . . . .	170
9.31 The effective area of ESTES . . . . .	172
9.32 ESTES's effective area shown with other selections . . . . .	173
9.33 A comparison of the effective areas of existing online selections . . . . .	175
10.1 The angular resolution for various event lengths in ESTES . . . . .	177
10.2 The angular resolution for various event engergies in ESTES . . . . .	178
10.3 The energy resolution of ESTES . . . . .	179
10.4 The distribution of true energy vs reconstructed energy . . . . .	180
10.5 Distribution of events in reconstructed energy and declination with their associated error bars .	182
10.6 Distribution of events in reconstructed right ascension and declination with their associated error bars . . . . .	183
10.7 Cosine zenith distribution for the burn sample with the vetoed atmospheric neutrino flux from the analytic parameterization . . . . .	184
10.8 Cosine zenith distribution for the burn sample with the vetoed atmospheric neutrino flux from CORSIKA . . . . .	185
10.9 Cosine zenith distribution for the burn sample with the atmospheric neutrino flux without the self-veto applied . . . . .	186
10.10 Plots of the burn sample and neutrino predictions in three slices of the sky with the analytic self-veto approximation . . . . .	187
10.12 Plots of the burn sample and neutrino predictions in three slices of the sky with the atmospheric contribution without a self-veto applied . . . . .	189
10.13 The true neutrino energy spectrum of ESTES . . . . .	190
10.14 Map of the ESTES acceptance convolved with the Fermi neutral pion map . . . . .	192
10.15 Likelihood profiles for three hypothetical astrophysical spectra . . . . .	193
10.16 Plot from showing the connection between the diffuse cosmic rays, neutrinos, and gamma rays .	195

Figure	Page
10.17 The true neutrino energy spectrum of ESTES with the atmospheric flux from the self-veto approximation . . . . .	196
10.18 The true neutrino energy spectrum of ESTES with the atmospheric flux from both estimates of the atmospheric neutrino flux . . . . .	197
10.19 The true neutrino energy spectrum of ESTES for various neutrino fluxes . . . . .	198
10.20 The reconstructed neutrino energy spectrum of ESTES for the atmospheric flux from both estimates of the atmospheric neutrino flux and the astrophysical neutrino flux . . . . .	199
10.21 The true cosine zenith distribution of ESTES for all energies from various neutrino fluxes . . . . .	200
10.22 The true cosine zenith distribution of ESTES for a few slices in energy from various neutrino fluxes	201
10.23 Sensitivity to $E^{-2}$ fluxes for ESTES . . . . .	203
10.24 Sensitivity to $E^{-2}$ fluxes with cutoffs for ESTES . . . . .	204
10.25 Sensitivity to $E^{-2.5}$ and $E^{-3}$ fluxes for ESTES . . . . .	205
Appendix	
Figure	
B.1 The file size and run time as a function of the fraction of events above a threshold energy . . . . .	211
B.2 The cumulative response and passing fraction of 50 to 55 TeV neutrinos from various primaries are presented for two different zenith bands . . . . .	213
C.1 . . . . .	216
C.2 . . . . .	217
C.3 . . . . .	218
C.4 . . . . .	220
C.5 . . . . .	221
C.6 . . . . .	222
C.7 . . . . .	222
C.8 . . . . .	223

# Chapter 1

## Preface

This thesis describes an event selection for use with the IceCube neutrino detector. The goal of the event selection is to produce a data set of neutrinos which begin in the detector and have a track-like topology for use in physics measurements involving the astrophysical neutrino flux.

The thesis begins by describing the unsolved mystery of the high energy cosmic ray sources and giving context to how neutrinos can play a role (Chapter 2). After setting the stage, some background information needed to describe the physical situations encountered en route to the final selection are discussed (Chapter 3). The only situation not described in Chapter 3 is the atmospheric neutrino self-veto which is given its own section (Chapter 4). This method offers a way to circumvent the abundant atmospheric muon and neutrino fluxes in the southern sky and is crucial to the event selection in this thesis. This is not the first attempt to measure the properties of the astrophysical flux. Three published analyses have successfully measured the astrophysical flux and are relevant for context of any results from this work. Detailed discussion of the selections and their results can be found in Chapter 5. With the physics landscape set, focus shifts to describing the instrument and tools used in IceCube to make such a measurement. This begins with a description of the hardware and protocols of the constructed detector and ends with a description of the ice which IceCube is embedded in (Chapter 6). In order to describe the events which pass through detector and the resulting response a full simulation is relied upon (Chapter 7). The final pieces to producing physics measurements are reconstructing events direction and energy (Chapter 8) and classifying them so that only those which are relevant participate in the final result (Chapter 9). The outlook for the final result is presented in Chapter 10.

A few additional appendices have been included. The first is an appendix with event views and information about the events from the sample which are likely to be astrophysical. The third appendix discusses a modification to the air shower simulation CORSIKA which optimizes its run time and putput file size for generating atmospheric neutrinos. The final appendix is not directly related to the event selection in

this thesis, but provides information on a proof of concept data acquisition system designed to replace the existing IceCube DOM's DAQ.

The sections which contain original work completed for this thesis are in Chapter 4, Section 6.7.4, parts of Sections 7.1.2.2 and 7.1.3.4, Sections 8.3.5 and 8.3.6, Section 9, Section 10, and Appendices A, B, and C. For those who are familiar with IceCube only this original material is necessary reading as the rest is a description of the standard tools and physics of IceCube.

## Chapter 2

### High Energy Cosmic Rays

This thesis revolves around the prospect of detecting neutrinos from astrophysical sources with the cubic kilometer neutrino detector IceCube. The main purpose of studying such neutrinos is not to learn more about neutrinos, but instead use them as a tracer particle of high energy cosmic-ray production. The study of cosmic rays began in 1785 with the first studies of electricity using an electroscope by Charles-Augustin de Coulomb [1]. Such devices allowed the deposit of charge on a plate to be measured by the increase or decrease of distance between two attached foils kept in a vacuum. This was a breakthrough for electrostatics, however it was observed that even when kept shielded and alone, the electroscopes would discharge [2]. The proposal was that a source of charged particles must be responsible. Researchers proposed and measured the radiation levels in caves, above and under the water, and at slight elevation, but it was not until they took to the sky that they found their culprit. In 1911 Victor Hess detected increased radiation levels at high altitudes. This was measured by observing the rate of discharges in an electroscope as a function of height on a balloon ride, as can be seen in Figure 2.1 [3]. With this discovery flight, and further confirmation flights, the study of cosmic rays began in earnest and launched over a century of discovery which is still ongoing today.

Since his inaugural flight a lot has been learned about the cosmic rays which impinge on the atmosphere of the Earth. Most of the knowledge can be summarized by the plots shown in Figures 2.2, 2.3, and 2.4.

At the lowest energies, direct measurements of the cosmic rays themselves can be made with satellite and long duration balloon flight detectors, allowing the most information to be extracted [7]. From these measurements we know that the majority of the particles are hydrogen with contributions from all the particles with atomic number up to iron, the final product of energy positive particle fusion which can happen as a source of fuel for stars [8]. There are contributions above iron, but their contribution is negligible due to the scarcity of their production. Most of the incoming flux has a power law slope of -2.7 which it continues from around 1 GeV until around 1 PeV where there is a slight change in slope from -2.7 to -3.1 around what is commonly referred to as the knee in the cosmic ray spectrum [9]. This change in slope is hypothesized to be a feature of a change in the class of cosmic accelerator from a galactic one to an extra-galactic one.



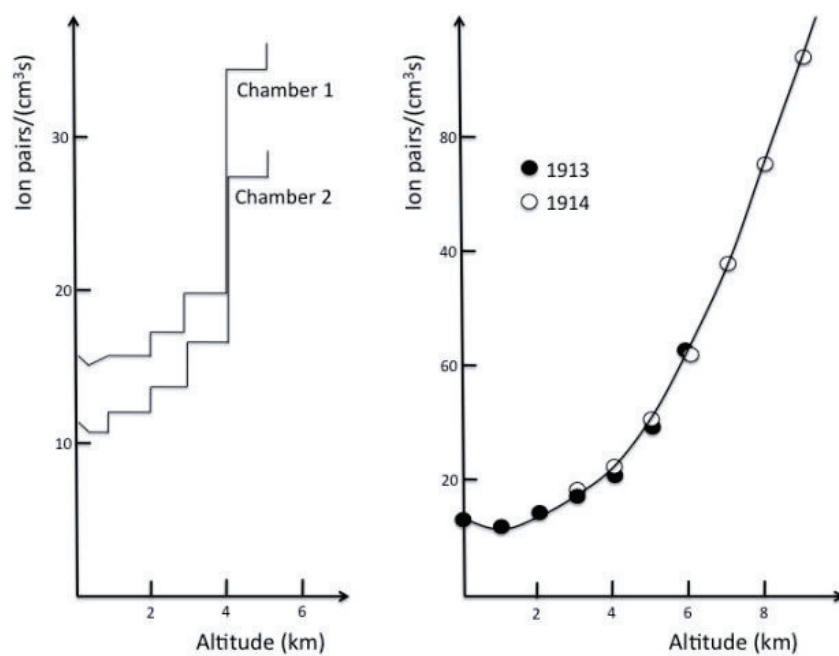


Figure 2.1: Results from Victor Hess' flights in 1912 at left and the follow up measurement by Werner Kolhörster in 1913 and 1914 at right. These results show a decrease in the number of observations before a steep rise at higher altitudes. The decrease originally had researchers convinced that the Earth must be the source of the radiation which discharged electroscopes, but Hess' results proved otherwise.

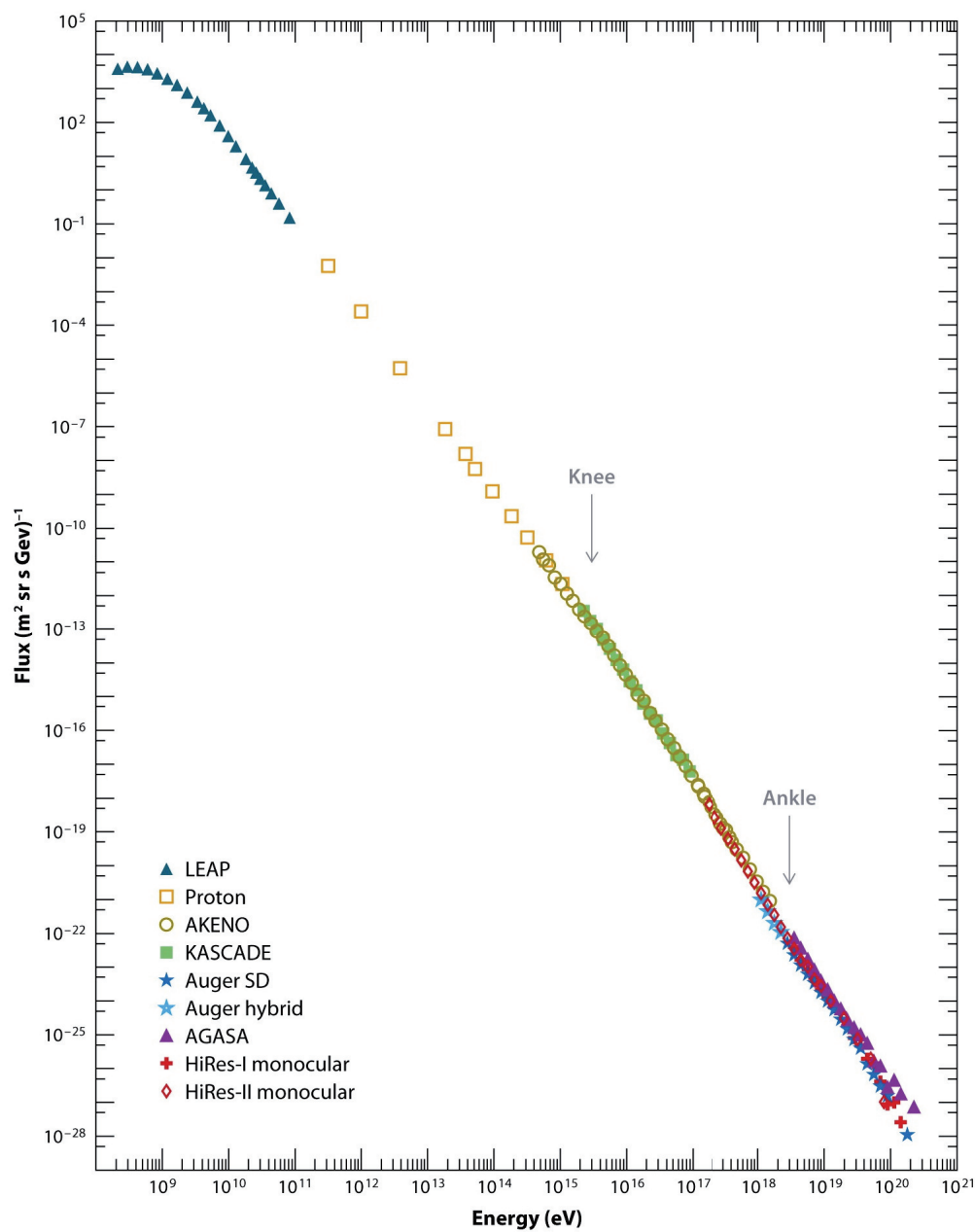


Figure 2.2: The full range of the cosmic ray spectrum from 100 MeV to 1000 EeV as measured by a handful of experiments from the review "The highest-energy cosmic rays" [4]. For the most part the spectrum has a constant index with deviations occurring only at the beginning and twice in the middle of the spectrum. A large number of experiments have measured a portion of the spectrum, but including all their results makes the figure incomprehensible.

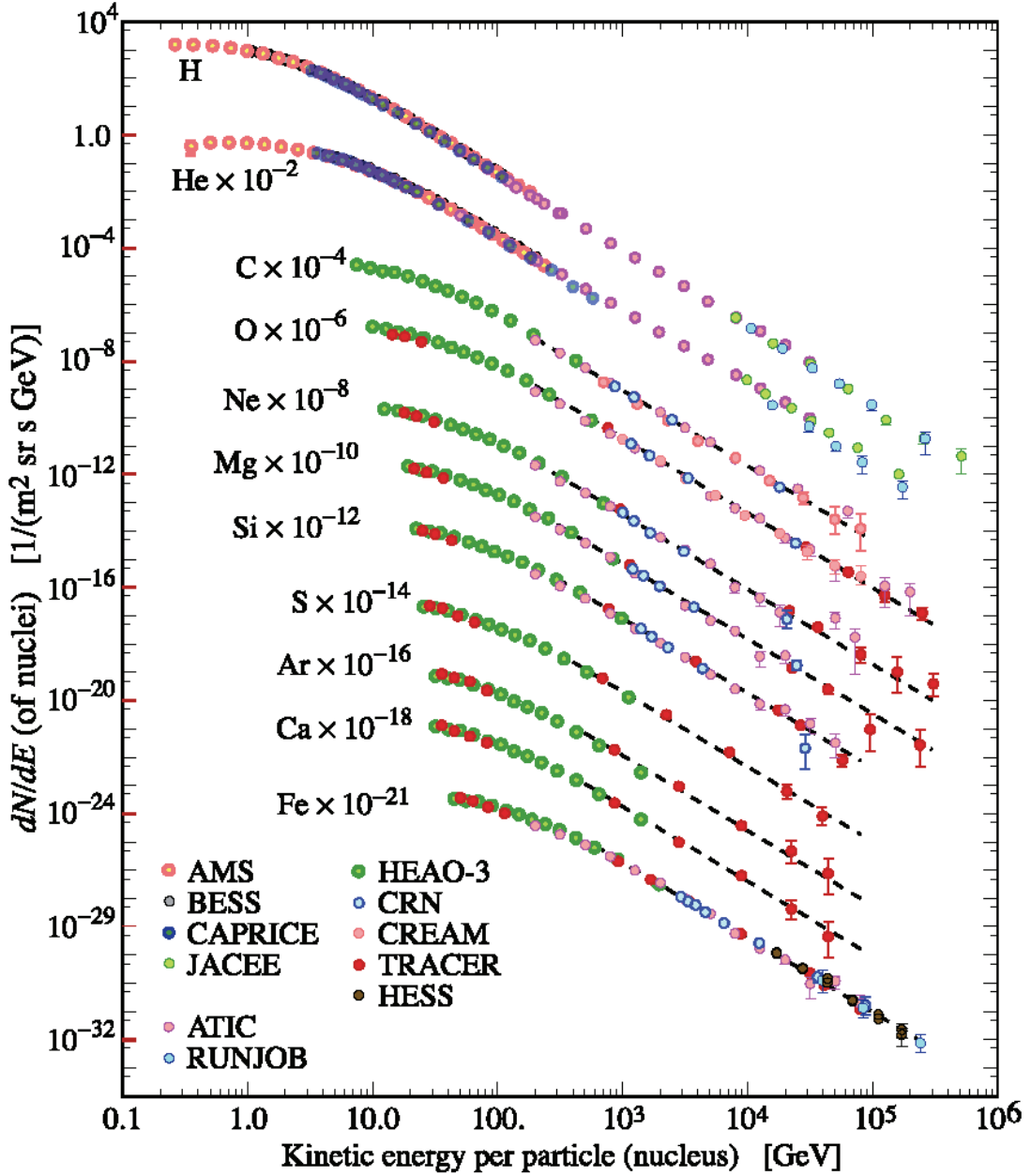


Figure 2.3: Cosmic rays of different types measured by a variety of experiments up to a PeV of energy. The most numerous are hydrogen followed by other nuclear types of decreasing quantity. Only trace amounts of nuclei heavier than iron can be found. The relative contributions of the nuclear types and the lack of particles above iron suggest a stellar origin for these cosmic rays. This figure comes from [5].

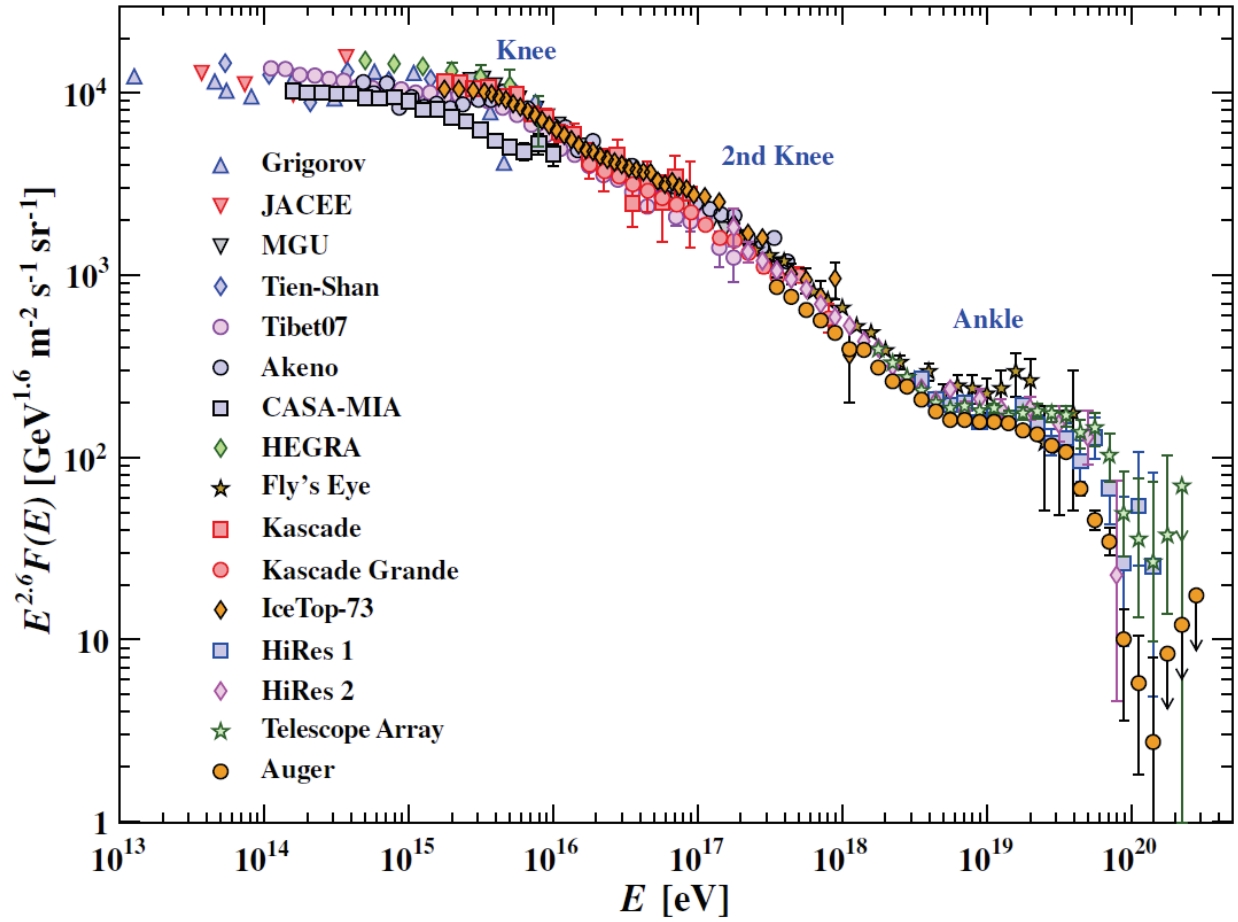


Figure 2.4: The total energy spectrum as measured by a variety of experiments from 10 TeV to 100 EeV. The spectrum is weighted by a factor of  $E^{2.6}$  to show the features which exist around the regions labeled knee and ankle. These are slight spectral changes which indicate a transition in the cosmic ray production sources. Also pictured is the cutoff in the cosmic rays due to the GZK beyond the highest energies in the plot. This figure comes from [6].

This finding is supported by energy budget arguments, but no individual source has been confirmed as the main contributor. At these energies, the flux is small enough that square kilometer size detectors must be used to acquire enough statistics to make strong statements about the cosmic rays. Detectors of this size are constructed on the surface of the Earth. These detectors are known as indirect detectors since the byproducts of cosmic rays which interact with the atmosphere after propagation are the detected particles. Because the byproducts are detected, rather than the parent cosmic rays themselves, inference of the parent particle's properties is subject to modelling of all the physics between the interaction and detection. Even so, it is agreed that the cosmic rays still have a mixed composition at these energies, and may not be dominated by hydrogen, instead it seems different particle types are dominant in different energy regimes. Moving higher still in energy the spectrum hardens again to an approximately  $-2.7$  around what is known as the ankle. This transition suggest that extra-galactic sources begin to dominate as the galactic sources lose power. Above the ankle are the highest energy particles which have ever been measured. The end of the spectrum at around 20 EeV does not mark a limit in our ability to measure higher energies, but an intrinsic limit set by the cosmic rays interacting with photons from the cosmic microwave background via the Greisen Zatsepin Kuzmin(GZK) process [10]. Measurements of the particles involves constructing extensive air shower (EAS) arrays of order 100s to 1000s of square kilometers in area. Two main experiments exist which can measure the highest energy particles of the flux. The experiments disagree about the cosmic-ray composition, but are actively working to unify the way modelling is handled between the experiments [11] [12]. However, both agree that the composition is not entirely iron or hydrogen, but some mixture or intermediate type.

The study of cosmic ray arrival direction as a proxy for the location of the cosmic ray production is a difficult task due to the presence of magnetic fields and the charged nature of cosmic rays. The presence of magnetic fields between the Earth and a source of cosmic rays means that in order to do self correlation, the source must be very close, or the cosmic rays must be very energetic. At the time of writing this, there are no confirmed sources of extra-galactic cosmic rays. However, this does not mean that the arrival direction of the cosmic rays is uniform. Thankfully, clustering analyses of cosmic rays is not the only way to search for their acceleration sites. This is where neutrinos come in. When cosmic rays are accelerated, they can interact with the matter or radiation of the source, before leaving the source. In the by-product of this interaction, neutrinos are created. Since neutrinos are neutral and interact very weakly they free stream from the source undeflected and unimpeded. IceCube is designed to detect these neutrinos, and with enough time possibly determine their sources.

## Chapter 3

### Physics Background

The large size and versatility of IceCube means that it is sensitive to particles from tens of GeV to tens of PeV in energy (further if you consider special data taking modes for MeV energy supernova neutrinos). The physics that must be considered across these energy ranges is similar, but contains nuances that must be understood for quality physics results to be produced. However, for this thesis particles in the detector in the energy range from roughly 1 TeV to 1 PeV need to be considered and this focus simplifies the picture. This section is focused on the physics background relevant for the rest of the thesis, specifically cosmic rays, neutrinos, muons, and Cherenkov radiation.

#### 3.1 Cosmic Rays

The term "cosmic rays" was coined before scientists understood what the building blocks of matter were, but after they observed the effects of radiation which was assumed at the time to be a form of electromagnetic radiation. Thus, the radiation from outside the Earth's atmosphere was given its name. Scientists now know that the cosmic rays are a combination of gamma rays, leptons, and ionized nuclei. For this thesis, we are concerned with cosmic rays for two reasons: their properties at the source where they are created and produce neutrinos, and their properties at Earth where they interact with the atmosphere creating atmospheric neutrinos and muons. For cosmic rays that are particles in nature and arrive at Earth with more than a TeV of energy it is known that the sources from which they originate must have processes which can accelerate particles up to very high energies. To give a sense of scale, a particle at 1 TeV has an energy over three orders of magnitude larger than the kinetic energy gained by a proton falling into a non-rotating black hole as given by

$$\begin{aligned}
 U &= \frac{GM_{BH}m_p}{R_{BH}} \text{ and } R_{BH} \approx \frac{2GM_{BH}}{c^2} \\
 \implies U &= \frac{m_p c^2}{2} \approx .5 \text{ GeV for a proton}
 \end{aligned}
 \tag{3.1}$$

where  $U$  is the potential energy,  $G$  is the gravitational constant,  $M_{BH}$  is the mass of the black hole,  $m_p$  is the mass of a proton,  $R_{BH}$  is the radius of a black hole, and  $c$  is the speed of light. Since these particles

possess much more energy than the gravitational potential of a black hole can contain, the regions in which the particles are accelerated must have another binding force. All of the candidate classes for cosmic ray acceleration possess large magnetic fields to keep these particles contained while they are being accelerated by non-gravitational means [13]. The simple relation between energy  $E$  and gyro radius  $R_{gyro}$  for a particle with charge  $q$  and mass  $m_p$  moving with velocity  $v$  in a magnetic field  $B$  is given by

$$F_{Lorentz} = qvB \text{ and } F_{cent} = \frac{m_p v^2}{R_{gyro}}, F_{Lorentz} = F_{cent} \implies R_{gyro} = \frac{m_p v}{qB} \quad (3.2)$$

$$\text{where } m_p v = \text{relativistic energy} \implies \frac{E}{c} = \gamma q B R_{gyro}$$

where the  $\gamma$  comes in to account for the possibility that the observer is not in the rest frame of the accelerator. This relationship shows that an interplay between the size of cosmic objects and their magnetic fields is at play. From this, one can evaluate which sources are able to accelerate particles to a certain energy based on measurements of their size and magnetic field, as is shown in Figure 3.1 [14]. For neutrino astrophysics we are only concerned about the sources which can accelerate particles to the highest energies and have nuclei available for acceleration. As such this chapter will have sections focusing on: pulsars, supernova remnants, x-ray binaries, blazars, gamma ray bursts, and star-forming galaxies. As far as cosmic ray nuclei are concerned some of these are still only theorized as sources since the only particles that have known origins at energies above a TeV are gamma rays. The reason for the lack of known sources for charged cosmic rays stems largely from the same property that allows them to get up to such high energies in the first place: their charge. As charged nuclei and leptons transit the cosmos, they are affected by local magnetic fields which have unknown characteristics. This means that only the cosmic nuclei with the highest measured energy have a chance to point back to extra-galactic sources if that is where they originate from. Currently, there are only two experiments that have measured cosmic nuclei at these energies and the experiment's results disagree if the nuclei point back to known objects or not [11] [12]. However, the existence of cosmic rays at these energies suggests an extra-galactic origin. Gamma rays do not share this problem and have been used to resolve sources, but also have their own problems. As gamma rays travel, they can interact with matter and other photons that they encounter and lose energy via electron-positron pair production. This means that low-energy photons from the cosmic microwave background or ambient photons from the sources where the gamma rays are created can abate the number of high-energy gamma rays. For two photons interacting to create an electron-positron pair, the minimum energy required in the parent photons is  $2m_e$  in the center of mass frame. Evaluating the incoming and outgoing 4-momenta of this interaction we see in

$$h\nu_2 \geq \frac{2m_e^2 c^4}{h\nu_1(1 - \cos(\theta))} \quad (3.3)$$

where  $\nu_1$  and  $\nu_2$  are the frequencies of the gamma ray and other photon respectively,  $h$  is the Planck constant, and  $\theta$  is the angle between the incoming photons. This means head-on interactions between 1 TeV

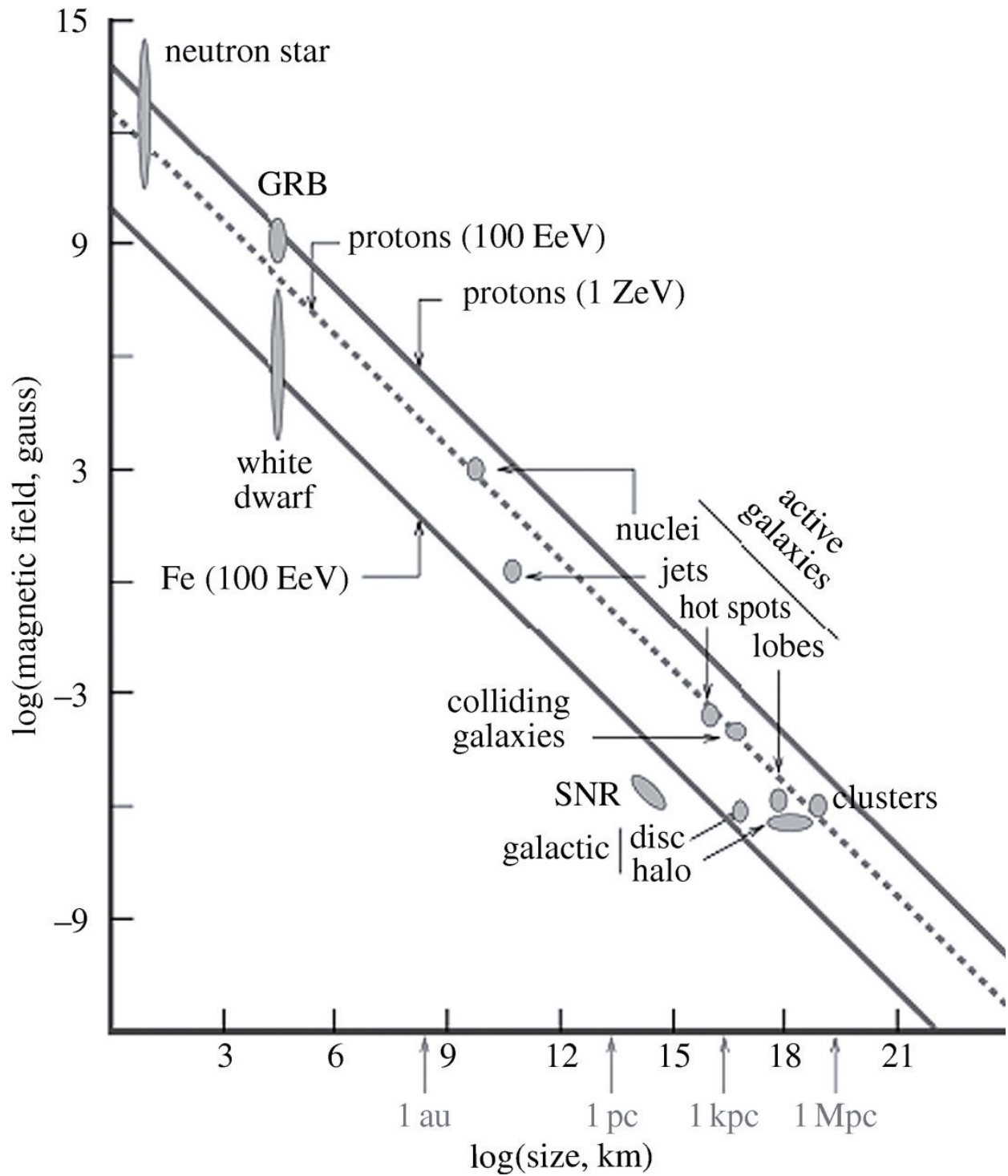


Figure 3.1: A version of the Hillas plot, named after its original creator, which outlines the magnetic fields around and sizes of objects which are needed to accelerate cosmic rays up to  $10^{20}$  eV. Only certain classes of objects are options for the highest energy cosmic ray acceleration. This figure comes from [15] and is a recreation of the original from [14].



gamma rays and infrared photons and 1 PeV gamma rays and microwave photons lead to pair-production and annihilation of the original gamma ray. This leads to a horizon beyond which gamma rays cannot be seen, as can be seen in Figure 3.2. The gamma rays which do come from identifiable sources have the further

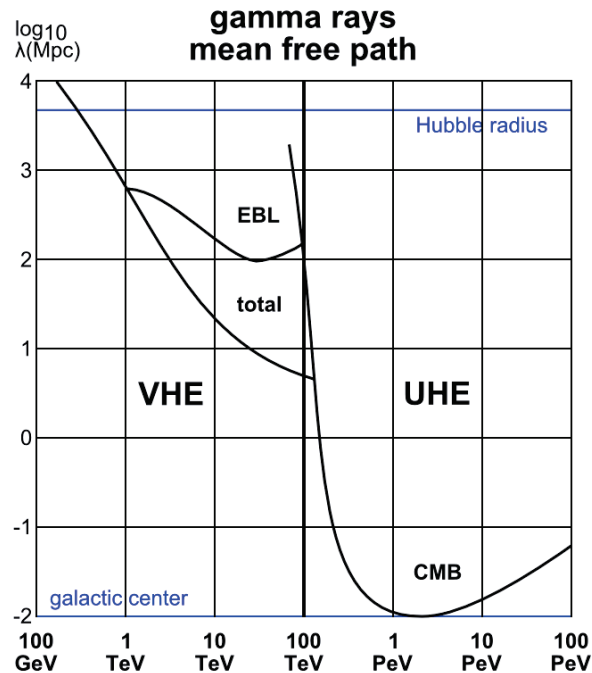


Figure 3.2: Mean free path of gamma rays as a function of energy. The mean free path is a calculation which involves both the interaction likelihood of a gamma ray with lower energy photons and the density of the lower energy photons. This figure is taken from [16].

complication that there are two ways to create them, a leptonic and a hadronic one. Leptonic gamma rays are largely produced by the up-scattering of synchrotron photons in collisions with high energy electrons, or by bremsstrahlung. On the other hand, hadronic gamma rays come from the decay of neutral pions after a cosmic ray nucleus interacts with a particle or photon. These neutral pions decay quickly and produce two gamma rays. Thus, the presence of a gamma ray source does not imply the existence of high energy cosmic rays, but high energy cosmic rays do imply the existence of gamma rays.

The limitations of the cosmic rays to do self-association, and the gamma rays' deficiency in penetrating power and origin ambiguity has left a hole the search for cosmic ray sources which neutrino astrophysics hopes to fill in. Specifics about the properties of neutrinos are discussed in the next section (3.2), but for now suffice it to say neutrinos possess a rare combination of properties in the particle world. They are nearly massless, neutral, interact very infrequently, and travel at nearly the speed of light. As a result they do not deflect, easily escape their sources, and transit extra-galactic distances. These properties make them

good candidates for finding the sources from which they, and their cosmic-ray relatives, originate. As was touched on with the gamma rays, cosmic ray nuclei with very high energies can interact with photons or other particles and undergo production of the delta resonance [17]. This delta particle then undergoes a decay into either a charged baryon and a neutral pion or a neutron and a charged pion. Neutral and charged pions occur with a frequency of about  $\frac{2}{3}$  and  $\frac{1}{3}$  respectively. Both neutral and charged pions decay quickly. For the neutral pion, the byproduct is two gamma rays as was already discussed and for the charged pion the decay results in a charged lepton and neutrino, most commonly an anti-muon and muon neutrino. For the charged pion branch, there is further contribution from the decay of the neutron and muon. The neutron will decay into a proton, electron, and electron neutrino. While the muon will decay to an electron and electron neutrino. All together the interaction is

$$\begin{aligned}
 p + \gamma_{target,p} + N &\rightarrow \Delta^+ \rightarrow p + \pi^0 \rightarrow p + 2\gamma \\
 p + \gamma_{target,p} + N &\rightarrow \Delta^+ \rightarrow n + \pi^+ \rightarrow p + n + \mu^+ + \nu_\mu \\
 &\rightarrow n + e^+ + \nu_e + \bar{\nu}_\mu + \nu_\mu \\
 &\rightarrow p + e^- + e^+ + \nu_e + \bar{\nu}_e + \bar{\nu}_\mu + \nu_\mu
 \end{aligned} \tag{3.4}$$

Of the four neutrinos in the final state of the charged pion decay branch, three of them are of roughly the same energy while the one resulting from the neutron decay will be about two orders of magnitude less energetic as a result of sharing the neutrons momentum with a proton in the decay. Combining together all possible outcomes, there are about two high gamma rays for every three or four high energy neutrinos produced by this mechanism [18].

As was discussed at the beginning of this section, there must be some mechanism present to accelerate these charged cosmic-ray nuclei up to the maximum of their host's magnetic containing ability. The understood phenomena which can drive such acceleration are described in the next section (3.1.1).

### 3.1.1 Charged Particle Acceleration

#### 3.1.1.1 Shock Acceleration

Basically put, shock acceleration occurs when a particle, relativistic or otherwise, encounters matter or a magnetic field moving at a different velocity than the particle's and has an interaction which alters the particle's energy. The original arguments for this process were laid down by Fermi in 1949 [19]. He argued that in the case of particles moving around weak magnetic field lines of the interstellar medium, there would occasionally be interactions with irregularities in the field which would on average cause a gain in particle energy rather than a loss since equilibrium between the degrees of freedom of the fields and the particle is preferred. These interactions can be portrayed by the simple mechanics problem of a small object moving with velocity  $v$  bouncing off a much more massive object which is moving towards the small object with

some velocity  $u$ . If this collision is viewed from a stationary frame with respect to the massive object then the small object is moving towards it with a velocity equal to  $(v + u)$ . After the collision, the ball moves away with the same speed in the opposite direction in the stationary frame. However, in the transformation back to the frame where the wall is moving with its original velocity the ball has now gained velocity and  $v' = -(v + 2u)$ . As a result, collisions that increase energy in this way stand to impart a positive energy change to the smaller particle which is proportional to  $v'^2$ . This mechanism is commonly referred to as second order Fermi acceleration since its energy gain goes like  $v'^2$ . This mechanism is most effective when the shocks are relativistic and less effective otherwise. From this process particles can gain energy exponentially with respect to the number of collisions they undergo. While this argument was laid out originally by Fermi for magnetic fields, it holds true for moving clouds of particles interacting with particles in less dense particle clouds as well. There is also a first order Fermi acceleration which is most effective when shocks are non-relativistic. This was also originally derived by Fermi but is taken from Gallant [20] for this discussion. For this situation, imagine a particle moving through space in the upstream portion of a medium separated by a shock. If the particle crosses into the shock with a relative angle  $\theta_d$  to the shock normal its Lorentz transformation will increase its energy by a factor  $\Gamma_{med}(1 - \beta_{med}\cos(\theta_d))$  where  $\Gamma_{med}$  and  $\beta_{med}$  are the Lorentz factor and relative velocity of the medium. The particle then has two options. It can escape and undergo no further shock acceleration, or it can cross the shock again this time incurring an increase to its energy given by  $\Gamma_{med}(1 + \beta_{med}\cos(\theta_u))$  where  $\theta_u$  gives the angle of incidence to the shock normal for this crossing. Thus, after two crossings

$$\frac{E_f}{E_i} = \Gamma_{med}^2(1 - \beta_{med}\cos(\theta_d))(1 + \beta_{med}\cos(\theta_u)) \quad (3.5)$$

if the velocity of the medium relative to the speed of light is much less than 1, the angles of incidence can be taken as isotropic and averaged over their relevant ranges giving

$$\langle \cos(\theta_d) \rangle = \int_{-\frac{\pi}{2}}^0 \theta \cos(\theta) d\theta = \cos(\theta) + \theta \sin(\theta) \Big|_{-\frac{\pi}{2}}^0 = 1 - \frac{\pi}{2} \approx -\frac{2}{3} \quad (3.6)$$

$$\langle \cos(\theta_u) \rangle = \int_0^{\frac{\pi}{2}} \theta \cos(\theta) d\theta = \cos(\theta) + \theta \sin(\theta) \Big|_0^{\frac{\pi}{2}} = \frac{\pi}{2} - 1 \approx \frac{2}{3} \quad (3.7)$$

thus since  $\Gamma_{med} \sim 1$

$$\left\langle \frac{E_f}{E_i} \right\rangle = \left(1 + \beta_{med} \frac{2}{3}\right) \left(1 + \beta_{med} \frac{2}{3}\right) \approx 1 + \beta_{med} \frac{4}{3} \quad (3.8)$$

This particle is once again able to escape or cross the shock again at a later time and further increase its energy. Through this mechanism, particles can increase their energy exponentially with the number of crossings as well.

### 3.1.1.2 Shear Acceleration

Shear acceleration operates with the same set of properties as those of first order Fermi acceleration but with a slightly different geometric setup. Imagine that there is a jet of material that is moving fast with respect to its surrounding material. A particle moving from the jet to the surrounding material or back will receive a Lorentz boost just as in the picture of a plane shock moving through a medium [21]. As a result, particles can gain energy exponentially with respect to the number of boundary crossings in shear acceleration around jets.

### 3.1.1.3 Voltage Drops Induced By Changing Magnetic Fields

Neutron stars commonly have high magnetic field strength, small radius, and spin very rapidly. The alignment of the magnetic pole for neutron stars is often not in line with the rotation pole and leads to an induced electric potential as given by the solution to Laplace's equation for a spinning magnetic field [22].

$$\Phi = \frac{-B\Omega R^3}{3c} P_2(\cos\theta) \quad (3.9)$$

where B is the polar magnetic field, R is the radius of the star,  $\Omega$  gives the rate of revolution, and  $P_2$  is the second degree Legendre polynomial. The maximum value for this potential is given when the rotation axis and magnetic pole are offset by 90 degrees.

## 3.2 Neutrino Physics

Neutrinos have unique properties in particle physics. Neutrinos are leptons which come in three flavors; electron, muon, and tau corresponding to their partner lepton in the standard model. They have three masses; heaviest, middle, and lightest and can be normal or anti-particles. In the standard model, neutrinos are massless, but since the original measurement of the anomaly in neutrinos from the sun in the 1960s [23] it has been suspected that they possess a very small non-zero mass [24] [25]. Neutrinos do not stay in the same flavor and mass state as they propagate. Instead they oscillate between the states as they propagate, a feature of their non-zero mass. Above 1 TeV the neutrinos IceCube detects come either from the atmosphere, which is too short a distance for oscillation to occur for these neutrinos, or in distant astrophysical sources where the propagation distance is so large that the oscillations yield complete mixing and a nearly 1:1:1 mixture of neutrino states regardless of the original composition [26] [27]. Neutrinos only interact weakly and as a result can pass through large amounts of matter, such as the entire Earth, without interacting. Neutrinos interact with nuclear matter in a number of ways but above 100 GeV only deep inelastic scattering and Glashow resonance interactions are relevant. In order for deep inelastic scattering to occur, the neutrino must enter the nucleus where it can interact directly with a quark and undergo either a neutral or charged interaction [28]. Neutral interactions involve the exchange of a neutral Z boson with the quark, ejecting it

from the nucleus and leading to the subsequent breakup and cascading of the nucleus. A new neutrino is created with energy equal to the original neutrino's less the exchanged energy and continues propagating on. Neutral current interactions are depicted in the left diagram of Figure 3.3. In a charged interaction

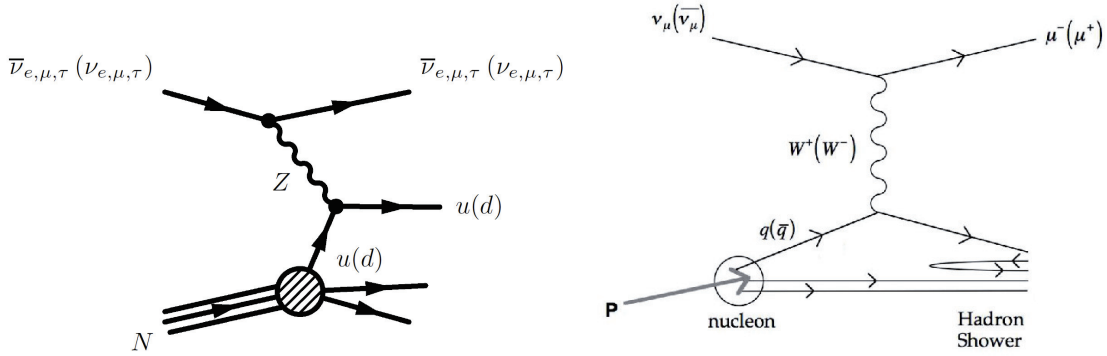


Figure 3.3: The figure at left depicts neutral current Feynman diagrams for a neutral current interaction. Neutrinos of all flavors are shown interacting with a neutral Z boson and ejecting the interacting quark from the nucleus. This figure comes from [29]. The right figure shows a charged current muon neutrino interaction Feynman diagram. Other neutrino types also can interact this way and are represented by simply exchanging the proper lepton labels for the muon labels. This figure comes from [28].

a positive or negative W boson is exchanged with the quark, depending on if a neutrino or anti-neutrino respectively is involved. Since the W is charged, an oppositely charged particle must be involved to keep the total charge content of the interaction before and after the same. This oppositely charge particle comes in the form of the partner lepton (or anti-lepton) of the interacting neutrino. Again, the quark with which the boson was exchanged is ejected from the nucleus and leads to the subsequent break-up and cascading of the nucleus. There is an accompanying outgoing lepton. The cross-sections for neutral current and charged current interactions depend on the kinematics of the reaction with quarks in the nucleus. The cross-sections for charged current interactions can be seen in Equation 3.10 while the neutral current interactions are in Equation 3.11.

$$\frac{d^2\sigma}{dx dy} = \frac{G_F^2 M E_\nu}{\pi} \times 2 \left( \frac{M_W^2}{Q^2 + M_W^2} \right) [xq(x, Q^2) + x\bar{q}(x, Q^2)(1-y)^2] \quad (3.10)$$

$$\frac{d^2\sigma}{dx dy} = \frac{G_F^2 M E_\nu}{\pi} \times 2 \left( \frac{M_Z^2}{Q^2 + M_Z^2} \right) [xq(x, Q^2) + x\bar{q}(x, Q^2)(1-y)^2] \quad (3.11)$$

In Equations 3.10 and 3.11  $Q^2 = -q^2$  is the transferred momentum from the neutrino to the created lepton,  $\nu = E_\nu - E_{(l, \nu)}$  is the energy lost in the rest frame,  $M$  is the mass of the nucleon,  $M_W$  and  $M_Z$  are the masses of the bosons that mediate the weak interaction, and  $G_F$  is the Fermi constant. This gives a cross section which is linear up to a few TeV with a decreased slope after that point from the  $1/Q^2$  term in the

propagator. These cross sections are plotted in Figure 3.4. Glashow resonance interactions occur when the

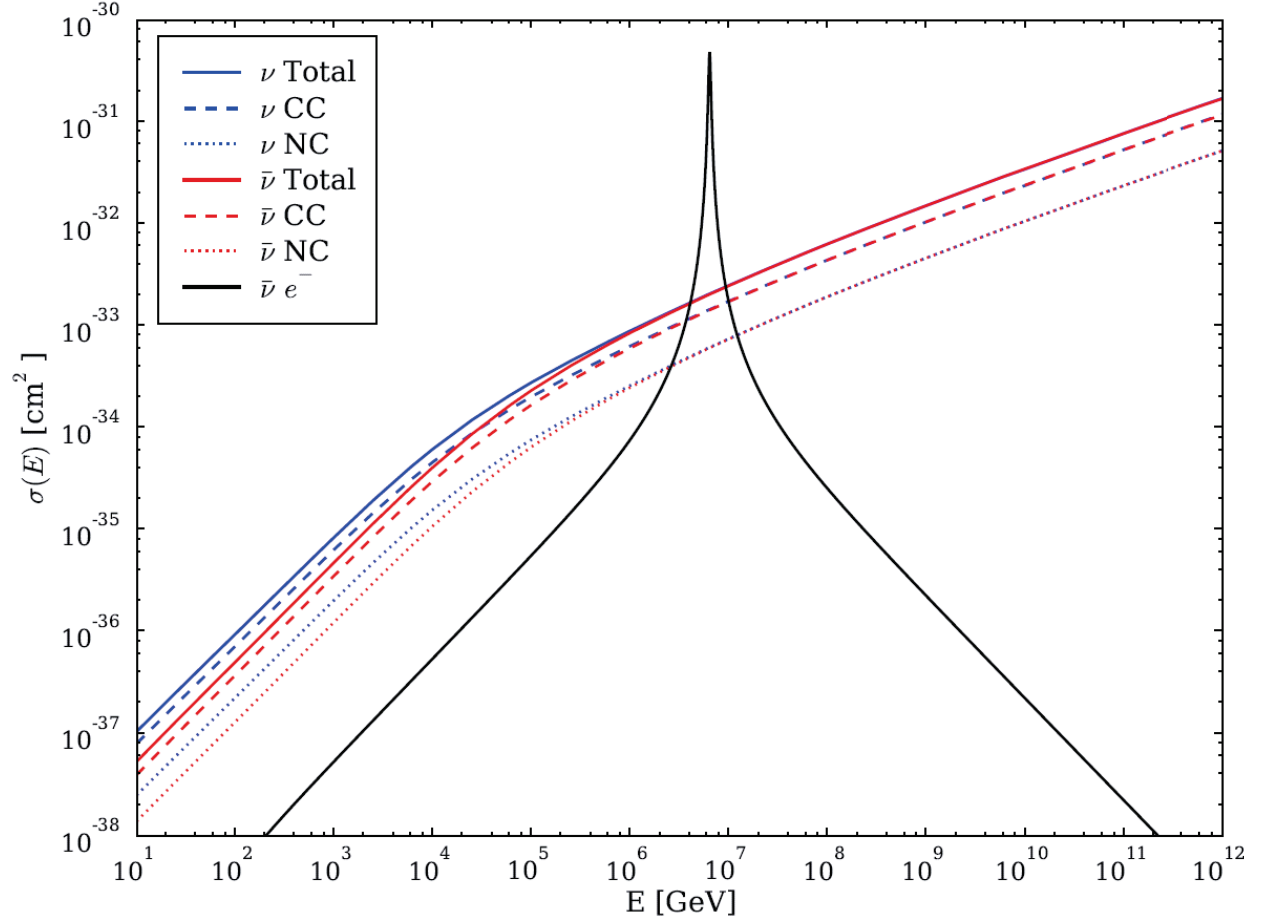


Figure 3.4: Neutrino-nucleon cross sections from 10 GeV to 100 EeV from [30] based on data from [31]. Linear behavior up to 10 TeV of the deep inelastic interactions can be seen as well as the decreased slope after 10 TeV. Also the Glashow resonance is shown as the sharp peak in  $\bar{\nu}e$ .

center of mass energy between an  $\bar{\nu}_e$  and an electron of the interaction reaches 6.3 PeV. This energy is high enough to directly produce a W boson. The outgoing boson then creates an anti-neutrino and corresponding lepton or hadrons.

### 3.3 Atmospheric Neutrino Production

The interaction of cosmic rays with the Earth's atmosphere leads to hadronic cascades which develop as the particles descend through the atmosphere. Of the hadrons produced, pions are the most numerous, followed by kaons. Together these particles make up what is called the conventional part of the atmospheric neutrino spectrum. The other part of the atmospheric neutrino spectrum is referred to as the "prompt"

component because the decay of the included particles happens very quickly. Often the prompt component is synonymous with charmed particles but there are many particles with prompt decays which are not of charmed origins. However, neutrinos produced via prompt decays only come from charmed particles. This makes them a good candidate for a measurement of atmospheric charm production if the neutrinos can be distinguished from other sources of neutrinos. At energies below 100 GeV neutrino production from muon decay is relevant, but above 100 GeV the muons have penetrated too far before decay for an appreciable flux to be accumulated.

### 3.3.1 Conventional Neutrino Flux

As was mentioned before, pions are produced more numerous than kaons in air showers and thus have a larger contribution to the neutrino flux. When pions decay, their most probable channel for doing so is via production of a muon with the same charge as the pion and the corresponding neutrino. Pions have a cross section that rises with energy such that around 115 GeV interaction with the atmosphere becomes more likely than decay for the pion [32]. At this point, the neutrinos from kaon decay dominate. Again the most likely channel for decay is via production of a muon with the same charge and the corresponding neutrino. However, there are other channels available to kaons such as the production of a muon and a pion, or production of an electron, electron neutrino, and a pion commonly known as associated production. Associated production is the only source of electron neutrinos above muon decay energies. Because both pions and kaons undergo decay to create their neutrinos the spectrum they assume is one power steeper (-3.7) than the parent cosmic ray spectrum of -2.7.

### 3.3.2 Prompt Neutrino Flux

Prompt neutrinos are largely the result of D and  $\Lambda$  decays in the atmosphere [33]. The amount of production of these charmed hadrons in cosmic ray interactions is not yet known because the very forward production region of the initial cosmic ray interaction is relevant and cannot be constrained by accelerator experiments [34]. As such there are a number of models which include charm production in full air shower Monte Carlo and analytical calculations [33] [35] [36]. The results of one of the more recent techniques is shown in Figure 3.5. For muon neutrinos the prompt flux does not dominate the atmospheric flux until a few hundred TeV due to the presence of a direct kaon decay channel to muon neutrinos. However, for the electron neutrinos there is no dominant conventional source of neutrinos and the prompt electron neutrino flux is the dominant atmospheric component above 10 TeV. Unfortunately for the measurement of the charm flux recent measurements of the astrophysical neutrino flux gives a normalization which is higher than that of the predicted charm flux. This means the charm flux is subdominant to the astrophysical flux, which

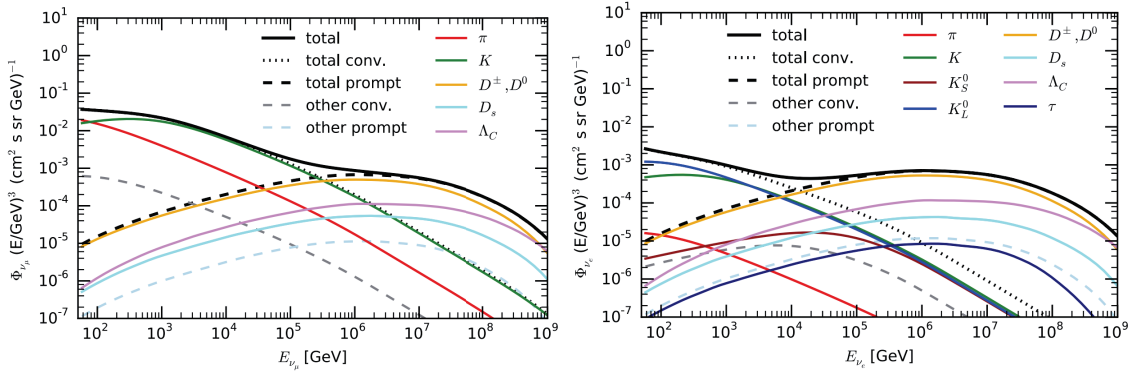


Figure 3.5: The atmospheric neutrino flux for muon type neutrinos is shown in the left plot while the electron type is shown in the right plot. The prompt flux for both types is dominant at the highest energies. These plots come from [33].



precludes a measurement of it in isolation. Still, IceCube is placing constraints which rule out the more optimistic models of charm and will continue to rule out models or make an observation eventually [37].

### 3.4 Astrophysical Neutrino Production

The mechanism for astrophysical neutrinos is actually very similar to that of the main production of atmospheric neutrinos. At their sources, cosmic rays are accelerated to very high energies and contained in the source. Also in the source are matter and radiation which were either blown out by a cataclysmic event which powers the cosmic ray acceleration or are accreting onto the massive object which is driving jet production [13]. This theoretical environment yields the perfect place for p-p or p- $\gamma$  interactions to occur. After interaction, pions are produced. If they are charged pions they subsequently decay in the rarefied matter of the source. The result is a muon and muon neutrino. The muon neutrino free streams from the source while the muon propagates and subsequently also decays into a muon neutrino and an electron neutrino which also free stream. The resulting neutrinos from these cosmic ray interactions typically have about 5% of their parent's energy [38]. If the pions are instead neutral they decay immediately to gamma rays. This forms an interesting link between neutrinos and gamma rays. The neutrino sources must also be gamma ray sources if the sources are not opaque to gamma rays. However, since gamma rays can be created by electromagnetic processes as well as the decay of neutral pions the gamma ray sources do not have to be neutrino sources. This is what makes neutrinos, and not gamma rays, the smoking gun signature of cosmic ray acceleration. In the following sub-sections a few proposed production sites of astrophysical neutrinos will be discussed.

#### 3.4.1 Diffuse Neutrinos from the Galactic Plane

The galaxy is believed to contain accelerators which are capable of producing cosmic rays up to the knee in the cosmic ray spectrum (3 - 4 PeV). These cosmic rays combined with the cosmic rays from other distant sources are trapped in the Milky Way and give the flux of cosmic rays detected at Earth. However, because of the concentration of point-like sources closer to the inner galaxy and the local heliosphere the flux at Earth is not the same as the flux throughout the galaxy. As a result extrapolations based on the measured flux at Earth and evidence from gamma ray measurements are used to estimate the galactic cosmic ray flux. Interactions of this cosmic ray flux with the material in the galaxy can be expected to produce a flux of neutrinos up to hundreds of TeV [38].

#### 3.4.2 Possible Astrophysical Sources of Neutrinos

Various classes of sources are potential accelerators of cosmic rays, and thus neutrinos. The sources range from energetic stars in various stages of their lives to super massive black holes accreting matter. Each has

the potential to accelerate particles to high energies through the mechanisms discussed in Section 3.1.1 and possesses large amounts of matter or photons to interact with.

### 3.4.2.1 Pulsars

When a star ends its life cycle in a supernova, one of the possible outcomes is a neutron star [39]. During the supernova, a large amount of material is blown away from the object and encircles the star; this is commonly referred to as the pulsar wind nebula [40]. Neutron stars commonly have high magnetic field strength,  $\sim 10^{12}$  G, small radius,  $\sim 10$  km [41], and spin very rapidly,  $\sim$  few hundred Hz. As was seen in the section on particle acceleration by induced potentials (3.1.1.3), these conditions can create a large potential difference around the poles of a neutron star if there is little to no scattering to affect the accelerating particles. Theoretically, the potential developed can be screened by electrons and positrons created by pair production by synchrotron gamma rays produced by other electrons and positrons moving around the strong magnetic fields. However, if one neglects this screening argument believing it to be a weak contribution and uses the values found for typical young neutron stars, the ions accreted from the surrounding wind nebula and brought to the magnetic polar regions by accretion and the strong magnetic fields can be accelerated to energies larger than an EeV [42]. As a result, the production of pions via the delta resonance in the star's atmosphere and surrounding nebula is possible and should occur. While this is the case, no observations of high energy gamma rays originating from young pulsars have been made to date which makes these sources unlikely to be neutrinos sources.

### 3.4.2.2 Supernova Remnants

Supernova remnants, as the name suggests, are what remains after a star's internal fusion energy is no longer enough to counteract the force of gravity resulting in a collapse and subsequent explosion which ejects a large portion of the star's mass away from the remaining compact object at around 10% of the speed of light [43]. There are two possible mechanisms by which the acceleration of ions can occur in the resulting environment. First, the resulting shell of ejected material produces a shock ahead of it which can accelerate particles via Fermi acceleration. This acceleration is thought to produce a large fraction of the cosmic rays with Galactic origin and could also produce higher energy ions and neutrinos as a result [44] [45]. Another possibility is that at the end of the supernova which created the remnant, a neutron star was created. In this case, the situation arising would be similar to that found with pulsars and acceleration could occur from the large potential resulting from the highly magnetized rapidly spinning star.

### 3.4.2.3 X-Ray Binaries

X-Ray binaries form when one of the stars in a binary system undergoes a supernova to become a black hole or neutron star. This conversion must occur such that the binary system remains bound and the compact object accretes matter from the companion star. When this happens large amounts of x-ray emission results from the accretion. With the compact object being either a black hole or a neutron star, there is a possibility for a jet outflow to form and shear acceleration of ions to occur as a result [46]. Additionally, if the compact object is a spinning neutron star, there is the possibility to create large potentials with which to accelerate ions, though they are likely to be shielded from the abundance of matter found in the accretion disk around the neutron star.

### 3.4.2.4 Blazars

Active Galactic Nuclei (AGN) are thought to be super-massive black holes occupying a small area at the center of galaxies. Blazars are a classification of AGN with unique properties. Blazars were originally found to have completely flat spectrum at radio frequencies and highly variable emission like BL-Lacertae objects. However, when surveys extending across larger frequency ranges set their sights on these objects they found that they also possess broad emission lines like those found in quasars. Thus, these objects which have emission features encompassing BL-Lacertae like objects and quasars were given the portmanteau Blazar to describe them [47]. These objects are among the most luminous cosmological sources, with jet emission perpendicular to the accretion disk formed around the black hole. The emission of Blazars is thanks to the alignment of the jet is such that Earth being within the jet's emission cone. Acceleration of ions in these jets gives a potential source of high energy particles [48] and the radiation and surrounding matter in the jet could provide a nice target [49] for photo-hadronic or nuclear production of the delta resonance and resulting neutrinos implied by the process.

### 3.4.2.5 Gamma Ray Bursts

When a gamma ray burst (GRB) occurs more energy is released in 10 seconds than the sun will emit in its entire lifetime. The mechanism behind these violent explosions is far from agreed upon, but the two leading models are shock collisions between slow and fast shells around black holes [50] and compact object mergers. Both models propose acceleration of ions by shocks resulting from violent events and interaction with other accelerated matter or resulting radiation [51][52].

### 3.4.2.6 Starburst Galaxies

Starburst galaxies are regions of dense matter where star formation occurs much faster than in other galaxies. As a result, high mass stars, which quickly go through their life cycles and end in supernovas, are

also relatively more abundant leading to many supernova remnants existing within a galaxy. With many supernova remnants existing, there is a possibility for acceleration of ions in shocks. Additionally, there are large amounts of dense matter in these galaxies which comes from the mass ejecta during the supernova and from which the stars were formed. As a result, there is good opportunity for neutrino production to occur [53], but recently limits have been placed on how much of the diffuse neutrino flux could originate from this class of sources [54].

### 3.4.3 Cosmogenic Neutrinos

At the end of the likely cosmic ray spectrum is a hard cutoff in the spectrum. This cutoff is due to the interaction of the ultra high energy cosmic rays with cosmic microwave background (CMB) photons [55] [56]. Cosmic rays' interactions often produce a charged pion which will decay as discussed in Section 3.1. Since there are no known sources of EeV cosmic rays within 30 Mpc of Earth, a depletion of cosmic rays and a build up of neutrinos should occur at EeV energies [57]. This flux is guaranteed by the presence of cosmic rays up to the cutoff energy but is predicted to be very small. IceCube can measure neutrinos up to the necessary energy but much of the flux lies above its reach and is the study of dedicated radio based neutrino experiments [58].

## 3.5 Muon Physics

Muons are the second heaviest charged lepton in the standard model. For all applications we will consider, muons travel at nearly the speed of light. They can be created and destroyed via the weak and electromagnetic force and interact with the media they are traversing and undergo energy losses via the electromagnetic force. The majority of the muons in IceCube are created via pion and kaon decay in the atmosphere, though there are other sources such as charged current muon neutrino interactions. The muons from pion decay in the atmosphere travel down through the atmosphere into the ice where they can survive all the way to IceCube, after traversing over 1.5 km of ice. Because their decay is governed by the weak force muons have a very long lifetime, around 2.2 microseconds in their rest frame [59]. Since these particles are traveling near the speed of light, this time is dilated in IceCube's frame of reference allowing the muons above 100 GeV to travel kilometers before decaying. As the muons propagate through the ice they undergo energy loss processes shown in Figure 3.6 [60]. Below approximately 2 TeV the dominant loss process is from the muon ionizing the media. This process is roughly uniform across all the energies we will consider and leads to a nearly constant loss rate of .2 GeV/m. Above 300 GeV ionization is still present but becomes sub-dominant to the stochastic processes of pair-production, nuclear interactions, and Bremsstrahlung interactions. The amount of energy lost in these interactions depends largely on the approach distance of the muon to the interaction center and is proportional to the energy of the muon, as is shown in Figure 3.6. In each of

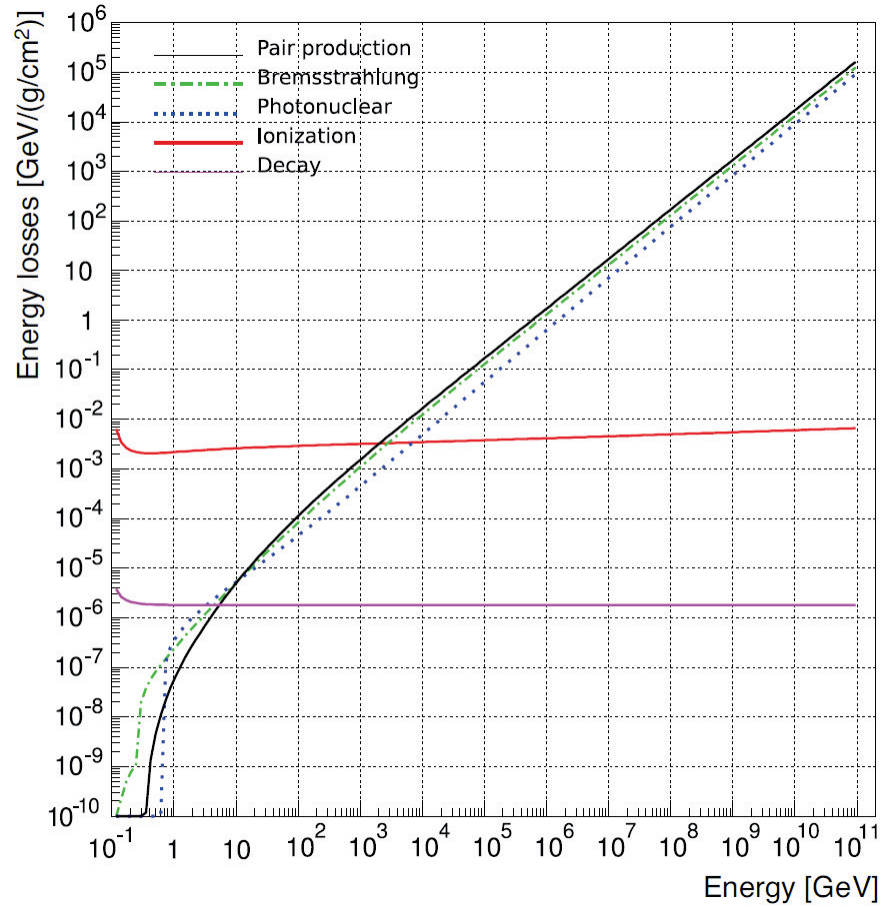


Figure 3.6: The average energy loss of muons as a function of energy. Below 2 TeV the losses are dominated by ionization; above 2 TeV the losses are dominated by pair production, bremsstrahlung, and photo-nuclear processes. This plot comes from [60].

the stochastic interactions, the final state includes the original muon and an out-going particle or particles (hadron, electron/positron, or gamma ray). Each of these out-going particles either is or will yield a charged particle traveling near the speed of light. Charged particles traveling near the speed of light in a medium leads to the emission of Cherenkov radiation, discussed in 3.6. Normally, Cherenkov radiation leads to emission of light in a characteristic cone, however since the out-going particles are not necessarily emitted in a co-linear direction with the muon, this cone becomes slightly smeared out and yields the emission profile shown in Figure 3.10. Because the muons themselves are charged particles traveling near the speed of light they emit Cherenkov radiation as well. Below 300 GeV the direct Cherenkov radiation from the muon is where the majority of the observed photons from an event in IceCube come from.

### 3.6 Cherenkov Radiation

Cherenkov radiation is a special case of light emission associated with a charged particle moving through a medium. The discussion here is based on the relevant section in Jackson's electrodynamics text [61]. Normally, a particle must be accelerating to emit light, in the form of Larmor radiation, however in the case of Cherenkov radiation it is the medium which is emitting not the particle itself. The emission occurs because the traversing particle is charged and attracts/repels the particles near it as it passes through the medium. These particles are thus accelerated and emit light. Recall that the speed of light,  $c$ , varies in materials according to

$$c = \frac{c_{vac}}{n_{medium}} \quad (3.12)$$

allowing particles to travel faster than light in that medium. This leads to two situations, one where the particle is traveling slower than the light being emitted, and one where the particle is traveling faster than the light being emitted. In the situation where the particle is moving slower than the speed of light in the medium, the possible light fronts always outrun the successor and as a result never cross. In this situation no interference can happen and as a result there is no emission. For the other case where the velocity of the particle is greater than the speed of light in the medium the possible light fronts cross in a repeated manner forming a light front, as depicted in Figure 3.7. This light front then represents the front from which the earliest emission could arrive from for detection. The angle of this light front is determined solely by the velocity of the particle and the velocity of light in the medium as the particle moves forward a distance  $vt$  while the light moves out from the same point a distance  $ct$ , leading to

$$\cos(\theta_C) = \frac{ct}{vt} = \frac{c}{v} = \frac{c_{vac}}{n_{medium}v} \quad (3.13)$$

Thus we are left with an equation that depends only on the material and the velocity of the particle. We can simplify this because

$$E = \gamma m_0 c^2 \quad (3.14)$$

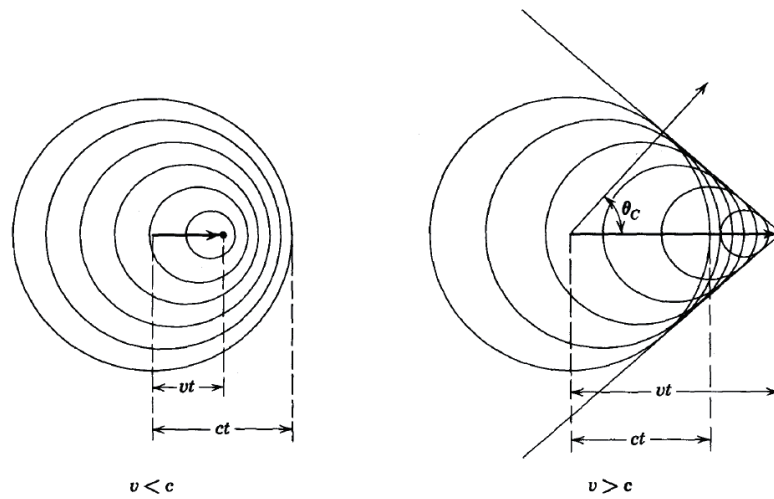


Figure 3.7: An illustration, from [61], of the situations for a charged particle moving in a medium. At left is the situation where the particle is traveling slower than the light being emitted, at right is the situation where the particle is traveling faster than the light being emitted. Only in the case where the particle moves faster than the speed of light in the medium does a coherent light front appear.

where

$$\gamma = \frac{1}{\sqrt{1 - \frac{v^2}{c^2}}} \quad (3.15)$$

thus

$$v = c \sqrt{1 - \left(\frac{m_0 c^2}{E}\right)^2} \quad (3.16)$$

Plotting the resulting velocity for electrons and muons, in Figure 3.8, we can see that both particles approach the speed of light in a vacuum by 1 GeV, which is below the particle energies relevant in IceCube, so we can safely approximate  $v \approx c$  and simplify to

$$\theta_C = \cos^{-1}\left(\frac{1}{n}\right) \quad (3.17)$$

With an index of refraction of around 1.32 the Cherenkov angle in ice is  $\approx 40.8$  degrees. The direction

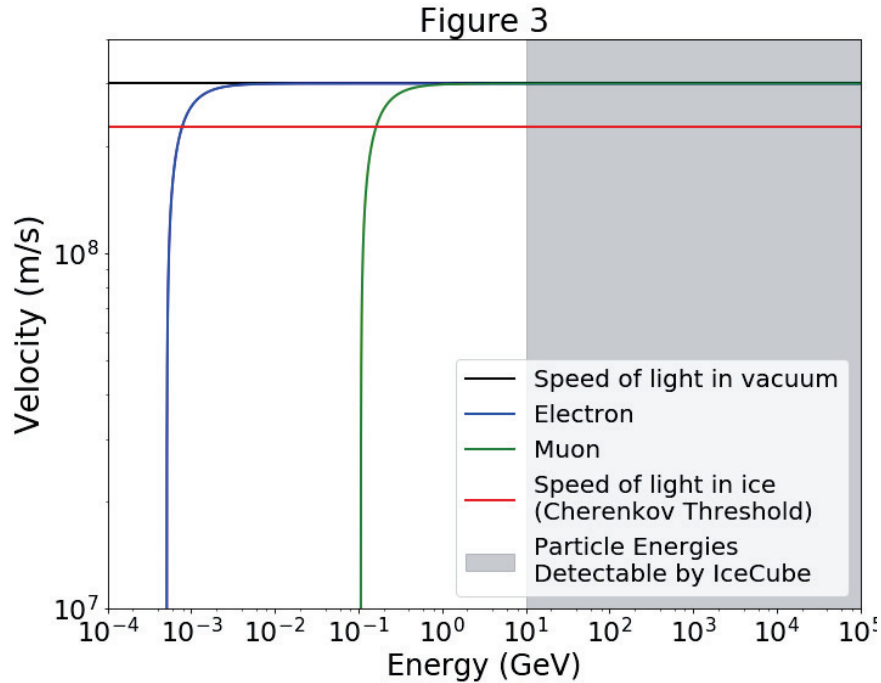


Figure 3.8: Velocity of muons and electrons as a function of energy. In a medium these particles can travel faster than the local speed of light and emit Cherenkov radiation as a result. The detection threshold for IceCube is much higher than the energy where the particles travel faster than the local speed of light.

the radiation produced by the particle will travel is determined by the solution for the potential. For  $v > c$  it must involve the combination of two potentials which originated at different points in time. The only real solution to the problem is for emission along the Cherenkov angle on the Cherenkov cone, where the two times converge to the same value. Thus Cherenkov radiation is a plane wave whose orientation and



constituent photons all point along the Cherenkov angle. The final piece of information we need about Cherenkov radiation for the purposes of IceCube is the photon yield. This can be found by converting from the potentials obtained in solving for the Cherenkov emission profile to the power per frequency and solid angle via a Fourier transform. The number of photons per unit length and unit wavelength is given by

$$\frac{d^2 N}{dx d\lambda} = \frac{2\pi\alpha}{\lambda^2} \left(1 - \frac{1}{n^2}\right) \quad (3.18)$$

where  $\alpha$  is the fine structure constant. Knowing

$$\cos(\theta_C) = \frac{1}{n} \implies \frac{1}{n^2} = \cos^2(\theta_C) \implies 1 - \frac{1}{n^2} = \sin^2(\theta_C) \quad (3.19)$$

gives us

$$\frac{d^2 N}{dx d\lambda} = \frac{2\pi\alpha}{\lambda^2} \sin^2(\theta_C) \quad (3.20)$$

We are most interested in the number of photons per unit length over a detectable range. Integrating we find

$$\frac{dN}{dx} = \int_{\lambda_1}^{\lambda_2} \frac{2\pi\alpha}{\lambda^2} \sin^2(\theta_C) d\lambda = 2\pi\alpha \sin^2(\theta_C) \left(\frac{1}{\lambda_1} - \frac{1}{\lambda_2}\right) \quad (3.21)$$

Notice that because of our assumption here that  $v \approx c$  the particles energy does not enter anywhere into the number of yielded photons. The detectors in IceCube are sensitive between 300-650 nm so we can integrate the resulting spectrum to obtain that  $\approx 350$  photons per cm of particle track are emitted in IceCube's sensitive range [62].

### 3.7 Light Emission Topologies

Cherenkov radiation is the basis for nearly all the light relevant to IceCube detections. There are a few main emission topologies which are relevant for this thesis which are discussed in this section.

#### 3.7.1 Muon Tracks Below 300 GeV

Below 300 GeV the stochastic energy losses of a muon are minimal so the energy emission is dominated by ionization, as show in Figure 3.6. Ionization does not lead to a significant emission of light so the bare Cherenkov light from the muon itself is the dominant illumination. Since the Cherenkov radiation is emitted by one particle a cone is formed with respect to the particle's direction at the Cherenkov angle. Cherenkov radiation's light yield per length is constant with energy within the applicable range for IceCube so it is difficult to determine the energy of a muon at these energies unless the track is contained within the detector allowing the length of the muon to be used as a proxy for energy.

### 3.7.2 Cascades

Cascades come in two varieties; hadronic or electromagnetic. Electromagnetic cascades begin with a high energy electron, positron, or gamma ray being created in or near the detector. Hadronic cascades begin with a high energy hadron being created in or near the detector. The simulation of a 24 GeV electron in iron in Figure 3.9 shows what occurs as the particle passes through the matter. After a short distance

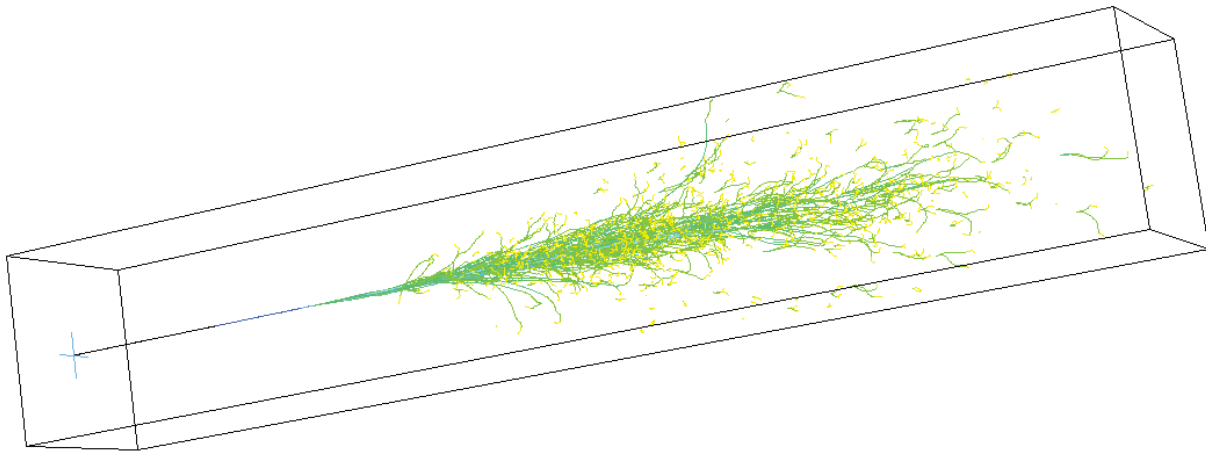


Figure 3.9: The results of a simulation of a 24 GeV electron in iron. Many particles are created after the initial interaction with the material. The shower develops from left to right and also spreads out laterally. As particles progress farther from the initial shower interaction point they have lower energy, indicated by the color of the line segment. Yellow indicates low energy, green indicates medium energy and blue indicates high energy. This figure comes from [63].

the single particle undergoes an interaction which creates other high energy particles. This continues in an exponentially increasing manner until the particles no longer possess the energy to produce new particles. From this point on the shower then gradually thins out as the particles are absorbed by the medium. In the simulation the colors indicate the energy of the particle. Yellow indicates low energy, green indicates medium energy and blue indicates high energy. In ice, the length of such a shower takes place in approximately 4 meters for a 1 TeV particle, and approximately 7 meters for a 1 PeV particle [64]. Note that as the particles move away from the core of the particle shower their energy tends to decrease and their direction becomes less oriented along the direction of the original particle. As long as a charged particle remains above the Cherenkov threshold it will emit radiation. This means that the emission profile of a cascade is the superposition of many misaligned Cherenkov cones with a preference towards the direction of the Cherenkov cone

of the original particle. The amount of dispersion varies as a function of the initiating particle's energy. A good discussion of this, along with results of simulation can be found in the paper "Calculation of the Cherenkov light yield from electromagnetic cascades in ice with Geant4" by Radel [64] which Figure 3.10 and its description are taken from.

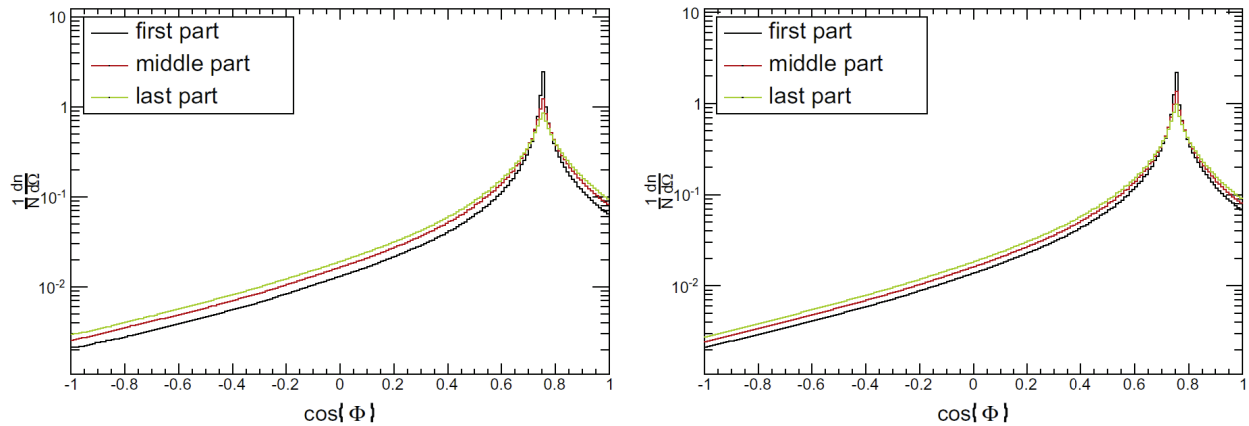


Figure 3.10: Angular distribution of the emitted Cherenkov photons for the different slices of the longitudinal shower evolution. The figures show the histograms for a primary  $\gamma$  with energy  $E_0 = 10$  GeV (left) and  $E_0 = 1$  TeV (right) normalized to the track length per particle. The longitudinal distribution has been split into three slices of equal track length.

### 3.7.3 Muon Tracks Above 300 GeV

Above 1 TeV the contribution to the total photon yield from sources other than direct Cherenkov light become non-negligible, as can be seen in Figure 3.6. The contributions are from bremsstrahlung radiation, pair production, and nuclear interactions. The effect of these is to randomly add cascades of varying brightness along the muon track. One can imagine that there is a chain of cascades of varying brightness emitting out from the track in addition to the regular Cherenkov cone from the muon. It is important to note that in Figure 3.6 the average energy loss rate becomes related to the energy of the muon in a one to one way. This fact means that the amount of light the particle emits is proportional the energy of the particle itself. This is what gives IceCube its ability to reconstruct the energy of high energy muons.

## Chapter 4

### Vetoing Atmospheric Neutrinos

Looking at events coming into IceCube from above is a bit like staring into the sun. The majority of the cosmic ray muons are reconstructed to come from this direction and give IceCube its approximately  $10^{10}$  events per year rate. There are neutrinos buried in this pile of events, but without a trick they are all but impossible to find. For this reason, it was long considered much easier to look for events coming up through the Earth. In this situation only neutrinos can survive and are thus much easier to detect. However, it was not with these upward-going events that the first discovery of astrophysical neutrinos was made, but instead with the downward-going ones and the so called atmospheric self veto. The theory of the veto was first discussed in "Vetoing atmospheric neutrinos in a high energy neutrino telescope" [32] and later expanded on in "Generalized self-veto probability for atmospheric neutrinos" [65]. The basics of both are summarized here.

#### 4.1 Theory

As has been mentioned before, the decay of pions and kaons in atmospheric showers often leads to the production of a muon and a muon neutrino. These pions are moving at near the speed of light when they decay. The resulting two-body decay has a maximum energy which one particle can take which is set by the situation where the particles are ejected back to back in the rest frame of the decaying particle. This means that the energy of the muon and neutrino are linked and a minimum energy for the partner particle can be computed given the energy of the maximal particle. Thus, the lowest energy muon which can accompany a muon neutrino can be analytically determined, giving atmospheric neutrinos a muon partner. For down-going neutrino astronomy this has huge implications for opening up a different channel for detecting astrophysical neutrinos. The key is that astrophysical neutrinos never have a partner, and thus can be identified as being alone if they interact and start inside the detector. The innovative realization is that they are the only particles which are reliably alone. Atmospheric muons always come into the detector from outside, and muon neutrinos are guaranteed by kinematics to be accompanied by their partner muon, which comes into the detector from outside.

The details of the partner muon and neutrino established in a pion or kaon decay are very simple. Pions and kaons commonly decay to a muon and the corresponding neutrino. Since this decay is two bodied it is possible to obtain the energy relationship between the decay products in the back to back emission case where the energy difference is the largest. Starting in the center of mass frame we have

$$P_i = (m_i, 0, 0, 0) \quad P_\mu = (E_\mu, \mathbf{p}_\mu) \quad P_\nu = (E_\nu, \mathbf{p}_\nu) \quad (4.1)$$

where i represents a pion or kaon and c has been taken as 1. With the constraint from the decay that

$$P_i = P_\mu + P_\nu \rightarrow P_\nu = P_i - P_\mu \quad (4.2)$$

the fact that  $P_\nu^2 = 0$  can be used to find

$$0 = m_\mu^2 + m_i^2 - 2m_i E_\mu \rightarrow E_\mu = \frac{m_i^2 + m_\mu^2}{2m_i} \quad (4.3)$$

Since the neutrino must take the remaining energy

$$E_\nu = E_i - E_\mu = m_i - \frac{m_i^2 + m_\mu^2}{2m_i} = \frac{m_i^2 - m_\mu^2}{2m_i} \quad (4.4)$$

To obtain the observed relationship in the detector frame a boost must be applied.

$$E_\mu = \gamma(E_\mu^{CM} + \beta p_{\mu x}^{CM}) \quad E_\nu = \gamma(E_\nu^{CM} + \beta p_{\nu x}^{CM}) \quad (4.5)$$

where x is the direction of the boost as shown in Figure 4.1. For a particle over a few GeV  $\beta \sim 1$  and

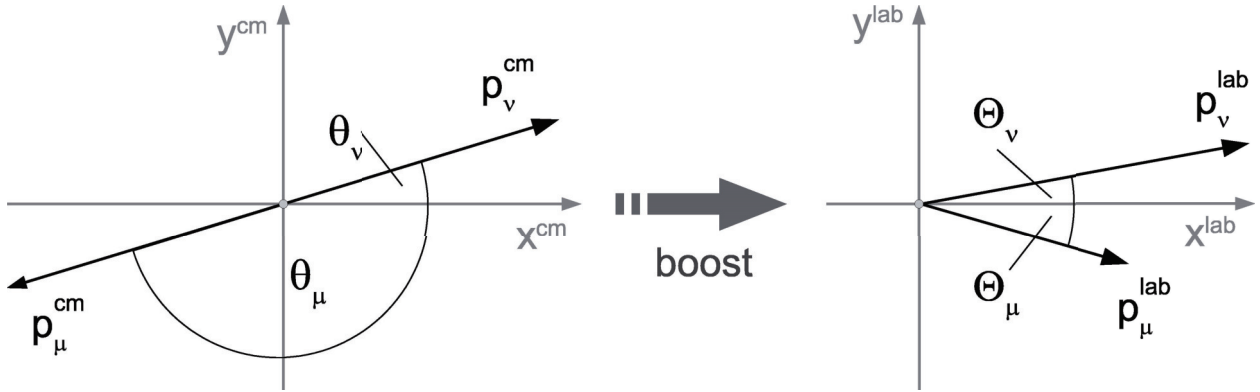


Figure 4.1: Diagram, taken from [32], of the two-body decay in the center of mass and lab(detector) frames.

This figure defines the coordinates and momenta of the equations describing the direct self-veto.

$$p_{\nu x}^{CM} = |\mathbf{p}^{CM}| \cos(\theta_\nu) \quad p_{\mu x}^{CM} = -|\mathbf{p}^{CM}| \cos(\theta_\nu) \quad (4.6)$$

$$E_\nu = \gamma |\mathbf{p}^{CM}| (1 + \cos(\theta_\nu)) \quad E_\mu = \gamma |\mathbf{p}^{CM}| \left( \frac{m_i^2 + m_\mu^2}{m_i^2 - m_\mu^2} - \cos(\theta_\nu) \right) \quad (4.7)$$

In the back to back case  $\cos(\theta_\nu) = 1$  which gives

$$E_\nu = 2\gamma|\mathbf{p}^{\text{CM}}| \quad E_\mu = 2\gamma|\mathbf{p}^{\text{CM}}|\frac{m_\mu^2}{m_i^2 - m_\mu^2} \quad (4.8)$$

this makes

$$E_\mu \geq E_\nu \frac{m_\mu^2}{m_i^2 - m_\mu^2} \quad (4.9)$$

For pions this means the muon has at least 1.342 times the energy of the neutrino while for kaons the muon has at least 0.048 times the neutrino's energy. Additionally, the angle between the muon and neutrino are constrained to deviate from each other by less than 1 meter over 10 kilometers for a pion decay and less than 10 meters over 10 kilometers for a kaon decay, implying they will arrive at the detector together. The constraint of the energy of the muon with respect to the energy of the neutrino allows for the fraction of vetoed events to be defined at depth based on the probability a muon will survive to depth with enough energy to be reliably detected. For most IceCube analyses 1 TeV is assumed.

In addition to the straight-forward muon neutrino case, there is also a more indirect veto which can be established for electron neutrinos. In the case of all electron neutrinos, there is no direct muon partner which can be used to defined a veto criterion, however the electron neutrinos come from air showers which generally produce muons. In this case, the connection which must be made is back to the cosmic ray parent which initiated the air shower. The flux of neutrinos of a certain energy can be calculated by integrating the production spectra of the mesons which produce them. This leads to the standard form for approximating the flux from pions and kaons where A, B and  $\epsilon$  are the standard definitions from [18].

$$\phi_\nu(E_\nu) = \phi_N(E_\nu) \left\{ \frac{A_{\pi\nu}}{1 + B_{\pi\nu}\cos(\theta)E_\nu/\epsilon_\pi} + \frac{A_{K\nu}}{1 + B_{K\nu}\cos(\theta)E_\nu/\epsilon_K} \right\} \quad (4.10)$$

As with the straight-forward direct self-veto covered earlier, computing the probability that a neutrino of interest is not accompanied by a muon of minimum energy which triggers the detector is the goal. However, since there is no sibling muon, we need an estimate of the average muon content of the same air showers which could have created the neutrino of interest. To obtain this information, what's known as the Elbert formula [66] is used.

$$N_l(> E_l, A, E, \theta) = K_l \frac{A}{E_l \cos(\theta)} x^{-p_1} (1 - x^{p_3})^{p_2} \quad (4.11)$$

This formula gives the number of leptons above energy  $E_l$  from a primary cosmic ray nucleus of mass A and total energy E. Furthermore  $x = AE_l/E$  and  $K_l$ ,  $p_1$ ,  $p_2$ , and  $p_3$  are fit constants shown in Table 4.1 for different leptons fit from CORSIKA data. The Elbert formula is valid above a few TeV when pions and kaons are more likely to interact than decay. To accommodate charmed leptons, the term of  $1/E_l \cos(\theta)$  which describes the probability of decay must be removed as charmed mesons always decay promptly. This gives Equation 4.11 the form

$$N_l(> E_l, A, E, \theta) = K_l A x^{-p_1} (1 - x^{p_3})^{p_2} \quad (4.12)$$

Type	K	$p_1$	$p_2$	$p_3$
Conventional $\mu$	49.5	0.626	4.94	0.580
Conventional $\nu_\mu$	79.9	0.463	4.37	0.316
Conventional $\nu_e$	0.805	0.619	9.78	0.651
Charm $\nu_\mu$ and $\nu_e$	0.000780	0.604	7.34	0.767

Table 4.1: Parameters for the elbert formula, Equation 4.11, found from fitting Monte Carlo.

To obtain the contribution of a primary of particular energy and type, one needs to evaluate the distribution of primaries which produce a lepton of energy  $E_l$

$$R_l(A, E, E_l, \theta) = \phi_N(A, E) \times \frac{dN_l(> E_l, A, E, \theta)}{dE_l} \quad (4.13)$$

which can be integrated over energy and summed over primary type to give the flux of a certain lepton.

$$\phi_l(E_l, \theta) = \sum_A \int R_l(A, E, E_l, \theta) dE \quad (4.14)$$

With a computable lepton flux, an equivalent unaccompanied probability can be obtained with

$$P_\nu(E_\nu, \theta) = \frac{\sum_A \int R_\nu P(N_\mu = 0) dE}{\sum_A \int R_l dE} \quad (4.15)$$

Modelling the probability that no muons above a certain energy reach depth as a Poisson probability, this equation is solvable for all neutrinos. Doing so yields the veto probabilities shown in the plots of Figure 4.2. For the case of muon neutrinos, both the direct and indirect probabilities are relevant and are thus multiplied to get the total passing rate.

This approximation brings up an interesting possibility for defining atmospheric neutrino vetos of another type, at the surface. In this case, the veto is not just on the muonic component of the shower, but instead any identifiable component of the air shower (such as charged particles or Cherenkov photons in the air). In this case  $P(N_\mu = 0)$  can be replaced with  $(1 - \epsilon(E))$  where  $\epsilon(E)$  is the efficiency of detecting the component.

## 4.2 Implementation

Implementation of a veto involves predicting when a signal is indicative of an incoming muon or other air shower component. This has been successfully implemented in the ice and is in a proof of concept phase for the surface array IceTop [67].

### 4.2.1 In Ice

In the in-ice detector, the challenge is separating particles coming into the detector from those which are starting (background and signal respectively). This is complicated slightly by the fact that IceCube is

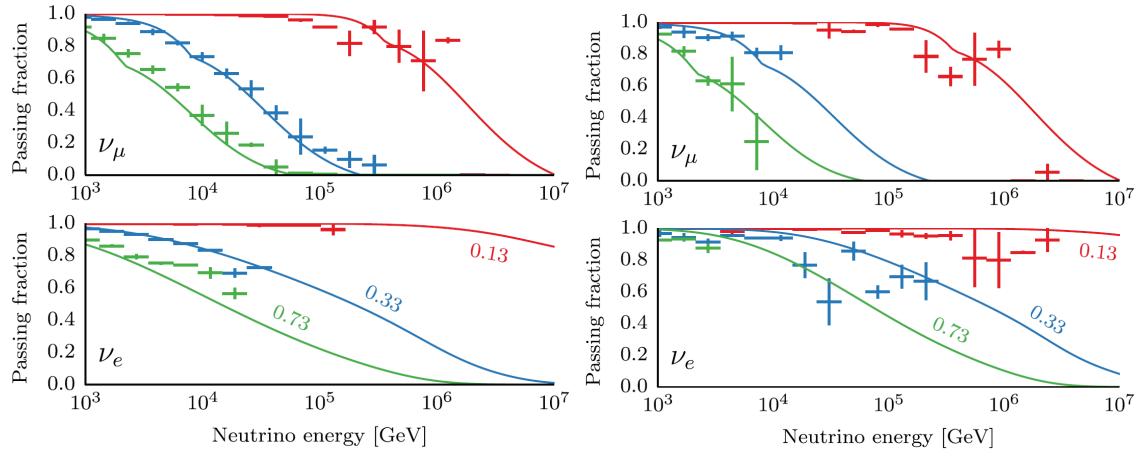


Figure 4.2: Plots of the veto probabilities obtained using Equation 4.15 from [65]. The plots on the left are for conventional fluxes while the plots on the right are for charmed fluxes. The crosses are from Monte Carlo simulation particle showers and confirm the findings of the analytic calculation.



a non-segmented and sparse detector. This means light created by a particle does not have to be detected by the nearest optical module. As such, vetos often look for light at the edge of the detector to indicate an incoming particle. At high energies, a single layer is enough, but at lower energies the veto must be thickened to use more layers of the detector and thus leave less of the detector open for the detection of starting signal events [68]. A new method for finding starting tracks is presented in Section 9 and is what separates this work from others.

### 4.2.2 Surface

Above IceCube is the surface detector IceTop. This detector is constructed of a station on top of almost all of the strings of IceCube. Each station consists of two tanks of pristine ice with two digital optical modules embedded in each tank. The main goal of the detector is to measure cosmic ray composition around the knee. However, it can also be used as a simple veto for vertical events in IceCube [67]. To do so, the IceTop signals are checked for temporal coincidence with air showers which could have created through-going tracks in IceCube. If there is a coincident signal in IceTop, then the in-ice event was likely from a cosmic ray. However, if there is not a coincident signal this is evidence for the detected muon being created between IceTop and IceCube, and thus being an astrophysical neutrino. Unfortunately, because IceTop is quite sparse the energy threshold for efficient detection is quite high. There are a number of ongoing research and development projects to improve this situation for a future surface veto.

## Chapter 5

### Astrophysical Neutrino Flux Measurements

When IceCube was completed in 2010, it became the largest neutrino detector in the world, making it the premier instrument for detecting the astrophysical neutrino flux. In 2012, when IceCube conducted a search for ultra high energy cosmogenic neutrinos with two years of detector data, it fortuitously discovered two cascades with PeV energy in the data [69]. The discovery was fortuitous because the event selection used was very simple, depending only on the deposited number of PE and the angle from a track reconstruction, which for cascade like events is essentially random. However, the discovery was astounding. With energies of a PeV each they were too low in energy to be consistent with the cosmogenic flux and too high in energy to be consistent with the atmospheric flux. This left only the option that these events were the first signs of the astrophysical or charm neutrino flux. Possibly the most surprising thing was the event's topology, cascades. Even though 7/9ths of a 1:1:1 neutrino flux is expected to have this topology at the time IceCube's stronger detection channel was viewed as the upward traveling through-going track events. This through-going muon selection can observe muon-neutrinos that have interacted outside the detector and had their out-going muon come in to the detector, thus greatly extending the effective size of the detector. In addition to being cascades, these events occurred well away from the edge of the detector. This suggested a simple selection could be made to search for more events like these by using the edge of the detector as a simple veto against incoming events. As was discussed in Chapter 4, vetoes in IceCube not only protect against penetrating muons, but also atmospheric neutrinos. Using this simple veto, IceCube discovered the astrophysical neutrino flux in 2014 [70], and ushered in the age of neutrino astronomy. Since that time, IceCube has measured the astrophysical flux in other channels as well, including the through-going channel. The rest of this section will be devoted to the different published analyses that have observed the astrophysical neutrino signal.

#### 5.1 Starting Event Analyses

##### 5.1.1 High Energy Starting Event Selection

As was mentioned before, a simple veto analysis called the high energy starting events (HESE) selection was the first selection with which astrophysical neutrinos were discovered. To perform the veto, the DOMs

in the detector were broken up into veto and fiducial volumes as is shown in Figure 5.1. The veto volume consisted of DOMs on the outermost ring of strings, 1 layer of DOMs at the bottom of the detector, roughly 7 DOMs at the top of the detector, and a region 80 meters wide surrounding the portion of the detector which is unfavourable for photon detection (see Section 6.7 for more details). The thicker cap of DOMs on the top

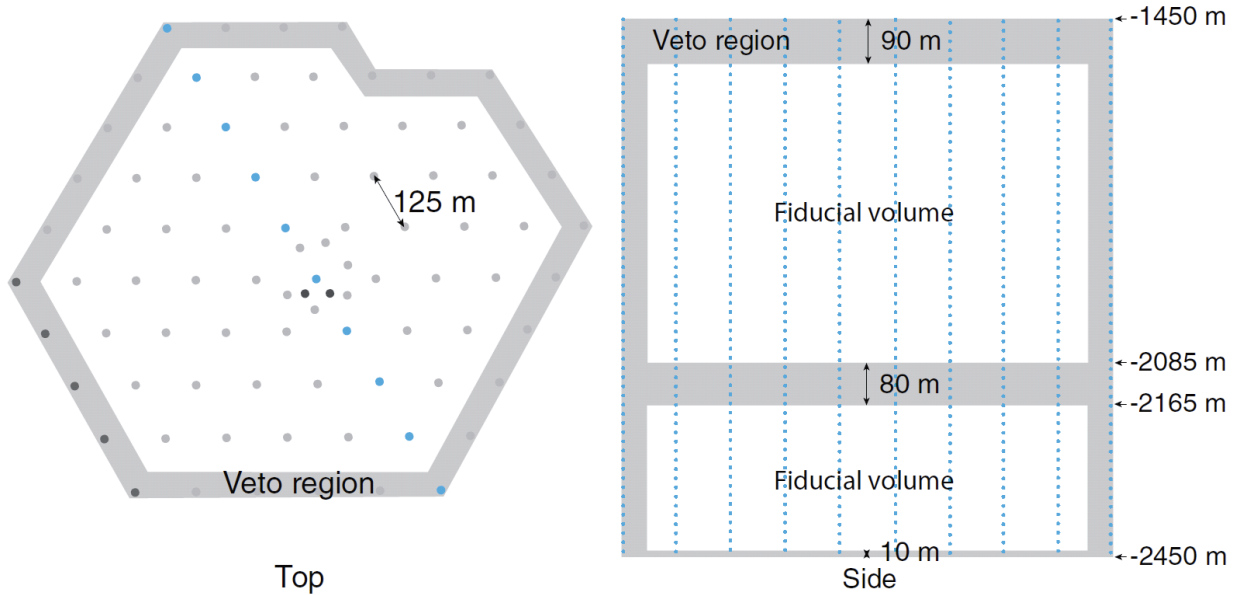


Figure 5.1: The veto layer definition for the high energy starting event selection. The figure comes from [70].

of the detector versus the bottom is a safe-guard against the numerous down-going muons from atmospheric showers. The veto region is used to detect light from incoming muons. Charge observed in the veto region before the bulk of an event's charge is deposited in the inner detector is indicative of an event coming in. However, charge deposited in the veto region after the bulk of an event's charge is deposited in the inner detector is indicative of an event going out. Since the veto itself has no sense of time, a time dependent definition of when the veto is active must be applied to prevent the veto from incorrectly removing out-going events. For HESE, the charge of an event is monitored until 250 PE are accumulated. If more than 2 PE of charge collected in that 250 is in the veto, then the event is removed from the selection. Figure 5.2 shows examples of the charge vs time for different event topologies and detector sections. This cut alone is not enough to remove all the penetrating muons since muons emit light in a stochastic manner. However, there must be an energy where a muon is guaranteed to be bright enough. In order to find this energy, the two PeV energy cascades and the burn sample from the two years of detector data in which they were found were run through the described veto selection and inspected as a function of charge, shown in Figure 5.3. The two PeV cascades, labeled Aya's cascades in the figure, are clearly separate from the bulk of the distribution at the left of the figure. There is one other event, labeled Interesting, which is separated from the rest of

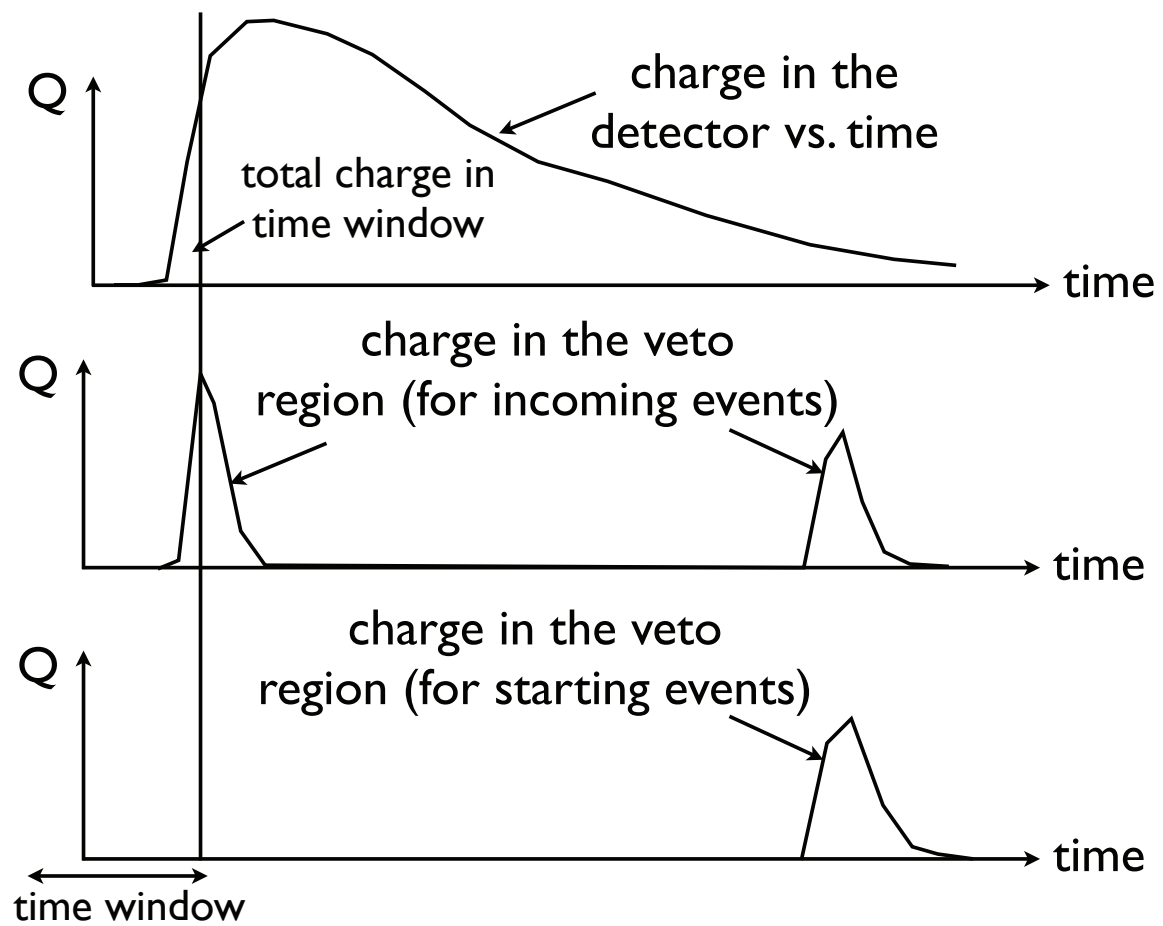


Figure 5.2: The veto time vs charge definition. The figure comes from [71].

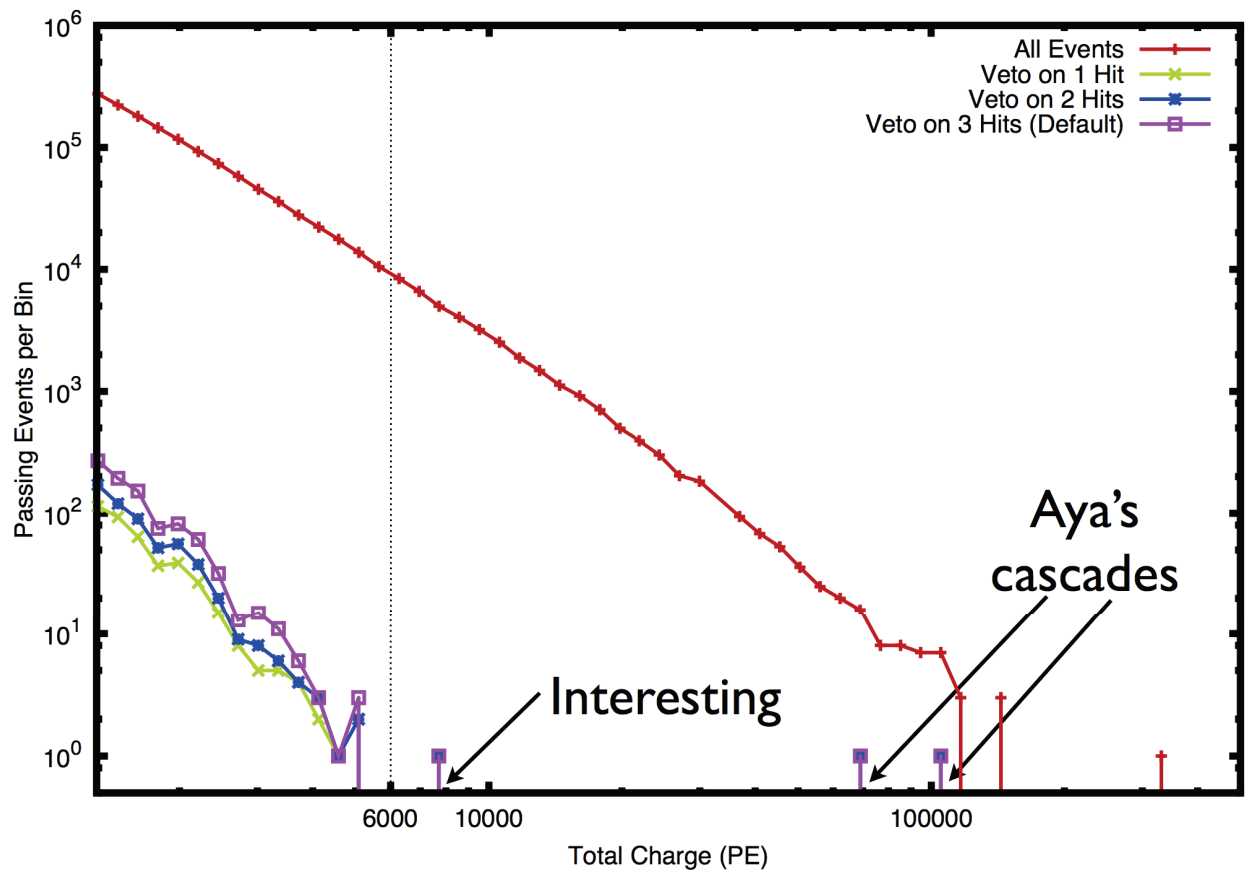


Figure 5.3: The charge of events which pass the HESE veto definition. The figure comes from [71].

the distribution. From this figure, a cut requiring at least 6000 PE of total deposited charge is made and completes the event selection.

Since the event selection is constrained to only include events which are contained inside the detector, it does not have the largest effective area, as is shown in Figure 5.4. However, it has a very high signal purity

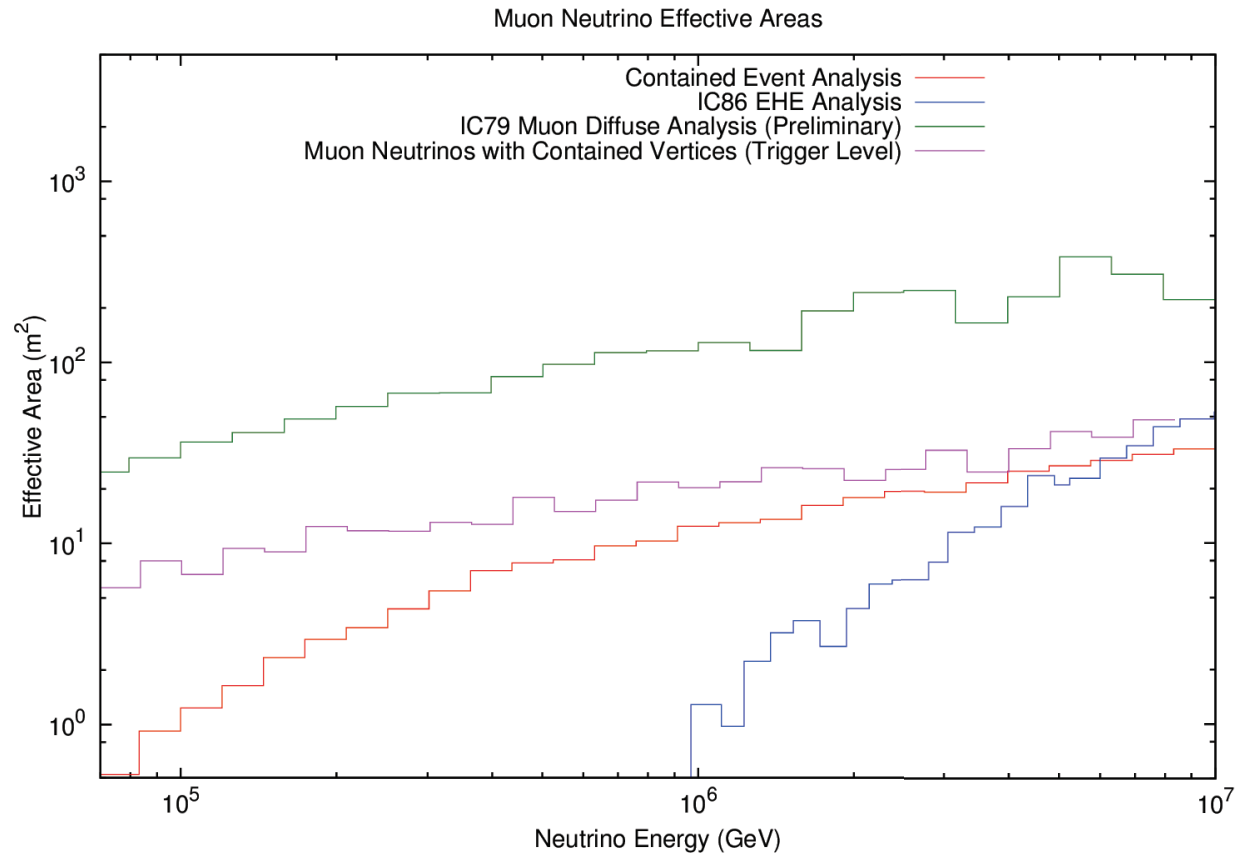


Figure 5.4: The effective area for muon neutrinos for the through-going muon neutrino analysis, the EHE analysis, and the HESE (labeled Contained Event Analysis). The figure comes from [71].

as is shown in Figure 5.5. The lower plot of Figure 5.5 is a plot of the purity when considering only neutrinos from a astrophysical  $E^{-2}$  flux and conventional atmospheric neutrinos. For the northern hemisphere, this ratio reaches 1 around 100 TeV as it does for all of IceCube’s astrophysical neutrino analyses in the northern hemisphere. However, thanks to the atmospheric self-veto, in the southern hemisphere, this ratio reaches 1 around 20 TeV. This means that a very pure signal is open for analysis if the penetrating muon background is quelled. The muon background can always be estimated from Monte Carlo, but questions about the muon flux at IceCube are still not conclusively answered. However, with such a simple veto technique, the number of unvetoes events can be estimated from the vetoed background. The method to do so utilizes the

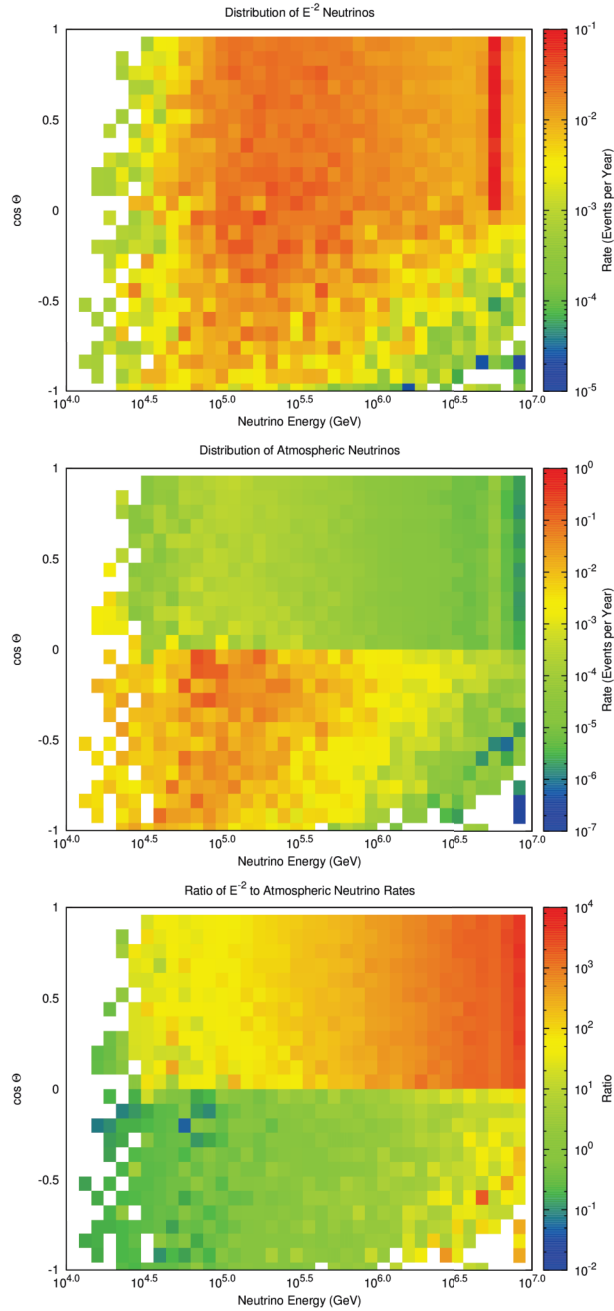


Figure 5.5: The top and middle figures show the expected rate of events for neutrinos from two sources in HESE. On the top is the expected rate per bin from a  $E^{-2}$  flux and in the middle is the expected rate per bin from a conventional atmospheric flux model. Taking the ratio of the top histogram and middle histogram yields the lower histogram. It can be seen in the lower plot that the ratio is right around 1 for all events above 100 TeV in the northern hemisphere and above about 20 TeV in the southern hemisphere. A ratio of 1 indicates that as many astrophysical events are expected as atmospheric. All of these figures are using the true value from Monte carlo and come from [71].

inter-changeableness of layers of DOMs as were defined for HESE. If an event fails the veto criterion on the first layer, it is identified, however its properties do not change much from this detection and one could see if it identified again on a nested layer as is shown in Figure 5.6. Thus, by counting the rate of events which

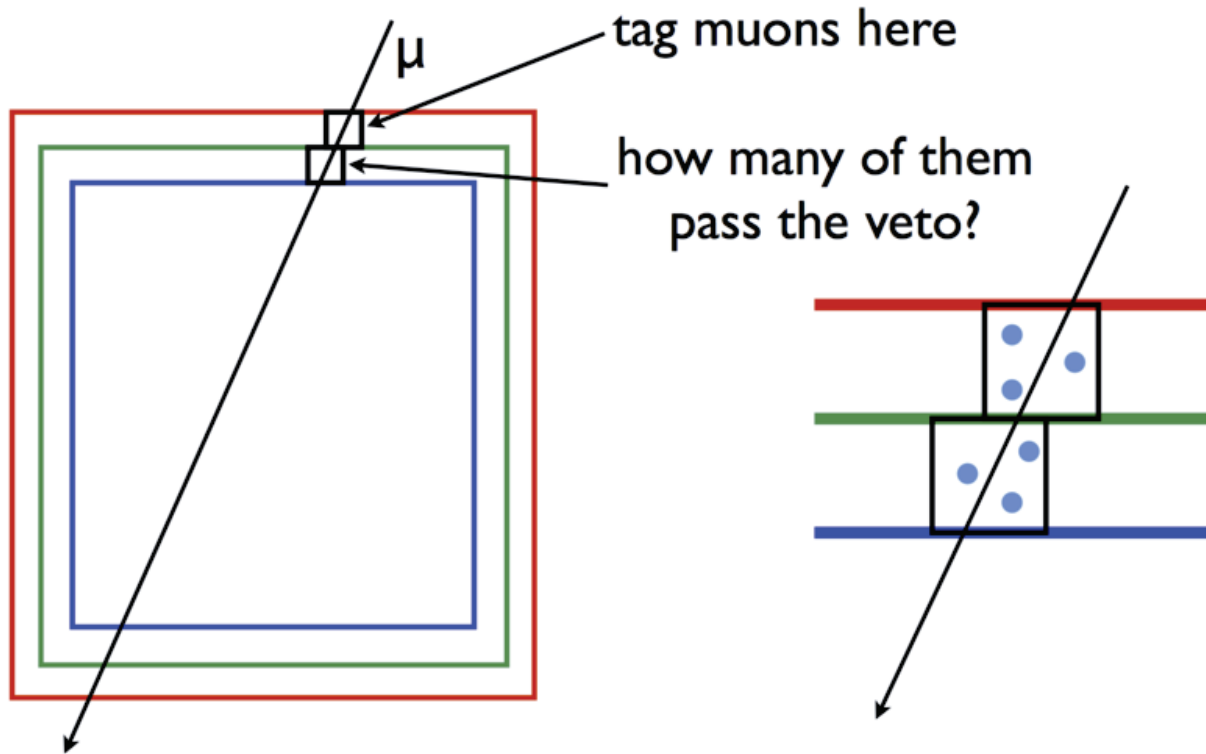


Figure 5.6: A figure displaying the nested layer veto used to estimate the penetrating muon background rate. The figure comes from [71].

do not pass the first layer, but do pass the second layer, one can estimate the background contamination. Figure 5.7 shows the estimation of the background using a small CORSIKA set and the rejected burn sample events. Both are in good agreement and estimate a passing background fraction smaller than the observed signal above 6000 PE.

With a handle on the signal and background rates, this selection has to date yielded 80 events in 6 years [72].

### 5.1.2 Medium Energy Starting Cascade Selection

While HESE was successful as a first detection selection it has a shortcoming. The veto definition is very rudimentary. This leads to a high minimum neutrino energy for measuring the astrophysical flux. With proper consideration of the veto definition, the minimum neutrino energy can be brought down to the energy



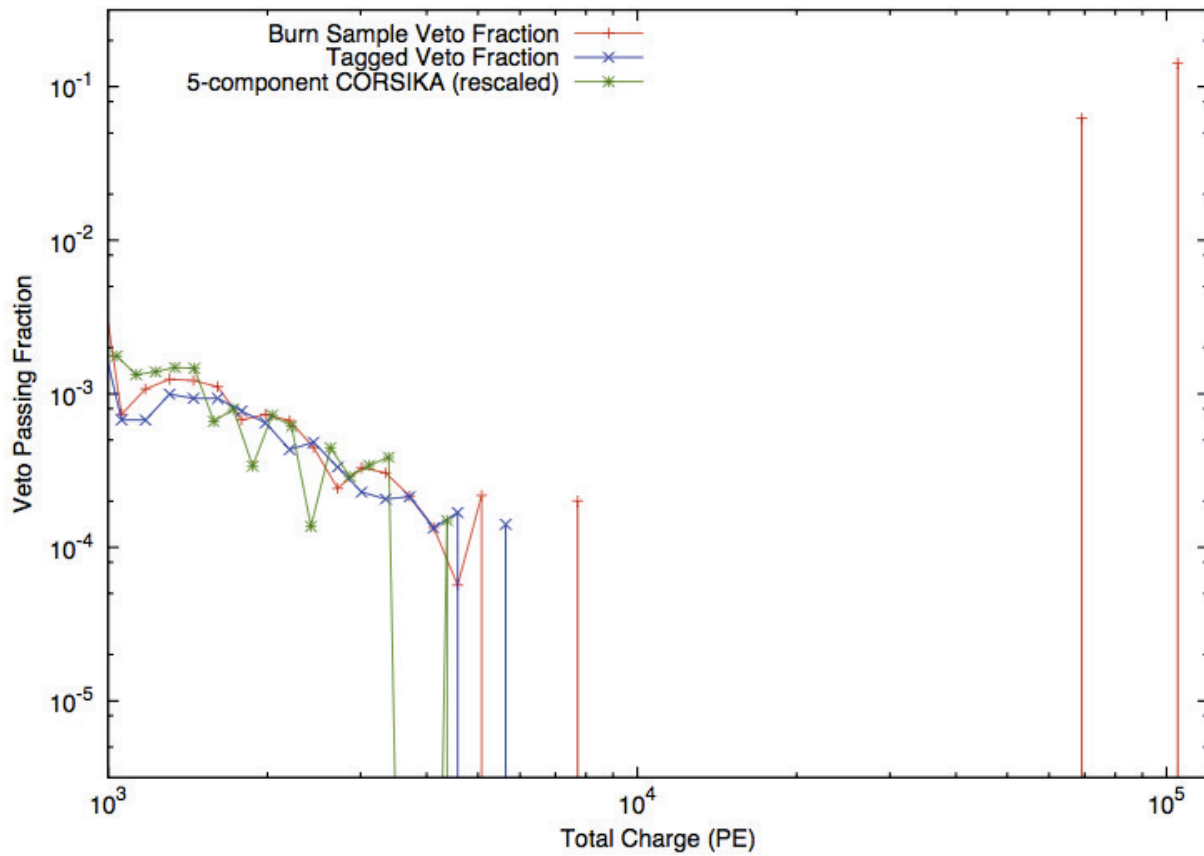


Figure 5.7: The estimated background contamination rates coming from CORSIKA and the nested veto calculation. The nested veto (labeled Tagged in the plot) shows good agreement with a smaller effective livetime CORSIKA set, but utilizes the higher statistic background from the selection. The figure comes from [71].

where the atmospheric and astrophysical fluxes are at the same level after the atmospheric flux is vetoed. Lowering the minimum neutrino energy was the main goal of the Medium Energy Starting Cascade (MESC) selection.

The MESC selection began as a selection to search for prompt atmospheric neutrinos in the form of electron neutrino cascade events. Work on MESC began before the results of HESE were published and affected the first result in a few ways. The main effect was on the data stream considered. If one believes they are after a cascade signature, then it makes sense to use cuts close to the filtering of the detector data which optimize the collection of cascades and rejection of tracks. As a result, the author initially worked on the IceCube's cascade channel Level 3 selection, which is based entirely off the cascade filter. One can refer to Section 6.6 for more information on filters. This resulted in a selection which had a very good acceptance for astrophysical neutrinos with a cascade topology, but a reduced acceptance for astrophysical neutrino starting tracks. That being the case, MESC was still able to observe the events from the astrophysical spectrum utilizing the event selection techniques which follow.

The selection begins with a outer-layer veto similar to that used in HESE. However, since the event selections were developed independently, and because MESC targets lower energy neutrinos, it varies slightly. For bright high energy events, accumulating 250 PE for definition of the veto region time threshold is easy, but for lower energy events 250 PE can be more than the entire energy of the event. As a result the starting charge threshold was made to be proportional to the total deposited charge between 72 and 6000 PE. Above 6000 PE, the threshold of 250 PE was kept, and below 72 PE a 3 PE threshold was required.

$$Q_{start} = \begin{cases} 3 \text{ PE} & Q_{tot} < 72 \text{ PE} \\ Q_{tot}/24 & 72 \text{ PE} \leq Q_{tot} < 6000 \text{ PE} \\ 250 \text{ PE} & Q_{tot} \geq 6000 \text{ PE} \end{cases} \quad (5.1)$$

Within the time window defined by the threshold, the amount of charge required was also changed. Since lower energy events were the target, any charge in the veto region during the veto time window leads to the event being removed from the selection. The outer-layer veto is good at removing bright events, but is too weak to remove the dimmer low energy events, just like HESE. The dominant background remaining after the outer-layer veto is single muons which penetrate into the detector when they are emitting small amounts of light, and suddenly become visible when they undergo a large energy loss. An example of such an event can be seen in the left illustration in Figure 5.8. When viewed only with the HLC pulses, the event appears to be a cascade, however with the addition of the SLC pulses, it is clear that the event was a penetrating muon. However, many noise hits are present in the SLC pulses. The trick is to identify which of the SLC pulses are in agreement with the hypothesis of an incoming track which passes through the cascade vertex. Since the events are cascades, there is no good pointing information to use. However, one can use many

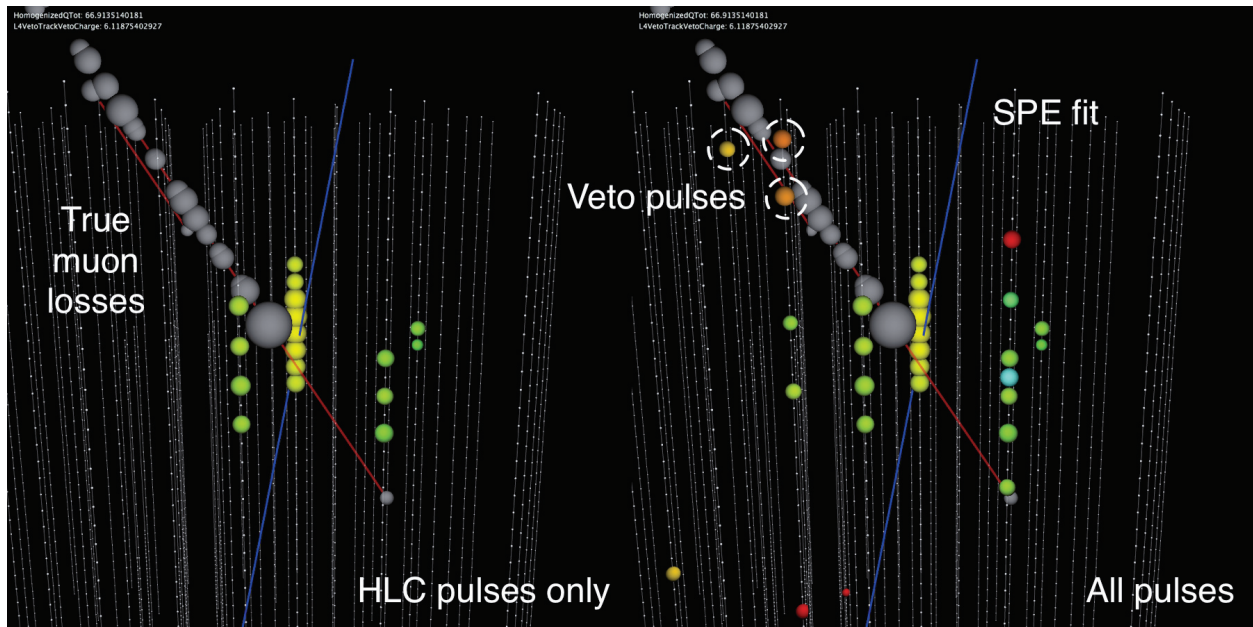


Figure 5.8: A figure displaying the penetrating muon background. The figure comes from [73].

incoming hypotheses and test if there is any light which can be causally connected to the track, but not the cascade emission. This works because the speed of light in ice is slower than that of the muon. Thus detected PEs which come after the causal limit from a proposed track, and before the causal limit of the identified cascade on any tested track direction can be considered evidence for a veto. The effect of the incoming

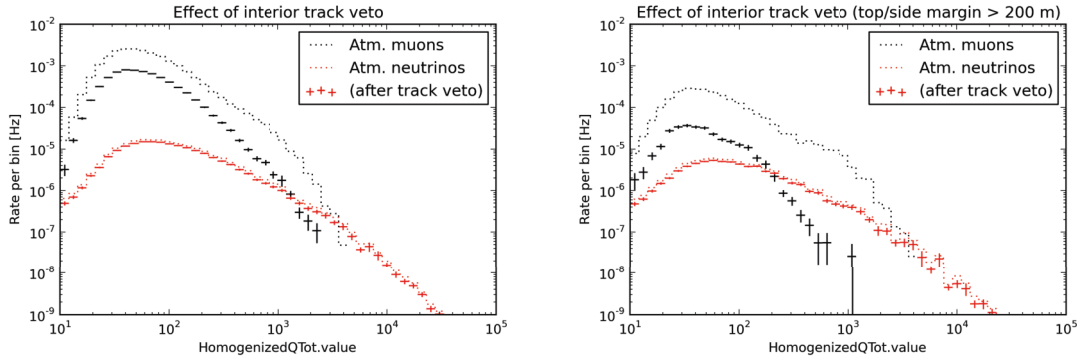


Figure 5.9: A figure displaying the penetrating atmospheric muon and neutrino background before and after the incoming track veto. The figure comes from [73].

track veto on the event rate can be seen in Figure 5.9. On the left is the overall effect of the incoming track veto. In the dashed lines are the atmospheric leptons, black for muons and red for neutrinos. The muon background is reduced by roughly a factor of 5 across all total charge values, however, the atmospheric muons are still the dominant component. On the right are the same events, but with only those more than 200 meters inside the detector displayed. The effect of the veto is much stronger for these events, at least an order of magnitude across all charges. This is because the events are penetrating through more volume of the instrumented detector on their way to being observed. More volume traversed leads to more light emitted, leading to higher chance for detection. This idea of using more of the detector for vetoing is the motivation of the final cut. Since events which deposit more charge are likely to be higher in energy, there is a charge dependence to the amount of volume, or equivalently distance to an edge, is needed to suppress the incoming atmospheric muon background. For this veto, only Monte Carlo can be used to estimate where the distance to edge cut must be placed. After rejecting all the incoming muon Monte Carlo available one arrives at the following charge dependent distance to edge cut.

$$m = a + b(c - \log_{10} Q_{\text{tot}})^{1/d} \quad (5.2)$$

Where  $a$ ,  $b$ ,  $c$ , and  $d$  come from Table 5.1. Figure 5.10 shows the position of the veto for an event with 2500, 1500, 300, and 100 PE from the top and side views. Below 100 PE essentially only DeepCore is used for detection. After this cut the muon background is essentially removed, by definition from the use of the Monte Carlo to define the cut, as is shown in Figure 5.11.

Face	a	b	c	d
Sides	0	17266	3.41	1.74
Top	100	23710	3.40	1.88

Table 5.1: Values to define the charge dependent distance to edge cut using Equation 5.1.2. The figure comes from [73].

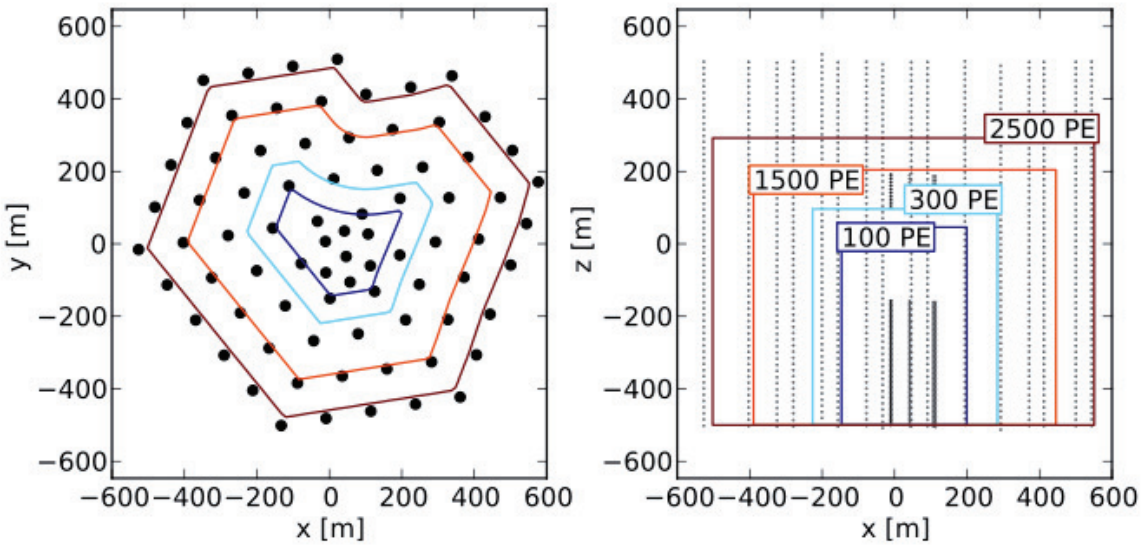


Figure 5.10: A few positions of the scaling veto for fixed charges from the top and side views. The figure comes from [73].

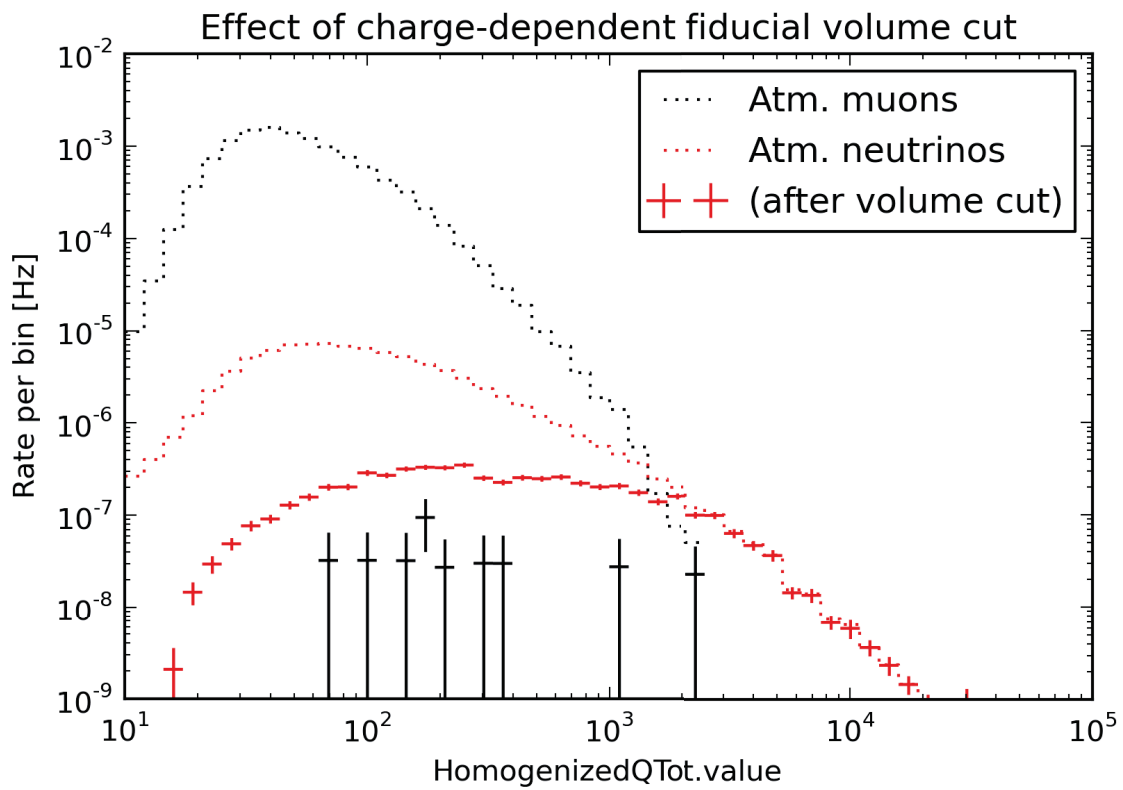


Figure 5.11: Events in the Monte Carlo set after applying the scaling veto cut. The atmospheric neutrinos dominate over the muon background. The figure comes from [73].

With the incoming muon background suppressed below atmospheric and astrophysical neutrino rates, a measurement of the neutrino fluxes can be made. After all the cuts are applied, the obtained effective areas for  $\nu_\mu$  and  $\nu_e$  are those shown in Figure 5.12. The results of this selection on two years of data were presented

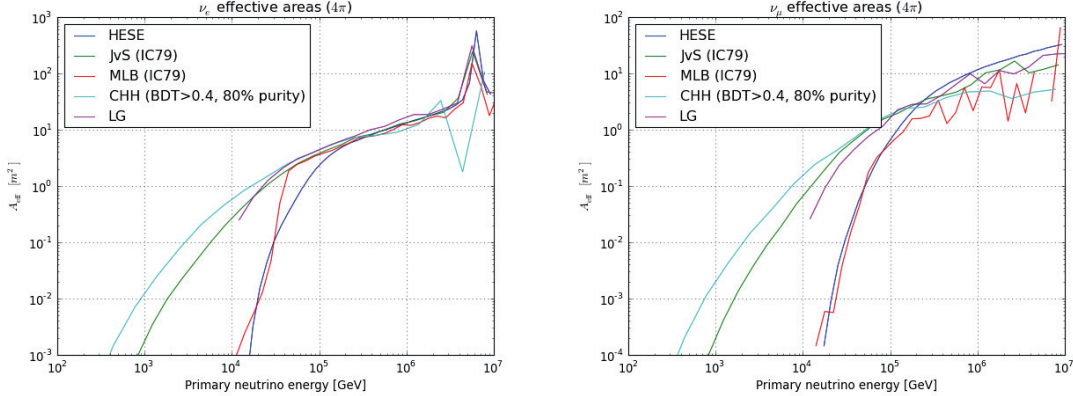


Figure 5.12: Effective areas for the MESC event selection (labeled JvS). The selection is nearly the same size as HESE for the overlap energies, but extends to lower energies. The figure comes from [73].

in the paper "Atmospheric and Astrophysical Neutrinos above 1 TeV Interacting in IceCube" [68] in 2015 and represent the third observation of the astrophysical flux. The final distributions are presented in Figure 5.13. The astrophysical neutrino signal, shown in teal, dominates above the atmospheric lepton signals above about 20 TeV in deposited energy. In the declination distributions, the evidence for astrophysical neutrinos is the strongest in the Southern Hemisphere where the self-veto is effective. With these two years of data, an astrophysical flux of

$$\Phi_{astro} = 2.06^{+0.35}_{-0.26} \times 10^{-18} \left( \frac{E}{100 \text{ TeV}} \right)^{-2.46^{+0.12}_{-0.12}} \text{ GeV}^{-1} \text{ cm}^{-2} \text{ sr}^{-1} \text{ s}^{-1} \quad (5.3)$$

was measured, while the prompt flux (the analysis' original goal) was found to be consistent with 0. This flux was softer than any other flux at the time, but was still consistent with the HESE and through-going muon fluxes at the 1 sigma level. One interesting feature of the energy distribution is a bump around 30 TeV which also presents itself in the declination distributions around  $-0.5$  of  $\sin \delta$ . However, this bump is not statistically significant. A bump as strong or stronger presents itself in re-samplings of the Monte Carlo at the  $2\sigma$  level.

## 5.2 Upward-Going Muon Neutrinos

Neutrinos which come up through the Earth can interact via charged current interactions. Being able to traverse the Earth is a unique feature of neutrinos, so any up-going muons are guaranteed to be from

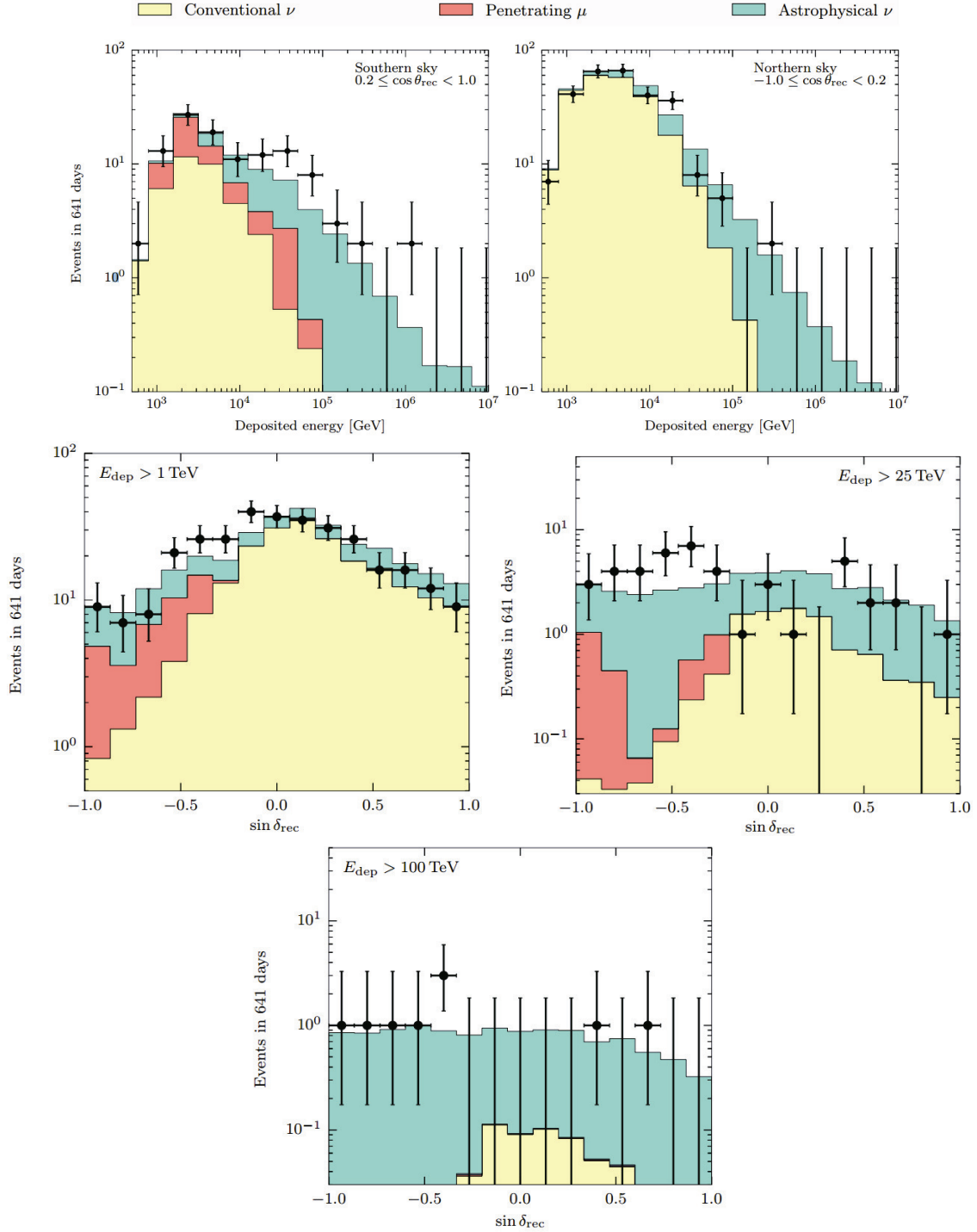


Figure 5.13: Results of the MESC selection on two years of data. The top plots are the energy distribution of events in the Northern and Southern Hemispheres. The bottom three plots are the declination distribution for three different minimum event energies. The figure comes from [68].



a neutrino. Muon neutrinos have the additional feature of being able to interact outside the detector and create muons which can travel into and through the detector to be observed. This is the basis of the upward-going muon neutrino event selection. Information about this selection is being taken from the analyzer's wiki page [74] and the paper "Observation and Characterization of a Cosmic Muon Neutrino Flux From the Northern Hemisphere Using Six Years of IceCube Data" [37] from 2016 which showed the first five sigma result for upward-going tracks. While not presented here, the earlier version of this analysis "Evidence for Astrophysical Muon Neutrinos from the Northern Sky with IceCube" is also worth reading and understanding [75].

As the title of the paper says, this selection is carried out using events from six years of IceCube data. Two of the years used were from the detector construction phase, IC-59 and IC-79. For the events from IC-59, the selection is presented in the analyzer's wiki page [76] and the paper "Search for a Diffuse Flux of Astrophysical Muon Neutrinos With the IceCube 59-String Configuration" [77]. For IC-79 and the four IC-86 years, the following method is used. The selection starts at muon Level 2 (see Section 6.6 for more information on filters) and selects only the events with a zenith angle larger than 85 degrees. The selection implements a few basic coincident event cuts to attempt to clean up the 10% of IceCube events which contain information from more than one particle in the detector. These coincident events are the main background to the analysis since IceCube reconstructions are easily fooled into mis-reconstructing these events as up-going, as is shown in Figure 5.14. After the cuts, the selection has a roughly 1 Hz rate. This is a small enough total number of events that CPU-intensive reconstructions can be performed on data and Monte Carlo. The work-horse of the event selection is a boosted decision tree (BDT). For training, up-going muon neutrino simulation weighted to an  $E^{-2}$  flux with a reconstructed resolution better than 5 degrees were used. The background was a combination of atmospheric muons from cosmic ray simulation and muon neutrino simulation weighted to an atmospheric spectrum. The following variables in Table 5.2 were used as features in the training after recalculation to remove the effects of DeepCore, presenting a more uniform detector. To verify performance of the BDT, K-fold cross validation was used. In this method, the training simulation is broken into K disjoint samples. The BDT was trained on K-1 of the samples, and tested with the 1 held out sample. This procedure is repeated with all the samples being held out exactly once. From this verification, an estimation of the average background contamination and signal efficiencies can be obtained from the average over the cross validation training samples. The output of a BDT is a per event score of the signalness from 0 to 1, where 0 is completely unsignal-like and 1 is completely signal-like. Since the background and signal change as a function of zenith angle, the final cut on BDT score is made as a function of zenith angle as is shown in Figure 5.15. The cut removes most of the remaining atmospheric muon background and cascade events caused by neutrinos. At the same time the cut is very effective at retaining the astrophysical events. Only at the horizon is some loss forced by the excess of muons which

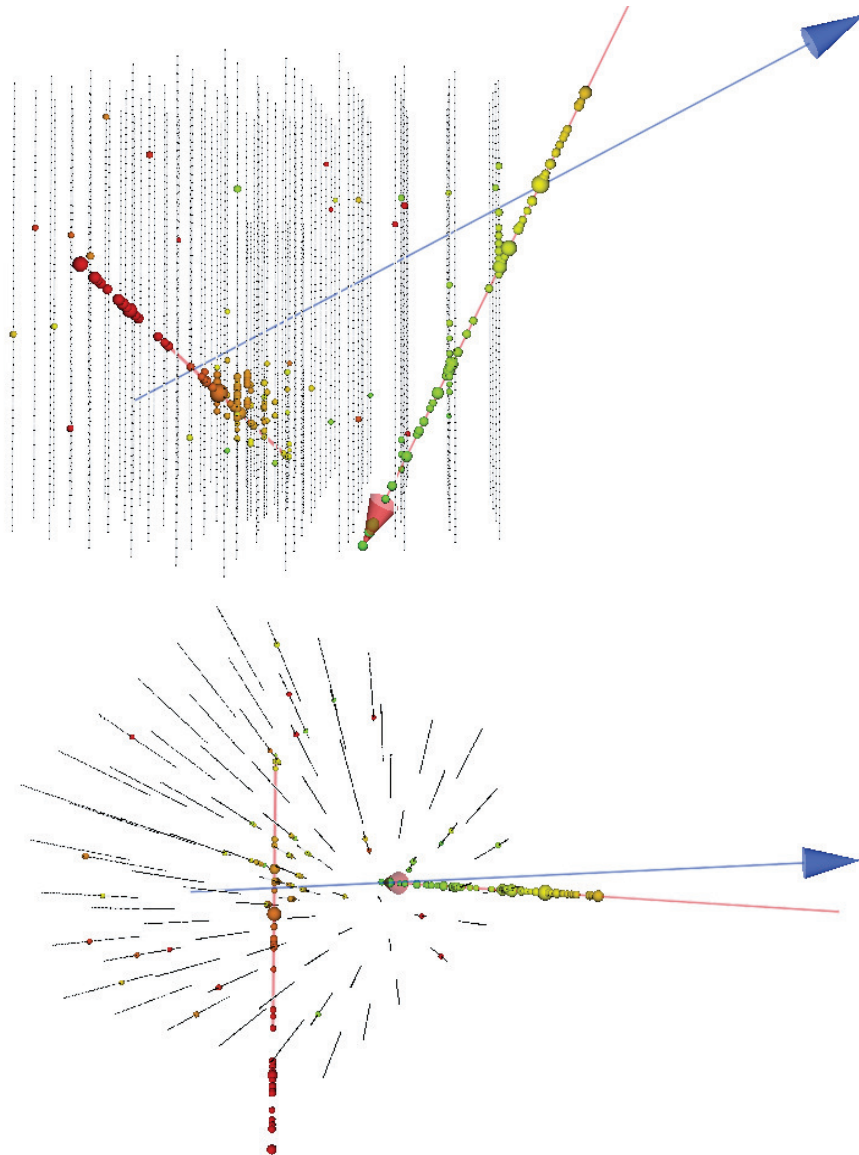


Figure 5.14: Side(top) and top(bottom) views of a Monte Carlo event where two coincident down-going muons arrive in time such that their hits appear to be an up-going track. The blue arrow is a standard IceCube fit which has been fooled by the event. Events like this form the background for the up-going muon neutrino analysis.

Variable Name	Description/Reasoning
<b>Bayesian likelihood ratio</b>	Each event is fit with a down-going muon hypothesis for the two-iterations SPE Fit The likelihood ratio of the reconstruction including the down-going hypothesis and the reconstruction that is free gives an estimate on how likely the alternative down-going hypothesis is.
<b>Center of gravity <math>\rho</math></b>	Events passing through the outer part of the detector are often reconstructed worse than events passing centrally through the detector.
<b>Center of gravity <math>z</math></b>	Due to the smaller overburden at the top of the detector compared to the bottom of the detector events near the top of the detector are more likely background. Also, events at the top and bottom of the detector are often mis-reconstructed.
<b>Number of hit DOMs</b>	Events with more hit DOMs are potentially more interesting because they are produced by higher-energy muons. Also, for track-like events the more DOMs have measured light the better they are reconstructable.
<b>Separation length spline-mpe</b>	The separation length is the distance between the centers of gravity of the first and last quarter of hit DOMs projected onto the reconstructed track. Large distances indicate a long track inside the detector.
<b>Number of directly hit DOMs</b>	Directly hit DOMs have seen light within a time window of -15ns and +75ns around the expected arrival time for unscattered photons from the track hypothesis.
<b>Direct track length</b>	The direct track length is the projected (Cherenkov angle) distance between the first and the last directly hit DOMs.
<b>Direct smoothness</b>	For well-reconstructed events direct hits should be smoothly distributed along the track. The direct smoothness a measure for this.
<b>Reduced log-likelihood</b>	An estimator of the SplineMPE likelihood reconstruction on the quality of the reconstruction.
<b><math>\sigma</math> paraboloid</b>	Estimate of the angular reconstruction error by a paraboloid fit to 8 points in the likelihood space around the reconstructed direction. Since this variable is energy dependent a correction function used in the IC86-2011 point source analysis is used.

Table 5.2: Variables of the upward-going muon neutrino selection's BDT. The information comes directly from [74].

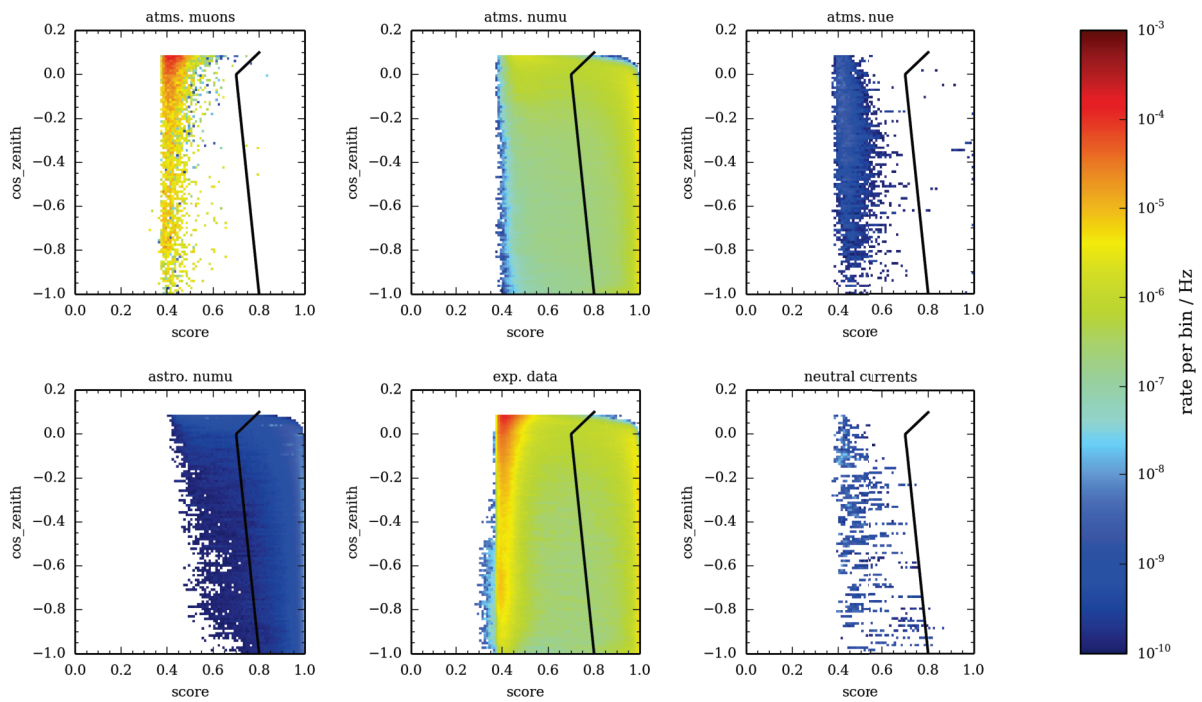


Figure 5.15: BDT score vs.  $\cos$  of the zenith angle for the background simulation (labeled atms. muons, atms.numu, atms. nue and neutral currents), signal simulation (labeled astro. numu), and a burn sample (labeled exp. data). This plot comes from [74].

overlap with the signal. Because the atmospheric and astrophysical events have no distinguishable features, except their energy spectra, a large portion of the atmospheric muon neutrino background is kept.

After the cosine zenith dependent BDT cut is applied, the selection is at its final level. The effective area at the final level is shown in Figure 5.16 and is larger than the previous selection which only used straight cuts (labeled IC79/86 diffuse analysis) [75]. Since the events are not contained in the detector, one cannot

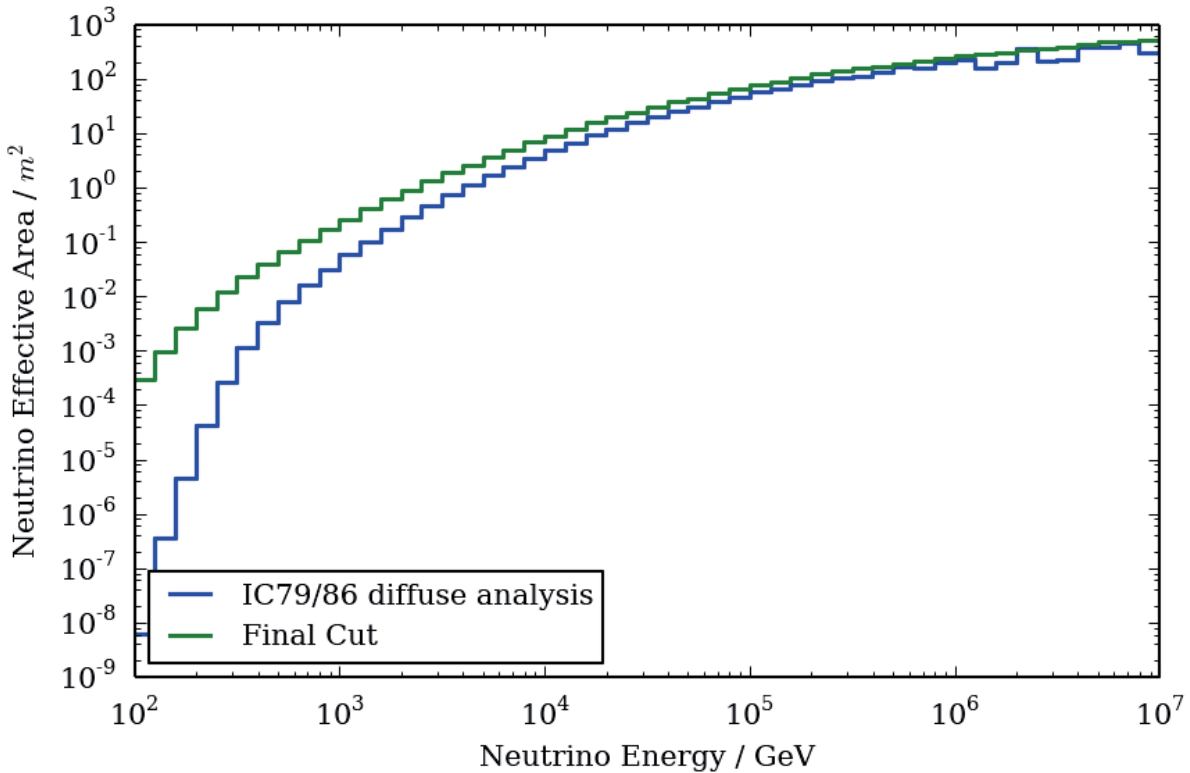


Figure 5.16: The effective area of the upward-going muon neutrino event selection. Using a BDT allows this selection to be larger than previous analyses which used straight cuts. This plot comes from [74].

directly measure the neutrino energy as in the analyses from Sections 5.1.1 and 5.1.2. The energy of the muon is estimated by an energy proxy which measures the energy loss per distance, often referred to as  $\frac{dE}{dX}$ , and can be mapped into muon energy via Monte Carlo. Figure 5.17 shows the muon energy resolution of the upward-going muon neutrino selection. The resolution across all energies is about a factor of 2 and scales linearly with the true muon energy. Because muons can travel and lose energy for many kilometers before entering the detector, the neutrino energy for an inferred muon energy proxy value can vary greatly. In order to account for this properly, the data and the Monte Carlo are compared and fit based on their energy proxy values. When the neutrino energy distribution is desired, the distribution of Monte Carlo neutrino

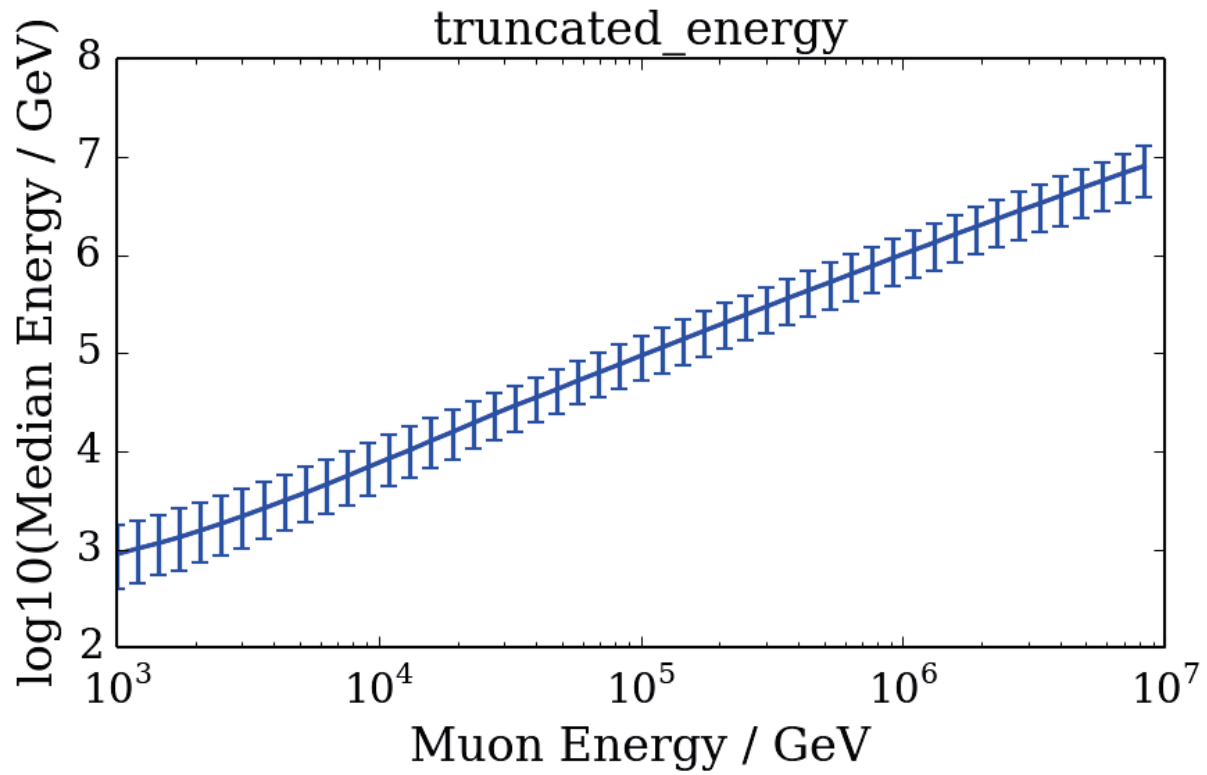


Figure 5.17: The energy mapping and resolution of the muon energy proxy, called Truncated Energy [78], used in the upward-going muon neutrino event selection. This plot comes from [74].

energies can be plotted with the events weighted to the best fit spectrum. Since the energy resolution is poor, the zenith dependence of the sample can also play an important role in determining the spectra of the atmospheric and astrophysical components of the fit. This can be seen by inspecting the atms. numu and astro. numu panels of Figure 5.15. The majority of difference comes at the horizon (cosine of the zenith angle equal to 0) where Earth absorption of high energy neutrinos allows the events from the harder astrophysical spectrum to come through more substantially. The angular resolution of the selection is shown in Figure 5.18 and varies from around 2 degrees at 1 TeV to 1 degree at 100 TeV and above.

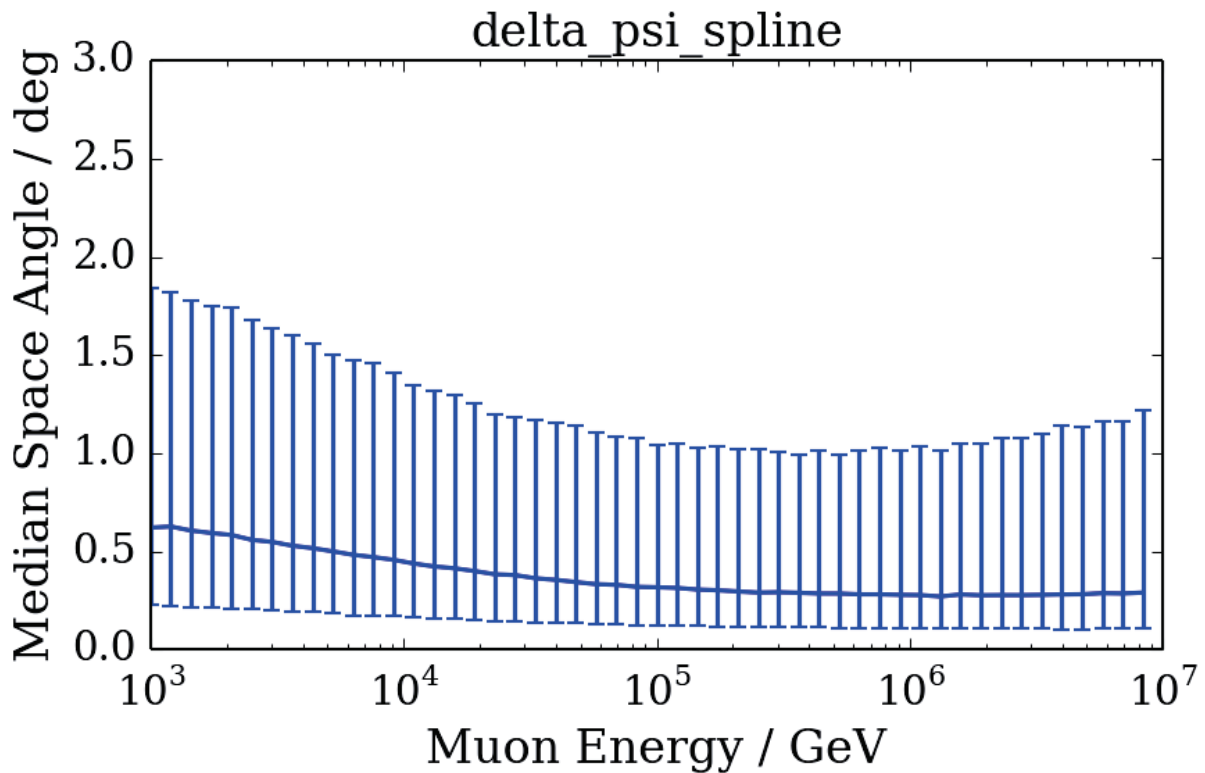


Figure 5.18: The zenith resolution of the muon direction reconstruction used in the upward-going muon neutrino event selection. This plot comes from [74].

The final result is obtained by fitting the Monte Carlo (with conventional atmospheric, prompt atmospheric, and astrophysical neutrino components) to best describe the data, shown in Figure 5.19. The fitting procedure to find the parameters which best describe the data involves binning the data in reconstructed energy and zenith. This binned data is then used in a per bin Poissonian likelihood. The Monte Carlo and data show clear agreement, as is verified by a 95.4% p-value on fits for random Monte Carlo ensembles. Events in support of an excess of astrophysical events above the atmospheric background are observed in

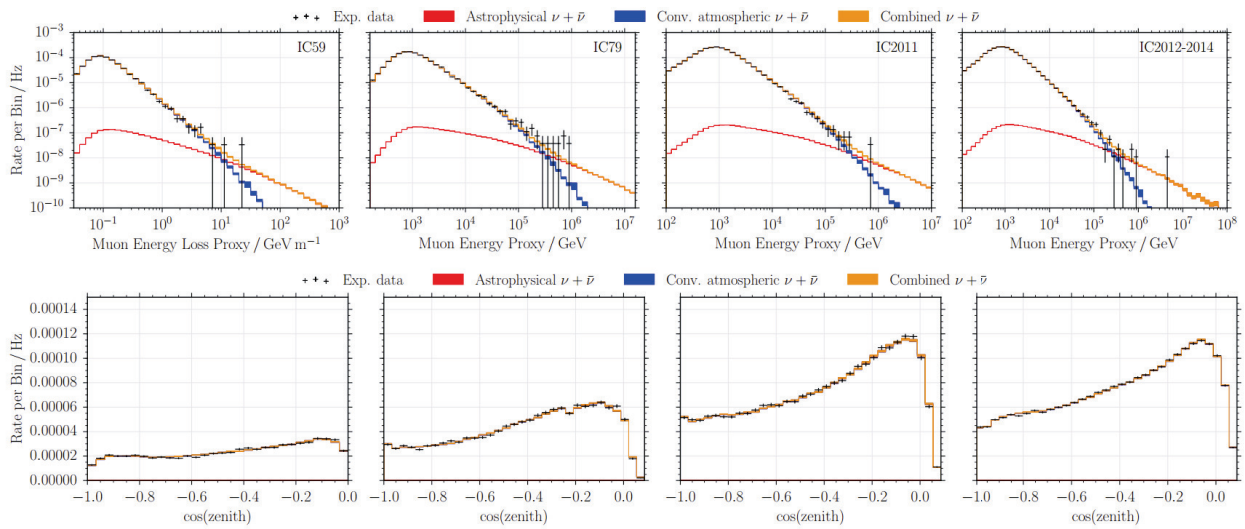


Figure 5.19: Best fit of the conventional atmospheric, prompt atmospheric, and astrophysical neutrino components to the data in the 6 years considered in the upward-going muon neutrino selection. This plot comes from [37].



every year of the selection, and represent a  $5.6\sigma$  excess over the atmospheric only hypothesis. The important result then is the constraint on the astrophysical excess, shown in Figure 5.20. The analysis finds a best fit

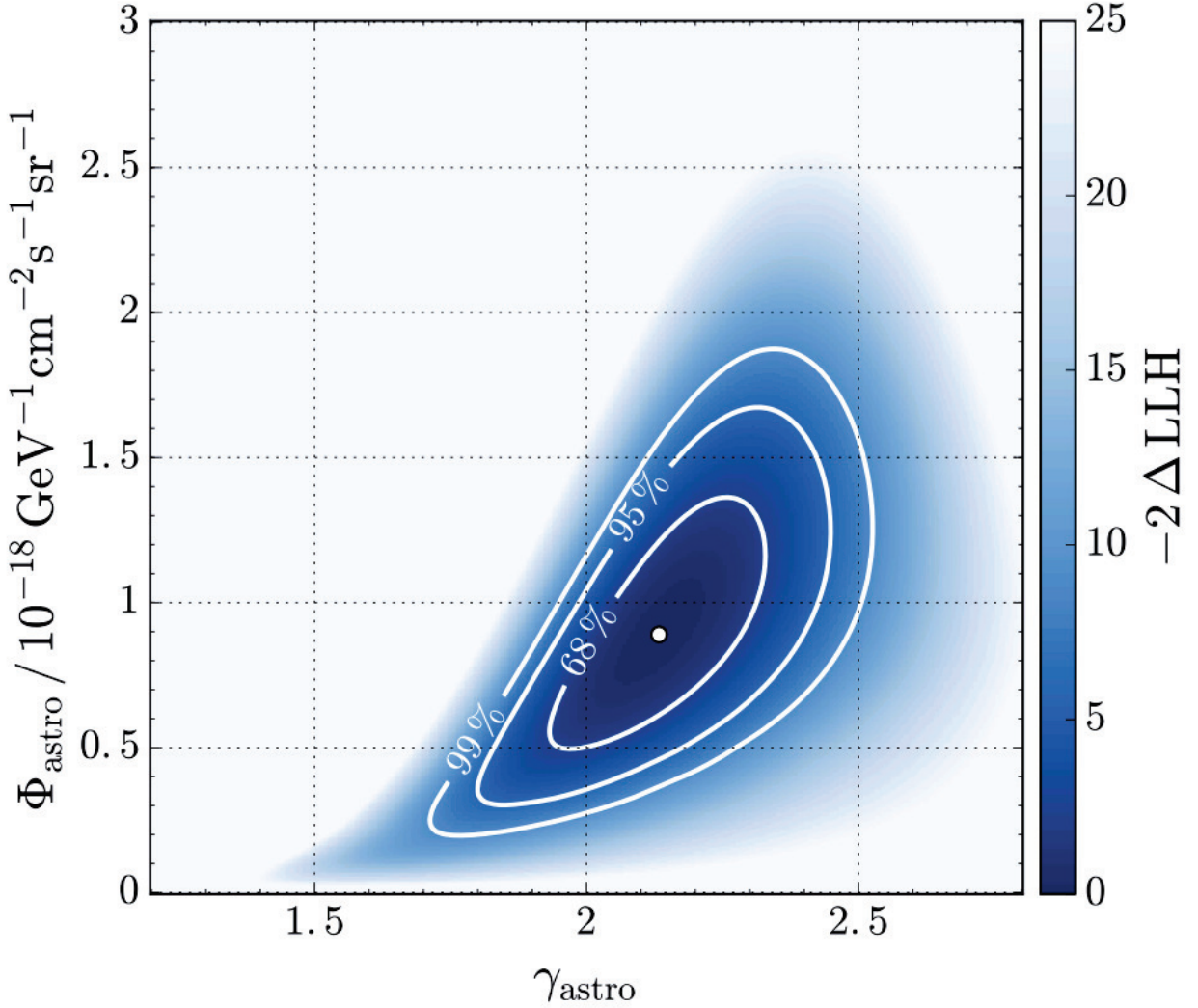


Figure 5.20: Constraint on the astrophysical normalization and spectral index from the upward-going muon neutrino selection. The best fit prefers a hard spectrum near 2. This plot comes from [37].

spectrum of

$$\Phi_{astro} = 0.90_{-0.28}^{+0.3} \times 10^{-18} \left( \frac{E}{100 \text{ TeV}} \right)^{-2.13_{-0.13}^{+0.13}} \text{ GeV}^{-1} \text{ cm}^{-2} \text{ sr}^{-1} \text{ s}^{-1} \quad (5.4)$$

which is consistent with initial predictions of astrophysical fluxes provided by theory [79].

### 5.3 Discussion of Astrophysical Flux Measurements

Three measured spectra for of the astrophysical flux have been published so far. Of the published results only HESE and MESC spectra agree with each other within one sigma confidence. The major outlier appears to be the upward-going muon neutrino measurement. This is not particularly alarming, but is of note and worth a brief discussion. There are four options to consider. One, some of the methods used to measure the astrophysical spectrum are flawed. Two, the spectrum has different properties depending on the part of the sky you look at. Three, the spectrum has different properties depending on what energy you look at. Four, the measured spectra are actually the same.

The methods used by the upward-going muon neutrino search is more sound than that of the starting event searches. This is because the upward-going muon neutrino search depends only on reconstructing track-like events to a few degrees with energy resolution of a factor of 2. The spectral change that is observed at 100 TeV in this analysis is a signature only of astrophysical neutrinos. The starting event analyses are subject to a little bit more modelling. This is because most of the starting events are cascades which can only be measured thanks to the indirect atmospheric self veto, see Section 4. If the self veto were weaker than predicted by the analytic calculations then it is likely that the measured spectrum which was previously thought to be astrophysical is in fact the charm spectrum.

Another option is that there is a dependence to what is measured based on what part of the sky is observed. This is motivated by the Galactic Center and most of the Galactic Plane being located in the southern hemisphere. These Galactic sources are predicted to be neutrino emitters at some level, all be it at a softer spectrum closer to  $E^{-2.7}$  with a possible cutoff like that of the cosmic rays which create it. If the Galactic sources were yet unresolved because of the limited resolution of cascades and the energy cutoff giving an insignificant result in the IceCube point source search then this would show up as a hemisphere dependent diffuse spectrum in IceCube's measurements first. This is in line with what IceCube observes. MESC and HESE are sensitive to lower energy neutrinos from the southern hemisphere and measure a spectral index closer to  $E^{-2.7}$  while the through-going muon search is sensitive to higher energy neutrinos from the northern hemisphere and measures a spectral index closer to  $E^{-2}$  as is expected from shock acceleration. This idea is partially covered in the third option, but there is also a possibility which does not have any zenith angle dependence. In this option it could be that the Galactic sources are not the class of sources which give a softer spectral index, but rather some extra-galactic class of sources. Thus IceCube is measuring two classes of diffuse sources and the different analysis styles are sensitive to the classes in different energy regions.

The fourth option is that only one spectrum is being measured and the two reported values are just statistical fluctuations. Figure 5.21 shows the current 90% contours for a few event selections. The relevant contours in this plot are the ones labeled IC tracks (6yr), IC HESE (4yr), and IC combined. The IC combined

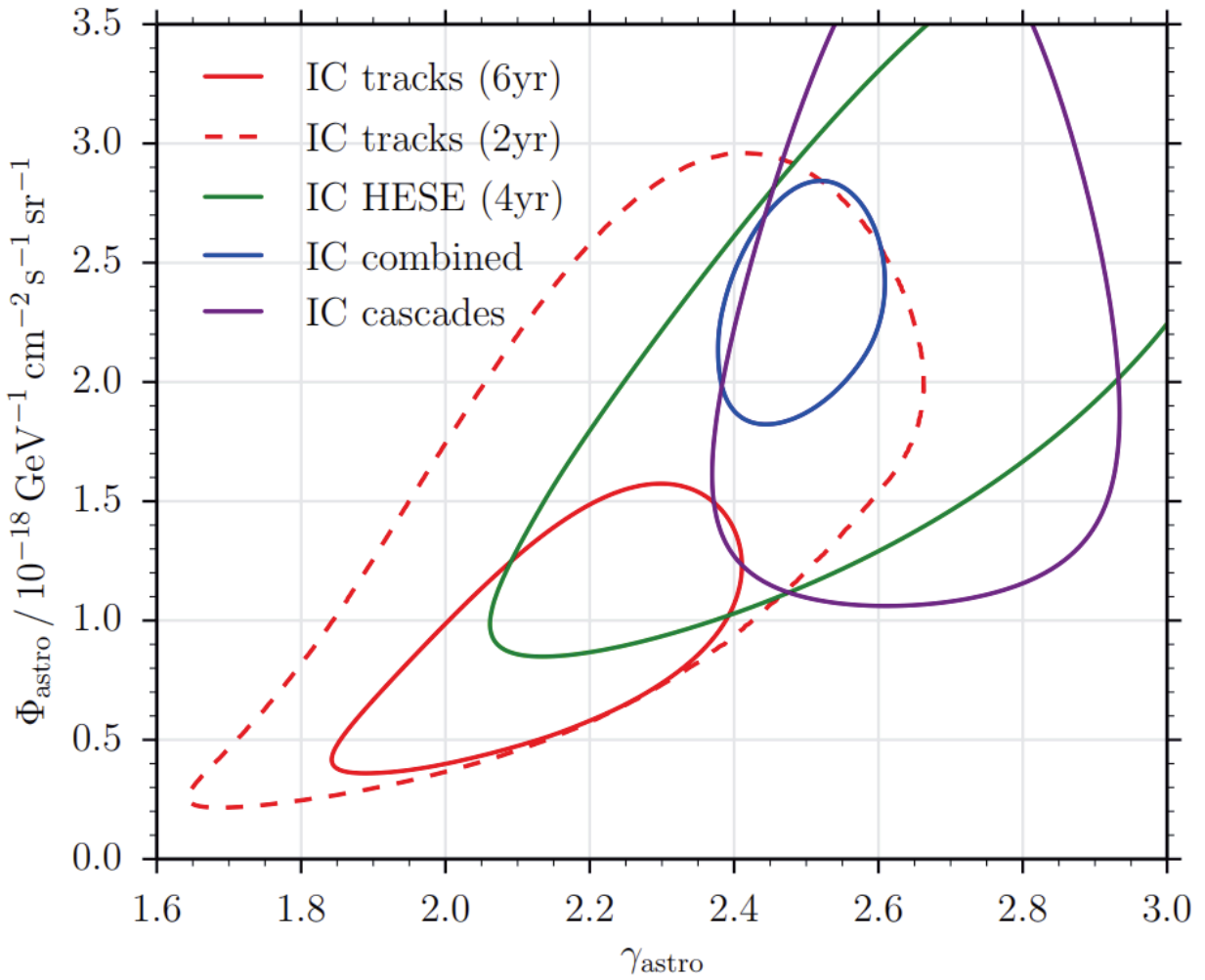


Figure 5.21: 90% contours of different analyses measuring the astrophysical spectrum with IceCube. All of the measured spectra agree with at least one other analysis within the one sigma contour.

and IC tracks (6 yr) contours are the only analyses that do not have overlapping contours. The tension that these two analyses have is 3.3 sigma. While this is not likely to happen by chance it is possible that this is a statistical fluctuation.

The event selection which is discussed in this thesis has a unique opportunity to assist in clarifying this picture. The events which will be clearly astrophysical will all be tracks between 10 to 100 TeV, and come from the southern hemisphere. The measurement of the spectrum with these events will provide another piece to this puzzle.

## Chapter 6

### IceCube Detector

IceCube's main goal is to measure the properties of the astrophysical neutrino flux and, with some luck, the sources which comprise the flux. As was eluded to in the background material of Chapter 3, this is accomplished by detecting the Cherenkov light given off by the byproducts of neutrino interactions. IceCube is deployed at the South Pole, near the Amundsen-Scott South Pole Station. The reasons for this location are two-fold. First, the ice properties in the glacier at the South Pole are quite pristine, allowing light to travel roughly 100 m before being absorbed. Second, the station offers logistical support for the detector construction and operation. The main in-ice detector consists of 78 strings of optical modules spaced on a 125 m triangular grid. The optical modules are deployed every 17 m between 1450 m and 2450 m. There is also a denser infill array of eight strings called DeepCore deployed from 1750 m to 2450 m with intra DOM spacings of about 7 m and intra string spacing of roughly 72 m. This infill lowers the minimum detectable energy of IceCube from 100 GeV to 10 GeV and allows IceCube to compete with dedicated experiments in neutrino oscillation measurements [80]. On the surface of the ice, there is a cosmic ray air-shower detector called IceTop. At the top of every IceCube string are two tanks which are filled with water and two optical modules each. The water is frozen in a controlled manner to make clear ice. IceTop detects the by product electrons, protons, gamma rays, and muons of cosmic rays between 1 PeV and 1 EeV, known as the knee of the cosmic rays. A schematic of the full detector is shown in Figure 6.1. The detector is operated entirely on the output of custom made Digital Optical Modules(DOMs) which collect information about light observed from events.

This section will cover the detector from photon collection to the initial event classification. Details on the detector design, construction, calibration, and operation can be found in "The IceCube Neutrino Observatory: Instrumentation and Online Systems" [81] while the details of the photo-multiplier tube (PMT) can be found in "Calibration and Characterization of the IceCube Photo-multiplier Tube" [62]. Information about the DOM and it's sub-systems is available in "The IceCube Data Acquisition System: Signal Capture, Digitization, and Timestamping" [82].

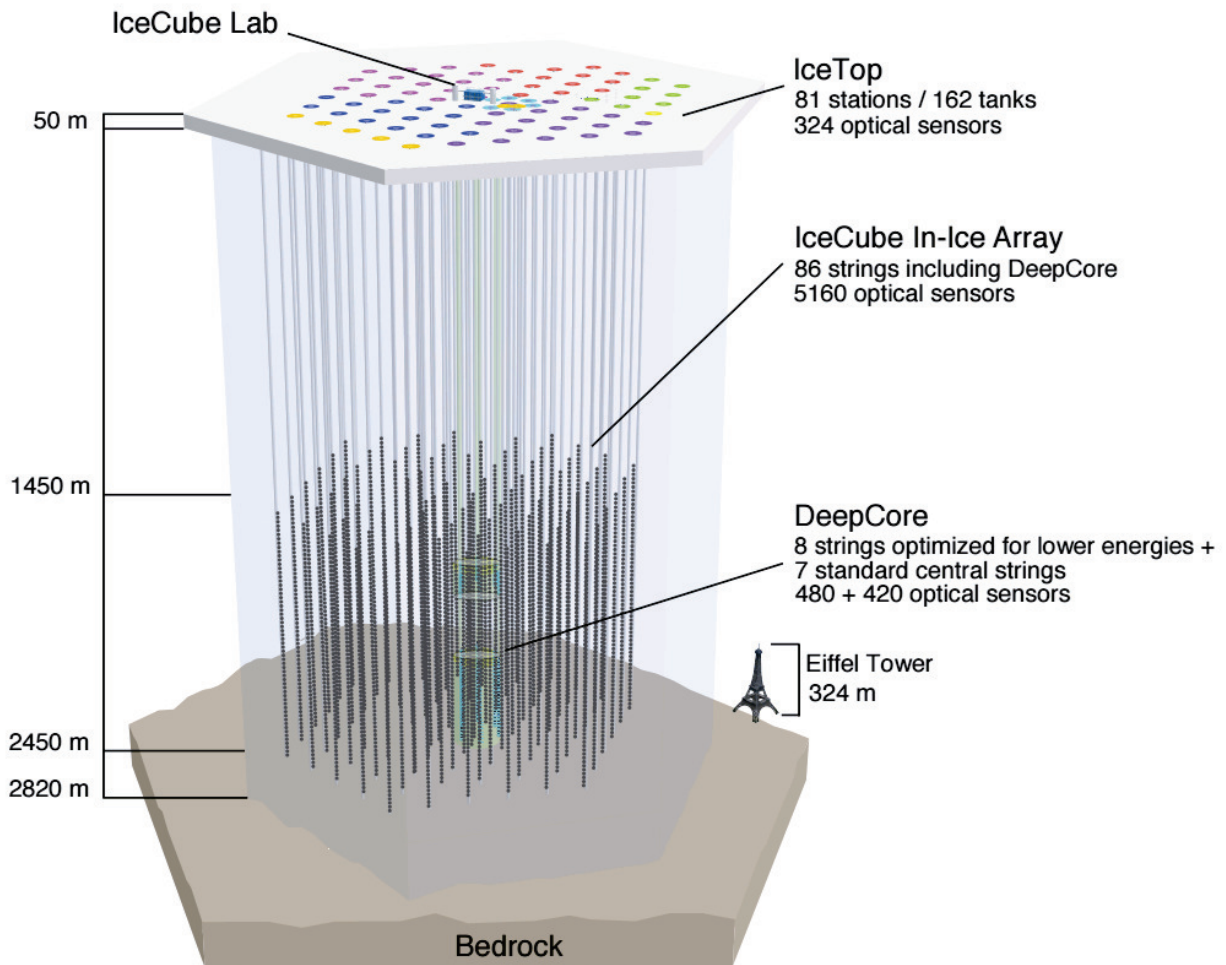


Figure 6.1: The IceCube Neutrino Observatory consists of the in-ice array, the sub-array DeepCore, and a cosmic-ray air shower array IceTop.

## 6.1 DOMs

IceCube's DOMs are the only detection unit in IceCube. The entire detector is constructed of a repeating pattern of strings of DOMs deployed over a cubic kilometer in the glacier below the South Pole. This section will focus on the hardware of the DOM and how it operates.

### 6.1.1 Hardware

The idea motivating development of the DOM was a large area light sensor with on board digitizing electronics encapsulated in an optically transparent pressure vessel. Light from events which impinges on the outer surface of the DOM has the potential to be detected, however it must make a detectable electric signal to do so. Before the process of detection begins, photons must transit the borosilicate glass pressure housing and an optical coupling gel. The glass housing, produced by Benthos, is 13 in in diameter and .5 in thick. Light which is normally incident on the glass has a measured transmission of 93% at 400 nm, 50% at 340 nm, and 10% at 315 nm. This coupled with the gel's transmission of 97% at 400 nm 91% at 340 nm, and 65% at 300 nm provides the short wavelength cutoff to light detection at around 350 nm. The glass and gel are optically matched so effects like reflection are minimized. Light that has transited the optical material then begins the detection process at the photo-multiplier tube(PMT) [62]. IceCube uses the Hamamatsu R7081-02 PMTs, shown in Figure 6.3, for normal IceCube DOMs and R7081-02MOD PMTs, which have a higher quantum efficiency, for the more sensitive DeepCore Strings. The dynode chain is a box-and-line design with 10 stages and is housed in the neck of the bulb while the photo-cathode is on the face of the bulb. All in-ice DOMs are operated at a gain of  $10^7$ . The PMT is oriented face down in all IceCube DOMs and is secured in the optical coupling gel. To reduce the effects on collection efficiency from the ambient magnetic field, a mu-metal cage surrounds the PMT from bulb to the neck. The rest of the components in the DOM are circuit boards. These are mounted to fit either around the neck of the PMT via a molded plastic collar or via direct soldering to the output pin base. The  $10^7$  gain of the PMT is supplied via the High Voltage Control Board and is deployed via a resistive voltage divider circuit on the PMT Base Board. The voltage generator can supply a maximum voltage of 2047 volts at  $30 \mu\text{A}$ . When the PMT attempts to source more than  $30 \mu\text{A}$  the DOM is said to be saturated. The PMT is operated with the cathode at ground potential, leaving the signal floating on the high voltage at the pin base. To read out the signal, a 1:1 bifilar-wound toroid transformer is used with one end coupled to the high voltage from the PMT and the other coupled to the Main Board where the signal is processed. Single photo-electron signals (SPEs) at this point are approximately 8 mV in height with a spread of 7-8 ns. The SPE signals are digitized and processed by the Main Board, described in [82].

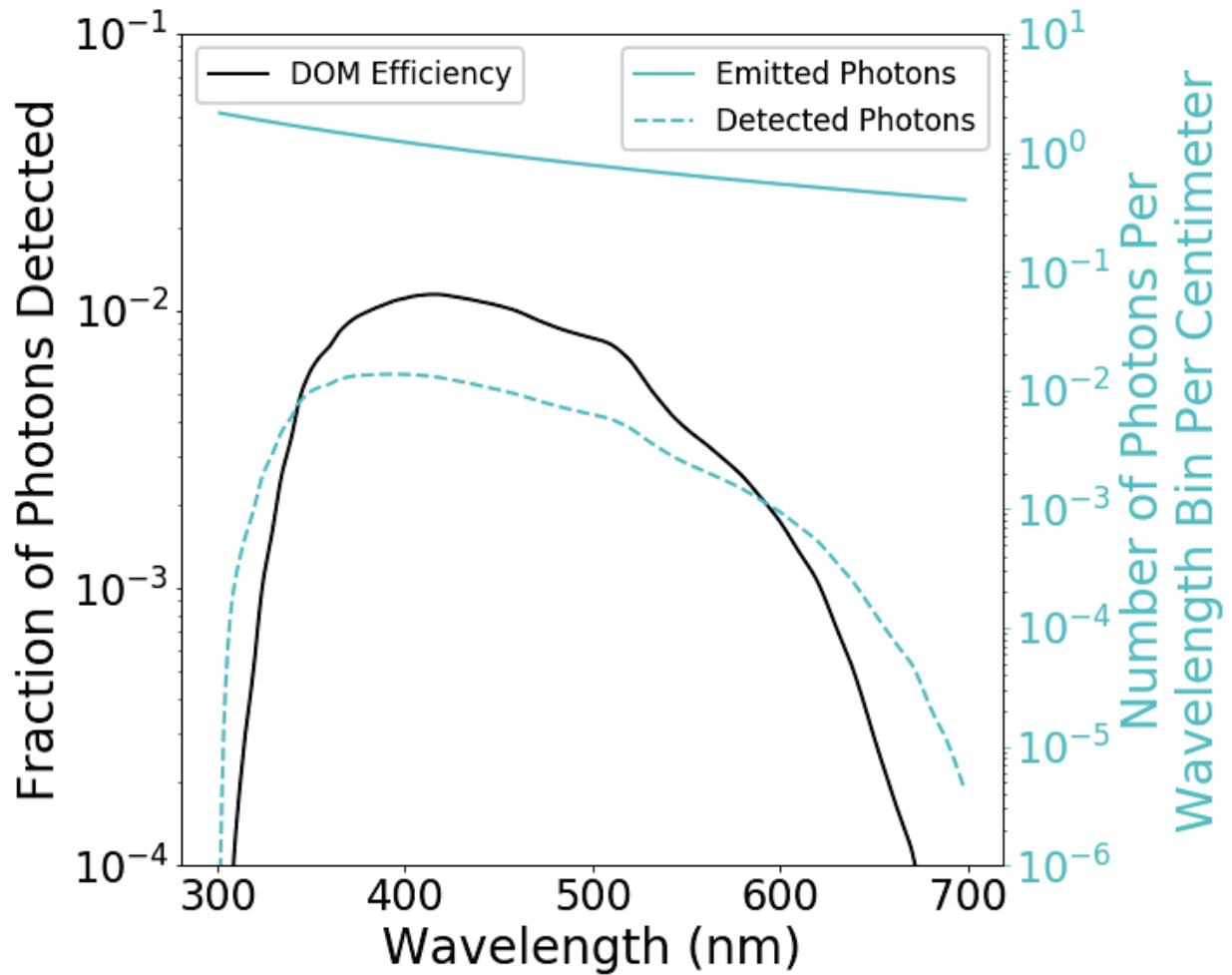


Figure 6.2: The efficiency of the DOM (Glass, gel, and PMT) for detecting light of wavelengths between 300 nm and 700 nm in black. The peak efficiency is at 416 nm. The Cherenkov spectrum, solid cyan line, is convolved with the efficiency to give the number of detected photons at different wavelengths, shown as the dashed cyan line. For a track, the  $\sim 350$  emitted photons per centimeter of track length in the direction of the DOM are reduced to  $\sim 2.1$  photons per centimeter of track length detected by the DOM.



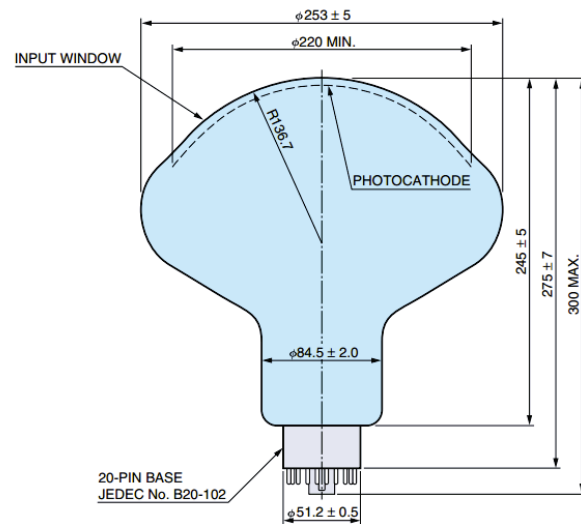


Figure 6.3: IceCube R7081 PMT from Hamamatsu. The dynode chain is housed in the neck of the bulb while the photo-cathode is on the face.

The Main Board is essentially a single-board data-acquisition computer which functions as a controller for all the on-board devices, digitizer, computer, communications system, and timing calibrator. Two other boards which are not directly related to data acquisition are also present, the Delay Board and Flasher Board. The Delay Board physically delays recorded signals by 75 ns via a 10 m long copper trace so that portions of the signal present before a threshold crossing can be recorded. The Flasher Board contains 12 LEDs (ETG-5UV405-30) arranged in pairs every 60° along the Flasher Board which emit light at 405 nm. There are also 16 DOMs, eight near the center of the detector and eight on the edge of the detector, which have LEDs of wavelengths other than 405 nm. These DOMs have three pairs of LEDs with each pair at 370 nm, 450 nm, and 505 nm. The colored and standard flashers are used to determine the timing, position, and wavelength dependence of the DOMs in-situ. Additionally, the flashers help with calibration tasks like measuring the optical properties of the ice and shower event reconstruction. A schematic of the full layout of the DOM, minus the glass pressure vessel and gel, can be seen in Figure 6.4

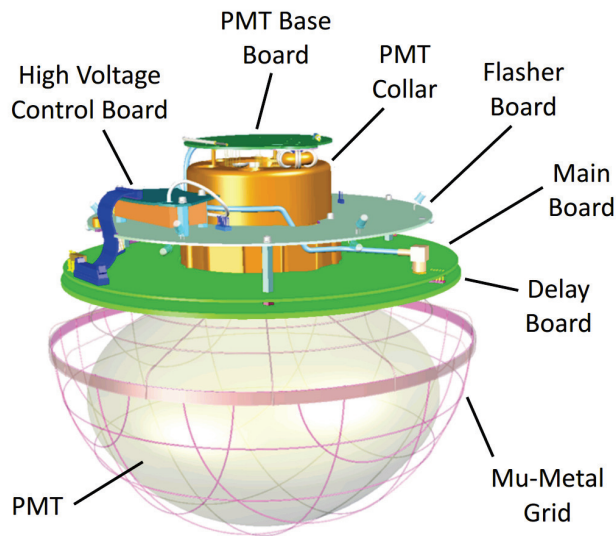


Figure 6.4: A schematic of the IceCube DOM with all the components discussed in Section 6.1.1.

### 6.1.2 Operation

IceCube operates by detecting photo-electrons (PEs), the electronic signal created by the PMT when 1 photon is converted. For DOMs in the ice the PEs which transit the PMT must pass a SPE discriminator trigger set at .25 PE. This begins a "launch" in the DOM electronics. After a launch PEs are recorded by the Main Board's four digitizers. Three of the digitizers are analog transient waveform digitizers (ATWDs) with a pre-digitization amplification gain of 16, 2 and .25 respectively. The difference in gains is designed to completely cover the dynamic range of the PMT output from single SPEs to 7.5 V when saturated. These

digitizers operate at 300 Msps and digitize 128 consecutive samples, leading to a 426.67 ns recording, with 10-bits per sample allowing for 1024 different voltage levels to be captured. The digitized voltage is known as a waveform. Since interesting parts of the waveform may occur before the discriminator is triggered the signal is delayed for 75 ns via the Delay Board mentioned in Section 6.1.1. Many signals are captured completely in the highest gain channel and only its information is kept. Signals which reach 75% of the range of a higher gain channel also have information kept for the next lowest amplification channel to ensure complete waveform information with no clipping. The ATWDs are designed to record light which has travelled with little scattering to the DOM, however, light may reach the DOM much later due to the light being emitted far away or being scattered more intensely. For these late photons there is a fourth digitizer, the fast analog to digital converter (fADC). The fADC samples continuously and is designed to capture information from the discriminator crossing to 6.4  $\mu$ s after the crossing at 40 Msps and 10-bits per sample with a dynamic range comparable to the highest gain channel. In order to accommodate the slower sampling of fast voltage changes additional pulse shaping is applied to the pulses. An example of a waveform captured in an ATWD and the fADC can be seen in Figure 6.5. Digitization does not occur continuously on a single ATWD chip since the ATWDs have a re-arm delay of 50 ns. To prevent a significant dead time which would occur for back-to-back launches a pair of the ATWD chips are operated alternatively. This limits loss to situations where more than one back-to-back launch occurs, amounting to a fractional loss of operating time of  $6.6 \times 10^{-5}$  per DOM on average. Digitized waveform information is saved in a "hit" record. The hits are transferred to a SDRAM look-back memory(LBM). The CPU on the Main Board bundles the hits together and transfers them to the surface computers when the surface computers initiate a request. The amount of information provided per hit depends on whether the hit was recorded in coincidence with a hit on a neighboring DOM. For isolated hits only the time of the hit and the charge from the integrated waveform are transmitted. If the nearest or next-to-nearest neighbour DOM, known as a local coincidence(LC), has launched within  $\pm 1\mu$ s then the full waveform is sent in a compressed format. The LC condition is determined by wire pairs in the main cable, discussed further in Section 6.2. The DOM Main Board also contains dedicated hardware for creating and recording LED flashes on the Flasher Board.

## 6.2 Design of a String

As discussed in the introduction of this Chapter, IceCube's in-ice detector consists of 86 strings of DOMs. These strings are deployed via a custom cable designed to provide structural, power, and communication infrastructure. Deployment of a string of DOMs begins after hot-water drilling of the 2.5km hole is complete. The assembly begins with the bottom DOM being attached first and continues up the string with the cable and attached DOMs being lowered into the hole as assembly continues. DOMs were designed in two versions. One has the communications connection electrically terminated (T) and one with the communications

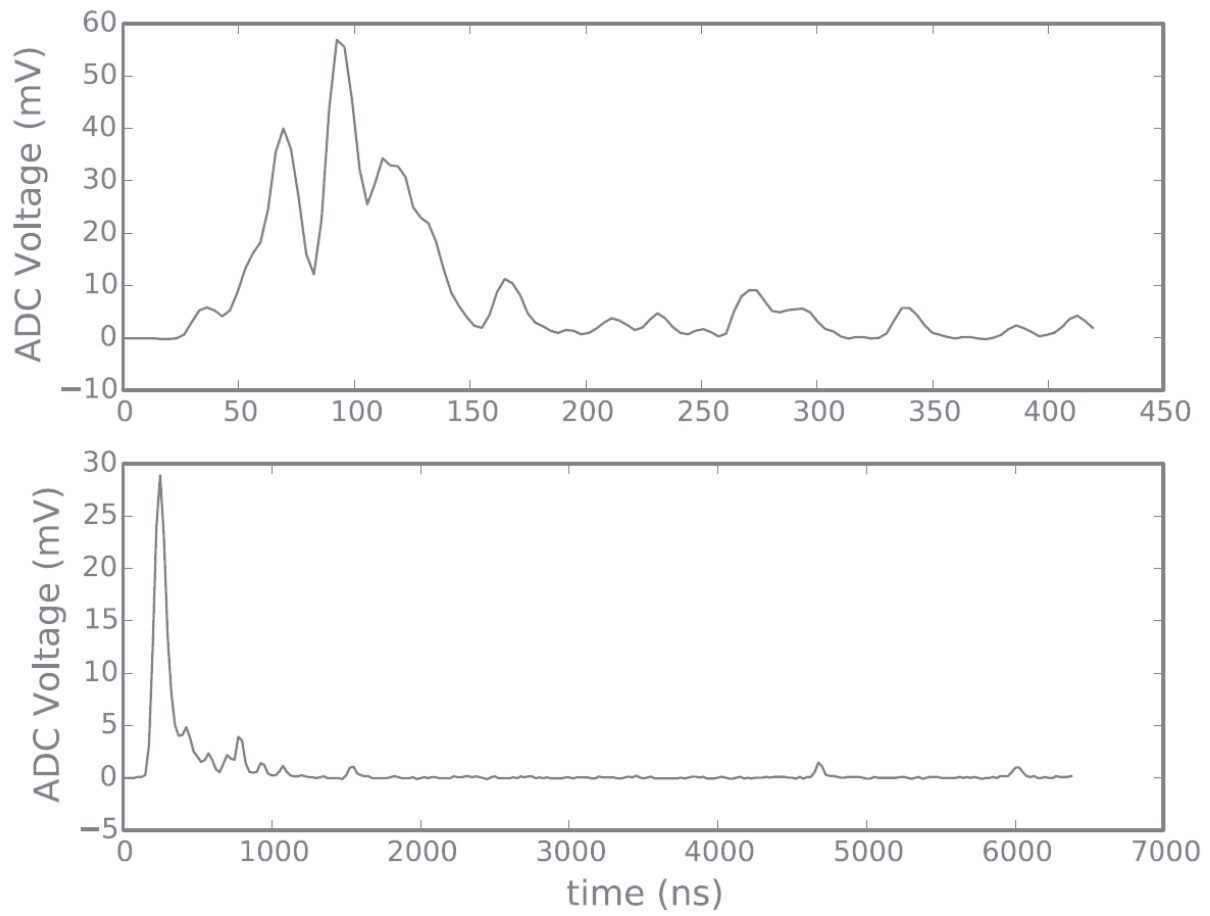


Figure 6.5: A waveform recorded in the ATWD(top) and fADC(bottom) from [81]

connection unterminated (U). The DOMs are deployed in pairs with the T DOM deployed 17m below its paired U DOM. This allows a pair of DOMs to communicate on one communications twisted wire pair. To attach a DOM to the cable a physical and electrical connection must be made. The physical connection is made by bending the cable and attaching a YaleGrip above and below the DOM's location. Each DOM is held by a harness which consists of a waistband around the DOM and three steel cables fixed to the harness and collected above. The YaleGrips are attached to the harness via a chain. The physical weight of all the DOMs is supported by the main cable with assistance from buoyancy of the DOMs in the water left in the hole after drilling. The electrical connection is made via a cable broken out of the main cable at the location of the U DOM. This cable provides electrical power and communications to the DOM. Additionally, the wires for determining coincidence between DOMs is contained in this break out cable. The mechanical and electrical connection of the DOMs to the cable is shown in Figure 6.6. Two pairs of DOMs have their wire combined into a twisted assembly of four wires, known as a quad. This configuration provides electrical cross talk reduction. Fifteen quads are needed to connect the 60 DOMs on a string. These 15 quads are bundled together with sections of filler and a strength membrane to make up the in-ice cable as is seen in Figure 6.7. After all the DOMs are connected to the cable, the assembly is lowered an additional 1.5 km to its final location. The top of the cable is secured to a trenched anchor at the top of the hole and the end of the cable is connected to the corresponding Surface Junction Box (SJB) for that string and the corresponding IceTop DOMs. Each string's SJB is connected to the centrally located IceCube Lab (ICL) via a surface cable. Data collected on the DOMs is constantly requested and collected from the DOMs via hubs for the data from each string, known as StringHubs, in the ICL. The StringHubs hold the data until the data is requested by the DAQ in the process of building triggers.

## 6.3 Calibration

With 5160 independent DOMs deployed in the ice calibration is crucial to the operation of IceCube. Without a uniform procedure for calibrating DOMs measurements in each DOM would be unique and render the detector ineffective. Calibration of the DOMs is conducted so that every measurement of a photo-electron has exactly the same meaning and every documented pulse has the same relative time frame.

### 6.3.1 Calibrating a DOM

The main board of a DOM has all the necessary components to calibrate itself. This includes a DC bias generator, a pulser circuit, and a LED on the mainboard. The first thing which must be done is calibration of the launch discriminators with the pulser circuit. Calibration of these discriminators is redone later with PMT waveforms after the PMT gain is known. After this the levels of the ATWDs are calibrated with a sweeping of the input voltage with the DC bias generator. The relationship between voltage and ATWD

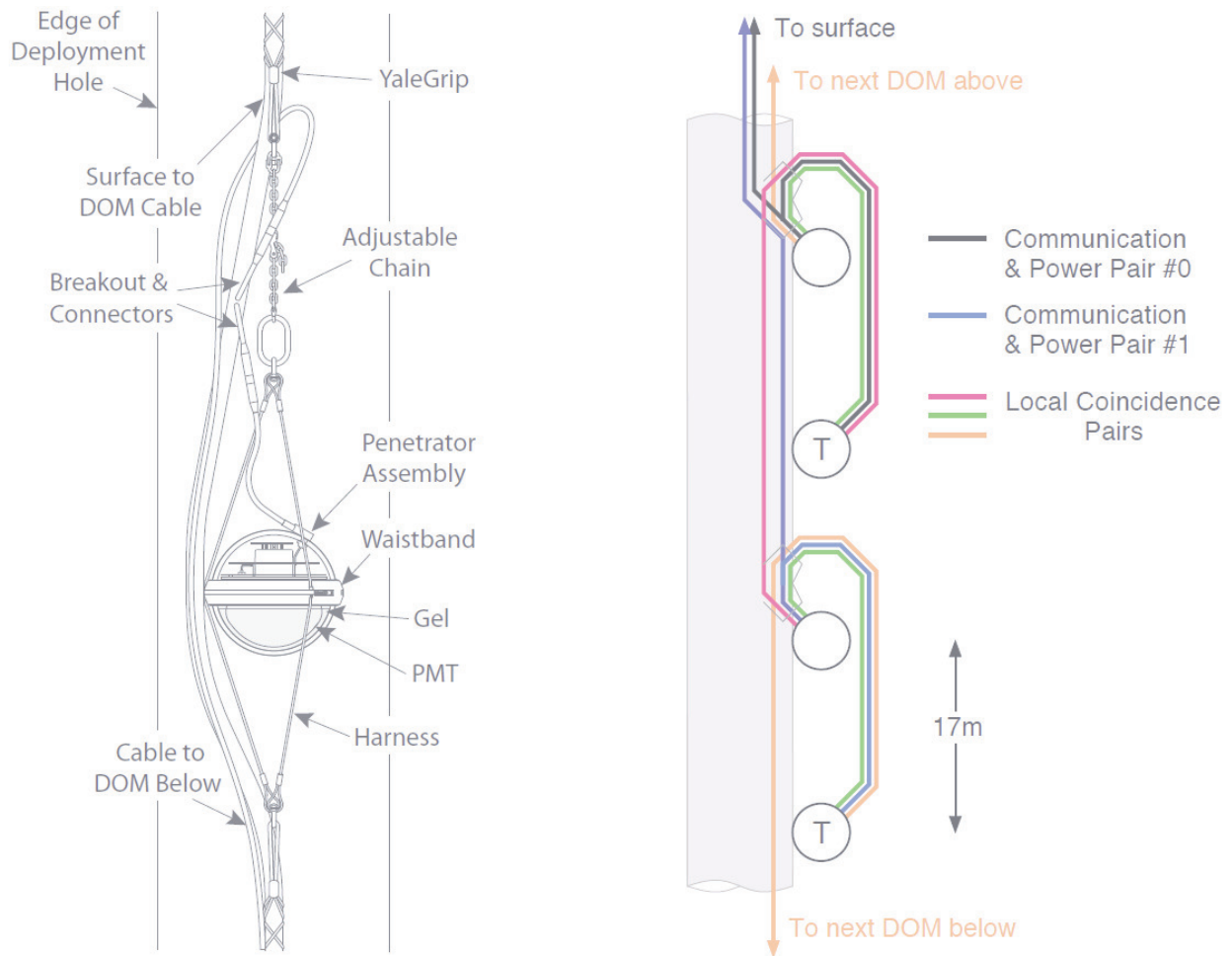


Figure 6.6: The mechanical connection of the DOM to the cable is shown in the left figure while the electrical connection of DOMs to the cable is shown in the right figure.

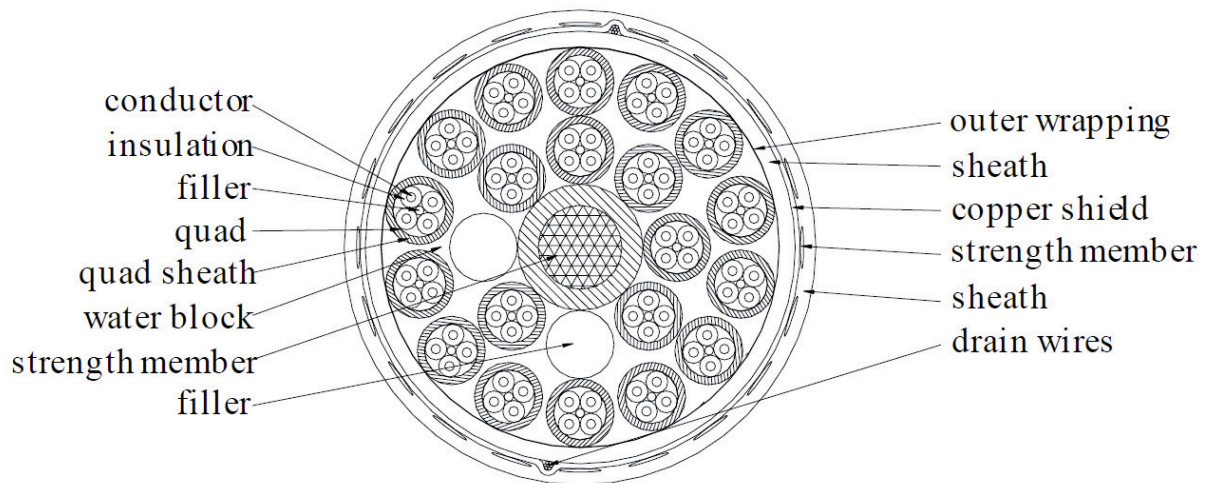


Figure 6.7: Cross-section of the in-ice cable. The 15 quads and strength membrane make up the electrical and mechanical backbone of the detector.

level is unique to each DOM and must be kept for later computations of charge. The voltage to ATWD relationship is also important for determination of the baseline since zero input voltage does not necessarily correspond to the lowest level of the ATWD. The levels of the highest gain ATWD channel is calibrated first and then used as a measuring stick in the determination of the response of the other ATWDs and fADC. The gain of the PMT is calibrated with dark noise hits. Since the charge of an electron from dark noise begins with a single particle it is known that the initiating charge is  $e$ . Inspecting the integration of these dark noise hits for different bias voltages is used to determine the gain of each DOM and tune their gain to  $10^7$ . With the information on the baseline, digitizer steps, and gain determined IceCube can be treated as a set of uniform detectors. Thanks to the stability of the operating conditions in the ice this calibration is only performed once per year, but some calibration values are constantly monitored during runs.

### 6.3.2 Time Calibration

The calibration of timing to a UTC GPS signal is accomplished with the Reciprocal Active Pulsing Calibration (RAPCal). The calibration operates by sending a bipolar pulse to each DOM over the power/communications wire pair. After the pulse has been received a similar pulse is sent back to the surface. These pulses are timestamped by the local clock at the transmission and reception point. Since the cable transmission is up-down symmetric a relative timing offset can be determined between the surface system and the DOM without any knowledge of the cable length. This is because the average of the transmission time of the pulse from the surface and received time of the pulse on the surface is the same as the average of the receive time of the pulse on the DOM and transmission time of the pulse from the DOM. Having this common time gives the timing offset needed to convert from DOM time to UTC time.

## 6.4 Modernization of the IceCube DAQ

While the design of the DOM is a technological achievement, its design was completed before the year 2000, almost 20 years ago at this point. With the success IceCube has had in measuring the astrophysical flux, there are plans to expand the detector in the future [83]. When such an expansion is realized, the advance in technology which has taken place in the years since the original DOM's design can be used to improve on the capability, complexity, and power consumption of the DOM. Work on improving the DAQ using a single Field Programmable Gate Array (FPGA) and Analog to Digital Converter (ADC) was accomplished as a part of this thesis and is presented in Appendix C.



## 6.5 Data Acquisition

The main goal of IceCube's Data Acquisition (DAQ) system is to reduce the data from all the DOMs into important physics events. This is made difficult from the start by the fact that the majority of triggered hits on the DOMs are the result of dark noise. In order to remove the isolated hits, software triggers search for spatial and temporal coincidence of LC hits on multiple DOMs which suggest the presence of an interesting physics event. These spatial and temporal coincidences constitute what is called a trigger of the detector. The main trigger for IceCube is the Simple Multiplicity Trigger (SMT) where a minimum (often 8) number of HLC hits are required within a time window of a few  $\mu s$ . Other triggers use a lower SMT value and impose a locality condition to the hits, such as a volume which other hit DOMs must occupy. Once an event's trigger time has been established, a time window designed to fully capture the information of that event is determined. All hits which fall within this time are saved with the event. For purposes of speed, the algorithm which searches for triggers is run across many processes in parallel. This can lead to events having overlapping trigger time windows. Any overlapping triggers are merged into one event. After a trigger window has been established, the information is passed along to the Event Builder. The Event Builder extracts the individual readout windows and requests the relevant subset of hits from the StringHubs to compose an event. Events are written to a temporary file which is renamed and sent to processing and filtering (PnF) when it reaches a preset size.

## 6.6 Data Filtering

All triggered events are inspected by the PnF system to determine the subset which is transmitted over the allotted 100 GB/day satellite connection available at the South Pole. Data which does not meet the criteria of the filtering stage are still archived and kept. The PnF system is a custom software system that occupies about 20 multi-processor servers of the South Pole System computing cluster located in the ICL. The first step to processing the data is the calibration of all the waveforms so that charge information is uniform across the detector. Next, a process known as Wavedeform is run to extract the individual PE pulses which can be inferred from the waveforms. Wavedeform operates by convolving known SPE shapes for each DOM with the waveform. The output are pulses which contain the time, amplitude, and width of all received photons on all DOMs. These pulses are the basis of all IceCube reconstruction. With all the DOM hits converted to calibrated pulses, algorithms which attempt to explain the collected pulses as either a track or cascade can be run. The vertex position, direction, amount of charge deposited, and goodness-of-fit in hypothesis tests are all used to determine if a particular event is interesting for a given analysis. Every year criteria to identify interesting events are proposed. These criteria define the filters which make up the base

of different high level physics analyses. In any given year there are around 25 filters which are operating to capture interesting physics events.

For the analysis discussed in this thesis, three filters in particular are of interest; the muon filter, the full sky starting filter, and the ESTReS(Enhanced Starting Track Realtime Stream) filter. All of these filters are designed to look for tracks. The muon filter is a simple filter with the objective of identifying muon neutrino induced tracks [84]. In the up-going region all events, with the exception of mis-reconstructions, are muons from neutrinos which have passed through the Earth. In the down-going region, a background of muons from the decay of hadrons in air showers dominates, thus different cuts are needed to obtain samples in the up-going and down-going regions. In both regions the filter starts from the SMT 8 trigger and has what is known as a trigger split applied to it to separate coincident events which ended up in the same trigger. The final common feature is an iteration of Line Fit which seeds a SPE Fit. From here the regions differ. In the up-going region (events with a SPE Fit zenith  $\geq 78.5$  degrees) only a fit quality cut is applied ( $\text{SPE Fit LogI}/(\text{Number of Channels} - 3) \leq 8.7$ ). For the down-going region (events with a SPE Fit zenith  $< 78.5$  degrees) the atmospheric muon background is removed with a zenith dependent charge cut ( $(\text{SPE Fit zenith} \leq (\arccos(1.5/3.3)*180/\pi) \text{ deg})$  and  $\log_{10}(\text{QTot}) \geq (0.6*(\cos(\text{SPE Fit Zenith})) + 2.15)$ ) This cut is visualized in Figure 6.8 and effectively removes low energy events which are largely composed of background muons. The full sky starting filter was designed to detect lower energy down-going muon tracks [85]. Since all incoming muon tracks are indistinguishable, events which appear to start in the detector are the focus of this filter. To quantify if a track is starting two cuts are applied. The first is a cut on the presence of any HLC hits in the outer layer or top 5 DOMs of the detector. The second uses the finiteReco reconstruction to determine the best fit track and starting/stopping points of the track in the detector. If the track starts 400 m above the center of the detector, it is rejected from the filter. The ESTReS filter was developed as a component of this dissertation and will be discussed in Section 9.7 where the ESTES event selection is presented.

Beyond the scope of the standard collected in-ice data's path from DOM to filtering are a plethora of components which are auxiliary to this topic. These components vary from additional hardware in the DOM to a live data monitoring suite that operates continuously with the South Pole. Many of the components are custom made and discussed in detail in IceCube's recent detector paper mentioned in the intro of this section.

## 6.7 Ice

All of IceCube's events are detected after the light emitted by the traversing particles has propagated through the ice in which IceCube is embedded. Thus all of IceCube's statements about particle direction and energy are tied directly to the ice. The knowledge of the ice properties in IceCube comes from flasher data.

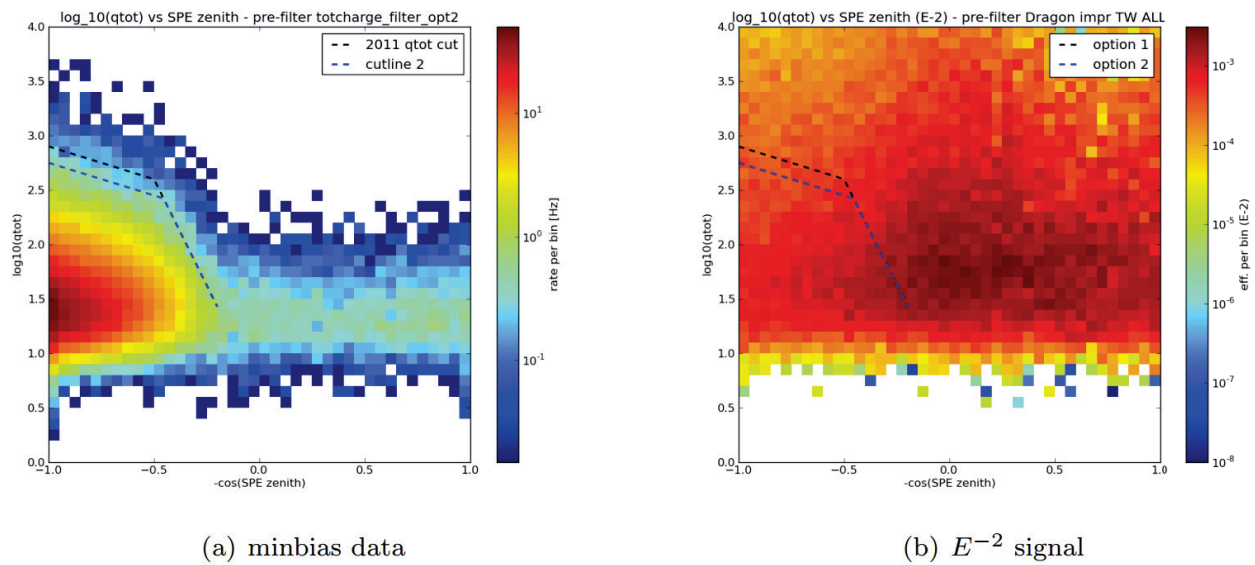


Figure 6.8: The cuts applied to obtain events for the muon filter displayed on background (a) and astrophysical signal (b). The up-going region has no cuts applied to it aside from a quality cut on the goodness of fit. In the down-going region a cut is applied to remove events below the dashed line in both a and b. The bulk of the down-going atmospheric muons are removed while many high energy astrophysical neutrinos are kept. The line used for the filter is the more permissive dashed blue line (labeled cut line 2 and option 2).

Flasher data refers to data taken while light is emitted from the DOM's LEDs. In the method used, the LEDs on one DOM are flashed together and the emitted light is recorded on all other DOMs in the in-ice detector [86]. A global fit of the collected data is performed to determine the model that best describes the full data set. At the time of writing, the best model of the ice is one which includes bulk ice scattering and absorption which vary in layers as a function of depth. These layers are known not to be horizontal, but instead have a tilt which is perpendicular to the flow direction of the glacier IceCube is embedded in [87]. In addition, there is an anisotropy in the absorption and scatter as a function of azimuthal angle in the detector with the direction of less scatter/absorption along the direction of the flow and more scattering/absorption in the direction of the tilt [88]. The reason for this correlation is currently unknown. There is also the possibility that there are effects local to the DOM from bubbly ice formed after drilling and the presence of the large IceCube cables which connect the DOMs and provide electrical connections. Both of these possibilities are being studied currently, and have not been verified yet. Each of the topics listed above will be discussed in more detail in their relevant section below. Much of the theoretical background described comes from the paper "Optical Properties of South Pole Ice" [89].

### 6.7.1 Scattering

Scattering of the optical light in the ice can be described by the scattering of electromagnetic radiation off microscopic dust grains. This is often referred to as Mie scattering after Gustav Mie who first described it [90]. In ice the typical distance between scatters is much larger than the wavelength of the light of interest (400 nm), but much smaller than the distance from DOM to DOM or typical particle to DOM. As such we can ignore interference effects from multiple close scattering centers, but must accommodate the fact that nearly all the observed light has scattered at least once on its way to the DOMs. Since particles emit many photons at once, it is important to consider not just the effect scattering has on the individual photons but the photon field as a whole. After  $n$  scatterings, the average deviation of the field can be expressed as  $\langle \cos\theta \rangle_n = \langle \cos\theta \rangle^n$  where  $\langle \cos\theta \rangle$  is the scattering after one interaction. Thus in the case that  $\langle \cos\theta \rangle \approx 1$  the net effect of a scatter or collection of scatters is small. The model used to describe the scattering function  $p(\theta)$  is a linear combination of the Henyey-Greenstein [91] and simplified Liu [92] functions.

$$p(\cos\theta) = (1 - f_{SL})HG(\cos\theta) + f_{SL}SL(\cos\theta) \quad (6.1)$$

where  $HG$  is the Henyey-Greenstein function

$$HG(\cos\theta) = \frac{1}{2} \frac{1 - g^2}{[1 + g^2 - 2g\cos\theta]^{\frac{3}{2}}} \quad (6.2)$$

with

$$g = \langle \cos\theta \rangle \quad (6.3)$$

and the simplified Liu function is

$$SL(\cos\theta) = \frac{1 + \alpha}{2} \left[ \frac{1 + \cos\theta}{2} \right]^\alpha \quad (6.4)$$

with

$$\alpha = \frac{2g}{1 - g}, \quad g = \langle \cos\theta \rangle \quad (6.5)$$

The shapes of the Henyey-Greenstein, simplified Liu, and Mie functions for  $g=.943$  is shown in Figure 6.9

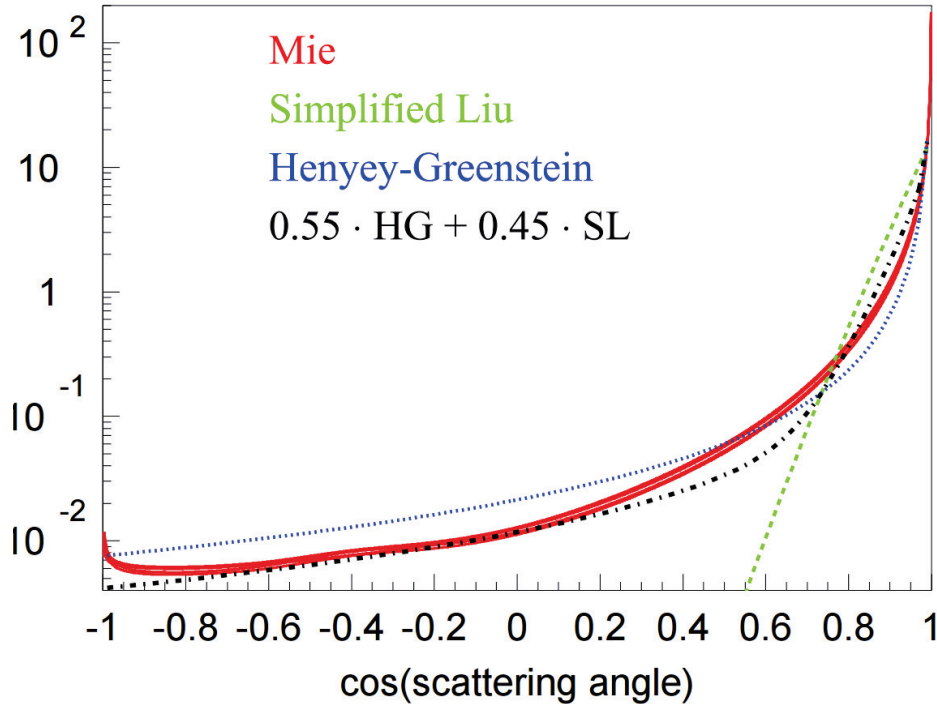


Figure 6.9: Comparisons of the Henyey-Greenstein, simplified Liu, and Mie functions for  $g=.943$ . The difference between the linear combination of HG and SL functions vs Mie is seen mostly in the forward region between above  $\cos=.2$ .

For global ice model likelihood fits,  $g$  is assumed to be .9, this means only  $f_{SL}$  needs to be determined by the global flasher likelihood fit. The power of such a fit is driven by the arrival distribution of photons at the DOMs. An example is shown in Figure 6.10. Various wavelengths of light will interact with scattering centers differently and thus have a different scattering lengths. From calculations in "Optical Properties of South Pole Ice" [89] the wavelength dependence of the ice is well described by a power law of the form

$$b_e(\lambda) = b_e(400) \left( \frac{\lambda}{400} \right)^{-\alpha} \quad (6.6)$$

Where  $\alpha$  depends on the size of the scattering centers.

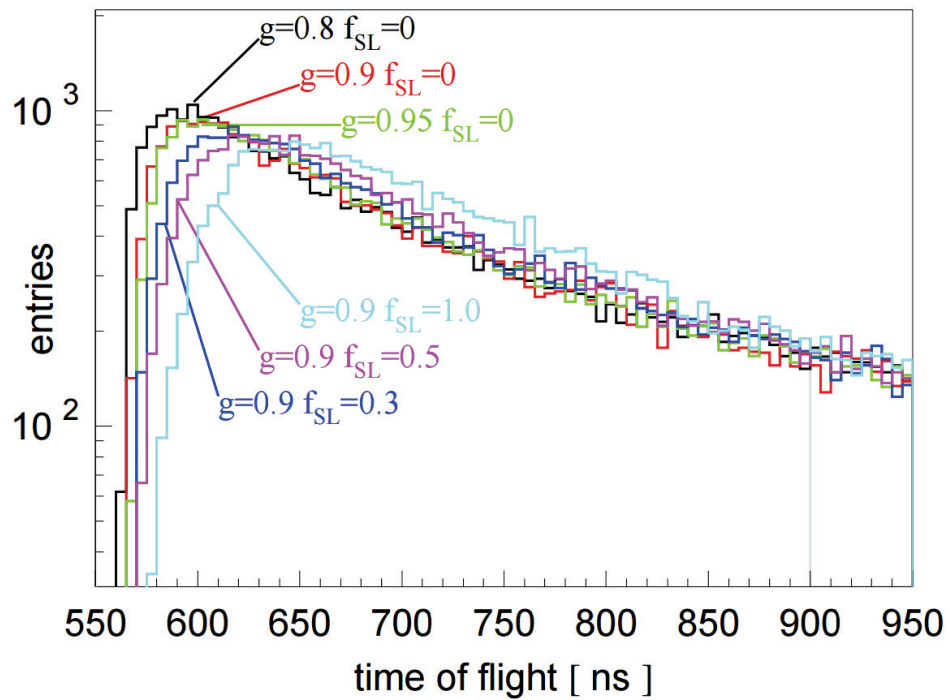


Figure 6.10: Comparisons of the arrival time distributions for various  $g$  and  $f_{SL}$  values. The difference in the distributions gives an indication of how flasher model fits can differentiate between the available options.

### 6.7.2 Absorption

In addition to light being scattered away from its original path, light can also be absorbed. It is common to quote the distance at which a beam of light is attenuated by  $1/e$ , but we often work with its reciprocal

$$a = \frac{1}{\lambda_a} \quad (6.7)$$

### 6.7.3 Depth Dependence and Layer Tilt

Since IceCube is deployed over a kilometer in the deep ice at the South Pole, which was laid down over millennia as precipitation in the region, it is not expected that the ice is uniform in its properties. As an approximation for simulation and modeling the ice is assumed to be composed of uniform horizontal 10 meter layers of ice. The variation of the scattering and absorption with respect to depth for a model of the ice is shown in Figure 6.11. The detector can roughly be broken into three regions given the information in this

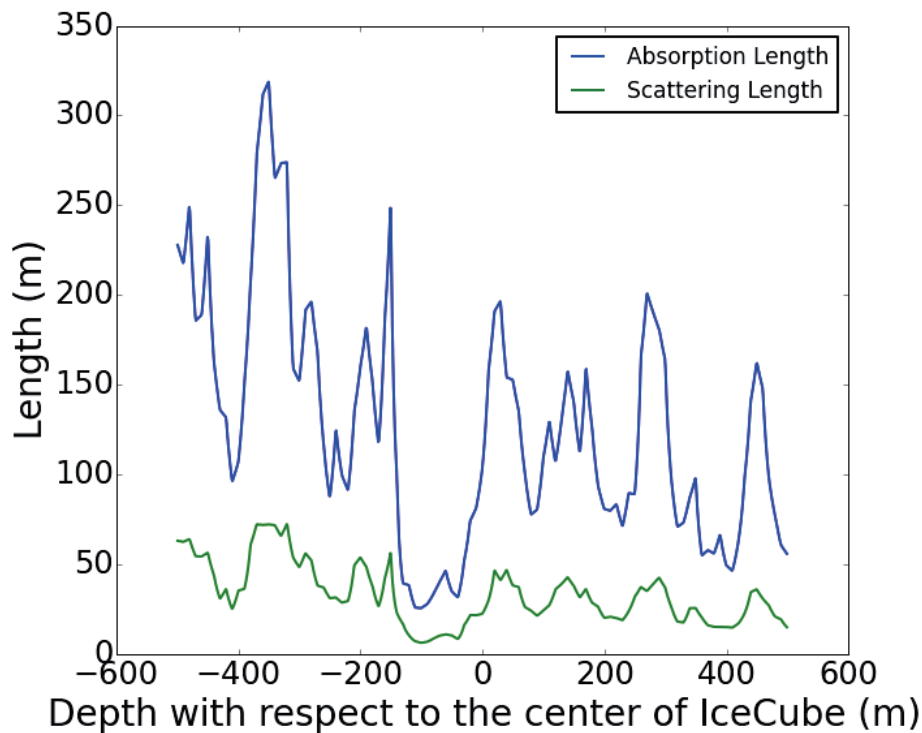


Figure 6.11: The effective absorption and scattering lengths as a function of depth centered on IceCube. Just below the center of IceCube is the dust layer where absorption and scattering lengths are shorter than usual. Above and below this are better regions of ice with the clearest ice being that in the deepest part of the detector.

plot. The clearest ice is in the deepest part of the detector where the ice is the oldest. Above this clear ice

is an obscured region known as the dust layer. Large amounts of dust are present here and lead to short absorption and scattering lengths. Above this is the ice in the upper detector. Ice here is again clear, but is younger so imperfections have had less time to be disperse scattering centers than the deep clear ice.

For some regions of the detector the layers are horizontal but for others it has been found that these approximate layers are not horizontal but instead are tilted. This can be seen in Figure 6.12 which shows

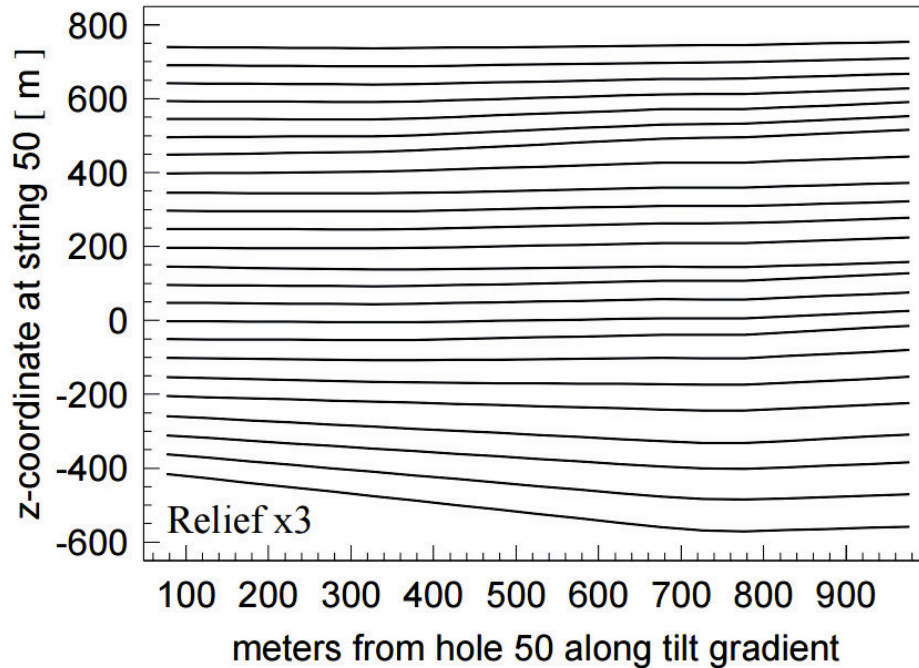


Figure 6.12: Tilt of the Ice near hole 50 in IceCube. Many of the layers are nearly horizontal, but deviations of up to 56 m are measured.

the tilt of fit layers of IceCube's ice model. The shift is strongest 47 degrees south of west in the x-y (horizontal) plane of the detector coordinates and shifts the layers by as much as 56 m. This direction of tilt is perpendicular to the direction of flow of the ice sheet.

#### 6.7.4 Anisotropy

After adding the varying layers of ice into the model another modifying effect was discovered. This effect is covered in the ICRC proceedings titled "Evidence of optical anisotropy of the South Pole ice" [88]. The original presence of this effect appeared in investigation of the response of DOMs on the strings surrounding string 63, shown in Figure 6.13 . The response of any ring of strings, such as 54, 55, 62, 64, 70, and 71, should be uniform if the ice is isotropic. However, the resulting data to simulation comparison yielded the plots in Figure 6.14. These plots show evidence for a deficit in the number of photons present in simulation along



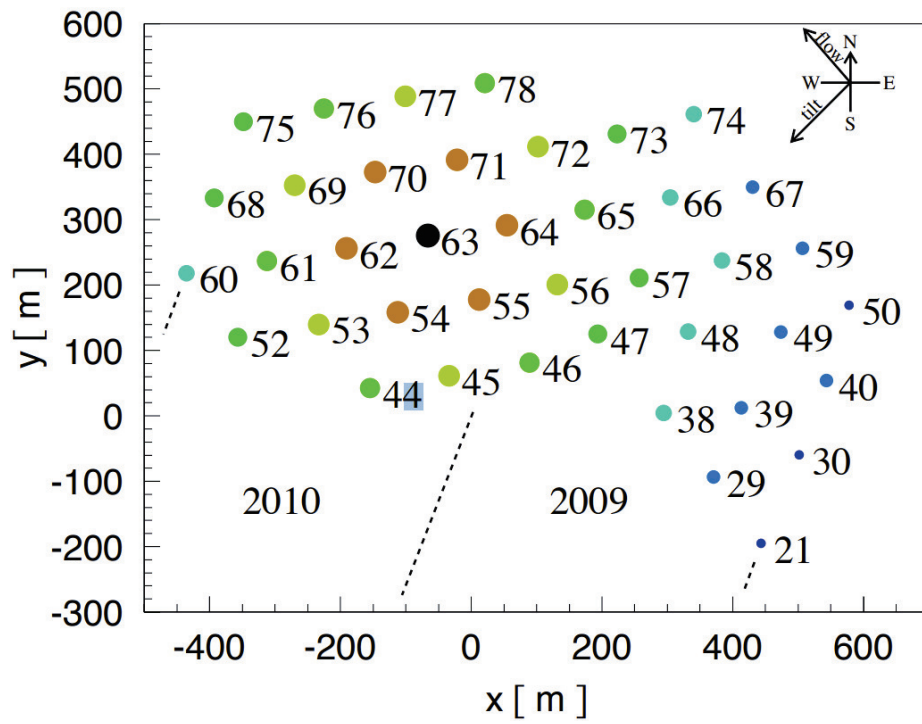


Figure 6.13: Diagram of the x-y position of strings used in the original study of ice anisotropy. String 63 was flashed for the study. The DOMs are color coded in rings to show what strings are at equivalent lengths from string 63.

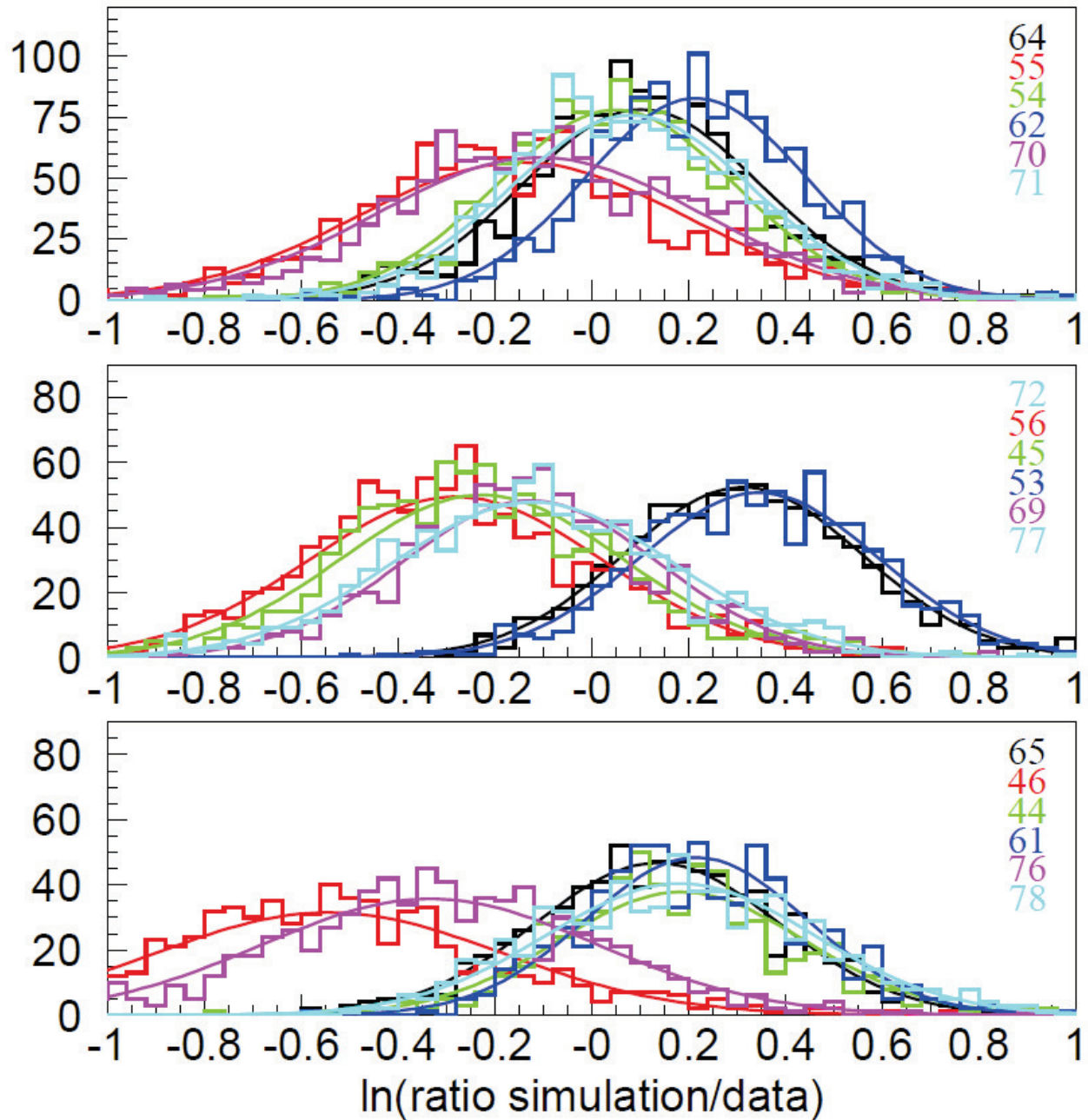


Figure 6.14: The natural log of the ratio of simulated photons divided by received photons for rings of DOMs surrounding string 63. The anisotropy is evident because none of the different emitter-recipient orientation agrees with 0.

the flow axis, and an excess in the number of photons present in the simulation perpendicular to that axis. This effect seems to get stronger as the distance between the emitter and receiver increases in the second and third plots of Figure 6.14. The physical situation such a signature suggests is ice which is anisotropic in its scattering and absorption depending on the azimuthal direction photons travel in the ice. The alignment of such an effect with the flow of the ice seems unlikely to be coincidental. The best fit directions line up within a few degrees, but currently no agreed upon explanation exists. At the time of discovery, it was worried that the anisotropy was a flaw in the analysis of the flashers so a verification method was developed to verify the findings with down-going muons. Down-going muons make a good calibration source because they are numerous and under the right conditions can be considered uniform emitters. In the case of the anisotropy analysis the idea is simple, vertical muons should bathe the detector in a uniform light so one should be able to find an anisotropic response in the detector with these events. The events were selected from the Muon Filter, see Section 6.5, with a NChannel over 70, an MPE Fit zenith less than 30 degrees, and a radius from the center of the detector at the top and bottom less than 300 m. For all pulse related calculations, the time window and radius cleaned pulses, known as SRT pulses, were used. For every event, the closest approach position to every DOM in the detector was calculated in addition to the angle from the DOM to the north direction with the coordinate system centered on the closest approach position to the DOM on the track. The charge deposited in the DOM was binned into a histogram of this angle in both data and simulation. The relative angular response can be obtained by dividing every bin value by the average charge across all bins in the histogram. For data this results in the black points of Figure 6.15 and for simulation this results in the red points on the same figure. The simulation was created with an ice model which contained no anisotropy so any deviations from 1 in the simulation is from geometric selection effects of the detector. Looking at the data and simulation, it can be seen that there is some agreement in trends, but they are far from a match. Taking the ratio of the data plot over the simulation plot should remove any detector effects from the data and yields the plots in Figure 6.16. These plots show a clear oscillatory behaviour with a relative excess around 20% and deficit around 15%. The phase and amplitude of the excess and deficit agree with the anisotropy found with the LEDs and confirmed the anisotropy. The anisotropy has been included in IceCube’s simulation since that time and work continues using the down-going muon approach. Recently, advancements have been made in quantifying the amount of anisotropy. This new idea utilizes Fourier analysis and has taken this method from a qualitative verification to a quantitative method to evaluate the parameters of anisotropy that should be in the ice model.

### 6.7.5 Local Effects

IceCube’s models of the ice continue to increase in complexity as more effects are discovered. In conjunction with increased complexity comes a decrease in the systematic uncertainty on the ice. At this point

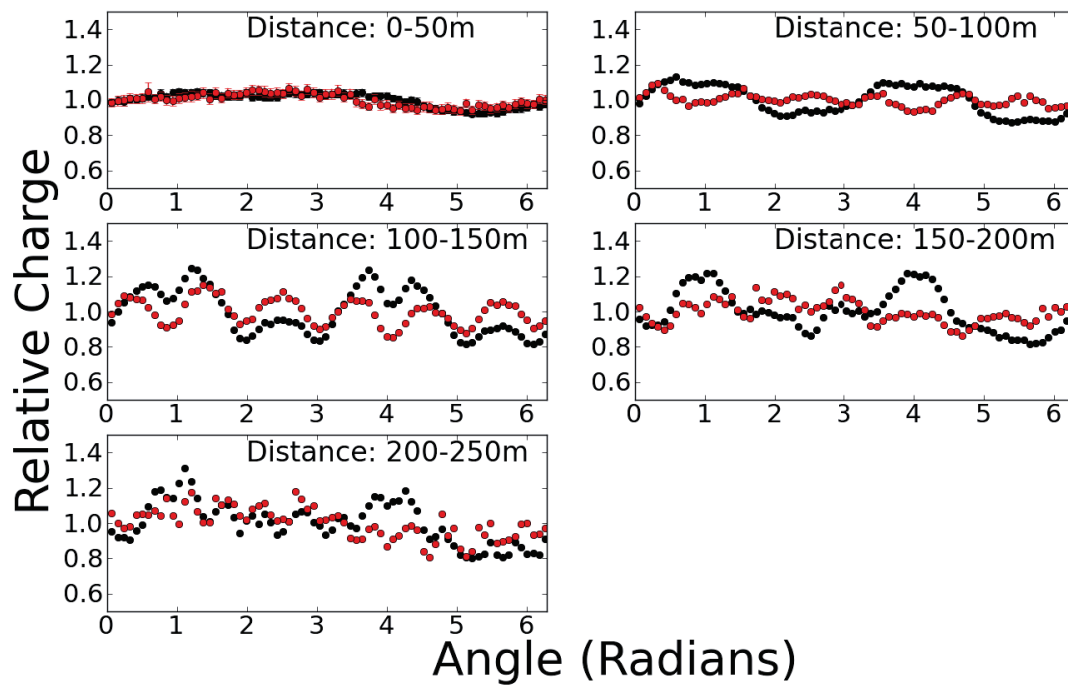


Figure 6.15: Relative charge per angular bin for simulation (in red) and data (in black). The six fold oscillatory structure in both simulation and data is due to the six fold symmetry of the detector. Any additional structure in the black which is not present in the data is evidence for azimuthal anisotropy.

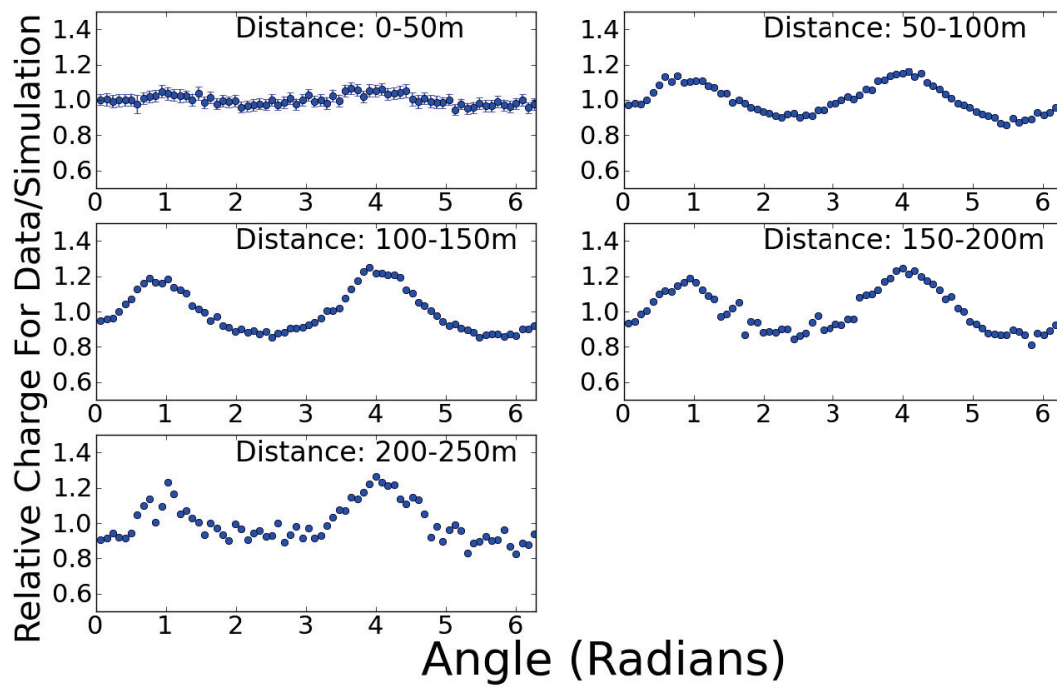


Figure 6.16: The ratio of the simulation and data from Figure 6.15. The six fold structure that was due to the detector geometry has disappeared and only the azimuthal anisotropy remains.

it seems that the majority of the bulk ice effects, effects which are in the ice outside the holes drilled for IceCube's construction, are described well. Now the main focus of study is on the local effects in the refrozen holes themselves. The two main effects that should exist are a shadow from the cable which lies alongside every DOM and a possible bubble column which exists in the center of the hole as a byproduct of drilling. These local effects are in a difficult area to study since most of the strings are spaced out by 125 m. However, a recent technique involving flashing single LEDs shows good promise since the LEDs have a fixed orientation with respect to the cable by design specification. As such, figuring out the orientation of the individual LEDs should give knowledge of the cable position for all DOMs in the detector, leaving only the bubble column left to be determined by fitting.

## Chapter 7

### Event Simulation

The main goal for IceCube analyses is to measure quantities from a set of events recorded in the detector. Before that can be achieved a number of things must be done and verified first. The first thing that must be done to get a suitable set of events is to remove the events which are considered background. Since IceCube has no external tagging system, there is no indication for the origin of a particular event. In order to have a good understanding of the possible origins of events, IceCube attempts to exactly simulate the origins of events that could be detected. Doing so allows analyzers to study the effect of cuts and methods on tagged sets of simulated events without having to compromise the events it hopes to make a measurement with. This method of using simulation assures the data is kept "blind" and is a means of assuring statistical integrity of results. The practice of blind analysis adopted in IceCube involves inspecting and comparing 10% of the full event sample to simulation for verification purposes. When good agreement between the 10% sample and simulation is achieved, there is good reason to believe that the simulation describes the measured data well and can be used for fitting and understanding of the full event sample. After the agreement is verified the full sample is "unblinded" and results are fit to the data with the simulation.

This section focuses on the process of recreating the physics events and the detector response of IceCube. This can largely be broken down into particle generation, particle propagation, photon propagation, and the detector response to the photons.

#### 7.1 Particle Generation

Everything must begin somewhere. In the case of IceCube simulation that thing is the primary particle. This is the particle which is or directly creates the particles which pass through IceCube. For standard simulation these particles can come in a few different forms: nuclei, muons, and neutrinos.

##### 7.1.1 Atmospheric Muons

Atmospheric muons are the most abundantly detected particle in IceCube, occurring at a rate of over 2000 per second. These particles are created in an extensive air shower which is the aftermath of a cosmic

ray nucleus interacting with a particle in the Earth’s atmosphere. There are two ways IceCube simulates this, with direct simulation of the air showers using CORSIKA, and with a parameterization of the muon flux known as MuonGun.

### 7.1.1.1 CORSIKA

CORSIKA (COsmic Ray SIMulations for KAscade) is an independent simulation package designed which was originally created for simulating extensive air showers for the KASCADE experiment [93]. Since its creation, the program has become one of the defacto air shower simulations used by particle detectors throughout the world. In the fashion IceCube operates the simulation, all simulations start with a proton, helium, nitrogen, aluminum, or iron primary at the edge of the simulated atmosphere. As the particle transits the atmosphere it is checked for an interaction with a particle in the atmosphere. This and all subsequent interactions in the shower are handled by an external hadronic model, generally SIBYLL 2.1 for IceCube simulation. After the interaction and determination of the outgoing particles is completed by the hadronic model, particles are given back to CORSIKA for further propagation. These particles are propagated down the atmosphere, with the relevant losses being tracked, until they decay or interact again. CORSIKA handles the decay of particles itself using branching ratios down to the 1% level. The particles created by the simulation are tracked until they reach the set observation level or go below the preset minimum energies which are defined separately for muons, electrons, gamma rays (and neutral pions), and hadrons. All particles at the observation level are then made available in a file that can be fed to the specific simulation of the detector. IceCube uses this program to generate the final state muon events at the surface of the ice sheet (propagation of these muons is discussed in 7.2). The propagation of the entire shower is rather fast, but since order  $10^{10}$  muon events per year are detected in IceCube it is still a difficult task to achieve even a years worth of livetime with this generator. This limitation gave rise to MuonGun, which is discussed in the next section.

One of the works completed in the progress of this thesis was modifications to CORSIKA’s internal particle management to speed up the simulation of rare particles. A proceeding on this modification is presented in Appendix B.

### 7.1.1.2 MuonGun

MuonGun hopes to solve the problem of slow simulations from CORSIKA by foregoing the simulation of the air shower. It does so by parameterizing the muon flux at the depth of interest from a CORSIKA simulation set. This parameterization is then used as a distribution to directly draw muons from the flux foregoing any simulation before the injection of the muons at the relevant depth in the ice. This is not a new concept. Such simulation is used almost exclusively by the Astronomy with a Neutrino Telescope and Abyss



environmental RESearch (ANTARES) collaboration for its muon simulation. ANTARES' implementation is called MUPAGE [94]. The IceCube implementation works equivalently, but with tuning to make muons in ice at different depths. However, IceCube's implementation has never produced the same results as the CORSIKA simulation for muon bundles, events from air showers with more than one muon present. As such it has largely been used as a specialty tool for atmospheric veto based analyses when they reach the final level and are only dealing with the most elusive single muons as a background.

### 7.1.2 Neutrinos

Neutrinos can reach IceCube in a number of ways, depending on their origin and flavor. For neutrinos which come alone, either by traveling through the Earth or by having an astrophysical origin, the routine called Neutrino Generator handles all the special cases which must be taken into consideration. For neutrinos which come together with air showers CORSIKA is used, this time though with the additional feature of neutrino production and tracking.

#### 7.1.2.1 Neutrino Generator

Neutrino Generator operates by injecting neutrinos one at a time on the surface of the Earth. The neutrino is then propagated through whatever material intervenes between its origin point and the IceCube detector. Though neutrinos do not interact often, the Earth is still opaque to neutrinos at the highest energies and longest transit distances. However, neutrinos which do interact in the Earth may not be lost due to neutral current interactions and tau regeneration. In the neutral current case the interaction of the neutrino with a nucleus produces a second neutrino of the same flavor but lower energy which continues propagating towards the detector. In the case of tau regeneration a charged current tau interaction occurs, and an outgoing tau lepton is created. After a short distance, with respect to the scale of the Earth, the tau decays and can produce a variety of neutrinos and in some cases more than one [95]. While these neutrinos may no longer be of the original flavor, it is still relevant to propagate them to the detector because of their contribution to the new flux type.

All neutrinos, original or created, are propagated to the detector for a forced interaction. For cases where more than one neutrino is present, a neutrino must first be selected as the interacting neutrino. Only one neutrino is ever selected as the interacting neutrino. The interaction occurs in a volume around the detector which the path intersects. A point along the track between the entrance and exit of the volume is selected randomly for the interaction point of the neutrino. For muon neutrinos where there may be an outgoing muon which can be detected the volume is extended by the maximum range of a muon with energy equal to the parent neutrino. The final step of a neutrino interaction is to determine the outgoing particles which result from the interaction. The details of this are covered in Section 3.2. In IceCube's simulation

all outgoing particles are recorded and tracked even if they do not create light or stand a chance of further interaction, such as the outgoing neutrino in a neutral current interaction.

### 7.1.2.2 CORSIKA Neutrinos

Generation of neutrinos in CORSIKA is possible, though it is not available as a default option. Using this option includes the generated neutrinos in the observation level output of CORSIKA. For IceCube this results in events which have both muons and neutrinos which need to be propagated and in the case of the neutrinos interacted. The interactions are performed with Neutrino Generator. Since this output has both neutrinos and muons it is only used to generate showers above the horizon where the muons stand a chance of making it to the detector.

### 7.1.3 Weighting

Weighting is the most important part of conducting simulations. If the weighting is wrong, the results of the simulation are essentially useless as the simulation cannot be used as a comparison to real data. But this begs the question of what weighting even is. Weighting is necessitated by the mismatch between the number of times particles of a particular combination of flavor, injection angle, and energy are created over a fixed time period in a simulation set. If this number is not exactly the number expected to be produced by nature then too many or too few examples have been created in the simulation and their relative value is too high or low respectively. In these cases it is up to weighting to give the proper correction.

Since IceCube has no limitations on the time, position, direction, or energy of arriving particles weights must be constructed as differential in all these quantities This is equivalent to a flux.

$$\Phi = \frac{dN}{dEdAd\Omega dt} \quad (7.1)$$

In the simplest terms weighting can be broken down into two pieces; the number generated and the number created in nature. Again these quantities are differential. The number generated is determined by the way the simulation was made. Different injected energy spectra, zenith biases, or particle type biases lead to different functional forms of the flux. However, the one thing a simulation does not account for is the time. A predetermined number of events is generated and spread over the differential space, but their temporal relationship is unspecified. This means that the generated flux is actually a fluence.

$$\frac{dN_{generated}}{dEdAd\Omega} \quad (7.2)$$

The number created in nature is often not known exactly and is usually an estimate based on theoretical models tuned on measurements from experiments.

To construct a weight, one simply takes the ratio between the expected flux from nature and the fluence from the simulation for a particular particle.

$$w_{primary} = \frac{\textit{natural flux}}{\textit{generated fluence}} = \frac{\frac{dN_{nature}}{dEdAd\Omega dt}}{\frac{dN_{generated}}{dEdAd\Omega}} = \frac{1}{dt} \quad (7.3)$$

The result is a rate  $\frac{1}{dt}$ . If the rate is exactly as expected from nature, the simulation was created at the natural rate and every particle can be thought of as representing one real detected particle. If the rate is smaller than what is expected from nature then the simulation has too few particles to represent all that nature would have created. If the rate is larger than what is expected from nature then the simulation has many particles to represent the single particle nature would have created. Generally the goal is to be in the regime of having many simulated particles representing a single particle in nature. This allows for good coverage of the statistical fluctuations which follow further in the process of propagation, detection, and reconstruction of the particle.

How the generated simulation term of the weighting must be constructed depends on what simulation is being dealt with. The following subsections describe weighting of different types of simulations from simplest to most complex.

### 7.1.3.1 Weighting MuonGun

MuonGun often is the simplest simulation to weight because by design it is created at the natural rate because it is a parameterization of weighted CORSIKA fluxes. However, it is possible to re-weight it to other primary fluxes. This is simply accomplished by extracting the generated fluence from the simulation information and calculating the flux for a different primary model. The ratio of the new flux and the simulation fluence gives the new weights.

### 7.1.3.2 Weighting CORSIKA

CORSIKA is weighted in much the same way as MuonGun. However, in this case the CORSIKA simulation is unweighted. Generally this means that the primary spectrum is generated in power laws, and the relative primary composition is constant. This is only ever the case in nature over very small energy intervals so weighting is always needed. To construct the weights one simply needs to be able to construct the natural flux and generated fluences for the various nuclear types of the primaries as in Equation 7.3. The total weight is the sum of weights from the simulated primary types.

### 7.1.3.3 Weighting Neutrino Generator

Weighting Neutrino Generator is very similar to weighting CORSIKA, except the primary is a neutrino instead of a cosmic ray nucleus. This means that one must take into account the probability of the neutrino interacting naturally on top of weighting the generated fluence in the form of a power law to a natural flux which can be the sum of many sources (see Section 3.3 for details). Getting from generated fluence and natural flux to weight is the same as in the Weighting CORSIKA section. The probability of such an interaction can be taken into account by calculating the probability of the neutrino interacting within the interaction volume and multiplying the weight by this probability. To calculate the interaction probability one can use the following.

$$p_{interaction} = 1 - p_{survival} \quad (7.4)$$

$$p_{survival} = e^{-\frac{\sigma_{all} \times L_d}{M_p \times C}} \quad (7.5)$$

where  $L_d$  is the total column depth within the interaction volume,  $M_p$  is the mass of a proton,  $\sigma_{all}$  is the total cross section at interaction point, and  $C$  is the unit conversion factor from millibarns to  $m^2$ . This is just a statement that the probability of penetrating through a material of a given density with a given cross section is given by an exponential distribution. Combining this with the fact that not surviving (interacting) is equal 1 minus all ways to survive gives the interaction probability. This times the primary weight represents the rate at which a neutrino passes through the detector times the probability it interacts.

### 7.1.3.4 Weighting CORSIKA Neutrinos

Weighting CORSIKA neutrinos is a combination of CORSIKA and Neutrino Generator weighting. To start, the particles in the simulation are generated by a CORSIKA simulation, so the generated fluence, and natural flux is determined by the nuclear primaries. In the ice the neutrino must interact within the specified volume. However, in an air shower there can be multiple neutrinos. This means that a neutrino must be selected from the bundle. As with the calculation of the primary weight this problem can be broken down into a ratio of natural rate over forced rate. Because the simulation uses an extended volume for the forced interaction only the forced rate is relevant. In order to get good statistics at higher energies, it is common to force interactions at a rate proportional to a power of the energy. This creates rates higher than the natural rate. This weight takes the general form

$$w_{selection} = \frac{E_i^n}{\sum_j^{all\ neutrinos} E_j^n} \quad (7.6)$$

where  $i$  is the selected neutrino and  $n$  is the power law. The selected neutrino must interact so an interaction probability must be calculated as well, just in weighting neutrino generator. The weight for this type of

simulation has the form

$$w = w_{primary} \times w_{selection} \times p_{interaction} \quad (7.7)$$

## 7.2 Particle Propagation

After the determination of final state particles is completed by the particle creation routines, propagation of the final state particles through the ice must be performed. This can be broken down into track-like particle tracking and cascade-like particle tracking which must be treated differently because of their topology.

### 7.2.1 Track-Like Particle Propagation

Track-like particles such as muons and taus are propagated through the ice via the program PROPOSAL (PRopagator with Optimal Precision and Optimized Speed for All Leptons) [60]. As discussed in the section on muon physics, Section 3.5, leptons in a medium undergo four relevant types of energy loss; ionization, Bremsstrahlung, pair-production, and nuclear interaction. PROPOSAL is designed to represent all of the losses from these processes. However, below some energy, the individual tracking of these losses becomes very computationally expensive, since their frequency goes like  $1/E_{loss}$ , while their contribution is indistinguishable from that of continuous losses. To deal with this, the program breaks losses into a continuous and stochastic category. Conventionally the continuous portion would consist of only the ionization losses while the stochastic losses would be the other contributions. However, in PROPOSAL the separation between these two categories is determined by the fraction of the total lepton energy a loss could have, called the  $v_{cut}$ .

$$v_{cut} = \frac{e_{cut}}{E_{\mu}} \quad (7.8)$$

Thus the cross sections of the different processes are only evaluated down to the energy  $e_{cut}$  and can include ionization losses which are large enough to be called "stochastic" under this paradigm. When a stochastic loss occurs, the information on the type, energy, and location of the energy deposit is recorded for use in photon generation. The location of the losses are calculated in 1 cm steps while the continuous is taken to be constant and of the form

$$\frac{dE}{dX} = -(aX + b) \quad (7.9)$$

where  $a$  is 0.249 GeV/mwe and  $b$  is  $.422 \times 10^{-3}$  1/mwe in ice.

In the IceCube simulation the muons are tracked as they propagate and lose energy in the ice. However the details of the losses are not kept until the muon reaches what is referred to as the simulation volume. Commonly the simulation volume is a cylinder 800 meters in radius and 1600 meters in height centered on the detector origin. This volume is large enough that all light producing losses which could be detected will

have their full information kept for inspection later. Losses in this region are kept and tracked further as cascade losses.

### 7.2.2 Cascade-Like Particle Propagation

In their simplest approximation, cascades can be considered as point-like emitters with a fixed emission pattern. IceCube represents these cascades with a spline derived from Monte Carlo simulations of electromagnetic cascades. In this representation the cascades emit from a point which is appropriate for many cases because of how sparse IceCube is. However, in reality if a cascade is above 1 TeV it can have an extension which is order a few meters in length. At this scale the extension begins to matter. Rather than produce each cascade in the simulation with full Monte Carlo, IceCube spreads a chain of energy deposits out over the extension of the cascade. The energy of each energy deposit is governed by its position in the cascade as seen in Equation 7.10 and is recreated from the same splines as in the point-like case.

$$\frac{dE}{dX} = E_0 b \frac{(bX)^{(a-1)} e^{bX}}{\Gamma(a)} \quad (7.10)$$

The values used in Equation 7.10 were determined by a GEANT [96] simulation and are detailed in Christopher Weibusch's thesis [97]. Above 1 PeV, the approximate emission profile method breaks down. In this case the cascades are simulated with full GEANT Monte Carlo [96].

## 7.3 Photon Propagation

Once all the tracks have been propagated and all the cascades have been placed it's time to create photons. There are two photon propagators in IceCube; CLSim (CL for the OpenCL heterogeneous platform framework) and PPC (Photon Propagation Code). Both have been tested to produce the same results when run, however they tend to have different uses. CLSim is the propagator for officially produced IceCube simulation sets while PPC is a more developmental implementation where the cutting edge ice models are implemented and tested (see Section 6.7 for detailed discussion of ice properties). Improvements in one routine tend to be added to the other after a short delay for validation of the improvement.

One important feature that is used in both codes is DOM over-sizing. DOM over-sizing works by enlarging the DOM's radius to be  $n$  times larger than a standard DOM. Commonly a value of 5 is used for over-sizing. An oversized DOM is not just a spherical volume that is larger, but instead a pancake which is always oriented perpendicular to the direction of the oncoming photon. This means that a photon can be detected if it intersects a disk with radius  $n$  times the DOM's radius which pivots on the DOM. Since this object has an area  $n^2$  times larger than the original DOM,  $\sim n^2$  more photons are detected and must be down sampled by this  $n^2$  factor. When light emitting particles are far from the observing DOM this approximation works

quite well and speeds up simulation  $n^2$  times. However, when the light emitting particles are close, photons can be detected too early giving incorrect arrival time distributions.

Photon propagation begins with the creation of the photons themselves. This is accomplished by searching the simulated event for particles which can create light, commonly muons and cascade-like energy deposits. The initial emission profile and spectra of light from these topologies is obtained from a parameterization. After this, photons are propagated until they are absorbed or detected. The propagation of a photon begins by drawing random numbers related to the absorption and scattering lengths from exponential distributions. The numbers are not themselves lengths but instead the mass overburden the photon can travel before absorption or scattering. This is necessary because the ice properties vary as the photon propagates, making the computation of the lengths a sum which is dependent on the photon's path. With these two numbers, the routine begins computing the length as the photon travels. If the scattering overburden is longer than the absorption overburden then the photon propagates until it runs out of absorption overburden and then is dropped by the routine. In the case where the scattering overburden is shorter than the absorption overburden the photon propagates until it runs out of scattering overburden. At this point a new direction is drawn from the scattering function, and a new scattering overburden is drawn. This process of propagating and scattering continues until the scattering overburden is longer than the absorption overburden in which case the photon is propagated until it runs out of absorption overburden and then is dropped by the routine. Between the beginning point, scattering points, and absorption point the routine checks for an intersection with DOMs. If the simulation is using DOM over-sizing 1 an intersection leads to the photon being recorded for further processing and propagation of that photon ceasing. If DOM over-sizing is larger than 1 the photon is recorded for further processing, but propagation continues. Recorded photons can impinge on any part of the DOM, even the inactive top portion. The determination of if a photon created a pulse or not is determined by the detector simulation.

## 7.4 Detector Simulation

With the impinging photons recorded, determination of the DOM's response can be simulated. This starts by determining which photons hit the DOM and transit the DOMs housing and which do not. Recall that even photons which hit the top of the DOM are recorded. To do this an angular acceptance function is used as a down-sampling factor. The angular acceptance varies as a function of the photons orientation with respect to the PMT axis (see Figure 7.1 for an example angular acceptance curve). The angular acceptance provides a phenomenological description of the intrinsic DOM acceptance and local effects like hole ice. Photons that are accepted by the angular acceptance curve are then down sampled again to account for the transmission properties of the Benthosphere and quantum efficiency of the PMT. These down-sampled photons are then run through a PMT simulation which accounts for the jitter, pre-pulsing, late-pulsing, and

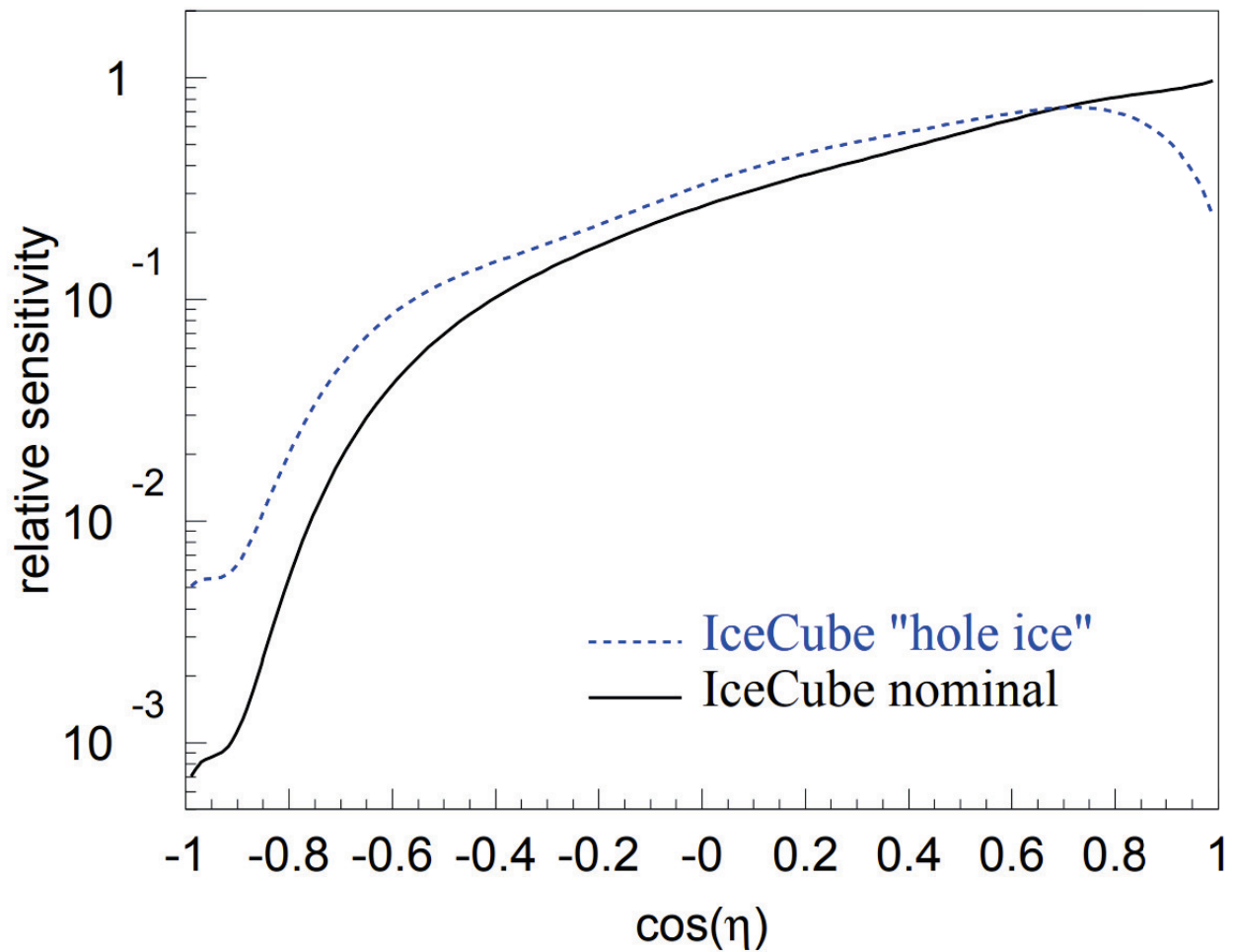


Figure 7.1: The angular sensitivity of the DOM as was measured in the lab before deployment of IceCube, labeled nominal, and the angular sensitivity as found by fits using flashers in the detector, labeled "hole ice". The "hole ice" model is used for simulations because it is a phenomenological description of the ice and local ice effects which best describes the data. This figure comes from [86].



after-pulsing of the PMT. DOMs which receive a large enough number of charge also are subject to saturation derived from lab measurements of DOMs. In order to save space, hits which reach the cathode within .2 ns of each other are merged together. Hits are then run through a recreation of the DOM's triggering and digitization system. From here DOM launches are combined to form events and trigger windows just as in the real detector (see Section 6). At this point the simulation looks identical to the detector produced events and all processing proceeds in the same fashion as the IceCube data.

## Chapter 8

### Event Reconstruction

When charged particles create light which is subsequently detected by the DOMs in IceCube, they do so in patterns which give an indication of their type, energy, and trajectory even though the particles themselves are not being detected. The job of winnowing down the likely origin of the detected photons is the job of reconstruction in IceCube. This task can be broken up into five categories for the different topologies which are known from the physics processes IceCube can detect: cascades, double cascades(double bangs), through-going tracks, starting tracks, and stopping tracks. For the purpose of this thesis one does not need to be concerned about double cascades or stopping tracks and only need to know about cascades because they are a building block for high energy muons. The double cascade topology is a signature of tau events, which this thesis does not focus on, and stopping tracks occur only when a muon runs out of energy in the detector, which is unlikely in the energy range this thesis focuses on.

Reconstruction in IceCube is an iterative process of determining what combination of hypothesized topology, position, direction, time, and sometimes energy gives the best match to the observed hits on the DOMs. As such, different algorithms exist which focus on minimizing error or computation time. This section will start with a brief discussion of cascade reconstruction and then move to focus entirely on the different types of track reconstruction, particularly the IceCube tool named Millipede.

#### 8.1 Cascade Reconstruction

As was discussed in the simulation section, 7, cascades can be treated as point-like emitters to first order. Additionally, because of the large amount of photon scattering which occurs in the ice, photon emission can be approximated as spherical. While neither of these is true, they allow for a quick first guess about the position, time, and orientation of the cascade thanks to a tie in to classical physics. If one considers the hits as a rigid body where the "masses" are the charge at each DOM it is easy to define a center of gravity and tensor of inertia. The center of gravity is given by

$$\vec{x}_{COG} = \frac{\sum_{Hit\ DOMs}^i q_i \cdot \vec{x}_i}{\sum_{Hit\ DOMs}^i q_i} \quad (8.1)$$

where  $q_i$  is the charge on the  $i$ th DOM, and  $\vec{x}_i$  is the vector to the  $i^{\text{th}}$  DOM from the origin. The center of gravity is a good guess for the origin of the cascade. The tensor of inertia elements are given by

$$I^{kl} = \frac{\sum_{Hit\ DOMs}^i q_i [\delta^{kl} (\vec{x}_i)^2 - \vec{x}_i^k \cdot \vec{x}_i^l]}{\sum_{Hit\ DOMs}^i q_i} \quad (8.2)$$

where  $k$  and  $l$  are axes of the coordinate system. Solving this system for its eigenvalues gives the 3 main axes of the event. The smallest eigenvalue corresponds to the longest axis of the hits. In a detector with uniform propagation this direction would correspond to the direction of the cascade if its energy and orientation were favorable. However, for IceCube this is rarely the case.

More advanced cascade reconstructions do exist, but the only reconstruction which reliably gives energy and angle information is the single cascade version of Millipede, known as Monopod. Discussion of that algorithm will be saved for the relevant part in this section.

## 8.2 Track Reconstruction

Reconstructing tracks in IceCube is usually done in two parts because one does not need to know the energy of the track to solve for its direction and vice-versa. As a result the discussion of direction fitting and energy fitting for tracks will be discussed separately.

### 8.2.1 Direction

Track reconstructions use the hypothesis that a particle moving at the speed light is uniformly emitting light. The track can be described with the following parameters

$$\mathbf{y} = (\vec{r}_0, t_0, \vec{v}) \quad (8.3)$$

Where  $\vec{r}_0$  is the position the track passes through at time  $t_0$ , and  $\vec{v}$  is the velocity vector. Often, the assumption is that along this track Cherenkov photons are being uniformly emitted and detected on the DOMs. What information is used from the detections, and how the photons are hypothesized to travel through the ice are the largest differences between IceCube's algorithms. The following sections present three different algorithms of increasing complexity which are used as an iterative seed chain to solve for the direction of tracks in IceCube.

#### 8.2.1.1 Line Fit

Many of IceCube's fitting algorithms are likelihood based, and need a seed to operate efficiently and effectively. This necessitates a simple deterministic algorithm to use as a first guess. Line fit is an algorithm which fulfills this need. Line fit's hypothesis is that the hits are from a plane wave moving through the detector. This makes the time of the first pulse on every DOM relateable to the position, direction, and

speed of the particle with the equation.

$$\vec{x}_{DOM_i} = \vec{x}_0 + \vec{v} \cdot t_i \quad (8.4)$$

Where  $t_i$  is the time of each hit on the DOM at position  $x_i$  and  $\vec{x}_0$  and  $\vec{v}$  are some position and velocity vector from Equation 8.3. In the ideal case  $|\vec{v}| = c$ , however, given enough hits to specify the six free parameters (3 position and 3 direction/velocity) one can solve for  $\vec{x}_0$  and  $\vec{v}$  using the reformulations of Equation 8.4 and finding the least squares solution.

$$\vec{x}_0 = \langle \vec{x}_0 \rangle - \vec{v} \langle t_i \rangle \quad (8.5)$$

$$\vec{v} = \frac{\langle t_i \cdot \vec{x}_{DOM_i} \rangle - \langle \vec{x}_{DOM_i} \rangle \langle t_i \rangle}{\langle t_i^2 \rangle - \langle t_i \rangle^2} \quad (8.6)$$

Where  $\langle A \rangle$  is the arithmetic mean over all the pulses in an event.

### 8.2.1.2 SPE Fit

Aside from Line Fit, the rest of IceCube's reconstructions are likelihood based. This is to say that the unknown fit parameters  $\mathbf{y}$  are determined by finding what combination of fit parameters maximizes the likelihood

$$L(\mathbf{x}|\mathbf{y}) = \prod_{AllDOMs}^i p(x_i|\mathbf{y}) \quad (8.7)$$

where  $\mathbf{x}$  are the observed values and  $p(x_i|\mathbf{y})$  is the probability density function describing the probability of observing  $x_i$  given a combination of fit parameters  $\mathbf{y}$ . As is common with likelihoods, the log of the likelihood is dealt with because of its mathematical properties. As stated before, the assumption is that photons are emitted uniformly at the Cherenkov angle from a particle whose motion can be described by Equation 8.3, which was not the case in Line Fit. In addition, improved handling of the photon tracking in the ice is used. In the ideal case where no scattering occurs in the ice, one could expect that all photons take the fastest path from the muon to the DOM via the Cherenkov angle. This time of travel from particle origin via the fastest path solution is commonly called the geometric time and is depicted in Figure 8.1 and can be represented by Equation 8.8.

$$t_{geo} = t_0 + \frac{\vec{p} \cdot (\vec{r}_i - \vec{r}_0) + d \tan \theta_C}{c_{vac}} \quad (8.8)$$

Within IceCube, the arrival time of photons is almost always delayed due to scattering in the ice. It is thus relevant to define a time residual with respect to the minimum travel time.

$$t_{res} = t_{arrival} - t_{geo} \quad (8.9)$$

Thus,  $t_{res}$  is negative for arrivals before  $t_{geo}$  and positive for delayed arrivals which come in after  $t_{geo}$ . How much the ice scatters photons directly impacts the distribution of residual times. While there is no exact solution to the  $t_{res}$  distribution, there are a number of approximations to it. The simplest description

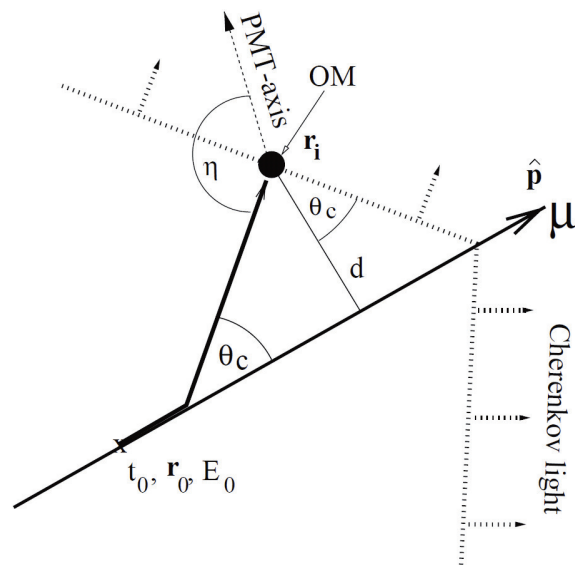


Figure 8.1: Depiction of the fastest travel time from a muon track to a DOM along the Cherenkov angle. This time is called the direct or geometric time.

is known as the Pandel distributions from the thesis work of Dirk Pandel[98]. These functions define the probability of a photon arriving at a time  $t_{res}$  for a DOM a distance  $d$  from the track using a normalizable functional description so that

$$\frac{dP(t_{res}|d)}{dt} \quad (8.10)$$

and can be calculated. This is seen for varied distance combinations in Figure 8.2. Using the information

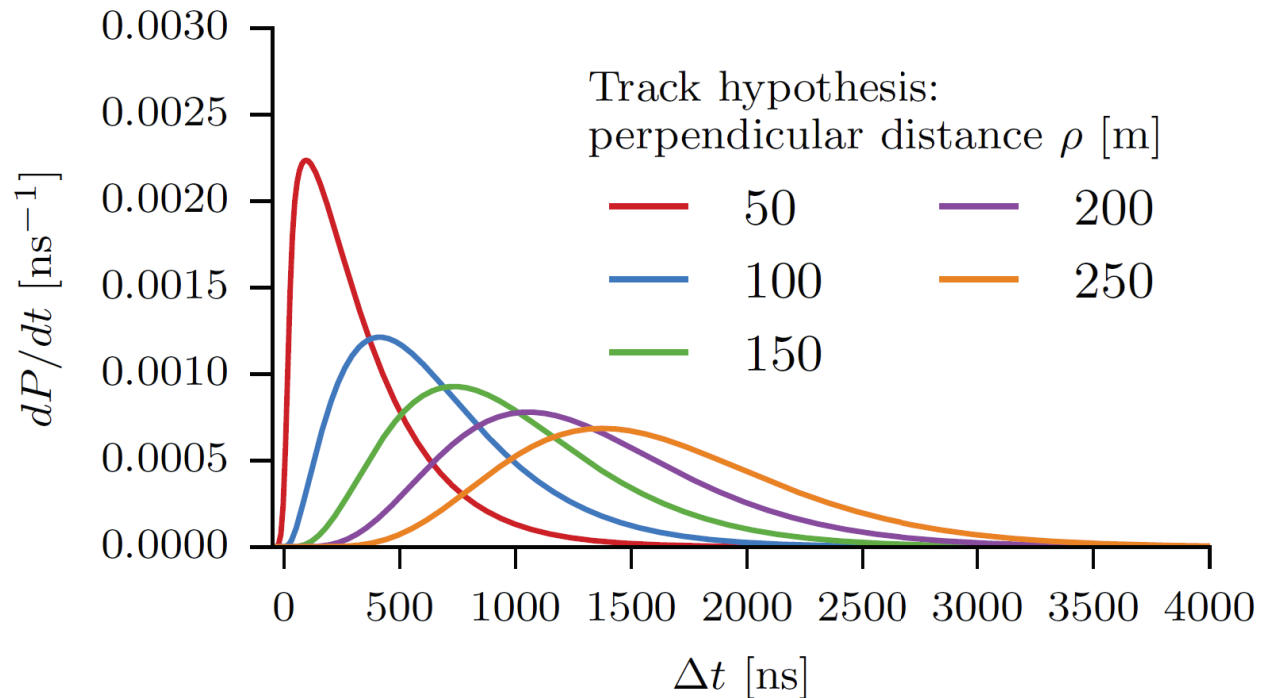


Figure 8.2:  $\frac{dP(t|d)}{dt}$  distributions for IceCube’s version of the Pandel distributions. As the emitter-receiver distance increases, the probability of an undelayed photon decreases due to scattering and the peak shifts away from  $\delta t = 0$ . This figure comes from [29].

from the Pandel distributions, one can fully construct the likelihood from Equation 8.7 for a given event using the Pandel distributions in place of  $p(x_i|y)$ . Although the formulation of this likelihood is only properly defined when the sum runs over all the detected pulses, it is common for it to only be run over the first pulse on each DOM because the first pulse is always the least delayed and carries the most information as a result. Instances where all the pulses are used are known as SPE ALL, while the first pulse solution is just known as SPE, where SPE stands for single photo-electron. Since this method gives the likelihood of a solution given a hypothesis, it is necessary to maximize the likelihood (minimize the negative log-likelihood), to find the best solution. This is a difficult problem for IceCube events because many observations are made and not all of them agree with each other, creating many false maxima (minima). One way to alleviate the issue of

false solutions is to give a good initial solution. IceCube uses a recursive approach to accomplish this. First the deterministic solution of Line Fit is found. This is then used as the seed for an SPE Fit. This fit is then further used as a seed for a MPE Fit. Final fits like the spline version of MPE and Millipede generally take an MPE Fit as a seed. The details of splines, MPE, and Millipede are discussed later in this section.

### 8.2.1.3 MPE Fit

MPE Fit is an extension to SPE Fit which takes advantage of the fact that the first photon observed from a collection is more likely to be a direct photon than the average photon description provided in the Pandel distribution. This can be viewed as a binomial probability where a success is  $k$  photons having no scatters out of  $N$  photons. This gives

$$p_{direct}(t_{res}) = \binom{N}{k} (\text{probability of success at } t_{res})^k (\text{probability of failure after } t_{res})^{(N-k)} \quad (8.11)$$

we are interested in the first photon so  $k = 1$  and the probability of success at  $t_{res}$  is given by the Pandel distribution. The probability of failures coming after this is given by

$$\int_{t_{res}}^{\infty} (\text{Pandel distribution}) dt = 1 - P(t_{res}) \quad (8.12)$$

where  $P(t_{res})$  is the cumulative probability of the Pandel distribution. This means Equation 8.11 becomes

$$p_{direct}(t_{res}) = N p(t_{res})(1 - P(t_{res}))^{(N-1)} \quad (8.13)$$

This additional factor reduces the width of the arrival time distribution to more properly accommodate the arrival of the first photon given a collection of other observed photons.

### 8.2.1.4 Using Splines

The Pandel functions are a nice description of the arrival time of photons after propagating through a diffusive media. However, they are limited in their ability. This is largely due to the fact that they do not have the capability to describe variations in the ice's properties. In order to capture the intricacies of the real ice, IceCube uses what is commonly called splines or tables. These are constructed by simulating an ensemble of events which provide adequate coverage of all possible combinations of directions and positions for tracks through the detector. To generally encode the response of the detector to these events would naively require the spline to cover nine dimensions: the position, time, and orientation of the event (6) together with relative position of the DOM (3). However, thanks to symmetries in the detector these nine can be reduced to six: the depth and zenith angle of the source, the displacement vector connecting it to the receiver, and the difference between the time of light detection and production. Since depth is included the variation of the ice discussed in Section 6.7 can be included. The only shortcoming to this approach is that azimuthal variations are

lost and are currently unrecoverable because the dimensionality of the problem already pushes the limits of reasonable memory use on computer nodes used for reconstruction. This means effects like anisotropy and ice tilt cannot be represented. Figure 8.3 shows the time delay probability for various emitter-receiver distances and orientations. As was the case with the Pandel distributions the distance shifts the peak probability away from the geometric time, but emission into the back of the DOM (130 degrees) also has this effect since the photons must scatter back into the other side of the DOM to be detected.

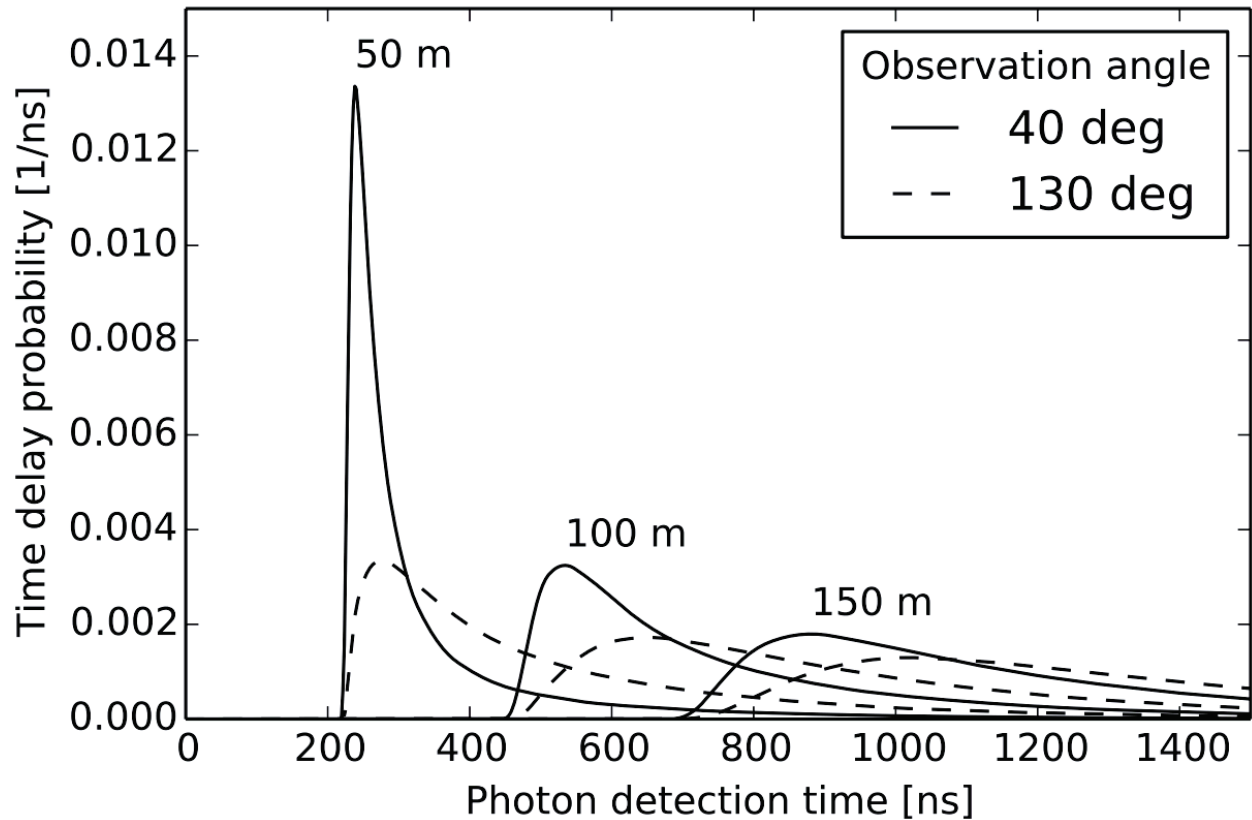


Figure 8.3:  $\frac{dP(t|d)}{dt}$  distributions for IceCube's spline fits to the ice. As the emitter-receiver distance increases the probability of an undelayed photon decreases due to scattering and the peak shifts away from the geometric time. The relative orientation of the emitter and the DOM's PMT are also relevant since the light must impinge on the PMT to be detected. This figure comes from [99].



### 8.3 Millipede

The most advanced reconstruction used in IceCube is known as Millipede, or Monopod if using the single cascade version. This method uses a binned likelihood approach together with the spline tables to provide an accurate a description of a hypothesis without directly re-simulating the event.

#### 8.3.1 Introduction

For many of IceCube's observed events, the emission can be approximated as an electromagnetic cascade or a set of cascades. These cascades give off light which is detected at the DOMs after propagating through the ice and undergoing scattering and absorption. With knowledge of the initial cascade's (or set of cascades') energy, position, time, and orientation and the ice's transmission properties it is possible to estimate the observed signal received in some finite time bins for each DOM within Poisson errors. This is the scenario represented in the per bin Equation

$$y_i = \sum_j p_{ij} x_j + n_i \quad (8.14)$$

where  $y_i$  is the predicted number of PE in bin  $i$ ,  $n_i$  is the mean number of predicted PE expected from noise in bin  $i$ ,  $x_j$  is the energy of the  $j^{th}$  energy loss, and  $p_{ij}$  is the transmission coefficient which provides the expected number of PE in bin  $i$  from each of the  $j$  hypothesized losses. For a full event, the problem can be written down as the matrix expression in Equation 8.15

$$\vec{Y} = \mathbf{P} \cdot \vec{X} + \vec{N} \quad (8.15)$$

where, similar to the per bin formula,  $\vec{Y}$  is the vector of predictions in PE,  $\vec{N}$  is the expected number of background PE per bin in  $\vec{Y}$ ,  $\vec{X}$  is the vector of energy losses, and  $\mathbf{P}$  is the transmission matrix from each bin to each loss. This is depicted in Figure 8.4. For observed events, it is the pattern of losses,  $\vec{X}$ , which needs to be recovered. However, solving for  $\vec{X}$  is an ill formed problem as Equation 8.14 cannot be inverted singularly since there are many possible ways to create a vector  $\vec{X}$  which would satisfy  $\vec{M}$ , the observed PE per bin, within statistical errors. Methods to solve problems of this nature are a field called linear programming, as they involve systems of linear equations with unknowns. A good reference on the field is Linear and Nonlinear Programming by David G. Luenberger and Yinyu Ye[101] which discusses a number of approaches to solving this class of problems.

Millipede utilizes an algorithm known as preconditioned gradient descent, as is defined in "The performance of monotonic and new non-monotonic gradient ascent reconstruction algorithms for high-resolution neuroreceptor PET imaging" [102]. This method and its application to IceCube can be found in Section 8.3.2. Since the method predicts the per bin number of photons for a given orientation of a chain of losses, the output of Millipede can also be used in combination with an external orientation minimizer. In doing so,

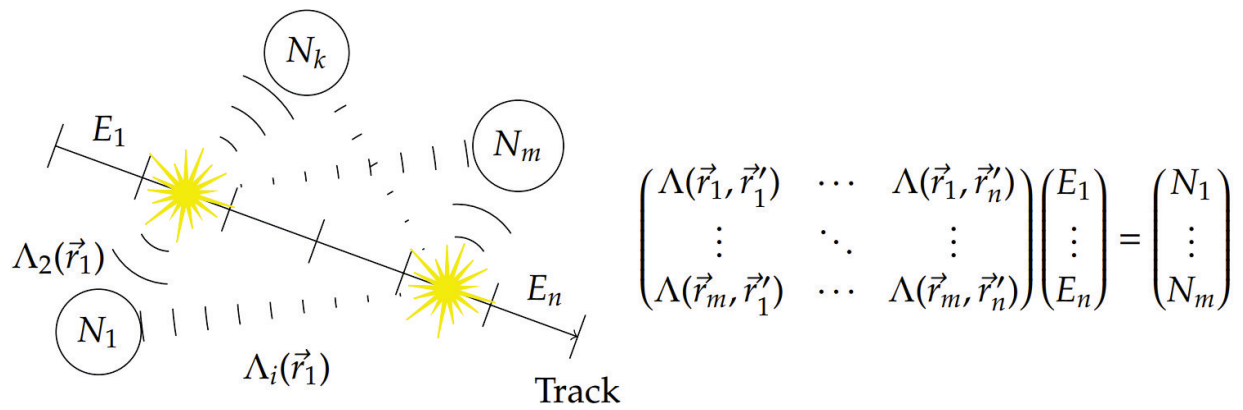


Figure 8.4: A depiction of the physics situation being modeled by the Millipede algorithm. There are a set of observing DOMs ( $N_i$ ), which receive light from each segment  $E_i$  via the path  $\Lambda_i$ . Solving this amounts to the matrix equation at the right of the figure. Millipede is solving for the energy vector so linear programming must be used to invert the solution. This figure is from [100].

changes to the log-likelihood reported by Millipede when the position or angle are changed can be fed to a minimizer. Ideally, the minima found should provide the best fit available for the observed information since Millipede is the most correct description of the underlying physics problem. However, Millipede has never been shown to provide a better angular fit than MPE fits with splines. Discussion of using Millipede as an angular fit can be found in Section 8.3.4, its performance can be found in Section 8.3.3, and its shortcomings are discussed in Section 8.3.5. Although the current performance is not as good as hoped, there have been some improvements and ideas which can be attempted which are discussed in 8.3.6.

### 8.3.2 Underlying Algorithm

The goal of Millipede is to solve Equation 8.15 for the loss vector  $\vec{X}$ . This is accomplished by minimizing the Poisson likelihood constructed from the observed PEs and expected PEs of the constructed bins. There are a number of ways to go about this, but IceCube uses the pre-conditioned conjugate gradient (PCG) method. This method works iteratively and chooses the direction and size of the cascade energy steps at the onset of every iteration. Since the goal is to minimize the Poisson likelihood

$$L(\vec{M}|\vec{X}) = \prod_i \frac{y_i^{m_i}}{m_i!} e^{-y_i} \quad (8.16)$$

where  $\vec{M}$  is the vector of binned observations. Note that it is mathematically equivalent to maximize the log-likelihood.

$$\log(L(\vec{M}|\vec{X})) = \sum_i m_i \log(y_i) - \sum_i y_i - \sum_i \log(m_i!) \quad (8.17)$$

The first derivative of Equation 8.17 gives the gradient to minimize this log-likelihood.

$$g_j = \frac{\partial \log(L(\vec{M}|\vec{X}))}{\partial x_j} = \sum_i p_{ij} \frac{m_i}{\sum_j p_{ij} x_j + n_i} - \sum_i p_{ij} \quad (8.18)$$

The preconditioning to be applied to the gradient and takes the form

$$c_{jj} = \frac{x_j + \epsilon}{\sum_i p_{ij}} \quad (8.19)$$

which is a matrix that corresponds to a weighting factor for descent. This leads to the definition of the preconditioned gradient  $v_j$

$$v_j = c_{jj} g_j \quad (8.20)$$

The preconditioner is designed to amend the gradient for the current strength of the emitter and the intervening ice properties. Stronger losses under the same ice conditions will receive a relative increase to their gradient, while constant losses in differing ice will receive an increase or decrease to their gradient relative to the transmission properties. The value of epsilon is kept small but non-zero to prevent the preconditioner

from eliminating a loss as a possible contributor. In the iterative search every subsequent search gradient is conjugate to the others, and is thus defined as a linear combination of the current gradient and past gradients

$$d_j^k = v_j^k + \beta^k d_j^{k-1} \quad (8.21)$$

where  $k$  indicates the iteration index and  $\beta$  is the Polak-Ribiere formula[103].

$$\beta^k = \max \left\{ \frac{\sum_j g_j^k (v_j^k - v_j^{k-1})}{\sum_j g_j^{k-1} v_j^{k-1}}, 0 \right\} \quad (8.22)$$

Once the new search gradient is found, the size of the step to be taken in this direction is determined by a line search utilizing the Newton-Raphson algorithm[104]. One precaution that must be taken with this method is to verify that all solutions are non-negative. This is done by performing the line search twice, once on the original solution  $\vec{X}$ , and a second time with all the negative terms set to 0. This guarantees that the final resulting solution is non-negative.

This algorithm is run recursively until the sum of the gradients, Equation 8.18, is found to be below a specified tolerance. For muons, this is generally on the order of 100 iterations for the default tolerance setting of .1. The output of Millipede is the best fit vector of losses, and the per bin fit statistics (log-likelihood, chi-square, and residuals). The per bin expected PE are used to determine the log-likelihood of the solution for direction and position fitting, discussed further in Section 8.3.4.

### 8.3.3 Performance

The performance of the preconditioned conjugate gradient(PCG) method is compared to that of: a maximum likelihood expectation maximization(MLEM) technique, an ordered subset expectation maximization(OSEM) technique, and a non-monotonic maximum likelihood(NMML) technique in[102]. The comparisons focus on a simple two observation bin case and reconstruction of a set of data from clinical positron emission tomography (PET) data. We will only focus here on the PET data since the two bin case is trivial and shows little difference between many of the methods aside from a faster rate of convergence for PCG and NMML.

In Millipede, only the PCG method is implemented, so methods cannot be compared. However, it should be noted that the PCG method was a replacement for a NMML technique used in earlier versions, so the authors must have preferred the results of the PCG method over those of the NMML technique.

One stark finding in the comparison paper is about the performance of different algorithms when reconstructing positron emission tomography (PET) images which are a close analogy to what IceCube hopes to accomplish with Millipede reconstructions. The first concern is about the rate of convergence of the algorithm. Figure 8.5 shows the convergence of different algorithms for four cases, with the top row focusing on entire regions of the brain, while the bottom row uses a subset of random pixels from different regions.

All figures show that the PCG algorithm is among the fastest to converge and achieves the best estimate. The solutions for the different algorithms are shown as images as a function of iteration number in Figure

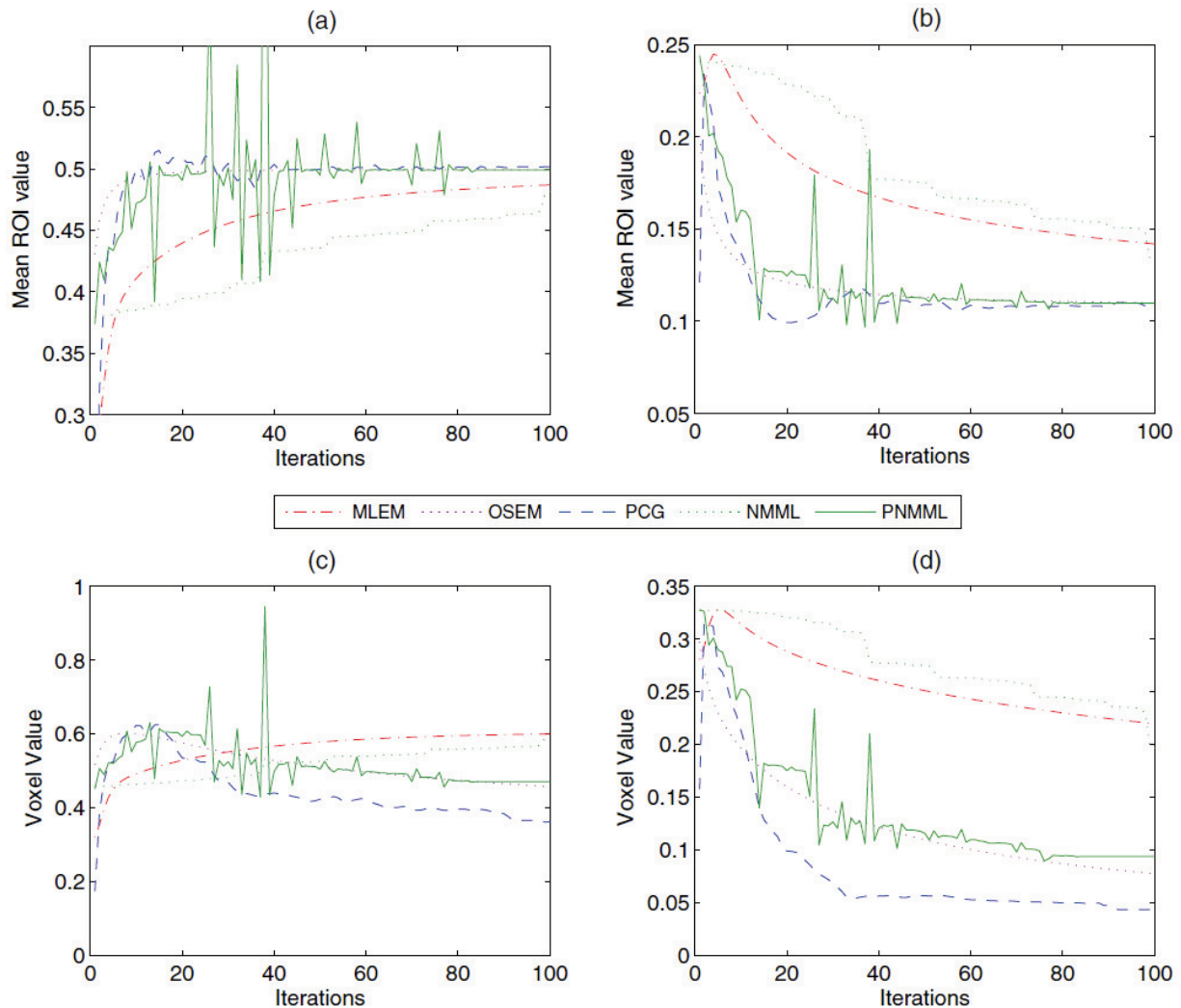


Figure 8.5: The convergence of different methods are compared against each other on a region of interest (ROI) in brain images. Plots a and b show the convergence in the hot region while c and d show the performance for the average of five random voxels. For plots a and b, fast convergence to values of .5 and .11 respectively are desirable. PCG is always among the best performers. For plots c and b, the convergence to a low value is desirable. This figure is from [102].

8.6. PCG very quickly converges to the crispest image of the brain, indicating it quickly found the solution it prefers. This is further confirmed by the one dimensional profiles of the images of Figure 8.6 in Figure 8.7. However, the final solution appears to be almost too sharp in the one dimensional profile. With large

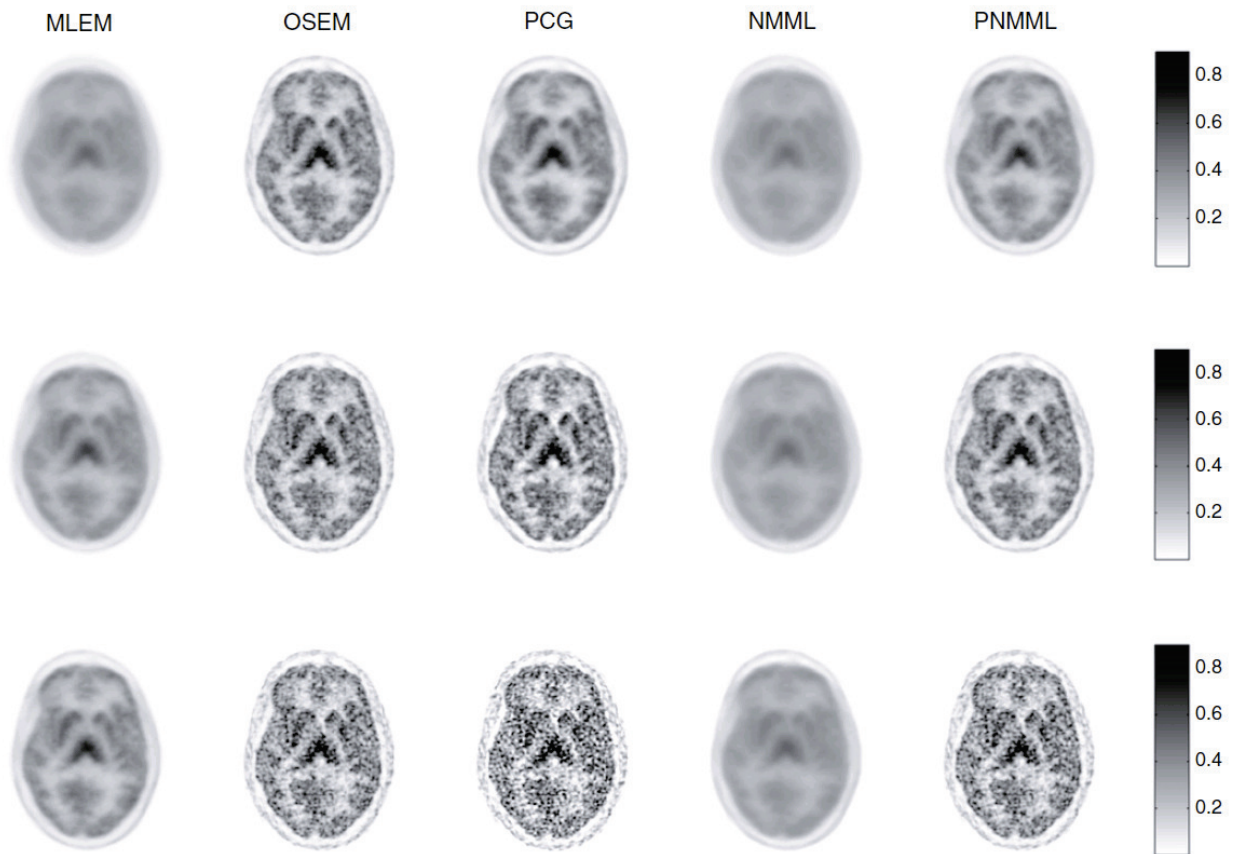


Figure 8.6: Reconstructed images from various algorithms after 7 (top row), 15 (middle row) and 30 (bottom row) iterations. PCG quickly converges to a solution but shows a brain with lots of fluctuations. This figure is from [102].

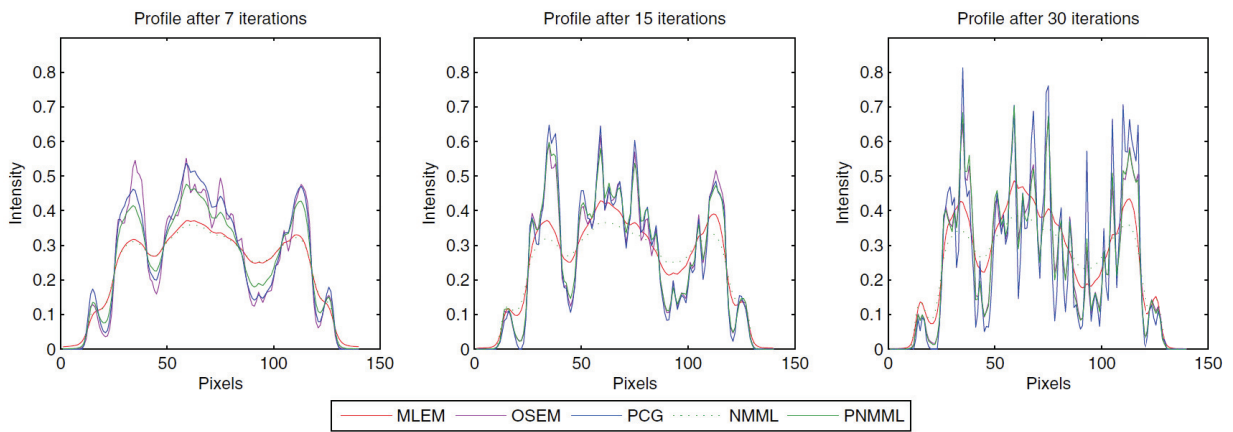


Figure 8.7: Profiles of intensity from the brains in Figure 8.6 after 7 (left), 15 (middle) and 30 (bottom) iterations. These profiles show the spiky over/under predictions from PCG with respect to other algorithms. This figure is from [102].

excesses being compensated for with deficits in neighbouring points. This behaviour is also observed in Millipede and is part of the focus of the section on Millipede issues, Section 8.3.5.

### 8.3.4 Use With an Angular Minimizer

After Millipede converges to the best solution it can find, a configuration of losses for a given track and the expected number of PE at the DOMs is available. The expected number of PE can be fed to a separate external angular minimizer to attempt to find a better track to use as a hypothesis for Millipede. This process happens recursively, with the angular minimizer giving Millipede new solutions to try, and Millipede giving back new per bin expectations for the angular minimizer to use, until both find solutions that move less than their respective tolerances. As mentioned previously, this should be the best angular solution IceCube can get for tracks, however the results have never backed this statement up. For example, Figure 8.8 shows a study by Jake Feintzeig when he was searching for the best reconstruction to use for the point source analysis. The figure shows the cumulative fraction of events with an angular error less than the specified amount. In this plot all the MPE based solutions perform better than Millipede. One problem that plagues Millipede based reconstructions is solutions which predict light arriving before the detected light on DOMs. Figure 8.9 shows the  $t_{res}$  distribution for the solution provided by Millipede. The shift of the peak from 0 to negative values indicates that this best fit track prefers to be too early, even unphysically so. This appears to be a real function of the likelihood space, as is shown in Figure 8.10 where the log-likelihood value is shown as a function of shifted time with respect to the true time (another way of expressing a shift in position). The true Monte Carlo information for the losses and track are used indicating that even with the proper information the solution still prefers a shifted result. Having such a shifted result likely affects the reconstruction's ability to reproduce the leading edges of the pulses, which provide the ability to point in IceCube, leading to a degradation of the information or an improper likelihood.

### 8.3.5 Issues

There are a few shortcomings with Millipede as it stands now. As was discussed in Section 8.3.3, the unfolded losses tend to be very sharp, which translates to very sparse energy loss sequences with a few very bright losses describing all the observations. This is illustrated in Figures 8.11, 8.12, 8.13, 8.14, and 8.15. Each plot has the solution of a Millipede fit which is unfolded using the true muon track (green histogram), as well as solutions shifted forward and backward along the track. The unfolding is performed on losses spaced uniformly every 5 meters along the track. Each of the figures has a different re-binning of these losses; 5m for 8.11, 10m for 8.12, 20m for 8.13, 40m for 8.14, and 75m for 8.15. The blue vertical lines are the true amount of energy lost over each bin. At the 5 meter binning, which is commonly used in fits, the unfolded energy tends to be a bad representation of the true bin to bin fluctuations. Often the true



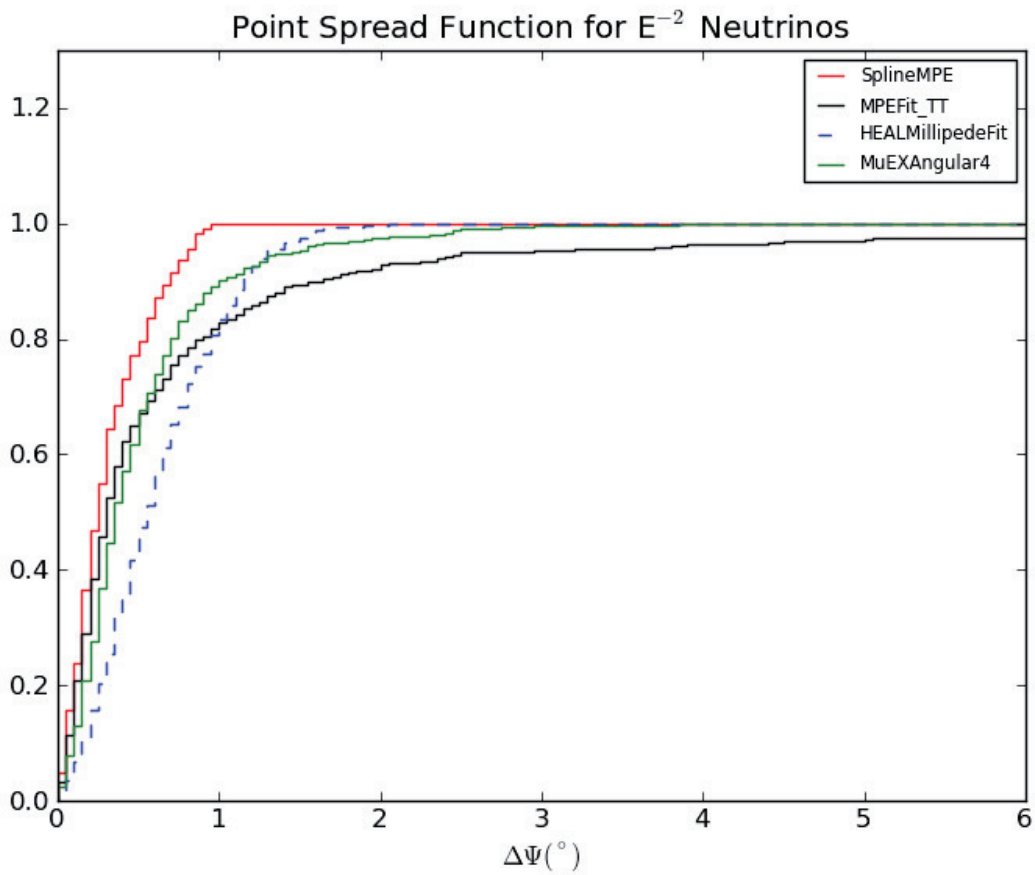


Figure 8.8: Point spread distributions for various track fits in the IceCube point source selection. Millipede shows the worst performance of all the algorithms tested. This figure comes from [105].

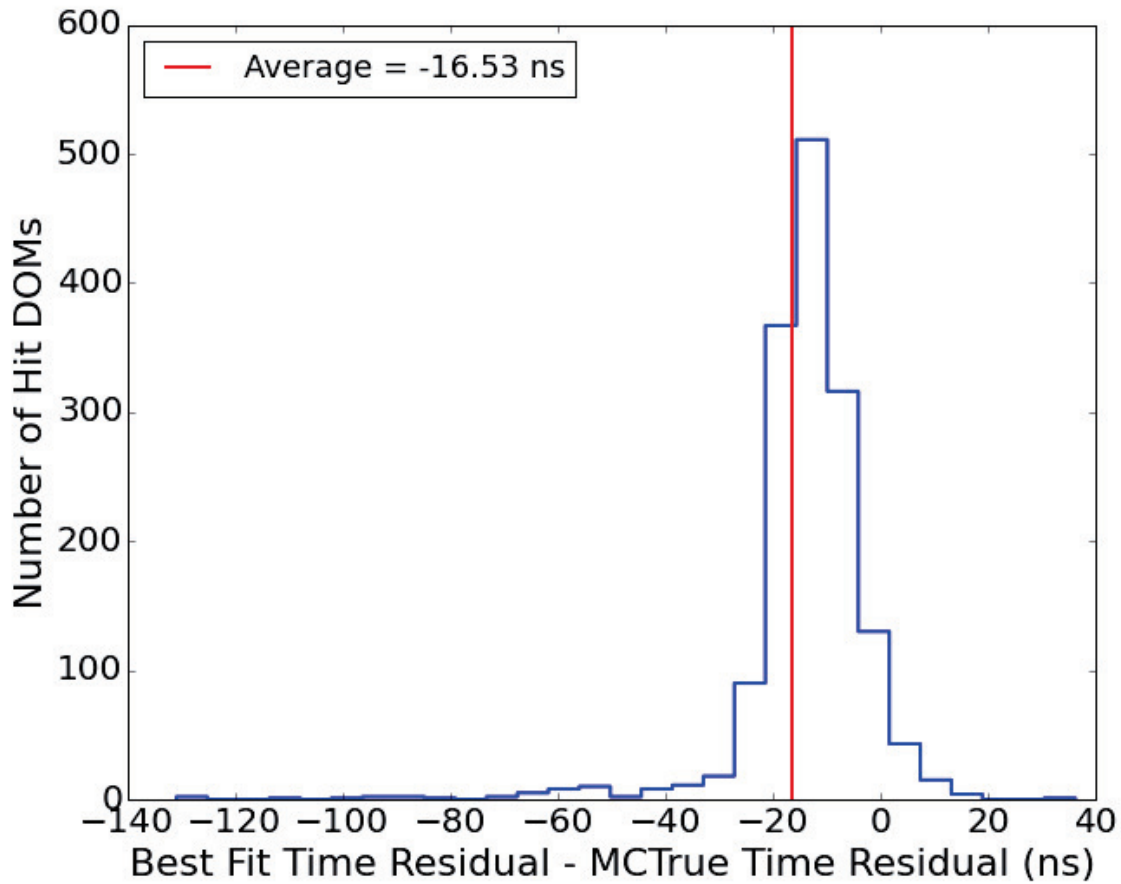


Figure 8.9: Distribution comparing the time residual of the best fit to the time residual from geometry (called the MCTrue Time Distribution). The negative shift suggest that the best fit is actually shifted earlier in time than the true track. This leads to the predicted photons arriving earlier than physically possible and could be an indication of a deeper problem

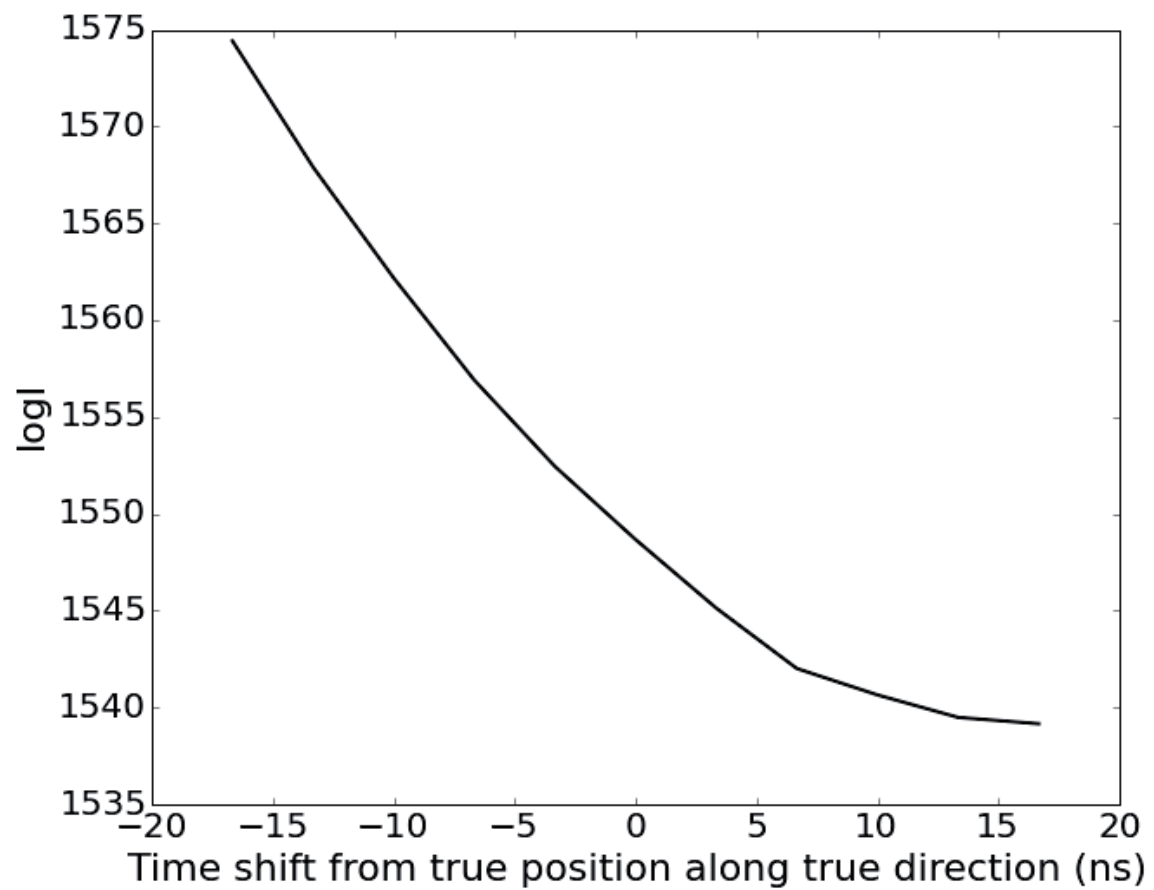


Figure 8.10: In connection with Figure 8.9, this figure presents the negative log likelihood value(logl) of a fit track as a function of time shift along the true direction. The minimal logl value is shifted forward in time with respect to the simulated Monte Carlo track and suggests there is an issue with the fit.

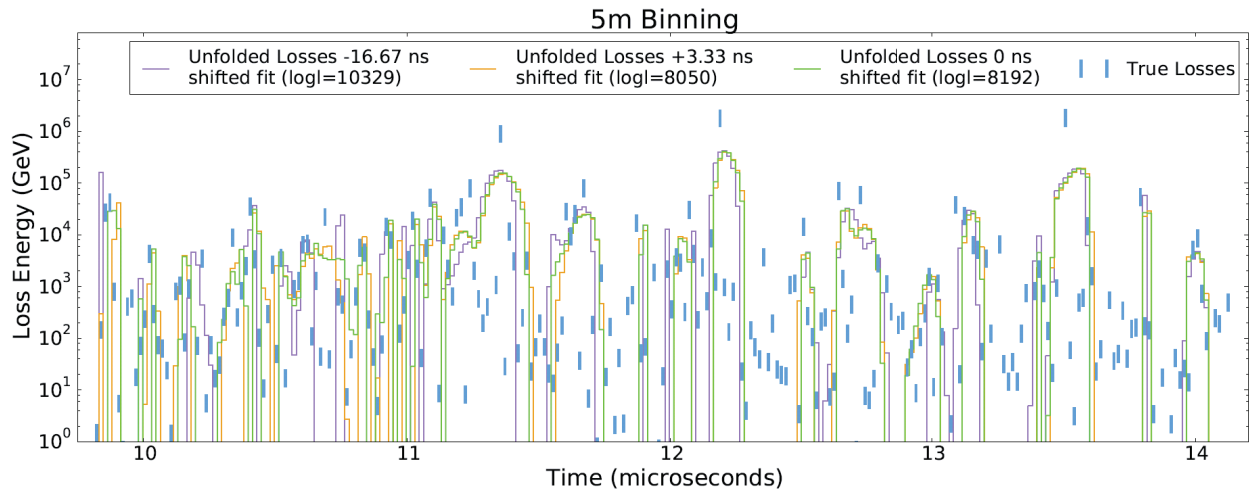


Figure 8.11: Millipede results in original binning.

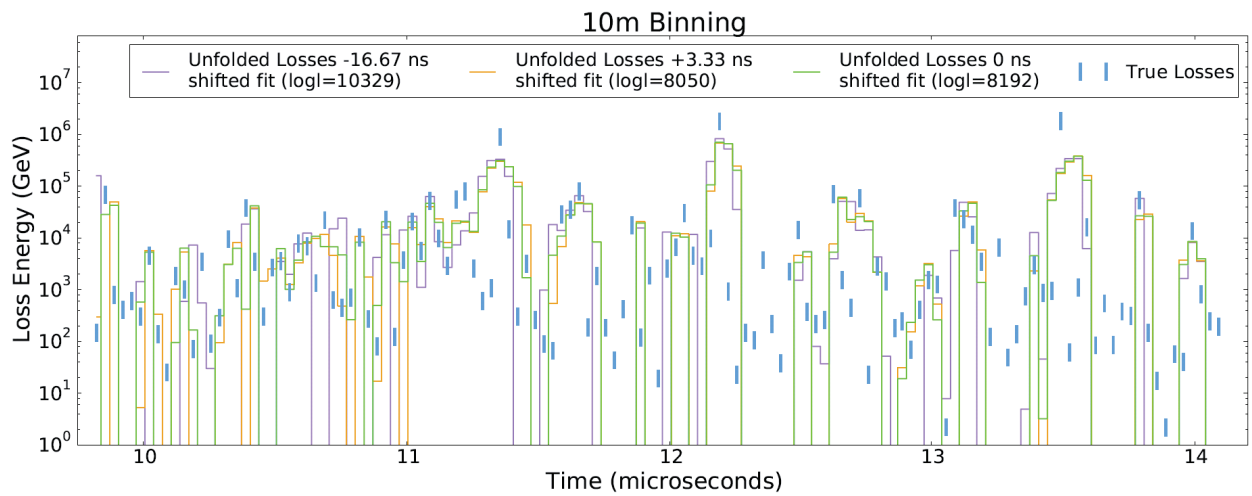


Figure 8.12: Millipede results regrouped into 10 meter bins.

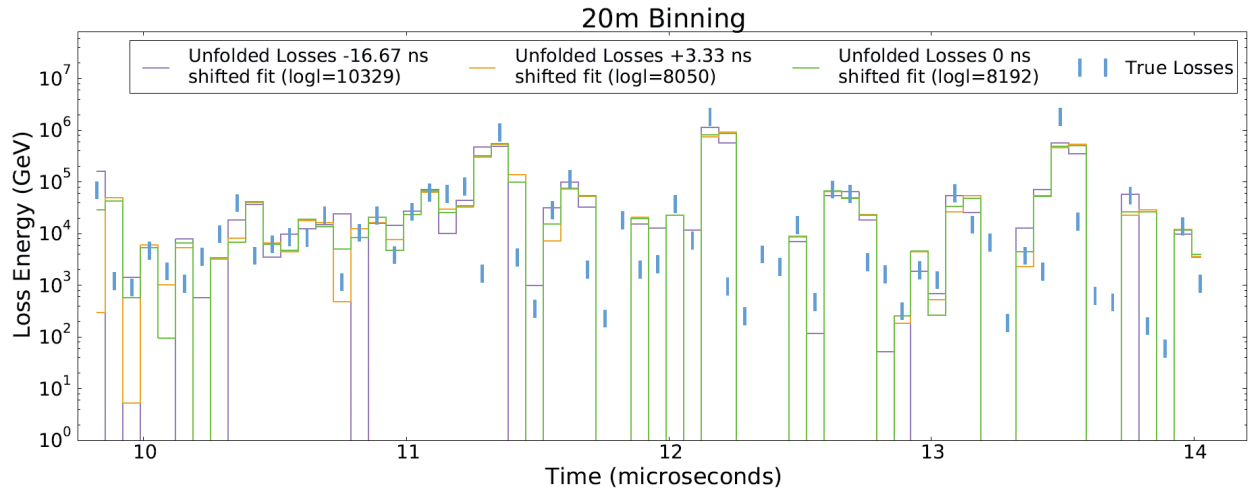


Figure 8.13: Millipede results regrouped into 20 meter bins.

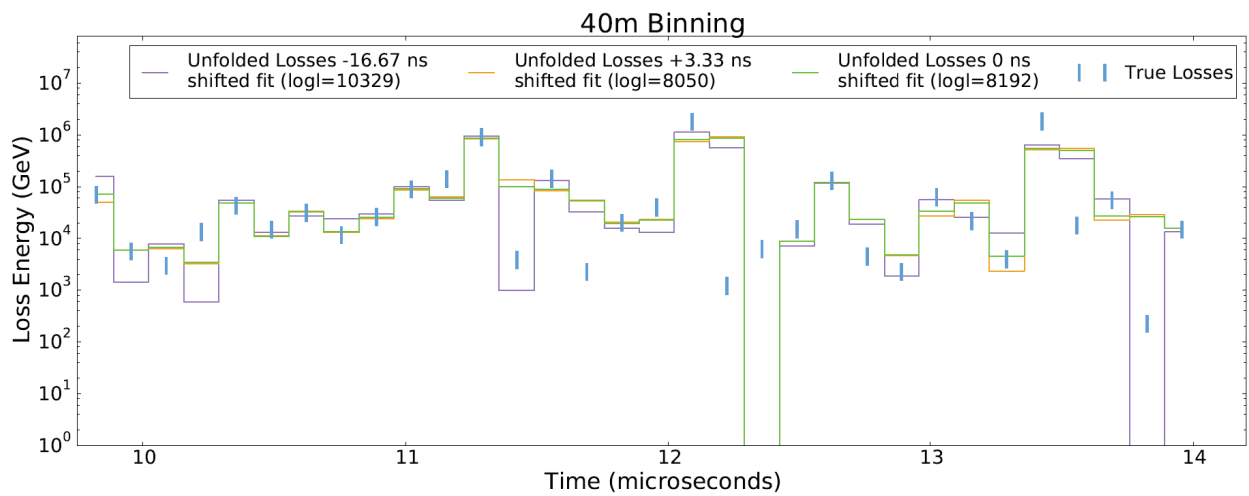


Figure 8.14: Millipede results regrouped into 40 meter bins.

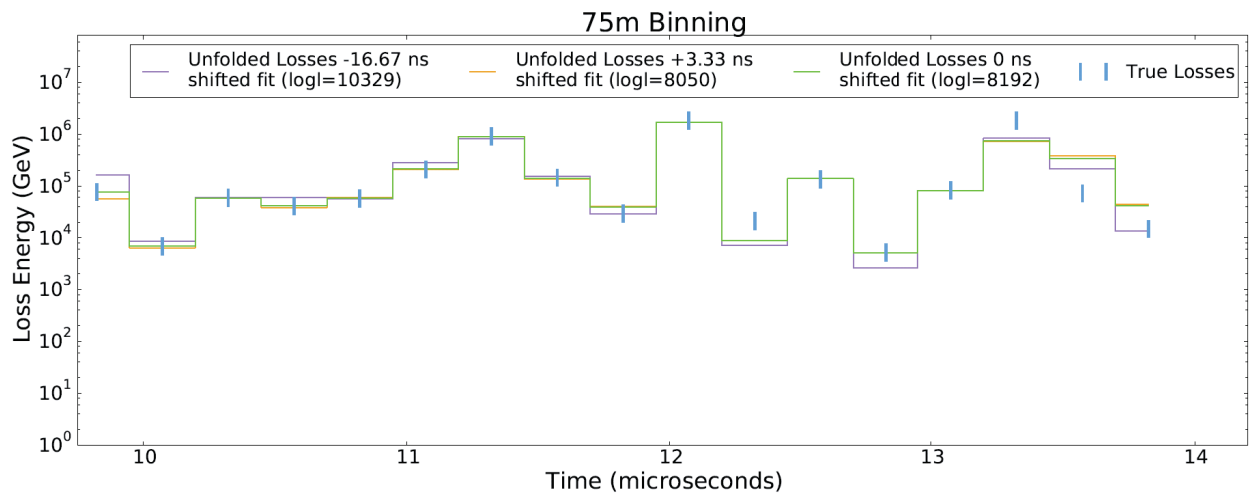


Figure 8.15: Millipede results regrouped into 75 meter bins.

energy is grossly over represented or under represented. As the bin size increases, the grouped together fit losses do a better job representing the grouped together true losses. This poor representation of the losses at fine binnings is the sharpness feature of the PCG method. The unfolded results are "spiky" and have large singular losses in regions where many of the neighbors are 0. This is likely due to the resolution the unfolding has to work with. This is because pulses recorded over long times after propagating through diffuse media don't point back to one particular loss. Thus the algorithm begins raising one of the losses to describe what is observed, and finds that loss is an acceptable way to describe everything which is occurring in that region. The fact that the true and unfolded losses agree well when the bin size is increased shows that the method is doing a good job predicting the total energy loss over large regions. This behaviour does allow for decent performance when a reconstruction attempts to infer the energy of an event from the loss distribution such as in Section 9.6. There are a few options to attempt to force the PCG method in Millipede to adapt to the reality of continuous emission along the track. These are discussed in the next section.

### 8.3.6 Ideas about Resolving the Issues

There are two main issues facing Millipede. First is its propensity to unfold bright isolated losses. Second is its propensity to find unphysical solutions. The isolated losses seem to be tied to the fact that Millipede has no idea of the physics it's attempting to understand. Since the algorithm is attempting to reconstruct muons, one solution is to combine its likelihood with one that knows about muons. This is the idea behind Millipede-Edepillim. Edepillim is a separate algorithm which combines the losses from Millipede with the pdf of muon losses for different energy muons. Edepillim's goal is to obtain the muon energy which minimizes the likelihood of the losses reported by Millipede. With Edepillim this process happens in two disconnected steps, with Millipede first proposing a solution and Edepillim proposing the muon energy, no feedback between the two happens. However, if the two were combined to form a joint likelihood this could help with Millipede's issues. Millipede would provide the information about what the likely losses are while Edepillim would condition what losses are possible. A further constraint could be made to condition that the distribution of losses in energy have a distribution like those found with real muons. This would make sure that not only are the loss energies appropriate, but that they occur in proper numbers. Millipede's propensity for finding unphysical solutions is a separate issue. This largely seems to be driven by an inadequacy of likelihood evaluation. In inspecting the per bin expectations from Millipede solutions with the waveform it often comes up that the leading edge of the expectation comes earlier than the waveform. This should not happen, but in the likelihood formulation there is nothing to stop this shift. Special formulation of the likelihood to respect the leading edges could help with problems in the likelihood space which affect the angular minimization.

Another idea involving millipede, but not directly tied to fixing the issues that plague the algorithm, is the introduction of ice model uncertainties into the algorithm's definition. IceCube's current ice model has

an approximately 10% uncertainty associated with it. This means that bins with more than 100 PE will have a statistical error on par or smaller than the systematic error. Currently there is no systematic error in Millipede, so these high PE bins are under predicting their error. One can introduce a systematic error into the algorithm by multiplying a normal distribution with the Poisson distribution of Equation 8.16. This normal distribution would take the form

$$P(x|m) = \frac{1}{\sqrt{2\pi\sigma^2}} e^{-\frac{(x-m)^2}{2\sigma^2}} \quad (8.23)$$

where  $m$  is the average value from the Poisson definition,  $\sigma = f \times m$ , and  $f$  is the fraction of uncertainty on  $m$ . When the log of this new combined likelihood is taken, the result is two independent terms which are summed. This results in a simple form to propagate through the algorithm and implement.



## Chapter 9

### Data Selection

As was discussed in Chapter 5, there has been a great deal of success in measuring the astrophysical flux with veto techniques in the southern hemisphere. However, up until now most selections were derived with the detection of cascades in mind. This is partially because most of the events with a contained vertex in a 1:1:1 neutrino flux are detected as cascades in IceCube due to the neutral current contribution and the cascade topology of the charged current interactions of two of the three neutrino types. Cascades in IceCube do not have good pointing resolution, so evidence for incoming muons in the veto definition must be searched for in every direction. Since the probability of detecting a muon is proportional to the amount of detector a muon traverses, the veto layers formed are simply uniform thickness layers of the outer detector (see the veto layers in Figures 5.1 and 5.10). Thus, much of the detector is lost in the veto construction and is unavailable for detection. However, an event that has pointing and timing can reveal which DOMs should actively participate in a veto and at what time. This motivates a special veto for starting track events which pass favorably through the detector. This is the idea of the incoming muon veto (sometimes called the starting track veto) which is utilized here to construct the Enhanced Starting Track Event Selection (ESTES). The ESTES selection is the basis for the science result of this thesis. Other selections, most notably the Starting TeV Events (STeVE), and Low Energy Starting Events (LESE) selections, have also attempted to take advantage of starting tracks for analysis [106]. However, it should be noted that ESTES deviates from these in two important ways. One, the goal of ESTES is to remove the incoming atmospheric muon background to the level that it is negligible unlike STeVE and LESE which were designed for point source searches where background is acceptable. Two, ESTES is designed specifically to use the track information to defined veto regions while both STeVE and LESE use layers of the detector for vetoing. It is not explicitly shown here, but even though ESTES pursues a higher purity than STeVE and LESE, it has a larger acceptance than these selections in the southern sky for events with energy between 8 and 200 TeV.

In the following the ESTES event selection is described. The event selection will be run over data from 10:05:49 UTC on May 15th 2012 to 03:56:15 UTC on May 18th 2017, using the detector configurations IC-86 2012 through IC-86 2016, where IC-86 stands for IceCube operating with 86 strings. 2011 will not be

processed for now because it does not have the full sky starting filter and for the first attempt it is desirable to keep the selection as uniform as possible. IceCube commonly breaks its data taking into 8 hour runs which can be marked as good or bad for physics analysis due to calibration activity or detector malfunction. In the case that the detector is not operating in a condition fit for physics analysis the run will be cut short and a new run will begin with changes intended to fix the detector. Runs are labeled with increasing integers. The labels of the runs relevant for this thesis are 120156 - 129519, minus those which are bad. In total 154227037.18 seconds (4.89 years) of live time are available for analysis.

The goal of the selection is to reject incoming muons. This involves rejecting  $7.5 \times 10^{10}$  events per year down to the level of at most 1 per year. To simulate this, a combination of CORSIKA showers and MuonGun (see Section 7.1) for a description, were used. CORSIKA is slow to generate so the entire livetime IceCube has available at the appropriate energy amounts to approximately 1/10th of a year, as is shown in Figure 9.1. In order to make up for this shortcoming, veto analyses commonly use MuonGun as well, but currently MuonGun also has a shortcoming. At this time MuonGun can only reproduce the results of single muon simulation, so it cannot be used as a replacement for the bundle simulation produced by CORSIKA. This is generally acceptable because single muons are the most difficult background to reject and years worth of livetime can be acquired, as can be seen in Figure 9.2. Using these simulation types in combination is acceptable as long as care is taken to make the weighting valid. Since both CORSIKA and MuonGun contain single muons, only one source of single muons can remain to avoid double counting. This is accomplished by removing all of the CORSIKA events with analysis cuts and using the remaining MuonGun for background estimates. Under these stipulations this section will show that ESTES can successfully reduce the simulated muon background to less than 1 event per year, but there are concerns that the incoming muon background is not completely removed. In order to address this, a new mode of MuonGun for multi muon generation must be validated. If this simulation is a good description of data then years of livetime can be generated to verify ESTES on.

## 9.1 Incoming Muon Veto

Assuming that you have identified a sample of tracks, to be discussed in Section 9.2, then the following is a general method to find out if an event displays starting characteristics or not. When an event enters the detector as a muon neutrino and undergoes a charged current interaction, it can be characterized by a region absent of light followed by a region where light from the hadronic interaction and outgoing muon is observed. The goal then is to determine how likely the region of missed light was, but to do this one needs to set up some expectations. IceCube commonly uses tabulated probability density distributions (muon tables) for these predictions. However, the energy of the particle of interest must be known to get an accurate estimate

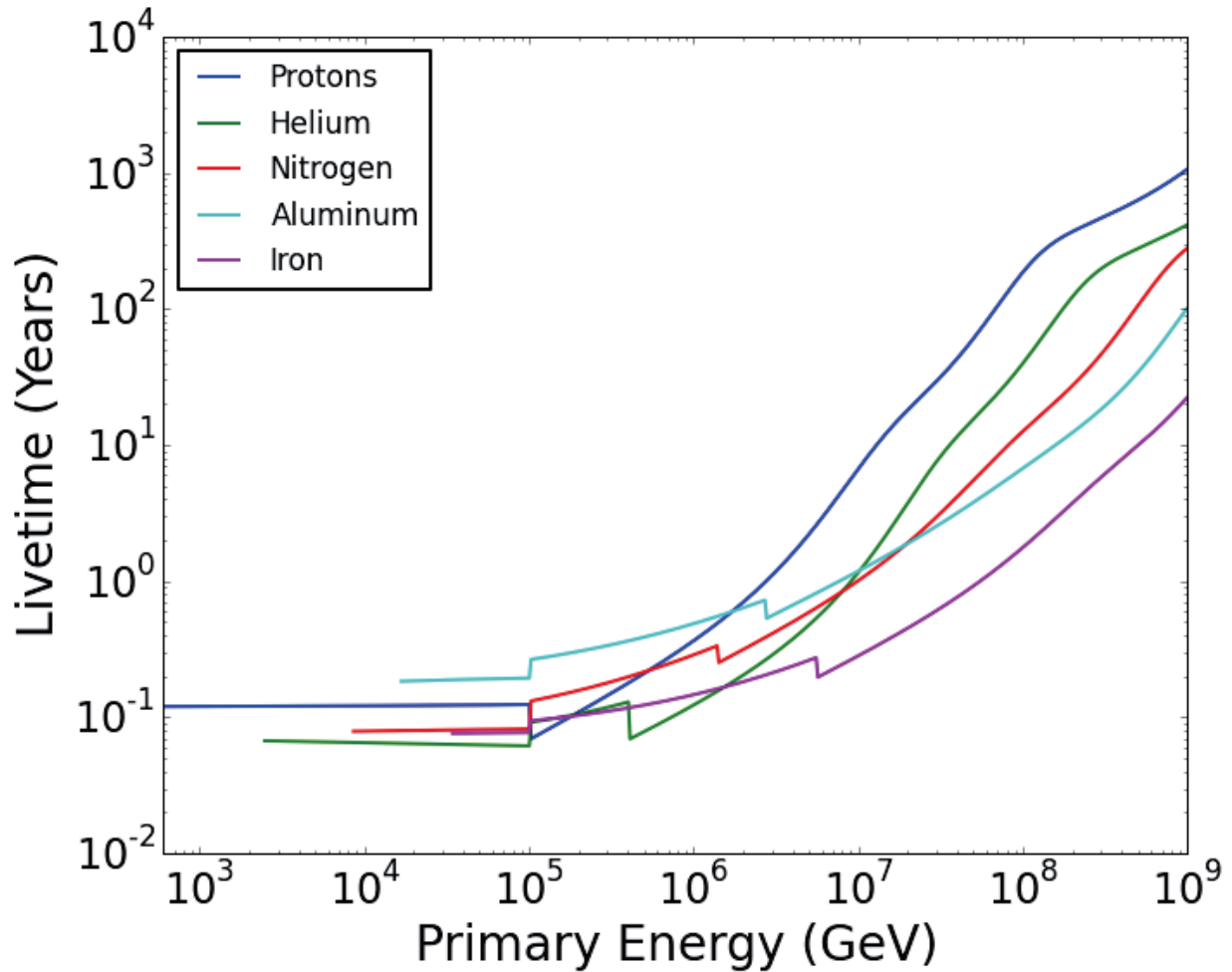


Figure 9.1: The effective livetime of the CORSIKA simulation used in this analysis as a function of primary energy. The sharp jumps come from combining sets in two different energy ranges, and the rise about  $\approx 1$  PeV is from a softer spectrum than is present in nature being simulated. There is approximately a factor of 10 difference between the average muon content of a shower at IceCube's depth and the original primary energy (eg. 100 TeV primaries on average produce 10 TeV of muons in IceCube). Since ESTES is most sensitive to muons around 10 TeV, this means the average livetime of the CORSIKA simulation set is around a 10th of a year.

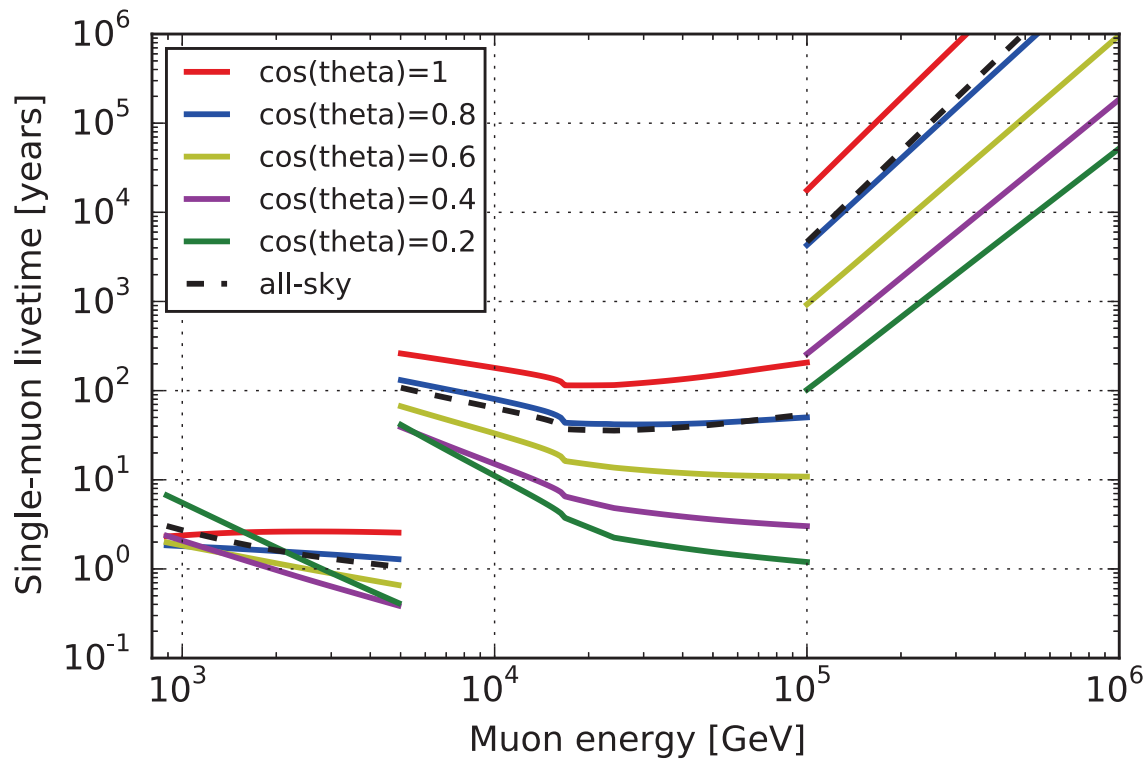


Figure 9.2: The livetime of single muons as a function of muon energy created by MuonGun. This simulation is used by ESTES for its background estimate to supplement the poor livetime of CORSIKA. The jumps are caused by the simulation set being composed of low energy, medium energy, and high energy parts which are not created such that the sets match at the boundary. The most relevant events come from the medium energy set around 10 TeV. In this region the livetime is at least a year, with an average of at least 30 years.

of the yield. IceCube has limited energy resolution on track-like events, so a simplified method is used to make the estimation. For the estimation, one must first find the regions with and without light.

### 9.1.1 Defining The Muon and Veto Regions

If one has an existing reconstruction as a hypothesis, then the regions can be defined by approximating that all light travels along the Cherenkov cone. This assumption is built into the infinite minimum ionizing muon (IMIM) photon tables which are used for the PE per ns yields discussed in this section. Using the Cherenkov angle assumption, and the expected arrival time and emission point of light for every DOM can be calculated compared to the observed photon arrival time. By sorting the emission points for DOMs which have observed PEs that match the expected yield. The photon emitted earliest along the track can be estimated. This method is displayed graphically in Figure 9.3. The incoming neutrino is represented by the dashed line which transitions to a solid line and arrow after the neutrino's interaction, the arrow's trajectory is assumed for this veto depiction. The observed hits are shown as colored circles in the usual manner, color indicating time and charge indicated by the circle's size. DOMs which did not observe light are shown as a grey dot. Below the event display are plots of the observed and expected PEs, with lines pointing to the DOM they represent. These figures depict the determination of the earliest hit. The figure farthest to the left is a DOM which was passed when the event was a neutrino, thus receiving no light. The red line in this plot is the expected number of PE/ns from the photon arrival spline of an IMIM. The grey band is the region where expectation is larger than .001 of the peak value. Since no observed PE are in this region, this DOM is not considered part of the event muon region. In the center plot a similar red line and grey band are presented. However, this time a PE was observed, depicted as a blue vertical line. To determine if this observed PE was the earliest, its origin position on the track is inferred assuming origination from the direct Cherenkov emission point on the track. After inspecting all the DOMs within 350m of the track in the in-ice detector and inferring their respective direct Cherenkov emission points, including the DOM represented by the right plot, the DOM represented by the center plot is found to be the DOM which has a hit and maps back the farthest along the track. This earns the plot the "Earliest Hit" label. A representation of the inferred direct Cherenkov emission cone is shown as a cyan line. The muon region is defined to be all the DOMs which have a Cherenkov emission point farther along the track than the identified earliest DOM and the veto region is defined to be all the DOMs whose emission point is earlier on the track. It should be noted that the veto region does not have to contain any DOMs, and often for incoming events does not.

#### 9.1.1.1 Refining The Emission Point

The assumption that emission occurs only along the Cherenkov cone breaks down quickly in IceCube because the ice scatters light after propagating a short distance. As such, the inferred position is often

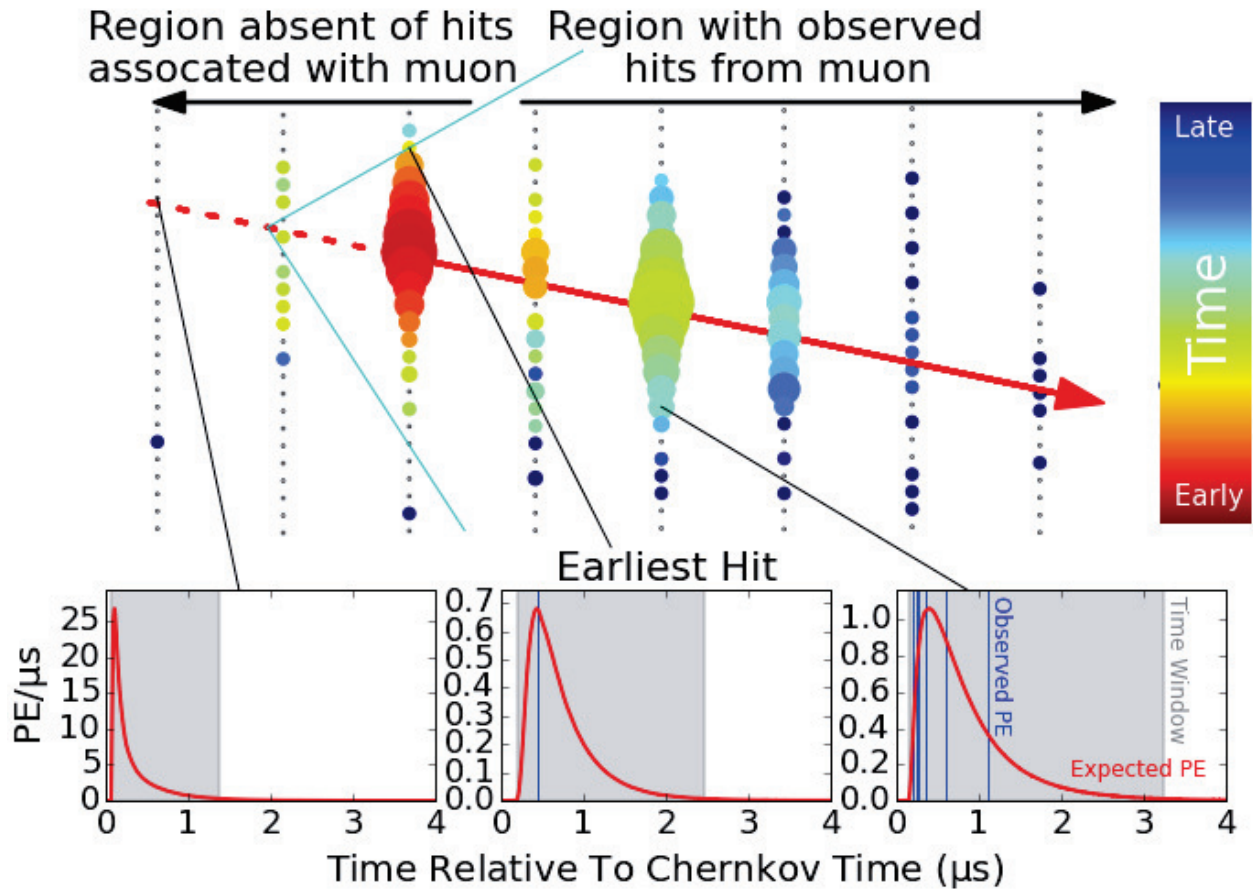


Figure 9.3: A depiction of how the incoming muon veto works on a simulated event. The incoming neutrino, dashed line, converts to a muon, solid arrow, and deposits the depicted hits, colored circles. Predictions from photon splines are used to find the earliest hit and the event is split into a muon region and a region before the muon. From here the probability of missing the hits before the muon can be assessed.

incorrect. Also for DOMs which are next to each other on a string, the farther DOM from the track will map farther back along the track. Often the earliest hit occurs in a region where hits are Poisson fluctuations of 0 or 1. In this situation, it is easy to encounter hit configurations where the first hit DOM was not the one which would always occur given more repetitions of the event. In these situations, it is easy to incorrectly define the veto region and infer the presence of a neutrino as a result. This lack of hits due to a neutrino is what we are testing for, so we don't want to begin calculating our veto with these possibly downward-fluctuated DOMs. For the infinite muon tables there is no further information that can be gleaned. However, it is also an option to use a set of the segmented muon tracks from the segmented tables. This option provides the same total yield information, however it is distributed over the segments. This allows one to know how much of the yield was predicted to be emitted from each segment. Using the per segment yield as a weight, the weighted average and standard deviation of segment positions can be calculated. The calculated average can be taken to represent the most likely emission point and the standard deviation an uncertainty on that emission point. Having this information allows a more confident definition of the DOMs which are in the veto region by extending the muon region. This is done by inspecting for veto DOMs where the average position plus 1.5 times the standard deviation have an emission from the track later in time than the first hit DOM's average position minus 1.5 times the standard deviation. The veto region DOMs which do not fall outside this new region are not included in the veto calculation and thus change the veto probability. The difference in the two approaches is illustrated upper image of Figure 9.4, the earliest hit is highlighted in the red box, the DOM above it is in the veto region. The red dot on the black track is the mapping point of the earliest hit while the blue point is the mapping of that veto DOM. The red dot being before the blue dot illustrates the point of this section. By using the segmented tables with the weighted average and standard deviation of each position, in the lower image of Figure 9.4, the blue dot now comes later than the red dot, indicating that this unhit DOM would not participate in the veto. Thus the veto is strengthened and has a better ability to identify the event as an incoming muon. The change is made even more clear by plotting the DOMs which participate in the veto and the DOMs which don't. This is shown in the upper and lower images of Figure 9.5. The upper image of Figure 9.5 shows the veto DOMs in pink and the muon DOMs in green when the infinite muon table is used. The lower image of Figure 9.5 has only green markers, indicating there are no DOMs to calculate the miss probability with.

### 9.1.2 Setting The Photon Table Scale

With the DOMs which can be attributed to the observed portion of the muon and the DOMs which did not observe light before this region separated into the muon and veto regions one can begin to infer a veto condition. This inference is dependent on knowing how many PE of charge each of the veto DOMs would have observed. The amount of charge is dependent on the track to DOM geometry and the local properties

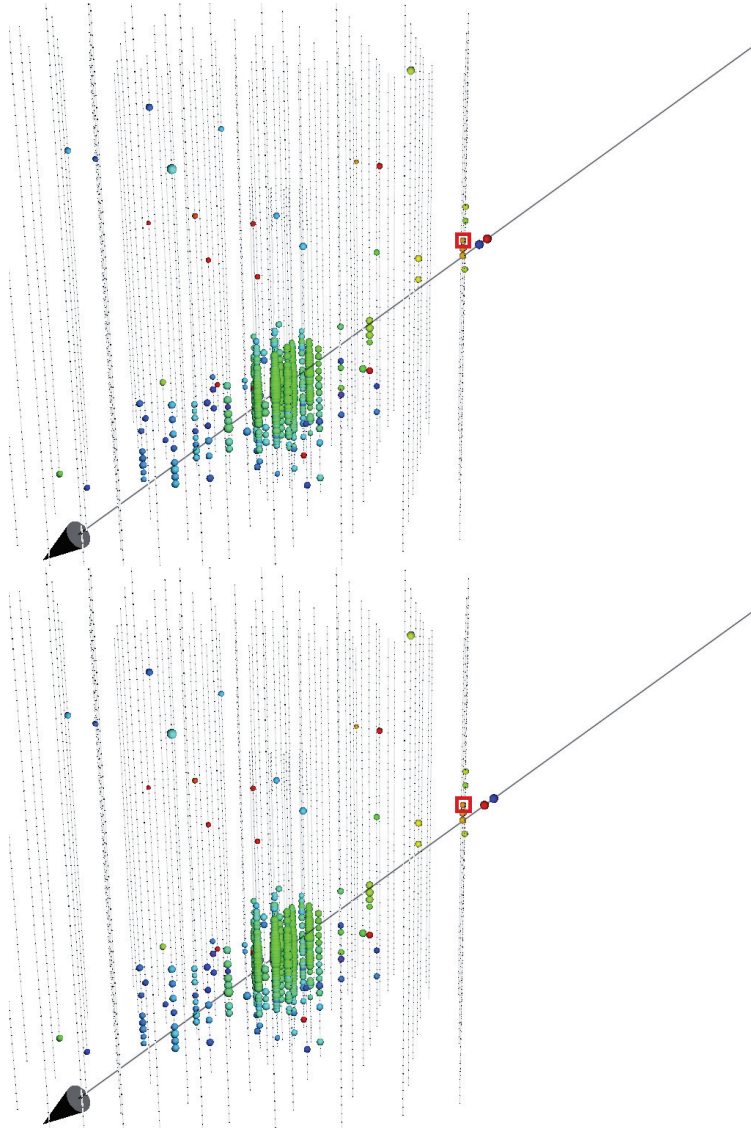


Figure 9.4: Figures showing the different earliest hit mapping assuming a definition using IMIM tables, top, and segmented muon tables, bottom. Using the segmented muon tables yields a better prediction but is slower.



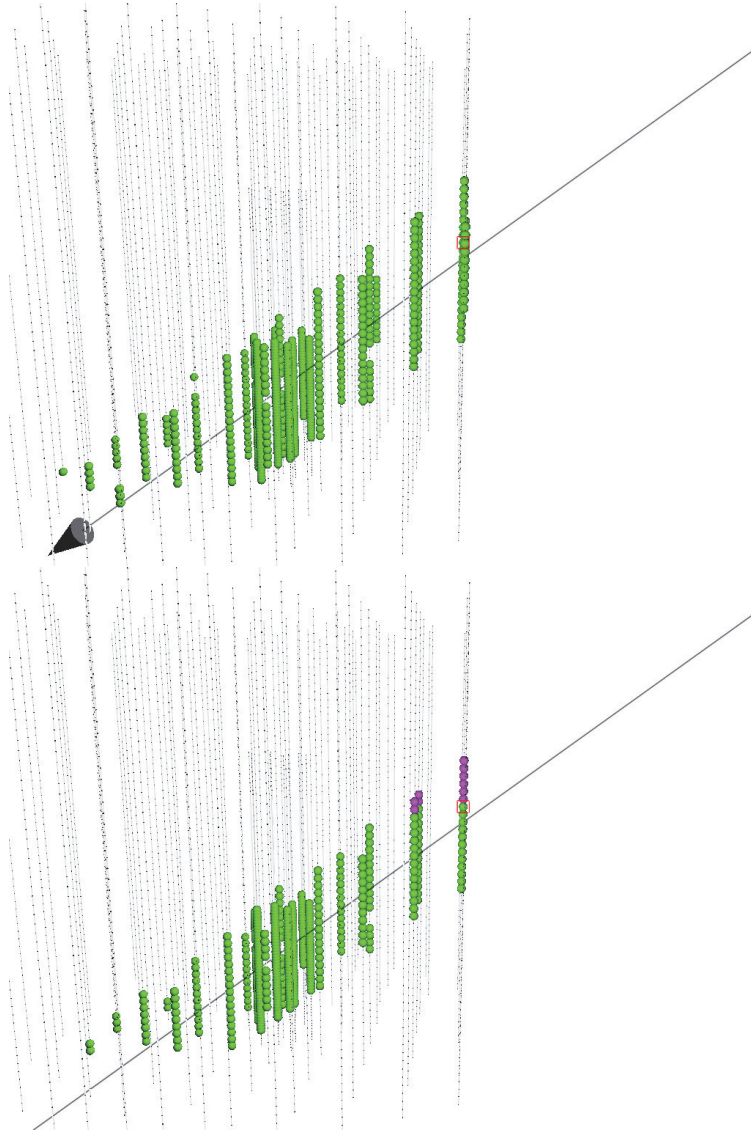


Figure 9.5: Figures showing the collection of hits which are in the muon and veto regions assuming a definition using IMIM tables, top, and segmented muon tables, bottom. Using the segmented muon tables yields a better prediction but is slower.

of the muon (i.e., if it had a large amount of energy lost in stochastic processes nearby). By picking a fixed track to analyze, the geometry is also fixed. This leaves only the muon properties to evaluate. To simplify and smooth over the fluctuations, the muon is considered to be a uniform and infinite light emitter. Since the table used for this is an IMIM table the assumed energy of the muon is too low and the expected PE at the DOMs is likely an under-estimate. To get a more appropriate estimate, one can scale the table's yield to match the observed output in a region where we know we observed the event. The muon region already does this. The scale of the muon is found by maximizing the following likelihood.

$$LLH = \sum_i^{\text{All Muon Region DOMs}} \log(p(\lambda_i, k_i)) \quad (9.1)$$

In this equation  $p(\lambda_i, k_i)$  is the Poisson probability of observing  $k$  PE on DOM  $i$  given the expected PE yield of  $\lambda$  from the scaled table and noise, shown as formulas below.

$$p(\lambda, k) = \frac{\lambda^k e^{-\lambda}}{k!} \quad \text{and} \quad \lambda_i = a \times \lambda_{\text{muon}} + \lambda_{\text{noise}} \quad (9.2)$$

The solution which maximizes the likelihood is found by varying  $a$ . Once the solution for the scale of the uniform light yield,  $a$ , is found, the evaluation of the probability of observing no hits on the DOMs in the veto region can be inferred. Since the value  $a$  scales with the brightness of the event, and the brightness roughly scales with energy of the event  $a$  is roughly an energy estimator. However,  $a$  does not use an appropriate physics hypothesis to arrive at its final value so it is not appropriate for use as an energy estimate.

### 9.1.2.1 Stochastic Suppression

Since the scale is set by averaging over the entire muon, this method is susceptible to errors in the estimation of the light yield. There are two main ways this can happen.

1. Track to DOM distances which are close, thus causing the estimate to come from a region where small deviations in the track cause large deviations in the light yield
2. Large stochastics distort the uniformity of the yield

To help mitigate these, an alternative mode of operation is available which makes an estimate of which DOMs are the product of uncharacteristic light and which are not. In this mode, the scale is only calculated using the DOMs which are not found to be the product of uncharacteristically bright losses. The identification of DOMs which are too close is based on the fact that the spline will expect many PE when in the rapidly changing region close to the DOM. Thus, DOMs where the expected yield from the IMIM table is more than 1 PE are removed. This may seem very restrictive, but only DOMS within 20 meters of the DOM can realistically have an expectation of greater than 1 PE from IMIM tables. The identification of DOMs affected

by stochastics is based upon the fact that stochastic energy losses produce too many PE with respect to the average observed PE or create PE far from the track where they are not expected. Thus, DOMs where less than .1 PE was expected, but a non-zero number of PEs was observed are removed and DOMs which have more than three times the average observed PE (rounded up to the nearest whole number since charge is roughly integer in value) are removed. Since this veto is searching for starting tracks, there is one caveat to this stochastic suppression. If an event is bright at the beginning of the muon region, it is an indication there was a hadronic shower of a starting track and is thus a neutrino. As a result, no DOMs are removed from this region, taken to extend 250 meters from the beginning of the muon region. Keeping these DOMs does cause true starting events to have higher values for  $a$ , however since the bias is towards the signal events it is taken as a feature not a concern. To visualize how this selection of DOMs affects events, two events are considered as a case study. The events are grouped into two sets of figures. The first set of pictures in Figure 9.6 depicts an incoming track and the second set of pictures in Figure 9.7 depicts a starting track. Remember that any DOM that occurs in the first 250 m of the muon region is exempt from the cuts described. The top left figure is a histogram of the expected charges for each event from a IMIM. Depicted as a vertical red dashed line is the .1 PE cut. DOMs which observe a hit but are below this line are not included. Also, DOMs which have an expectation larger than 1 are removed. The bottom left figure is a histogram of the observed PEs in the event. The solid vertical red line is the average of this distribution and the dashed vertical red line is three times the average of this distribution (rounded up to the nearest whole number). DOMs which are above the dashed red line are removed. The bottom two figures depict the event without (bottom left) and with (bottom right) the removed DOMs masked. Also shown are the Monte Carlo losses. For the incoming muon track the regions where there are the largest stochastic losses, many of the DOMs are masked to mitigate their effect on the scale calculation. For the starting track, this is not true because the largest loss is the hadronic interaction which is protected. For the incoming track, the scale value drops from 45 to 19 when the suppression is applied. For the starting track, the scale remains 6 whether suppression is applied or not. Both indicate that suppression is doing its intended job of weakening incoming stochastic events, leaving starting tracks minimally affected.

### 9.1.3 Calculating The Veto Probability

The veto probability is the probability of observing light on any of the DOMs in the veto region. The original definition was the inverse of this and so it is often called  $p_{miss}$ . It can be formulated in much the same way as the LLH in Equation 9.1, but with  $k$  always being 0.

$$p_{miss} = \prod_i^{All\ Veto\ Region\ DOMs} \log(p(\lambda_i, 0)) \quad (9.3)$$

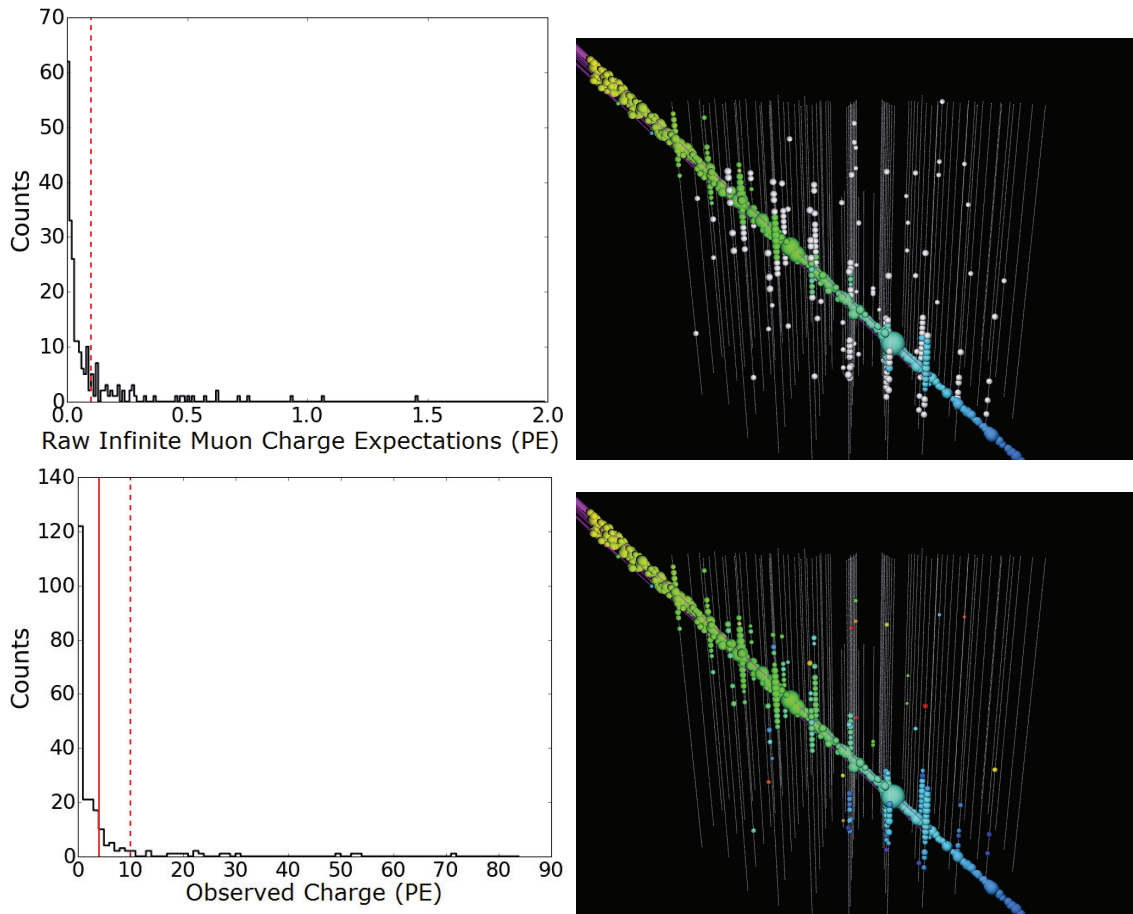


Figure 9.6: A set of figures depicting the cuts made on an incoming muon event. The histograms show the distributions of observed and expected PEs with lines showing the cuts made. The full pulse series is shown in one figure while the removed DOMs are masked in white in other. Many of the DOMs are masked in this case and help temper the contribution from stochastic losses. The noise hits are also largely removed, but this is not a designed consequence of the suppression.

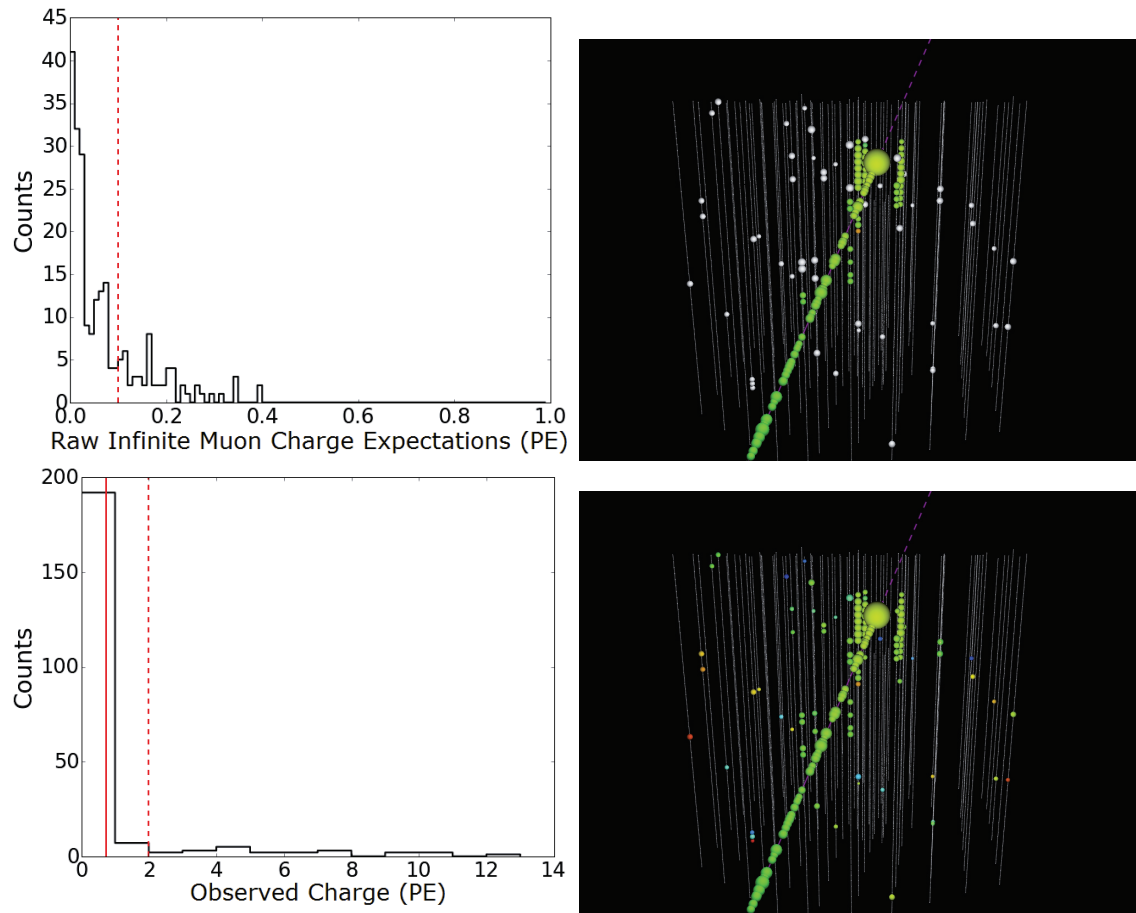


Figure 9.7: A set of figures depicting the cuts made on a starting track event. The histograms show the distributions of observed and expected PEs with lines showing the cuts made. The full pulse series is shown in one figure while the removed DOMs are masked in white in other. Many of the DOMs in this event are left untouched indicating the contribution from stochastics is minimal.

Since this is a probability,  $p_{miss}$  can range from 0 to 1 with values close to 1 indicating the event does not have evidence for being a starting event.

## 9.2 Cuts

This section details the cuts used to get from Level 2 filters, discussed in Sections 6.6, to a high purity neutrino sample. Using the information from the self-veto, discussed in section 4, one can construct contours of astrophysical purity as a function of zenith angle and neutrino energy, as shown in Figure 9.8. This plot

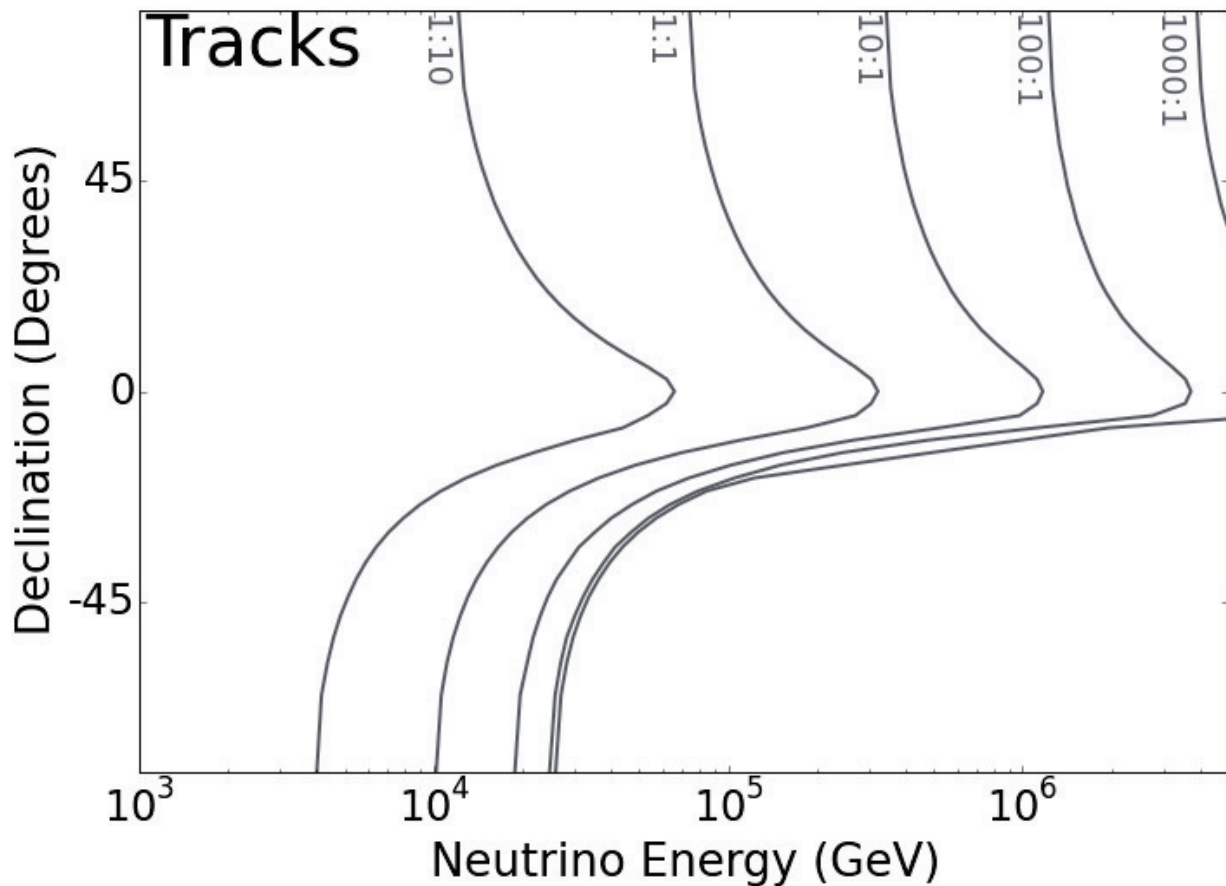


Figure 9.8: Contours of atmospheric to astrophysical ratios, indicated by the astrophysical:atmospheric numbers at the top of the figure. There is a large region in the southern hemisphere where the self-veto removes atmospheric events and lowers the energy needed to identify astrophysical neutrinos.

tells us that the interesting events for astrophysical searches lie in the southern hemisphere and have energy above 10 TeV. As a result the selection is geared towards detecting those events.

The discussion which follows is a rather technical description of the reconstructions and cuts which are implemented for ESTES. As a result a few aides have been put in place to assist with understanding the event selection at a higher level. The first aide can be found in Figure 9.9 and its associated caption. This figure describes the event selection with a flow chart complete with a short description in the caption and links to the relevant sections of the text. Secondly, lists of the steps performed and cuts applied in each section are explicitly listed in a sub-section labeled Applied Cuts at the end of each section. A reader who is only interested in a high level understanding should be able to manage with these pieces of information alone.

### 9.2.1 Pre-Cuts

Since we are searching for events above 10 TeV which are tracks, we can make a cut first on the level 2 filter which the events originate from and an energy proxy, total charge. In the southern sky, only the muon and full sky starting(FSS) filters provide track-like events. Furthermore only events which have deposited 200 PE of homogenized total charge are interesting in the context of searching for 10 TeV events. After this simple cut on filter and homogenized total charge has been performed, a quick test of the event's startingness is performed on one track fit. Since the incoming muon veto needs good reconstructions to work with, a SPE Fit is chosen to seed a SplineMPE fit. If the SplineMPE fit fails, the event is dropped. The output of the SplineMPE fit is used as the track hypothesis for an iteration of the incoming muon veto. From this iteration of the incoming muon veto two things can be used to determine if the event was a starting track.

1. If the length of the muon region is under 350 meters, it is difficult to distinguish if the event was a track. Thus these events are removed.
2. If the event has a  $p_{miss}$  value less than 0.001 then the event is not likely to be starting and is removed.

These cuts remove many of the events present at Level 2, making the more computationally expensive steps which follow feasible.

#### 9.2.1.1 Applied Cuts

1. Events must have passed the muon or full sky starting filters
2. Events must have 200 PE of detected charge
3. Run SplineMPE fit seeded with existing SPE fit
4. Run incoming muon veto on SplineMPE fit
5. Events must have a muon region larger than 350 meters as reconstructed by the incoming muon veto
6. Events must have a  $p_{miss}$  value less than 0.001 as reconstructed by the incoming muon veto

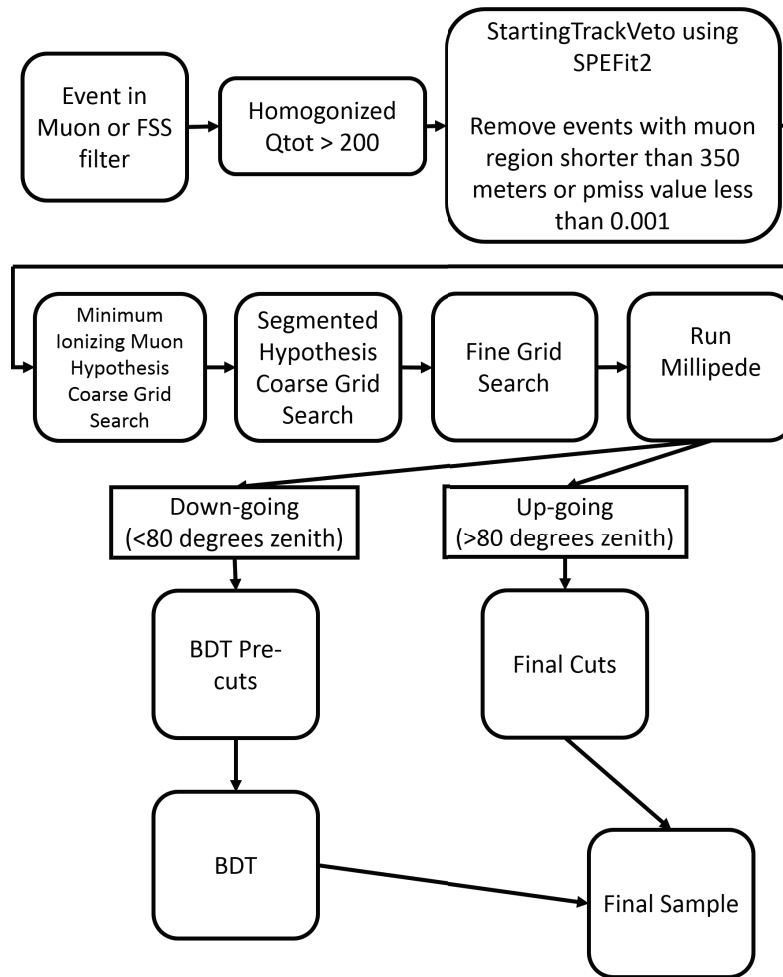


Figure 9.9: ESTES begins by selecting the muon and full sky starting filters which contain down-going muons (9.2.1) and requires that events have at least 200 PE of charge deposited (9.2.1). This 200 PE is a conservative cut which keeps almost all events above a neutrino of 10 TeV. After this, the incoming muon veto is run on a SplineMPE Fit. The output of the incoming muon veto is tested for a satisfactory length and  $p_{miss}$  value (9.2.1). These cuts are followed by what’s known as the Coarse Grid Search. This search consists of determining what the best fit solutions are which satisfy the detected charge while passing unfavourably through the detector for vetoing. These best fit solutions are tested with the incoming muon veto and again must satisfy length and  $p_{miss}$  criteria (9.2.2). This process is conducted twice, once with a faster but less accurate version of the starting track veto, and once with a slower more accurate version. Following this, a search in the same vein is conducted focused on hypothesized tracks which surround the best solution found in previous searches (9.2.3). All events which pass to this point are reconstructed with Millipede for direction and energy information (9.3). From here the selection breaks into two pieces. The simpler path is the Up-going region (events with zenith  $>80$  degrees) where only events from atmospheric and astrophysical neutrinos already dominate. A few simple cuts are applied here to remove the small remaining muon background (9.4.2). The more complex Down-going region (events with zenith  $<80$  degrees) is still dominated by atmospheric muons and uses machine learning in the form of a boosted decision tree to perform the final separation(9.4.1). The output of the Down-going and Up-going data paths are combined together



### 9.2.2 Coarse Grid Search

After the initial cuts, a search for the best sneaking track hypothesis is conducted in two stages. First a coarse search which covers the entire detector (described in this section), followed by a focused search around the best solution found in the coarse search (described in 9.2.3).

It is not very hard to remove obvious incoming events from consideration in the ESTES selection. They have hits on the border of the detector and their track fit is good. The difficult events to remove are those which sneak through at least one layer of the detector and/or have a track fit which poorly describes the event. These events require accurate knowledge of the path that the event took through the detector to get the incoming muon veto calculation correct. It was conceived in an earlier version of ESTES that minimizers could decipher which tracks were good and bad, however large data/Monte Carlo disagreement at the final level indicated otherwise and led to this more brute force technique. The technique which is used now aims to determine if there is a track which sneaks through the edge of the detector that is a better description of the deposited hits than any of the track reconstructions existing at Level 2. To test this hypothesis, tracks are constructed which pass through holes in the edge of the detector with particular focus around the dust layer and in the caps. These hypothesized tracks must also pass through the shifted center of gravity of the charge (COG) of the event at the proper time. The shifted COG is the COG shifted 300 m along the SPE Fit direction to avoid the fitted track variations being dominated by the first cascade loss of starting muon neutrinos. The points in the holes which are used are shown Figures 9.10 and 9.11. Additionally, there is a set of uniform down-going points which are also tested so that events at the edge of the detector have incoming hypotheses, shown in Figure 9.12.

In these figures, the COG is shown as the slightly opaque red sphere which is larger and in the center of the red deposited hits. The cyan spheres are the tested hole points which a track must pass through to test for a sneaking muon. The trajectories of the hypothesized tracks are shown as a sequence in Figures 9.13, 9.14, and 9.15. Figure 9.16 shows the tested tracks in cyan and highlights the Level 2 tracks in red. The result of the fits is one track which is better than all others by 2% in the reduced log-likelihood (rlogl). The reduced log-likelihood is defined to be the log-likelihood divided by the number of channels in the event. It is shown as the sole red track in Figure 9.17. Figures 9.18 and 9.19 show the same thing as Figures 9.16 and 9.17 but for a different event.

In this event more than 1 solution is found to be within 2% of the minimum rlogl value. Both Level 2 fits and fits originating from holes are found. In the end, over 935 tracks are tested on every event with the best being kept for farther consideration. While the incoming muon veto is not slow (about .1 seconds per tested hypothesis) it is not wise to test all 935 tracks with it. Instead, all the tracks are first refit with a SplineMPE fit where only the time is left free for the fitting algorithm. All 935 tracks take less than 1 second to compute

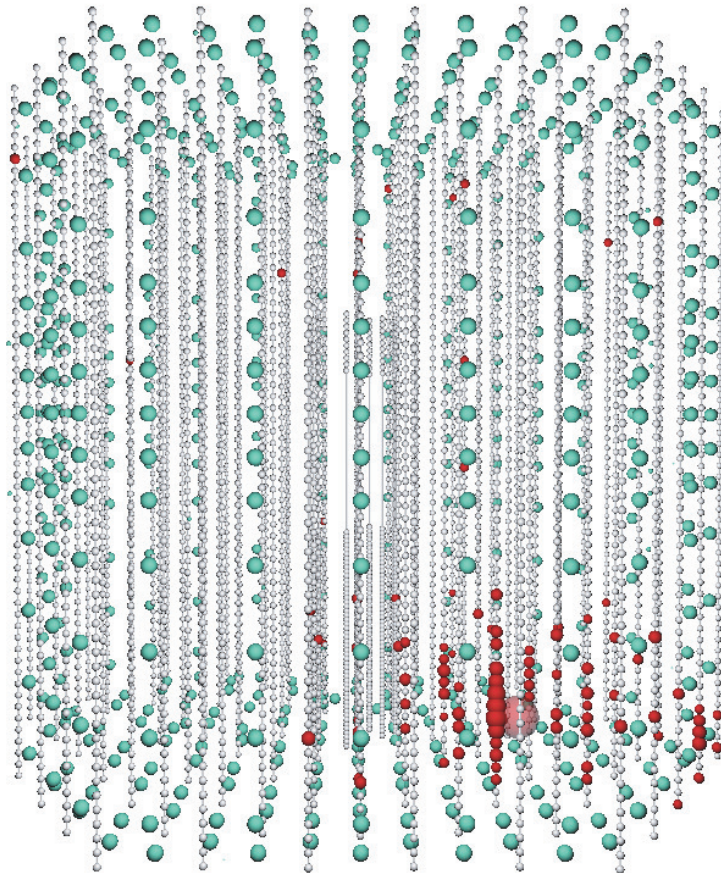


Figure 9.10: Side view of the holes in the edge of the detector. The center of these holes are shown as cyan spheres while the DOMs are shown in white. The holes are likely locations for a track to sneak in and appear to start in the detector. Also shown in red is a starting event.

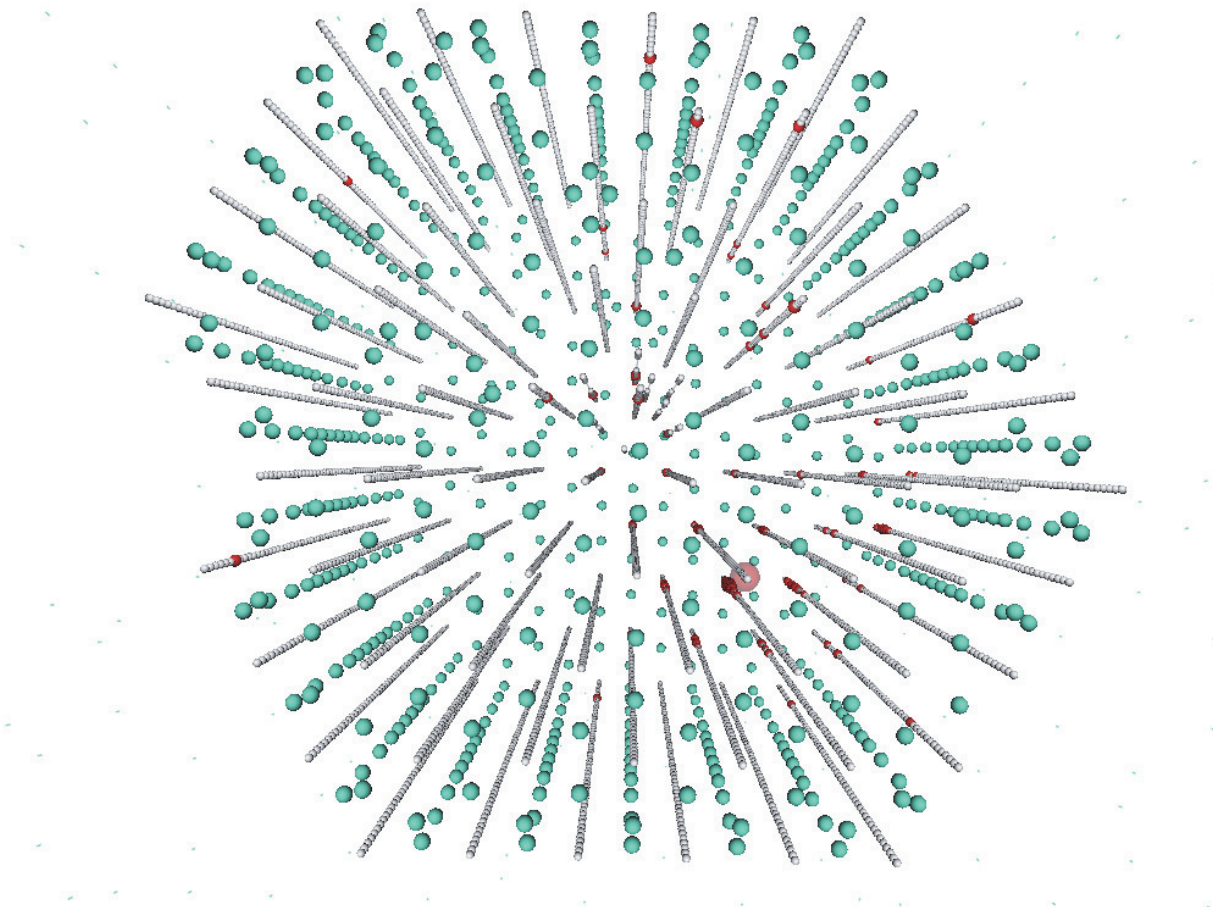


Figure 9.11: Top view of the holes along the edges of the detector. The center of these holes are shown as cyan spheres while the DOMs are shown in white. The holes are likely locations for a track to sneak in and appear to start in the detector. Also shown in red is a starting event.

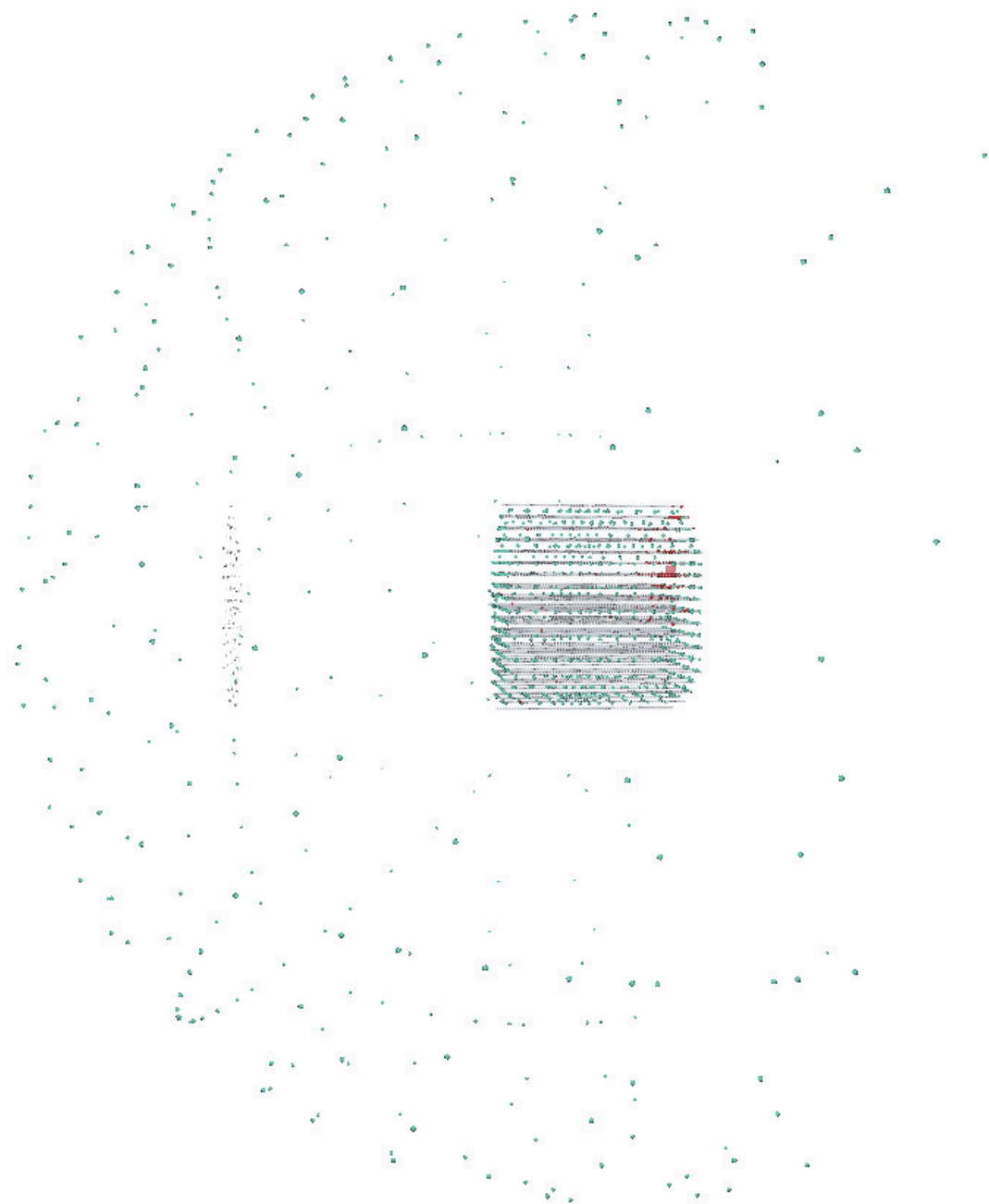


Figure 9.12: A zoomed out view of the holes in the detector is shown to display the uniform set of points used to identify events which are near the edge of the detector where the point at the edge of the detector are ineffective.

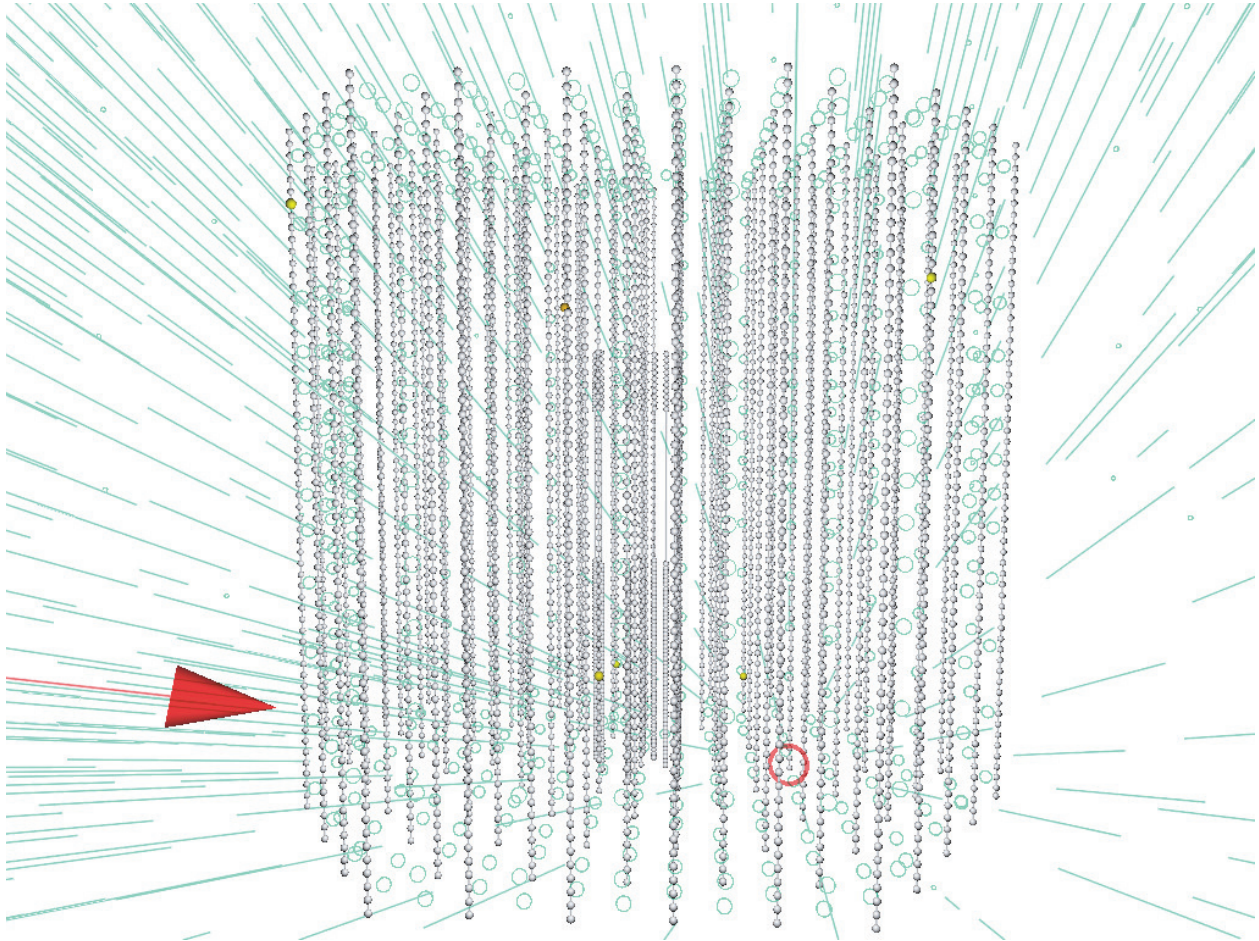


Figure 9.13: Figure 1 of 3 depicting how the tracks in the coarse veto are constructed to move through the holes in the detector. All the tracks converge through the COG of the event at the same time to preserve the information from the hits.

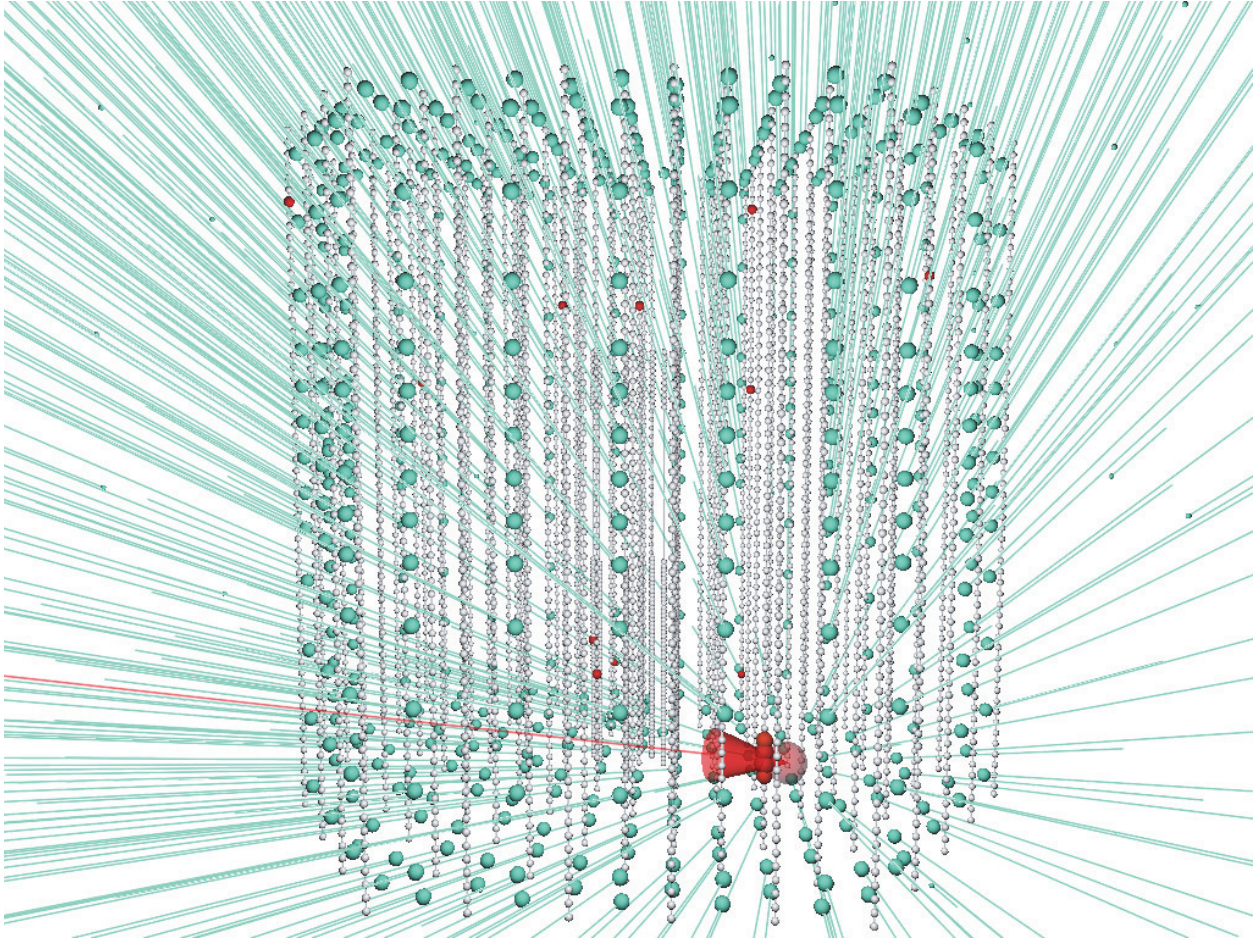


Figure 9.14: Figure 2 of 3 depicting how the tracks in the coarse veto are constructed to move through the holes in the detector. All the tracks converge through the COG of the event at the same time to preserve the information from the hits.

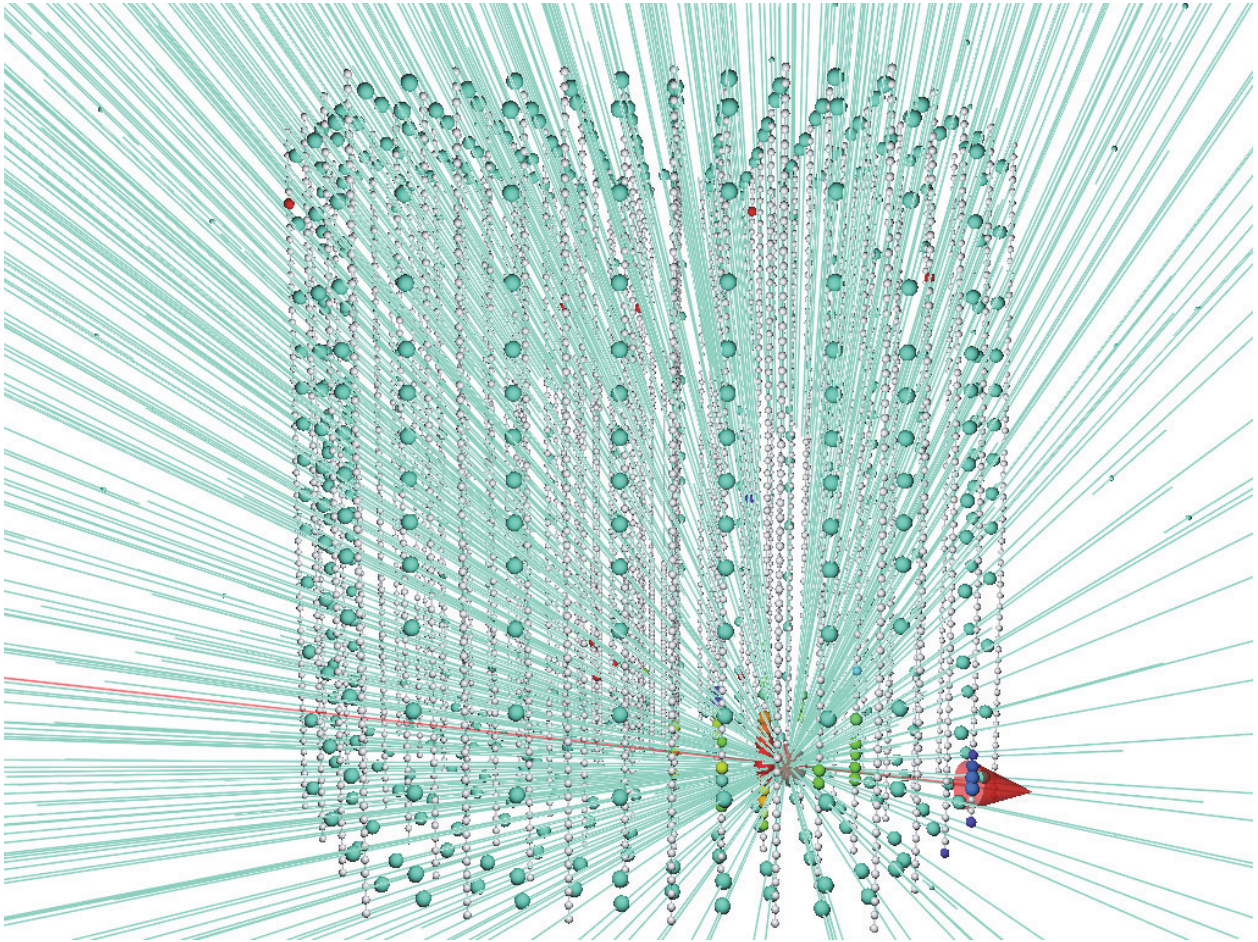


Figure 9.15: Figure 3 of 3 depicting how the tracks in the coarse veto are constructed to move through the holes in the detector. All the tracks converge through the COG of the event at the same time to preserve the information from the hits. The best fits from this set are likely to be the ones which agree with the original direction of the Monte Carlo track depicted as the red track.

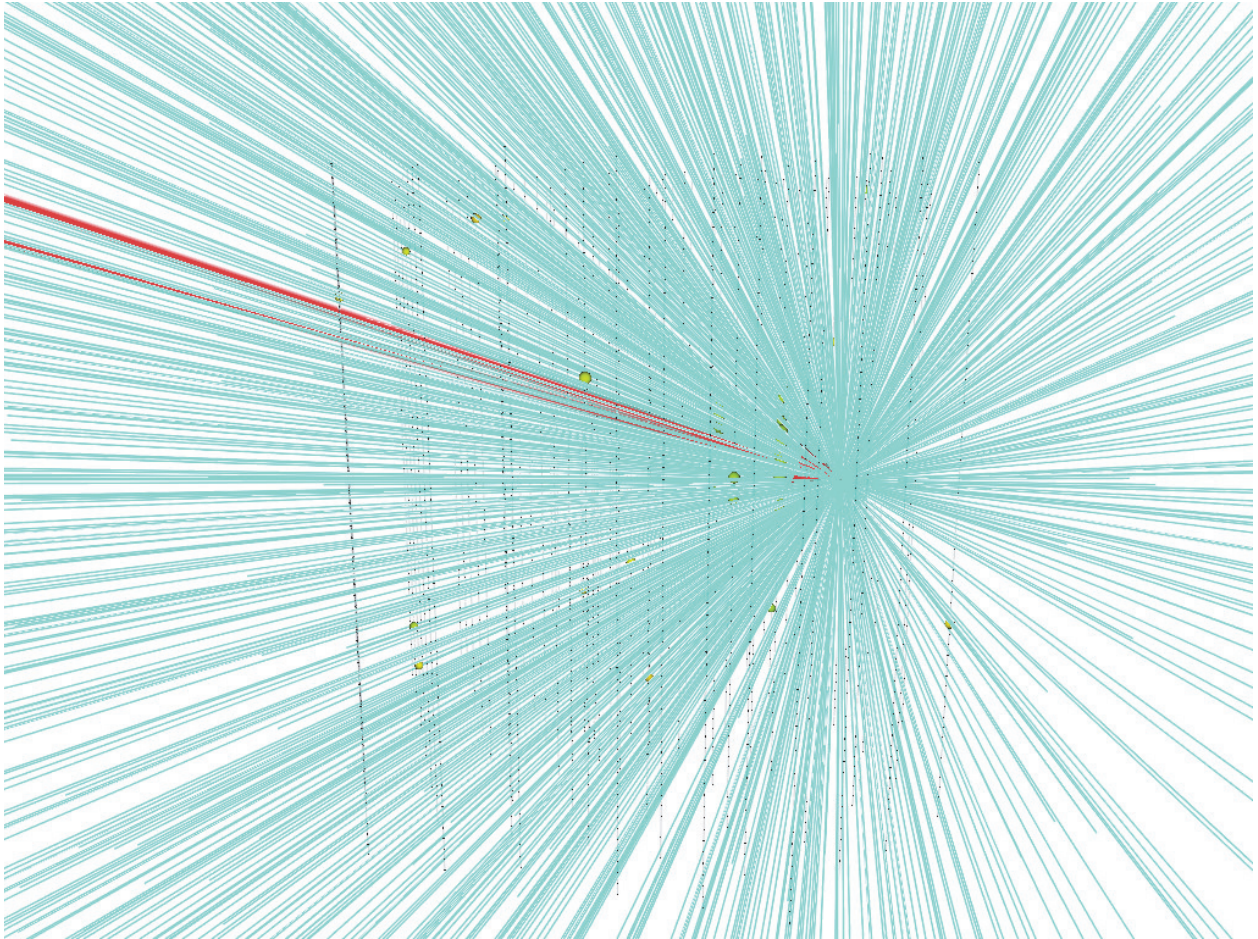


Figure 9.16: Side view of the tested tracks used in a different starting track event from that in Figures 9.13, 9.14, and 9.15.



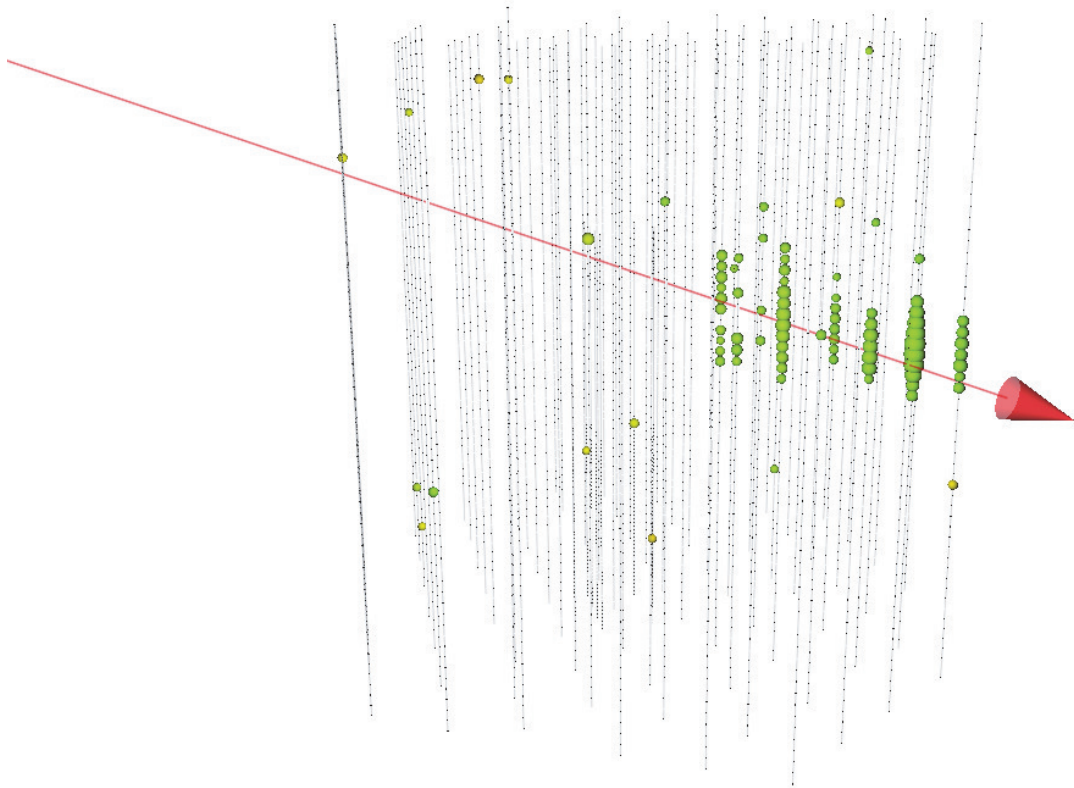


Figure 9.17: Event view of the best fit track found from testing all the hypotheses in Figure 9.16.

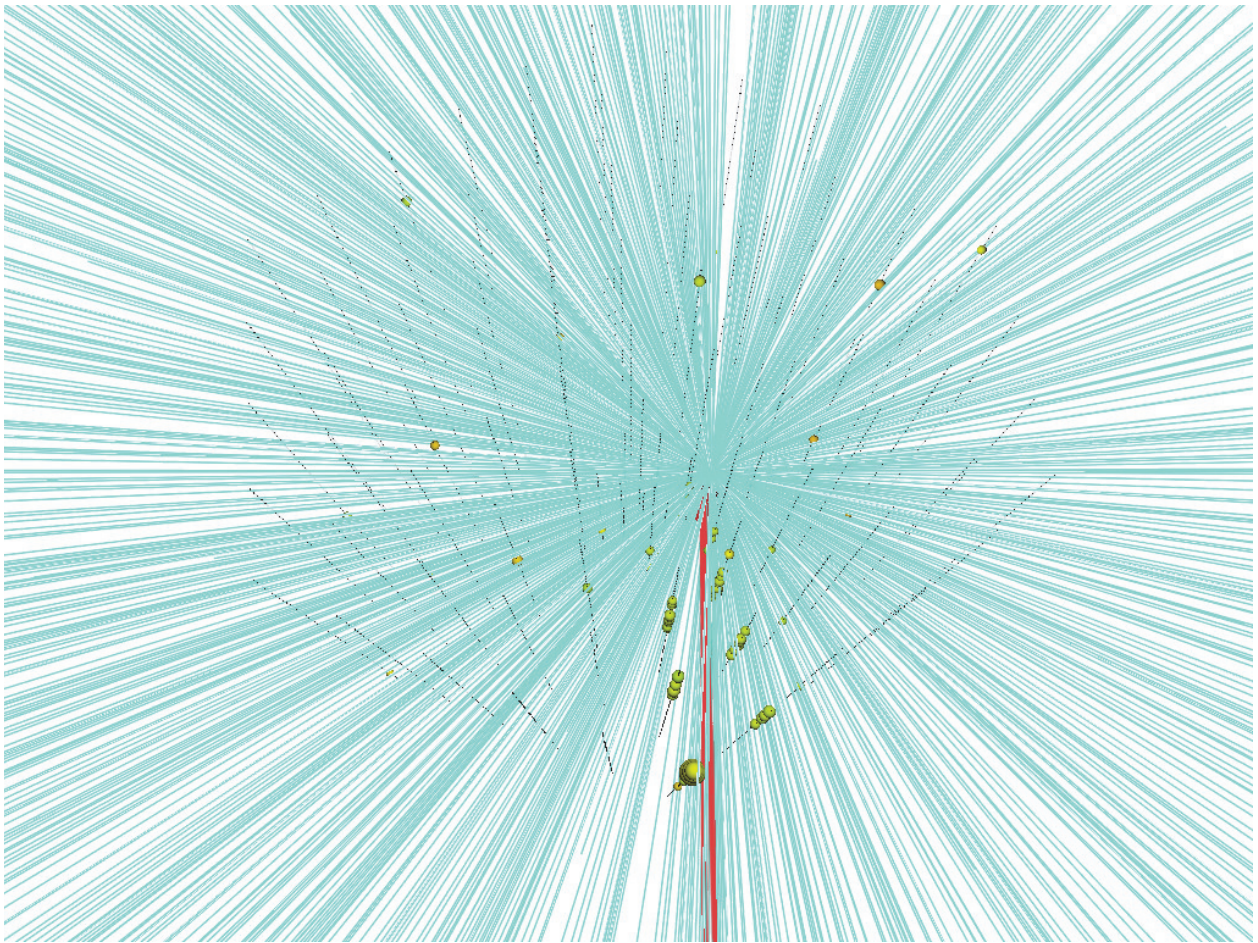


Figure 9.18: Top view of the tested tracks used on an incoming track event.

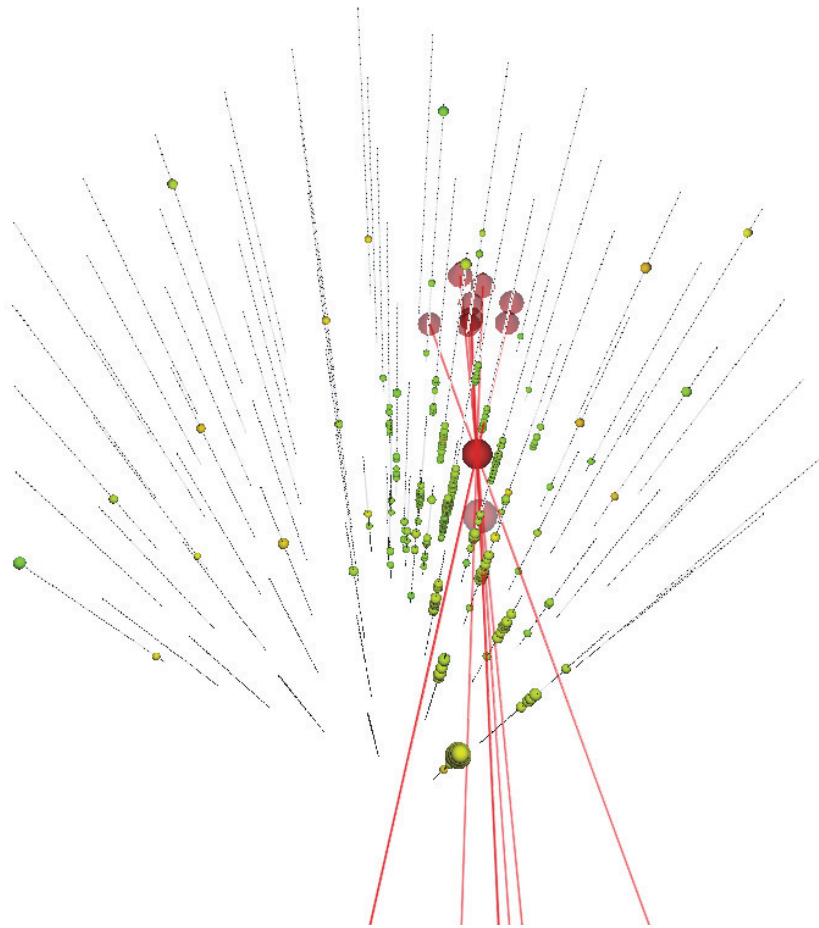


Figure 9.19: Event view of the best fit tracks found from testing all the hypotheses in Figure 9.18.

with this fit. The outcome is a reduced log likelihood (rlogl) for every track. Inspecting these fits for the lowest rlogl indicates which fit provided the best solution to the deposited hits. The solution which provides the best rlogl is used to determine if the event is on the edge of the detector. The edge of the detector is a problematic place for reconstructions since the observed hits are not symmetric. Without a reliable reconstruction, it is meaningless to apply the starting track veto, so these events must be removed from the selection. Events which have most of their hits on the edge of the detector cannot be reliably reconstructed and must be removed. Additionally, events which only have some hits on the edge of the detector, but are short also do not have reliable reconstructions. To remove these events the following criteria are constructed.

1. If more than 90% of the hits coincident in time with the track solution are on edge of the detector
2. If more than 5% of the hits coincident in time with the track solution are on edge of the detector and the muon region length is less than 500 m

If an event meets either criterion it is removed. If this edge cut is passed then the results of the incoming track veto are inspected. To give some leeway to coarse grid search, the fits where the rlogl is within 2% of the best rlogl are subjected to testing with the incoming muon veto. If any of the tracks have a muon region length shorter than 300 meters then the event is dropped. If the length is OK, all of the track's  $p_{miss}$  values are inspected for the lowest value. If this value is lower than 0.001 the event is kept, otherwise it is rejected. Events which have a value smaller than  $10^{-30}$  are passed on to the fine grid search while events which have a value larger than this have their fits within 2% of the minimal rlogl tested again using the segmented muon tables instead of the MIMI tables. These new resulting calculations are inspected for a muon region length over 300m and for the lowest  $p_{miss}$  value this cut requires the minimal  $p_{miss}$  be less than 0.00001. This cut leads to around an order of magnitude reduction in the incoming muon rate is achieved at each cut while the starting event rate is minimally affected.

### 9.2.2.1 Applied Cuts

1. Run SplineMPE fit for each of the hypothesized tracks
2. Determine the fits which have an rlogl value within 2% of the minimum rlogl, these are the best solutions
3. Run incoming muon veto with MIMI tables on the best solutions
4. All of the best solutions must have a muon region length over 300 meters as reconstructed by their incoming muon veto
5. All of the best solutions must have a  $p_{miss}$  value less than 0.001 as reconstructed by the incoming muon veto

6. If there is a solution whose  $p_{miss}$  value from the incoming muon veto is less than  $10^{-30}$  then it forgoes the next steps, otherwise
7. Run incoming muon veto with segmented tables on the best solutions
8. All of the best solutions must have a muon region over 300 meters as reconstructed by the incoming muon veto
9. All of the best solutions must have a  $p_{miss}$  value less than 0.00001 as reconstructed by the incoming muon veto

### 9.2.3 Fine Grid Search

The main goal of the cuts described here are to remove events which passed DOMs in the detector without leaving any hits and events where existing reconstructions are wrong. The coarse grid search handled the broad case of looking at all the holes in the detector. The fine grid search is used to search the local space of the best rlogl reconstruction for each event. To do this, small variations in position and angle are combined to search out the best fits. In Figure 9.20 is a sample true starting track to be inspected. All the fits defined are focused around the fit with the smallest rlogl found in the coarse grid search, shown as the line in Figure 9.20. First, as in the coarse grid search, the position of the COG is shifted 300 meters along the direction of the best coarse grid search fit (BCGSF). From here, variations (-50, -25, 0, +25, and +50) are defined as a cross along the x, y, and z axes of the detector. Next, the angle which moves the entry position of the BCGSF by 25 meters is found. Tracks are constructed with angular variations in zenith or azimuth of +/- 1x, 2x, 4x, 6x, and 8x for every position. All totalled, 1625 tracks are hypothesized for consideration and run through a time only SplineMPE fit. As with the coarse grid search, the track fits which have an rlogl within 2% of the minimal rlogl are run through the incoming muon veto, but this time only with the segmented muon tables. If any of the tracks have a muon region shorter than 300 meters or the smallest  $p_{miss}$  is larger than 0.00001 then the event is dropped. Figures 9.21 and 9.22 show the position variations and the angular variations respectively.

#### 9.2.3.1 Applied Cuts

1. Run SplineMPE fit for each of the hypothesized tracks
2. Determine the fits which have an rlogl value within 2% of the minimum rlogl, these are the best solutions
3. Run incoming muon veto with MIMI tables on the best solutions

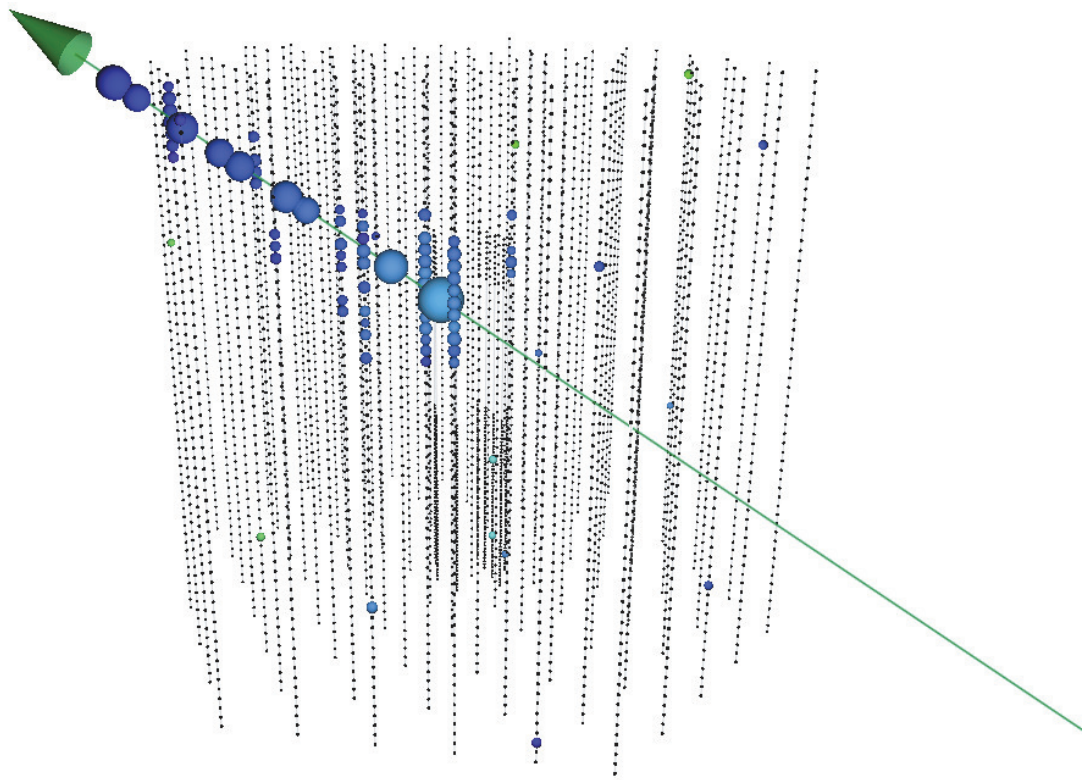


Figure 9.20: Event view of a starting track to be tested with the fine grid scan.

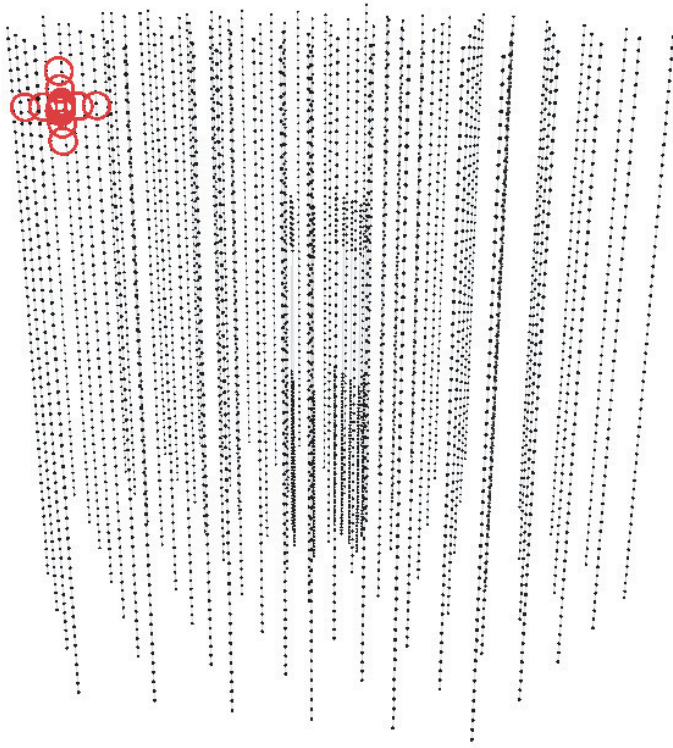


Figure 9.21: Depiction of the x, y, z axis cross for position variations of the fine grid scan.

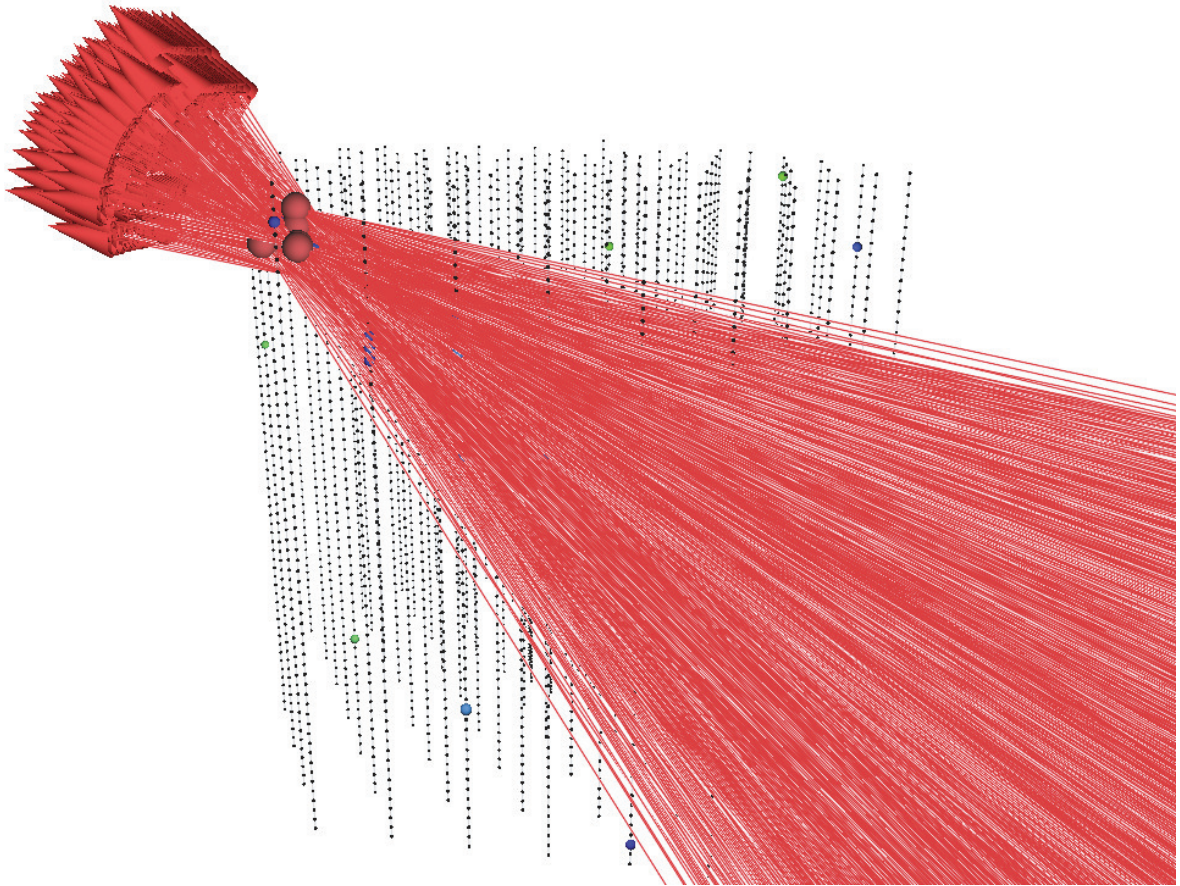


Figure 9.22: Depiction of the set of tested tracks in the fine grid scan for the event from Figure 9.20.



4. All of the best solutions must have a muon region over 300 meters as reconstructed by their incoming muon veto
5. All of the best solutions must have a  $p_{miss}$  value less than 0.001 as reconstructed by the incoming muon veto
6. If there is a solution whose  $p_{miss}$  value from the incoming muon veto is less than  $10^{-30}$  then it forgoes the next steps, otherwise
7. Run incoming muon veto with segmented tables on the best solutions
8. All of the best solutions must have a muon region over 300 meters as reconstructed by the incoming muon veto
9. All of the best solutions must have a  $p_{miss}$  value less than 0.00001 as reconstructed by the incoming muon veto

### 9.3 High Level Reconstruction

Events which pass the grid searches are at this point run through Millipede (see discussion of this algorithm in Section 8.3) to facilitate energy reconstruction later. No cuts are made on the output of Millipede at this point.

### 9.4 Final Cuts

After the grid searches, all the events left have the appearance of starting tracks. However, there are still over 6000 events per year expected from incoming cosmic ray muons. While they have a similar appearance to the true starting neutrinos, they are still different. To name a few differences, the penetrating muons are not able to "start" as deep in the detector as the neutrinos, neutrinos tend to have a bright start due to the hadronic interaction, and penetrating muons tend to be lower quality events because they are often mis-reconstructions.

#### 9.4.1 Down-going Selection

The down-going region is the area where interesting new astrophysical events are likely to be found in this selection due to the atmospheric self veto. However, because of the down-going muon flux, it is also the hardest to purify to the final level. The down-going region is defined to be events with a Millipede zenith angle between 0 and 80 degrees. To get to the final level, some straight cuts and a boosted decision tree (BDT) are used.

### 9.4.1.1 BDT Pre-Cuts

Events can enter into the sample for BDT training and evaluation by being either high energy events with a bright start or a general high quality track. Before BDT pre-cuts there are 2300 CORSIKA events and 9.8 astrophysical neutrinos expected in a 4 year burn sample (also commonly called a the test sample) with 146 days of live time. After the cuts there are 960 CORSIKA events and 2.4 astrophysical neutrinos expected, with over half of the loss in neutrinos coming from the zenith cut to divide the up-going and down-going samples.

### 9.4.1.2 Applied Cuts

#### High Energy Events with a Bright Start

1. Millipede deposited energy  $> 5$  TeV
2.  $>50\%$  of the Millipede energy in the first 50m of cascades
3. Line Fit speed  $> .1$  m/ns
4. 250 m of Millipede losses
5. Largest  $p_{miss}$  from coarse and fine grid searches  $< 10 - 6$
6.  $<50\%$  of the charge on the edge of the detector
7. Average of 1 Millipede loss every 80 meters

#### High Quality Track

1.  $<30\%$  of charge on the edge of the detector
2. Millipede to Line Fit angular separation  $< 30$  degrees
3. Line Fit speed  $>.15$  m/ns
4. Millipede deposited energy  $> 1$  TeV

### 9.4.1.3 Boosted Decision Tree

In order to remove the final background events in the down-going region a boosted decision tree, the scikit-learn ada-boost implementation [107], is trained to separate the incoming muons from the true starting tracks. The BDT uses 15 raw variables and a classifier variable to separate the signal from the background. The raw variables can be seen in the Table 9.1. The classifier variable is derived from a set of if-elif statements which separate signal and background events. These statements derive from an earlier implementation of these final level cuts which also was able to separate signal from background, albeit with worse signal efficiency.

If an event evaluates to true on a statement, it is assigned the number from that statement, as shown in Table 9.2. Since the classifier is an if-elif chain, only one number can be assigned to each event. In this way the variable encodes previous knowledge for the BDT to take advantage of. The statements of the classifier variable are

Depth of entry position to the detector
Number of Millipede losses
Fraction of charge on the edge of the detector
Distance from the first Millipede loss to the closest edge of the detector
Total energy of Millipede losses
Number of fits tested in the coarse grid search
Fraction of energy in the first Millipede loss
Fraction of hits that are within -15 to +75 ns of the geometric time
Line Fit speed
Distance to the edge of the detector along the track
Length of the Millipede losses
$p_{miss}$ from infinite track calculation
$p_{miss}$ from segmented track calculation
Millipede zenith angle
Millipede to Line Fit zenith angle

Table 9.1: Table of the variables used in ESTES's BDT.

Classifier Statement	Assigned Number
Millipede energy > 15000 GeV	1
Loss density >= 60	5
Millipede length <= 200 m	6
Number of Millipede losses <= 3	7
Number of direct hits < 11	8
Number of direct hit strings <= 2	9
$P_{\text{miss inf}} \times P_{\text{miss seg}} < 10^{-50}$	11
Fraction of charge on border > .75 and length < 600	13
Fraction of charge on border > .2 and length > 350	14
$P_{\text{miss inf}} \times P_{\text{miss seg}} < 10^{-50}$ and distance from Millipede loss to border > 125	16
Millipede energy > 8000 GeV	4
$P_{\text{miss inf}} \times P_{\text{miss seg}} < 10^{-45}$	2
$P_{\text{miss inf}} < 10^{-8}$ and $P_{\text{miss seg}} < 10^{-8}$ and Millipede length < 400	15
Z of entry position in dust layer 0 > Z > -150	10
Z of entry position in top of detector Z > 450	12
All else	3

Table 9.2: Table of the variables used to construct the classifier variable.

The number assigned are not in numeric order so that cuts which identify background or signal better can be grouped together. The if-elif chain is defined in the order seen above. The settings for the BDT are

- Number of Trees = 5000
- Learning rate = 0.01
- Depth of trees = 3
- Minimum number of events to split a node = 2
- SAMME.R boosting algorithm

The weighted and unweighted contribution of each variable in the final BDT can be seen in the second and third columns of Table 9.3 respectively.

Variable Name	Weighted	Unweighted
Depth of entry position to the detector	0.070	0.057
Number of Millipede losses	0.104	0.049
Fraction of charge on the edge of the detector	0.008	0.035
Distance from the first Millipede loss to the closest edge of the detector	0.044	0.057
Total energy of Millipede losses	0.076	0.069
Number of fits tested in the coarse grid search	0.005	0.023
Fraction of energy in the first Millipede loss	0.166	0.115
Fraction of hits that are within -15 to +75 ns of the geometric time	0.055	0.061
Line Fit speed	0.043	0.079
Distance to the edge of the detector along the track	0.121	0.097
Length of the Millipede losses	0.049	0.051
$p_{miss}$ from infinite track calculation	0.044	0.063
$p_{miss}$ from segmented track calculation	0.042	0.050
Millipede zenith angle	0.043	0.057
Millipede to Line Fit zenith angle	0.066	0.064

Table 9.3: The weighted and unweighted separation gained by using cuts involving each variable in the BDT. This shows that the most important variables in the BDT are the fraction of energy in the first Millipede loss and distance to the edge of the detector along the track.

The BDT is trained on a signal set of muon neutrinos which undergo a charged current interaction and subsequent conversion to a muon with over 8 TeV of energy and a true zenith angle  $< 80$  degrees. The neutrinos are weighted to the best fit flux of the MESC result from Section 5.1.2. The background events are CORSIKA and MuonGun events, weighted to the H3a cosmic ray flux. The combination of MuonGun and CORSIKA presents double counting of single muon events, however, this is acceptable if the cut used at the end removes all the CORSIKA events present, leaving only MuonGun events to estimate background rates. To verify the BDT, two validation techniques are used together. First, the simulation set for signal and background are split into a test and verification sample (70% test, 30% verification). The verification set is held out until the final stage to provide an unbiased set to validate the final BDT on. The test set is used to explore the performance of the BDT under different settings. For this exploration, 10-fold cross validation

of the test set is used. K-fold cross validation is a common way to estimate the performance of a classifier without need for more simulation statistics. The idea is to break the existing set into K independent and roughly equal sub-sets. Each sub-set is then involved in the training of K-1 classifiers and the testing of the 1 classifier that did not participate. By doing this, an estimate of the classifier performance on unseen data can be obtained. Since there are K folds, the average and error of the performance is also obtainable. Figure 9.23 shows the figure of merit for the K-folds BDTs. The BDT is required to retain less than 1 background muon present per year (vertical black line in the figure). For all the cross validation BDTs, less than 20% of the astrophysical flux is lost by the BDT while less than 1 background event per year is expected. Comparable performance is also obtained for the held out verification sample, where only 10% of the neutrino signal is lost while  $< 1$  background event per year is expected from Monte Carlo.

Over-training is always a concern that must be checked when working with machine learning. Two ways to check for over-training have been used thus far. The first way is to verify that the accuracy of the training and validation converge as more simulated events are used in the training of the BDT, indicating that the training data is not over-fitting and generalizes well to unseen data. Figure 9.24 shows these curves for the BDT used by ESTES. Both agree well within the errors of the simulation sets used. The other way which has been tested to verify that the BDT is not over-trained is recommended by IceCube's pybdt user guide [108]. In the user guide, it is recommended to compare the distribution of the BDT output for the training and test sets with a KS test. KS test values which suggest compatibility of at least 1% don't need to reduce over-training. For the K-folds cross validation and final 30% validation, the smallest KS test value found is 0.35. The final check to perform is a comparison to data. For ESTES, a four year burn sample has been processed for comparison to Monte Carlo expectations. The cumulative distribution of the decision score is presented for different simulated event types in Figure 9.25. Events with a score  $< 0$  are more background-like while events with a score  $> 0$  are more signal-like. Looking from left to right, one can see the simulated background (blue histogram) is mostly around -1 but is offset in number from the burn sample (black histogram). This is because single muons are being double counted in the MuonGun + CORSIKA background estimate. The offset is consistent with the difference between CORSIKA and the burn sample. At a score of 0.075 the last CORSIKA event is removed and the expectation drops below 1 event per year. In testing, this was the place our cut (vertical black line) was found to be optimal. Above the cut the sample is dominated by neutrinos and the burn sample is in good agreement with the more numerous atmospheric neutrinos (cyan histogram). It is important to note that the score is representative of how likely an event is to be a starting neutrino track, not an astrophysical starting track. This means that nothing can be read out of the astrophysical neutrinos (red histogram) being sub-dominant to the atmospheric neutrinos for all scores. The optimal way to separate these two types is as a function of zenith angle and energy. Assuming the MESC best fit spectrum, over two astrophysical neutrinos are expected in the burn sample.

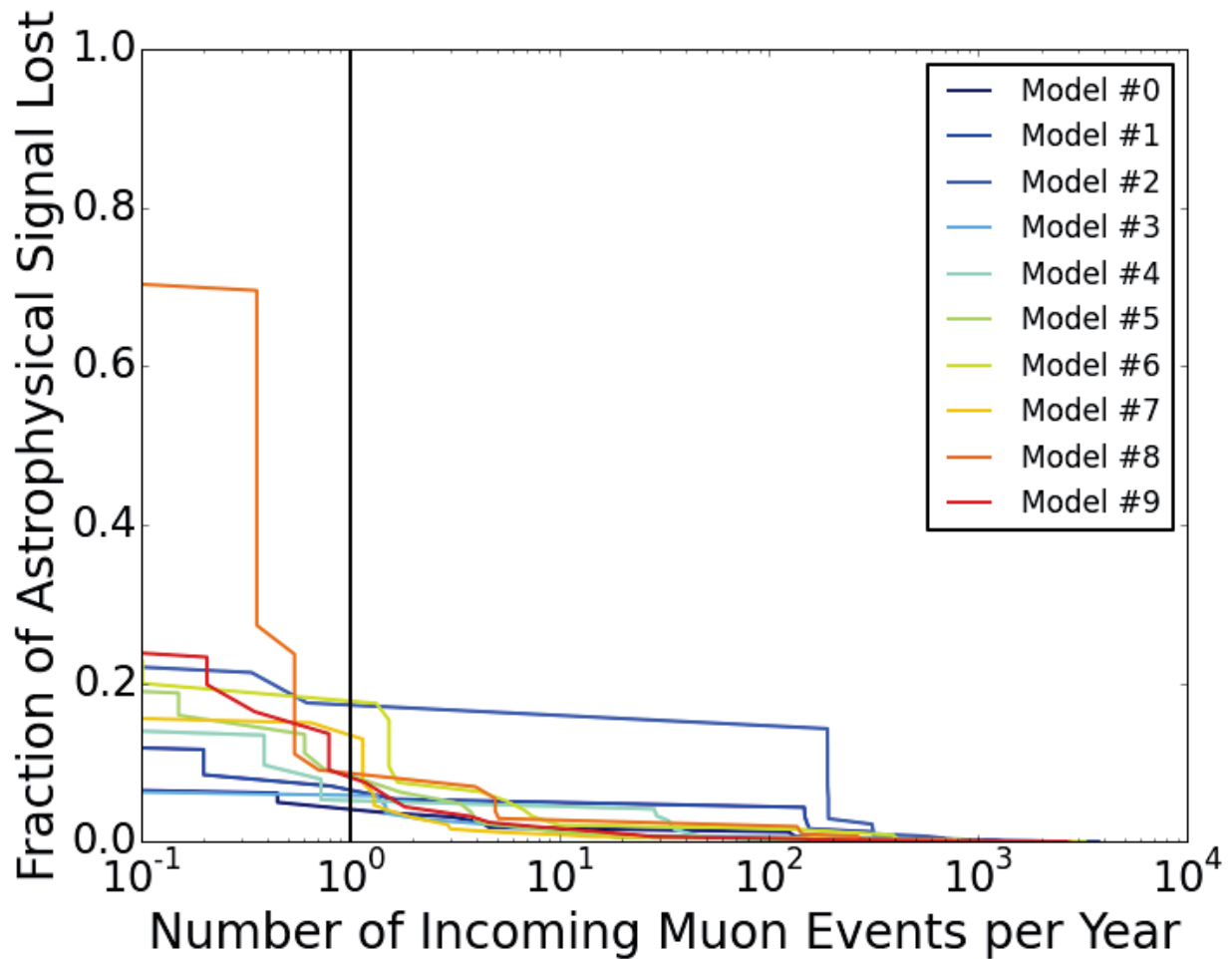


Figure 9.23: A plot of the fraction of astrophysical signal that is lost for different cut values of the BDT. These cut values also have a number of kept incoming muons found per year. This value is plotted for every model in the K-Folds testing. The analysis should have less than 1 incoming muon a year for purity, so a signal loss of around 10% is expected.

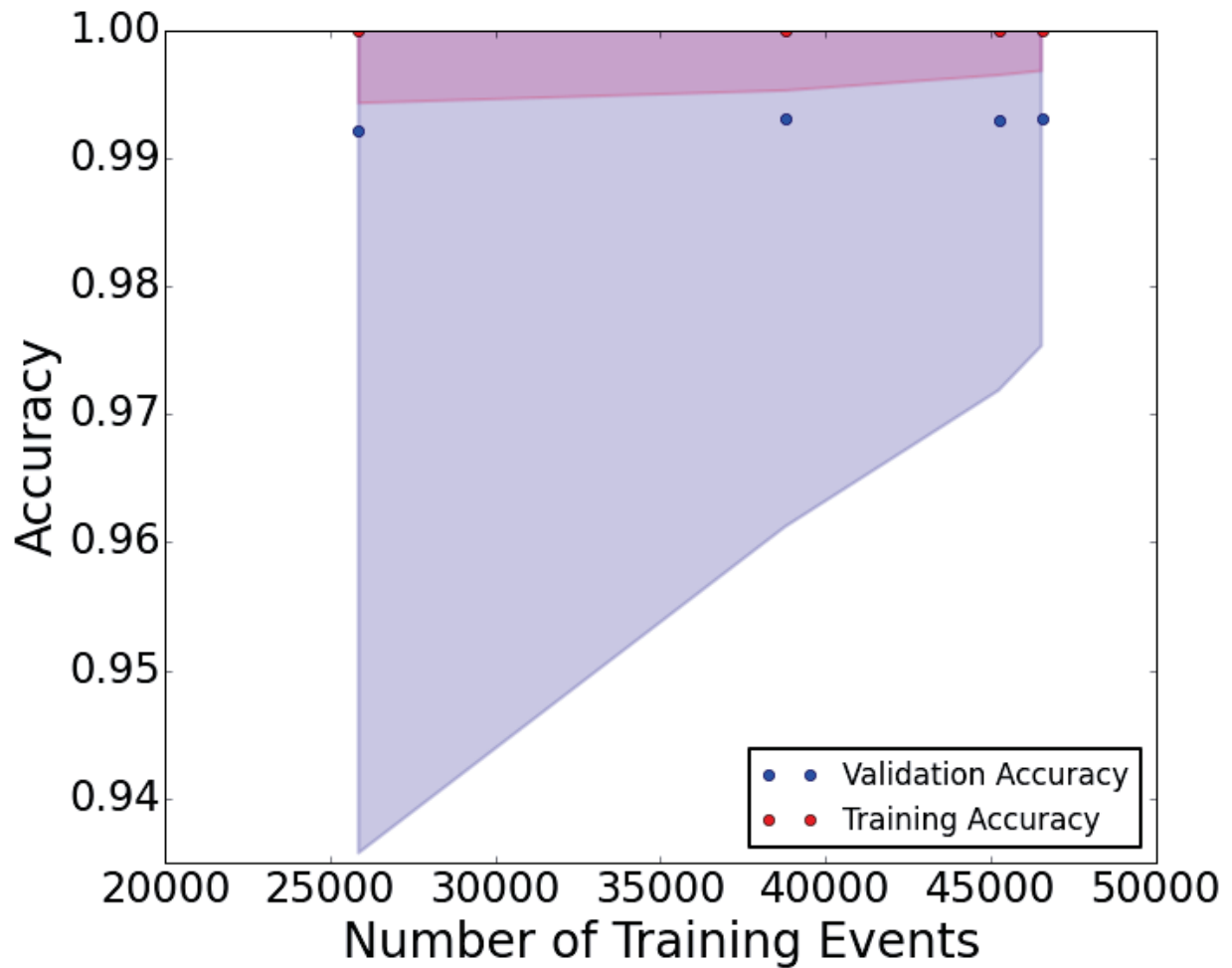


Figure 9.24: A validation of the training of the BDT. The validation set's accuracy (mean shown as blue points and error shown as shaded blue area) should overlap with the training sets accuracy (mean shown as red points at 1 and error shown as shaded red area). If these curves overlap it's an indication that nothing new is being found when the BDT is validated.



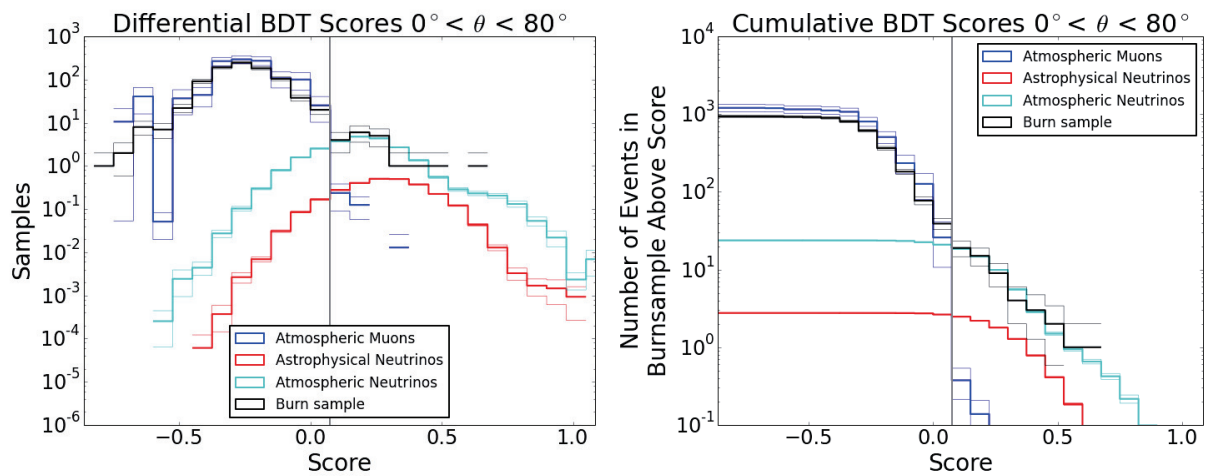


Figure 9.25: The differential(left) and cumulative(right) distribution of the decision scores from the BDT. The negative decision scores are largely background events in the blue histogram from atmospheric muons, while the positive decision scores are largely starting neutrino events in the cyan histogram from atmospheric neutrinos. Also plotted is the burn sample as the black histogram. The black curve matches well with the cyan histogram above the cut value shown in Figure 9.23. Below the blue histogram is offset because of double counting of single muons in CORSIKA and muon gun.

#### 9.4.1.4 Applied Cuts

1. Calculate variables for the BDT
2. Remove events which receive a value from the BDT less than 0.075

#### 9.4.2 Up-going Selection

In addition to the events in the down-going region, ESTES also keeps events in the up-going region. These events are kept for measuring the atmospheric neutrino flux with ESTES. This is quite important because the atmospheric self-veto is still under study and having the ability to measure its effect in a self-consistent way within ESTES will give confidence in models used to describe the self-veto. In contrast to the down-going region, the up-going region is relatively clean at this point. Only a few straight cuts are needed to remove the background muon events in simulation.

##### 9.4.2.1 Applied Cuts

1. Millipede zenith  $> 80$  degrees
2. Fraction of charge on edge of detector  $< 0.75$
3. Number of track reconstructions tested with the StartingTrackVeto  $< 10$
4. Millipede to Line Fit space angle  $< 10$  degrees
5. Average of 1 loss per 80 meters of track in Millipede reconstruction
6. Over 60 hits in the detector on non-DeepCore DOMs

#### 9.5 Event Rate At Different Cut Levels

Applying ESTES to different types of simulation allows estimates of the event rates to be made. These rates are collected in Table 9.4 for the major cuts of the selection. Each of the reported cuts reduces the number of atmospheric muons per year by over two orders of magnitude while the astrophysical flux is reduced by just over two orders of magnitude after all the cuts.

Cut	Atmospheric $\mu$ Rate (Hz) Number per Year	Atmospheric $\nu_\mu$ Rate (Hz) Number per Year	Astrophysical $\nu_\mu$ * Rate (Hz) Number per Year
All Filters	$2.31 \times 10^3$ $7.29 \times 10^{10}$	$1.70 \times 10^{-2}$ $5.36 \times 10^5$	$1.5 \times 10^{-4}$ $4.75 \times 10^3$
Filter and Charge Cut	$1.63 \times 10^1$ $5.15 \times 10^8$	$3.07 \times 10^{-4}$ $9.67 \times 10^3$	$2.12 \times 10^{-5}$ $6.68 \times 10^2$
Coarse Grid Cut	$1.01 \times 10^{-1}$ $3.20 \times 10^6$	$6.17 \times 10^{-5}$ $1.95 \times 10^3$	$2.17 \times 10^{-6}$ $8.56 \times 10^1$
Fine Grid Cut	$2.87 \times 10^{-4}$ $9.05 \times 10^3$	$1.66 \times 10^{-5}$ $5.22 \times 10^2$	$9.07 \times 10^{-7}$ $2.86 \times 10^1$
BDT Cut	$2.54 \times 10^{-8}$ $8.00 \times 10^{-1}$	$5.07 \times 10^{-6}$ $1.60 \times 10^2$	$4.46 \times 10^{-7}$ $1.41 \times 10^1$

Table 9.4: \*Astrophysical neutrino rates are derived using the MESC flux [68]. The cuts in the selection are very good at removing background while leaving some signal neutrinos for measurements.

## 9.6 Neutrino Energy Estimate

As was mentioned, Millipede is run on all the events, simulation or data, to facilitate energy reconstruction. Millipede reconstructs a sequence of energy losses (in the form of electromagnetic cascades) which have a light yield that best matches the observed hits. It is important to note that Millipede does not have knowledge of any of the underlying physics and uses an ice model without anisotropy. As a result a few modifications need to be made to the collection of output losses before energy reconstruction can be performed. Because Millipede does not know about muon physics, it assumes any loss is possible at any point along the hypothesized track. This is generally OK when losses have multiple DOMs surrounding them to make inferences with, but quickly degrades when losses are outside the detector. As a result some losses outside the detector and in the dust layer are overestimated in energy. To mitigate this, at least 2 DOMs within 75 meters of the loss must have a hit within 300 ns of the light travel time assuming the light travels directly from the loss to the DOM. This selection results in more reliable losses. Because of properties of the ice, the exact location of the reconstructed losses is often not well known. However, by compromising precision one can obtain good estimates of the energy lost along a segment of track.

This is illustrated for a simulated event in Figures 8.11, 8.12, 8.13, 8.14, and 8.15. Only the green histogram and light blue points need to be focused on for the following explanation. The images were constructed using a Millipede reconstruction on simulation with cascades available to Millipede every 5

meters. These cascades were then group into the specified size segments. As the size of the segments increases, the accuracy of the reconstructed energy per bin increases. By around 50 meters the reconstructed energy per segment is a good approximation of the true energy per segment. This 50 meter binning, starting with the first non-zero loss, is used the Millipede losses of ESTES. The energy losses reconstructed by Millipede are dependent on the underlying type of interaction. For a starting track there are two different processes to consider for the underlying energy losses, the hadronic shower at the neutrino interaction, and the stochastic losses of the outgoing muon. The energy distribution of both of these is related to the energy of the parent particle. As a result it is possible to relate the energy losses from Millipede to the energy of the parent particles. Statistically, we can phrase this as the following likelihood problem.

$$\text{minimize}_{E_\nu} \left( \sum_i^{\text{losses}} \log(p(\text{loss}_i|E_\nu)) \right) \quad (9.4)$$

This problem depends on knowledge of the distribution  $p(\text{loss}|E_\nu)$  which can be derived from the simulation at the selection's final level. Recall that it is important to consider the distributions of the processes separately. Figure 9.26 shows the distribution of the first loss energies for given neutrino energies. The lack of losses in the 0 bin are a result of starting the binning at the first non-zero loss. Figure 9.27 shows the distribution of the other loss energies for given neutrino energies. Both distributions show an upward trend in most probable loss energy with increasing neutrino energy. These distributions are quite wide and fold in information about the underlying selection. To help constrain the distributions it is important to note that  $E_\nu = E_{had} + E_\mu$  which tells us that constraints on  $E_{had}$  and/or  $E_\mu$  will focus the distributions to relevant neutrino energies. We have direct access to  $E_{had}$  via the energy of the first loss. There is no way to measure  $E_\mu$  directly since the muon exits the detector for the relevant energies. However the average energy lost per distance  $\frac{dE}{dX}$  which is a proxy for  $E_\mu$  can be measured. To apply the constraints, every reconstructed event has  $p(\text{loss}|E_\nu)$  constructed from events which have an  $E_{had}$  within 50% of the  $E_{had}$  of the event being reconstructed and a  $\frac{dE}{dX}$  within 50% of the  $\frac{dE}{dX}$  of the event being reconstructed. Additionally, the distributions of reconstructed losses with respect to the true losses are sensitive to the local ice properties so  $p(\text{loss}|E_\nu)$  is also only constructed with losses which overlap in z with the event being considered for reconstruction. As an example, consider the case of a 46362 GeV neutrino. The event has reconstructed 50 m regrouped losses of 13001, 68, 2, 169, 561, 0, 462, 771, 815, 0, 336, 43, 70, 291, 107, and 1893 GeV. This gives a constrain on  $E_{had}$  of 6500 - 19502 GeV and  $\frac{dE}{dX}$  of 3.73 - 11.19  $\frac{\text{GeV}}{\text{m}}$ . This yields the  $p(\text{loss}|E_\nu)$  distributions in Figures 9.28 and 9.29 for the hadronic and muon energies, which are focused to neutrinos between 20 and 70 TeV. Computing the LLH for all neutrino energies yields the distribution in Figure 9.30. The inferred energy is taken as the weighted average where the log-likelihood is used to weight the neutrino energies. The final result is an estimate of 35875 GeV for the neutrino in this case.

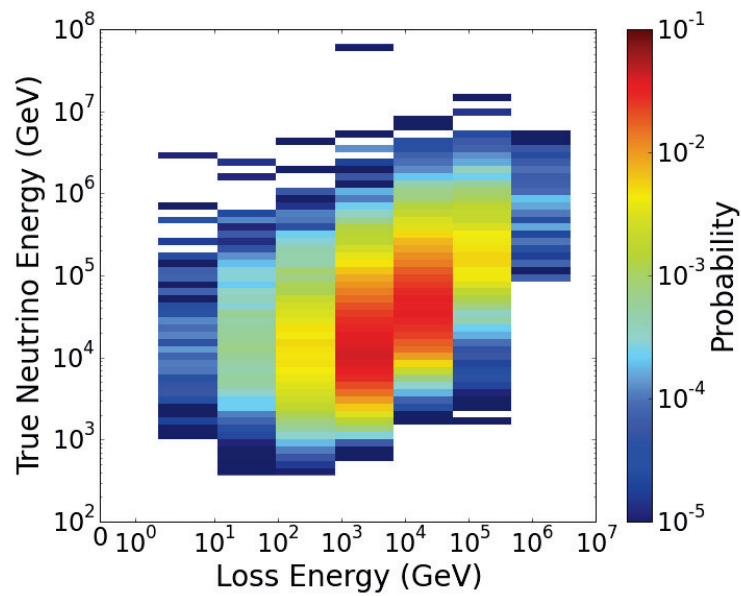


Figure 9.26: Probability distribution for the first loss reconstructed by Millipede, which represents the hadronic shower of a starting track with a contained vertex. There is a positive correlation between the shower's reconstructed energy and the true neutrino energy which is expected.

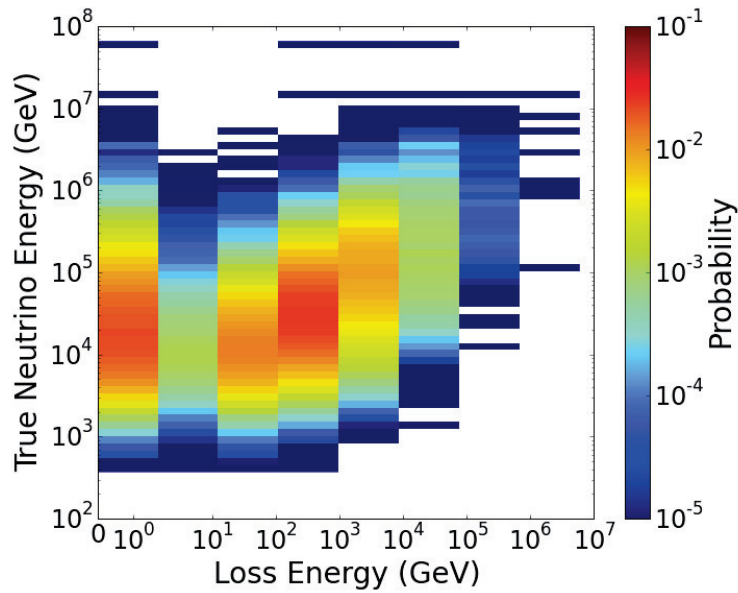


Figure 9.27: Probability distribution for the the losses after the first as reconstructed by Millipede. These losses represent the muon losses of a starting track with a contained vertex. There is a positive correlation between the losses reconstructed energy and the true neutrino energy which is expected. Additionally there is are a large number of occurrences of 0 which is a by-product of issues discussed in the section on Millipede issues (8.3.5).

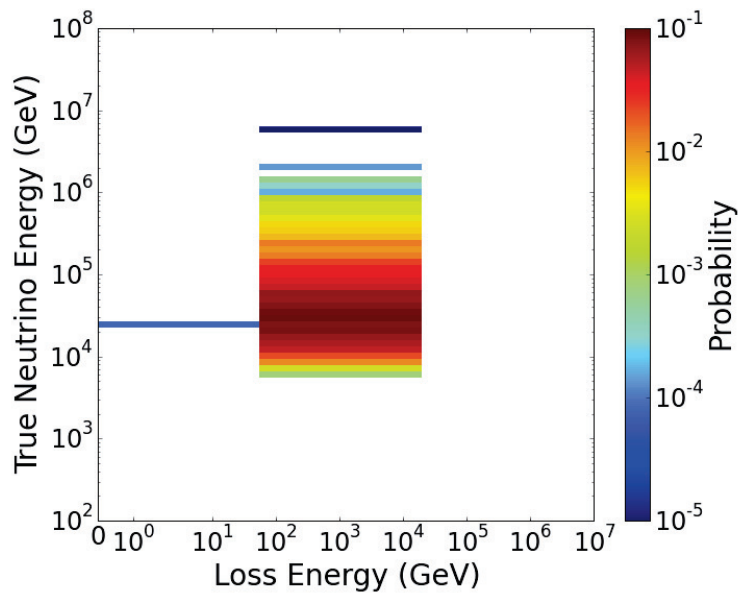


Figure 9.28: By conditioning the distribution on the energy of the hadronic and muonic components of the event a much tighter distribution is achieved.

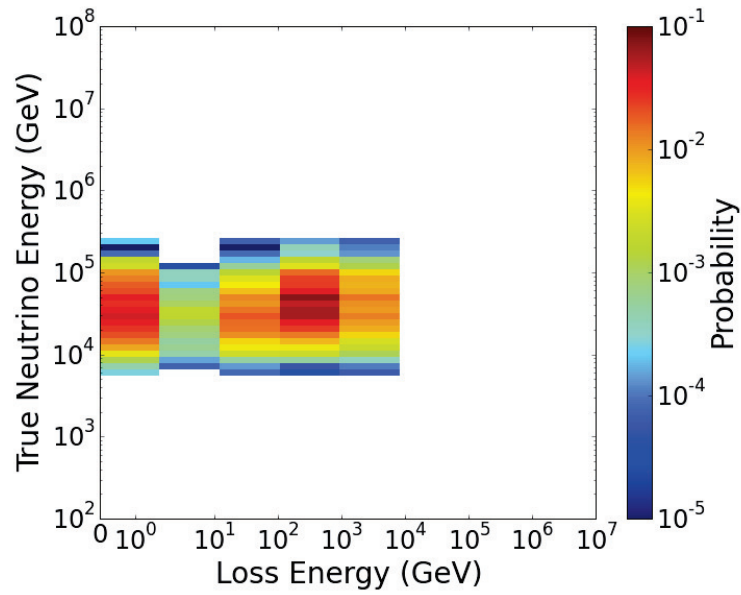


Figure 9.29: By conditioning the distribution on the energy of the hadronic and muonic components of the event a much tighter distribution is achieved.

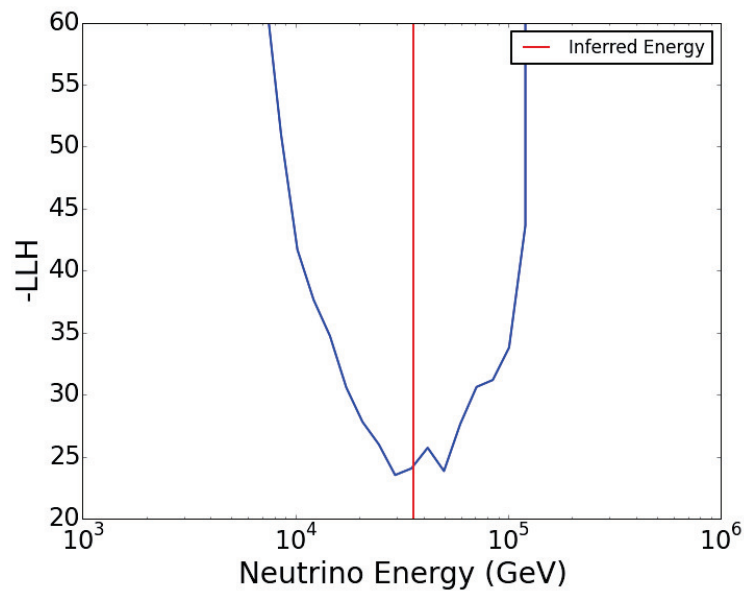


Figure 9.30: The negative log-likelihood distribution puts the event's energy between 20 and 70 TeV. A weighted average is used to obtain the inferred energy since the log-likelihood can have multiple minima.

## 9.7 ESTReS Filter

ESTES is an event selection designed to find useful starting tracks in archival IceCube data. However, discovering transient events can and must happen in real time if measurements from other experiments are of importance. ESTReS is a near realtime selection designed to run quickly online at the South Pole. Candidate events are subject to a few simple cuts and events which pass are considered candidates. These cuts are:

1. SplineMPE fit with zenith  $< 75$  degrees
2. Homogenized charge  $> 400$  PE
3.  $p_{miss} < 10^{-8}$  for a run of the Starting Track Veto run on the SplineMPE fit
4. Muon region length from Starting Track Veto  $> 450$  meters

This filter is expected to yield 3.5 candidates per day which are muons, 7.5 candidates per year which are atmospheric neutrinos, and 2.8 candidates per year which are astrophysical neutrinos. 2.4 of the astrophysical neutrino candidates should occur at or above the 50% purity point. All of these candidates are shipped to UW Madison via an iridium satellite link for farther processing. After arrival, the events are run through the entire ESTES selection described in this section. Since the start of the 2017 season on May 15th ESTReS has been actively running online at the South Pole. Through October 30th 2017, 409 events have been detected and flagged as candidates in 154 days. No ESTReS candidate events have passed the ESTES selection after the events arrive in the north for farther processing. There is no official plan for release of these events publicly, but it is likely the events will utilize the Astrophysical Multimessenger Observatory network (AMON) to issue alerts to other subscribing members [109].

## 9.8 Effective Area

After running the full ESTES selection on Neutrino Generator simulation, one can obtain the efficiency of the selection. This quantity is called the effective area. The effective area is an expression for how large your detector would be if it was fully efficient at detecting neutrinos which passed through it. Below two figures are presented. The first one, Figure 9.31, shows the effective area for uniformly spaced cosine bands of the zenith angle. Overall the selection has very little difference with respect to the direction of an incoming event. Recall that the selection is designed to find astrophysical neutrinos in the region above cosine zenith of 0.5 and above 10 TeV. The plot shows that 10 TeV is roughly the cross over point for the bands below and above cosine zenith of 0.5. Overall the selection achieves an effective area of 1 square meter by 20 TeV. Understanding if that is profound or not needs context. In Figure 9.32 ESTES is presented with other track searches in the southern sky, defined to be declination less than -30 degrees. Additionally, the IceCube point source selection in the up-going region is shown for context of the size of traditional incoming track



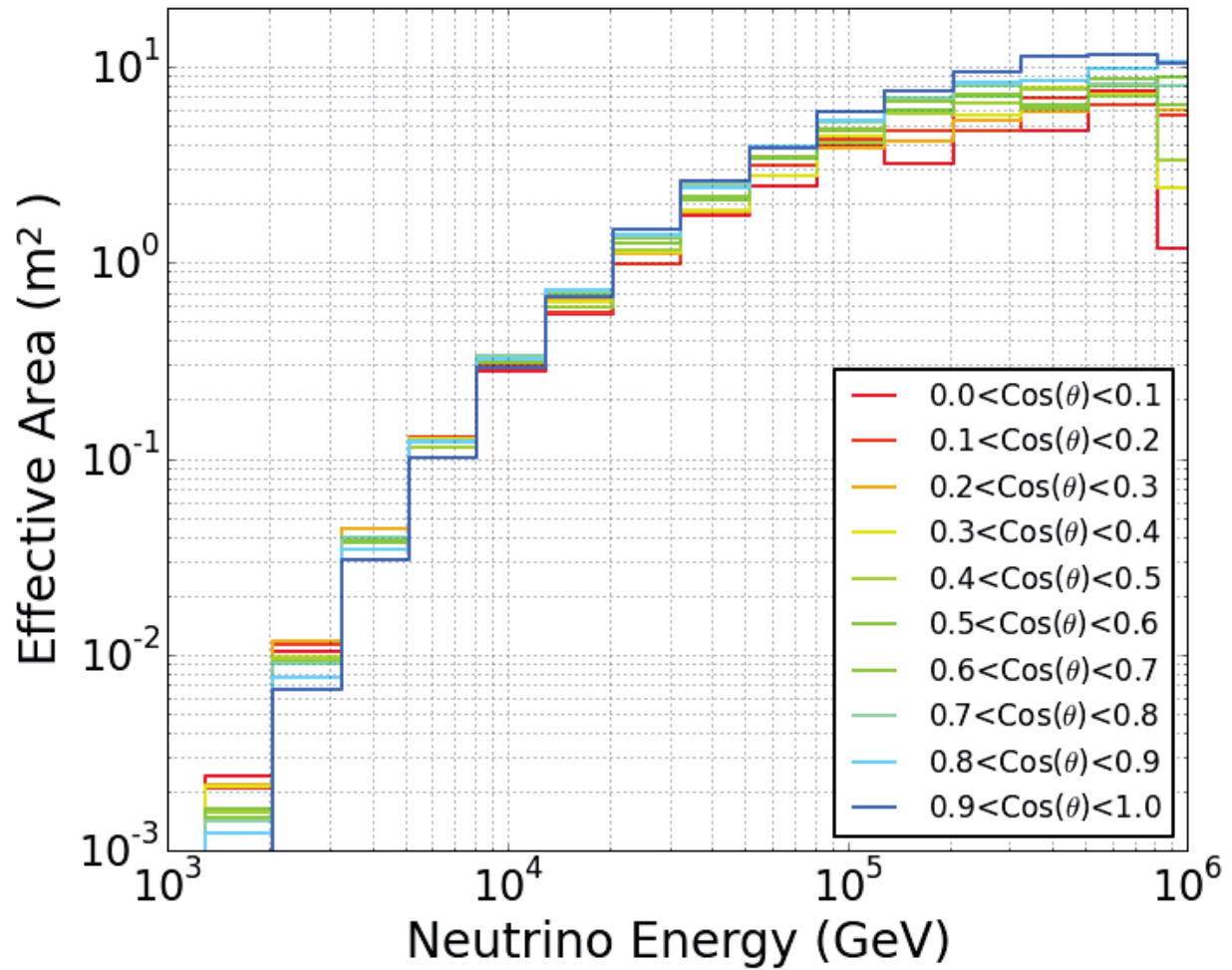


Figure 9.31: The effective area of ESTES as a function of the cosine of the zenith angle. The selection is rather agnostic to the direction of events due to the definition of the coarse and fine grid selections. The selection rises to around 100 TeV where the size of the detector begins being prohibitive to the veto definition and the selection obtains a fixed size.

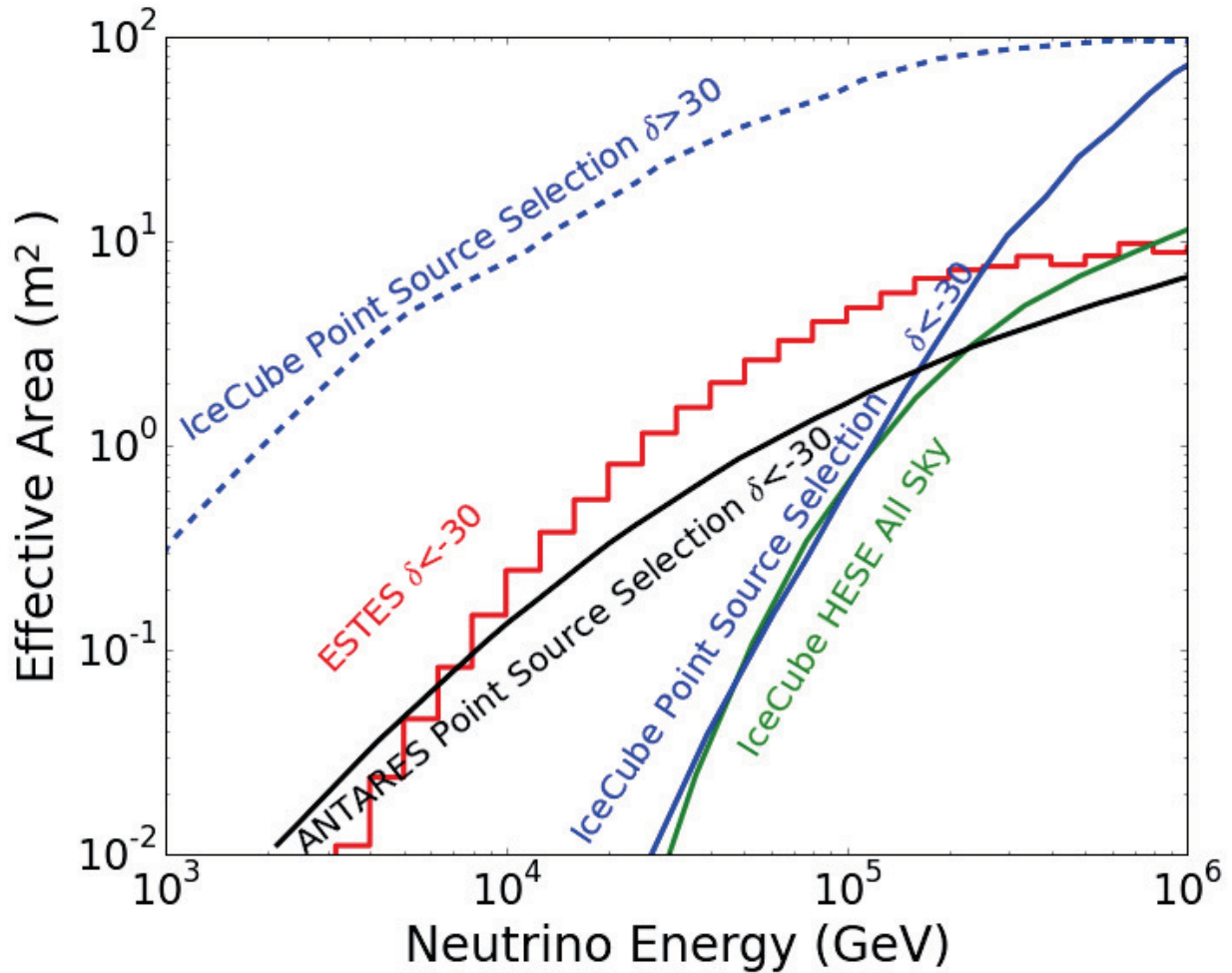


Figure 9.32: ESTES's effective area is shown with other selections for the southern most quarter of the sky. ESTES is the largest selection in this area, and has the lowest background of any selection. This makes ESTES a good selection for sources in this region. ESTES is roughly a factor of 10 smaller than the IceCube point source selection in the opposite hemisphere, but has a much lower background. This leads to ESTES having a competitive sensitivity to this larger selection in its own part of the sky.

selections. In this region ESTES has the largest effective area from around 8 TeV to 200 TeV with up to a factor 3 improvement. It is important to note that although the traditional incoming track selection is a factor of 10 larger, the background to signal ratio is also much higher (1000:1) when compared to ESTES (4:1). Not pictured but also relevant are the tracks from the MESC, see Section 5.1.2, which is being updated to 7 years of data. This selection also could measure tracks in this region of the sky, but due to background contamination has cut these tracks out. While ESTES might not be the largest selection in a large portion of the sky or over a large energy range, it hits a sweet spot for the declination and energy of hypothesized Galactic emission.

Recall that the ESTReS near realtime online filter also searches for neutrino candidates for fast inspection. Because of the limitations of near-realtime bandwidth only a few candidates per day can be sent north. This leads to a more stringent set of cuts than the full ESTES selection and as a result, a smaller effective area. The effective area for ESTReS is presented with the ESTES, HESE, MEST, and the extremely high energy (EHE) event selection effective areas in Figure 9.33. All of these selections, except ESTES, are run online to select realtime events. The only slight exception is the selection labeled MEST which is only used to verify that the HESE selection is running. ESTReS is by far the largest selection at energies below 200 TeV. By chance, the effective area of ESTReS stops becoming larger at the same energy the other selections overtake ESTReS in size. This makes the selections complimentary to each other in the search for transient neutrino events.

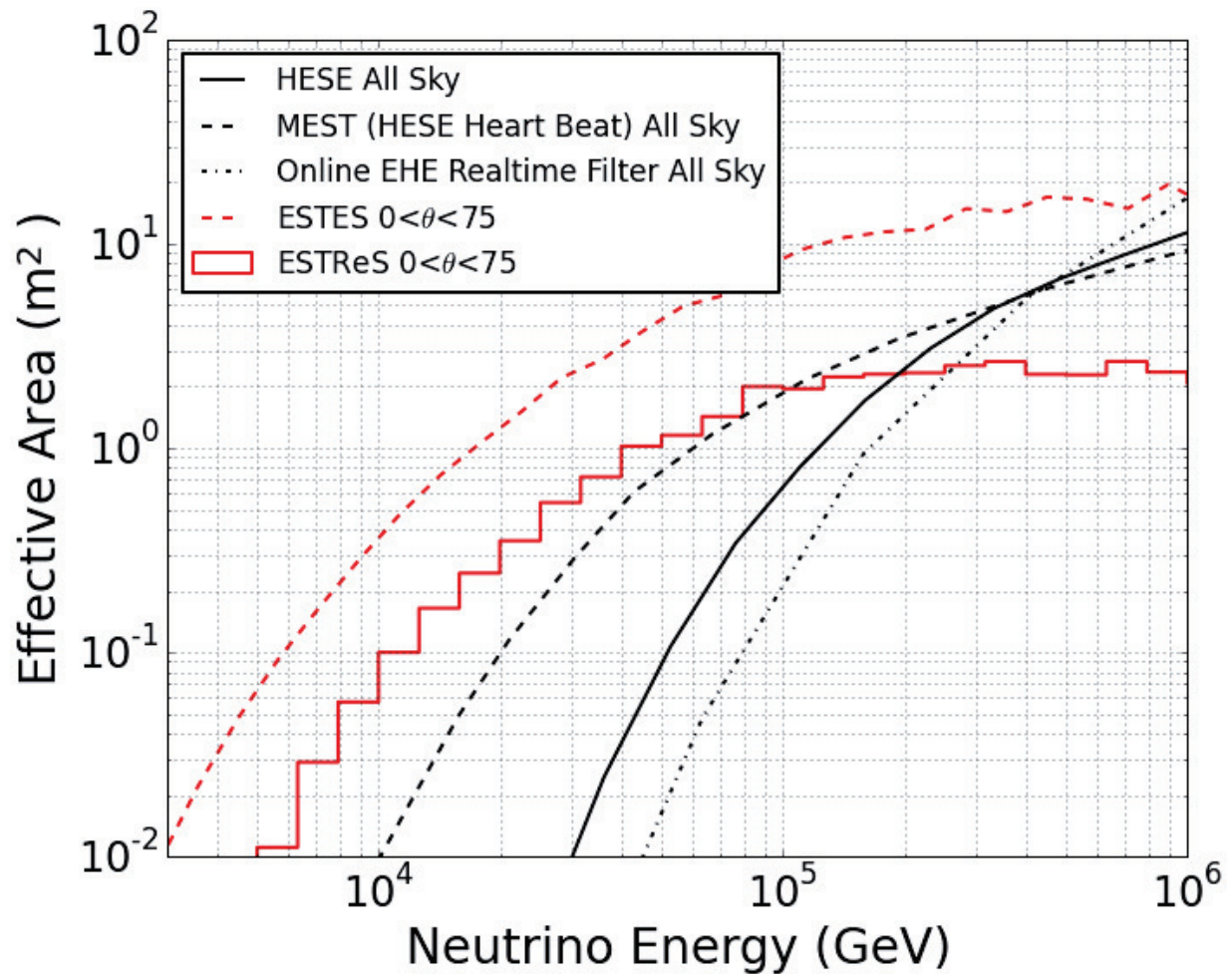


Figure 9.33: A comparison of the effective areas of existing online selections. Both the EHE and HESE filters send events in realtime while the MESE filter only sends basic information on an event to ensure that the HESE filter is running. Also shown is the ESTES effective area. The ESTReS effective area is smaller than the ESTES effective area, but this is because they are designed to do different things.

## Chapter 10

### Analysis, Results, Outlook, and Conclusions

This section will cover the events found by ESTES (see Chapter 9 for details) and the relevant results from these events. First, the properties of the dataset determined from simulation will be covered. After that, a comparison to the burn sample with fits and results will be presented. Finally projections for the final full sample will be discussed.

#### 10.1 Expectation From Simulation

The analysis of the events from ESTES will use forward folding. This means that in order to understand the results from data, simulation must be used. This event selection can include events of four different types that must be represented with appropriate simulations. In the up-going region, unaccompanied atmospheric neutrinos and astrophysical neutrinos are possible event source candidates. In the down-going region, bare astrophysical neutrinos, accompanied atmospheric neutrinos, and atmospheric muons must be considered. As was discussed in the simulation section (7), there are two ways to account for the accompanied atmospheric neutrinos in the southern hemisphere; neutrino generator simulations with the analytic self-veto from Chapter 4 applied and full atmospheric shower production with CORSIKA. The full shower treatment is a new option which is being pioneered in this thesis. As a result, the two will be compared in this section after a discussion of the general properties of neutrinos found with this selection.

##### 10.1.1 Angular Resolution

ESTES is an interesting selection in terms of the resolution for both the angular reconstructions and energy reconstruction. The angular reconstruction is an angular fit with Millipede, see section 8.3. This reconstruction is chosen because it is the only reconstruction which can properly describe the event morphology of a starting track and provide useful information for energy reconstruction as well. Since the events are contained, their length is constrained to be less than the geometric size of detector. Having a shorter length adversely affects the angular resolution an event can achieve. Figure 10.1 shows the angular resolution for different lengths of events. Events with a length over 400 meters have a resolution less than 2.5 degrees. For

context, IceCube's point source analysis has a resolution around .7 degrees for 10TeV through-going tracks and 2.5 degrees for starting tracks [110]. Below 400 meters the resolution quickly degrades.

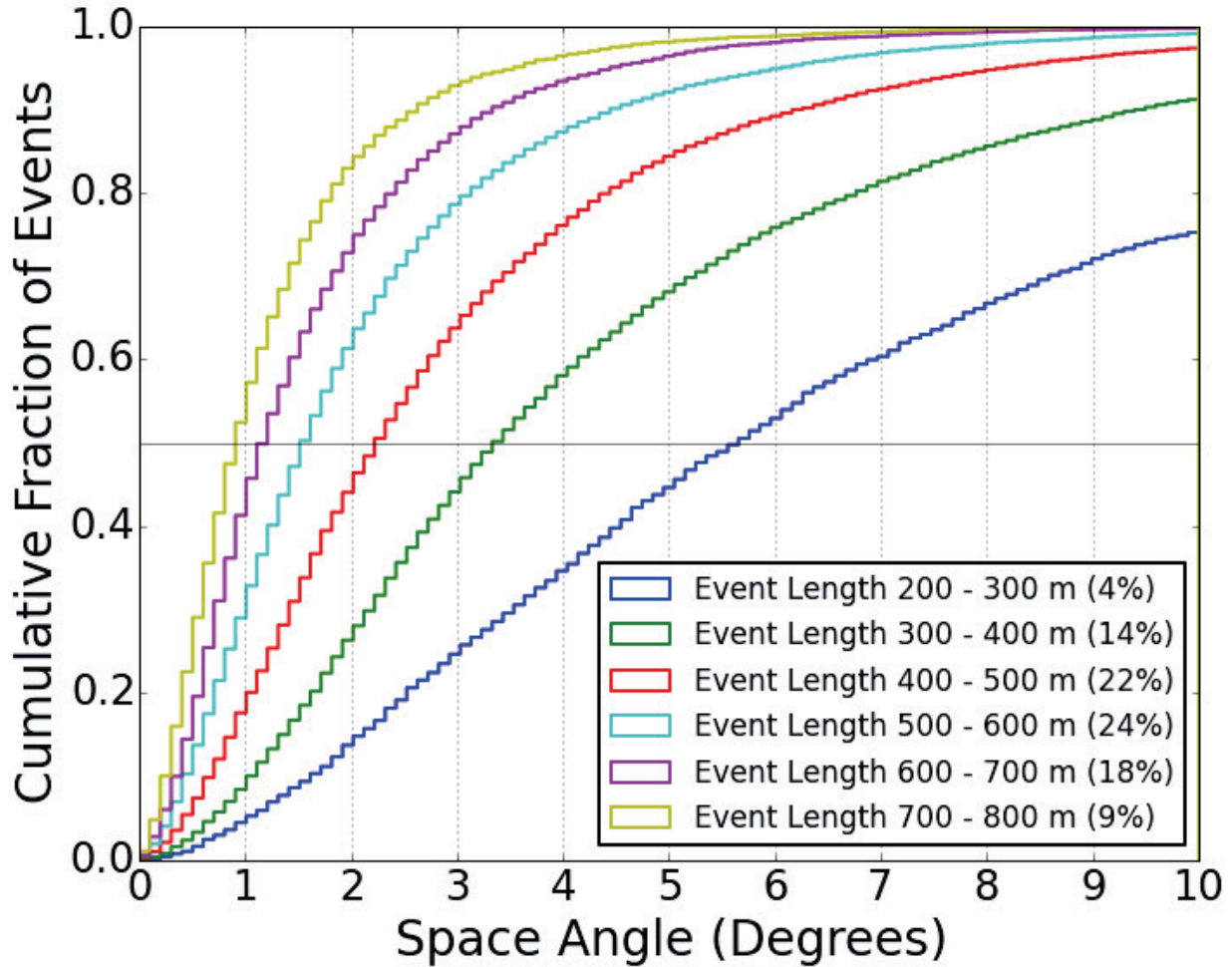


Figure 10.1: The angular resolution of a selection is given by its 50% crossing of the cumulative space angle distribution. This plot shows the angular resolution for various event lengths in ESTES. Over 50% of the events have a resolution better than 2.5 degrees.

### 10.1.2 Energy Resolution

Using the Millipede losses from the angular fit discussed above and the method outlined in Section 9.6 an energy estimate for each event is made. Because the estimate is composed of a contained loss which has an energy which can be determined calorimetrically and a muon whose energy can only be inferred by the loss rate before it exits the detector these events have an energy resolution which is a compromise between

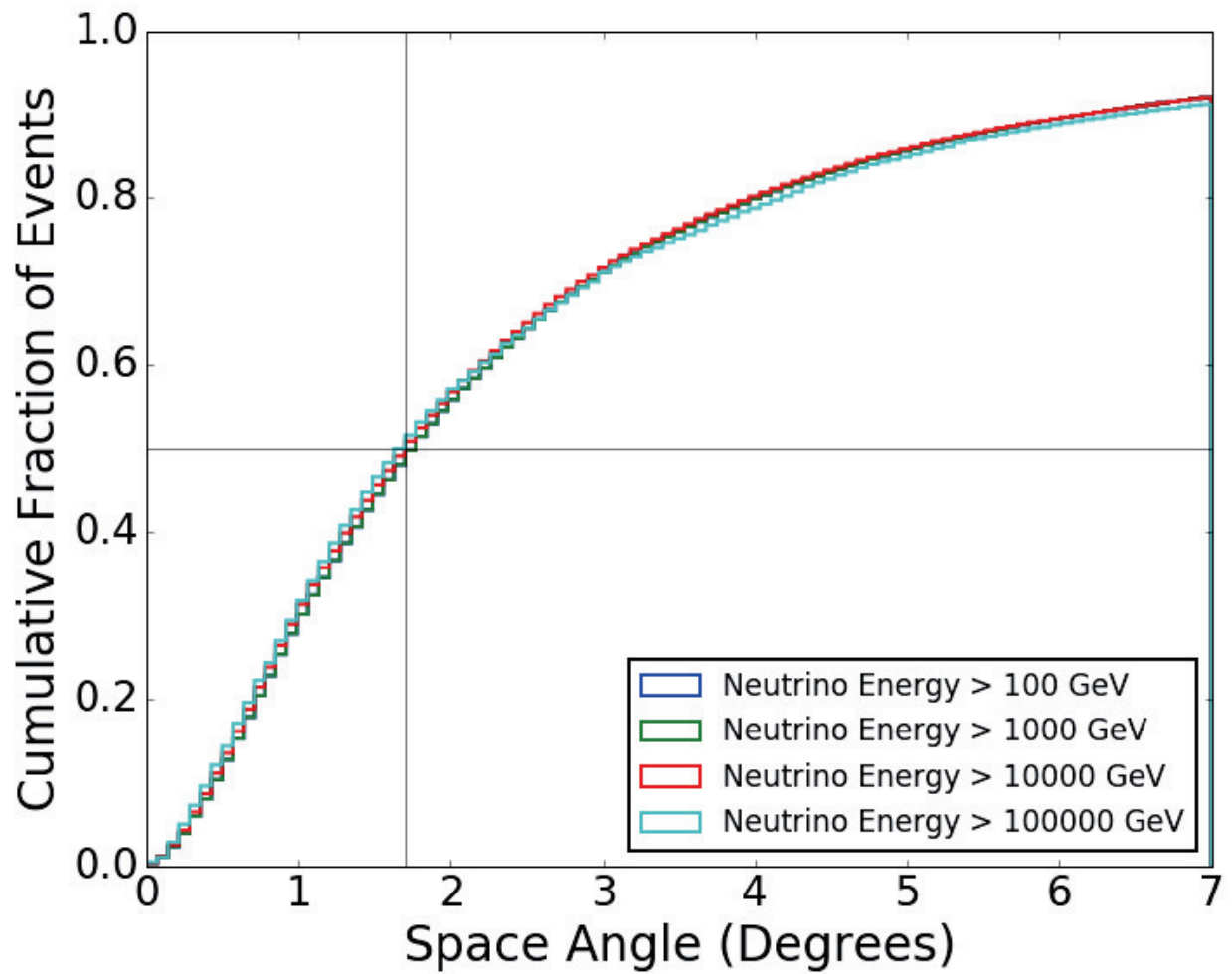


Figure 10.2: The median angular resolution of a selection is given by its 50% crossing of the cumulative space angle distribution. This plot shows the angular resolution is not strongly dependent on the energy of the event.

the two. Traditionally cascades which can be measured calorimetrically have a resolution of .15 in the log of the neutrino energy while muons which exit the detector have a resolution of .33 in the log of the muon energy. ESTES's energy resolution as a function of energy is shown in Figure 10.3. The fluctuations in the resolution are largely a result of low statistics and fine binning. Overall the resolution is around .23 in the log of the neutrino energy. Such a resolution plot is obtained in a standard way across IceCube analyses by

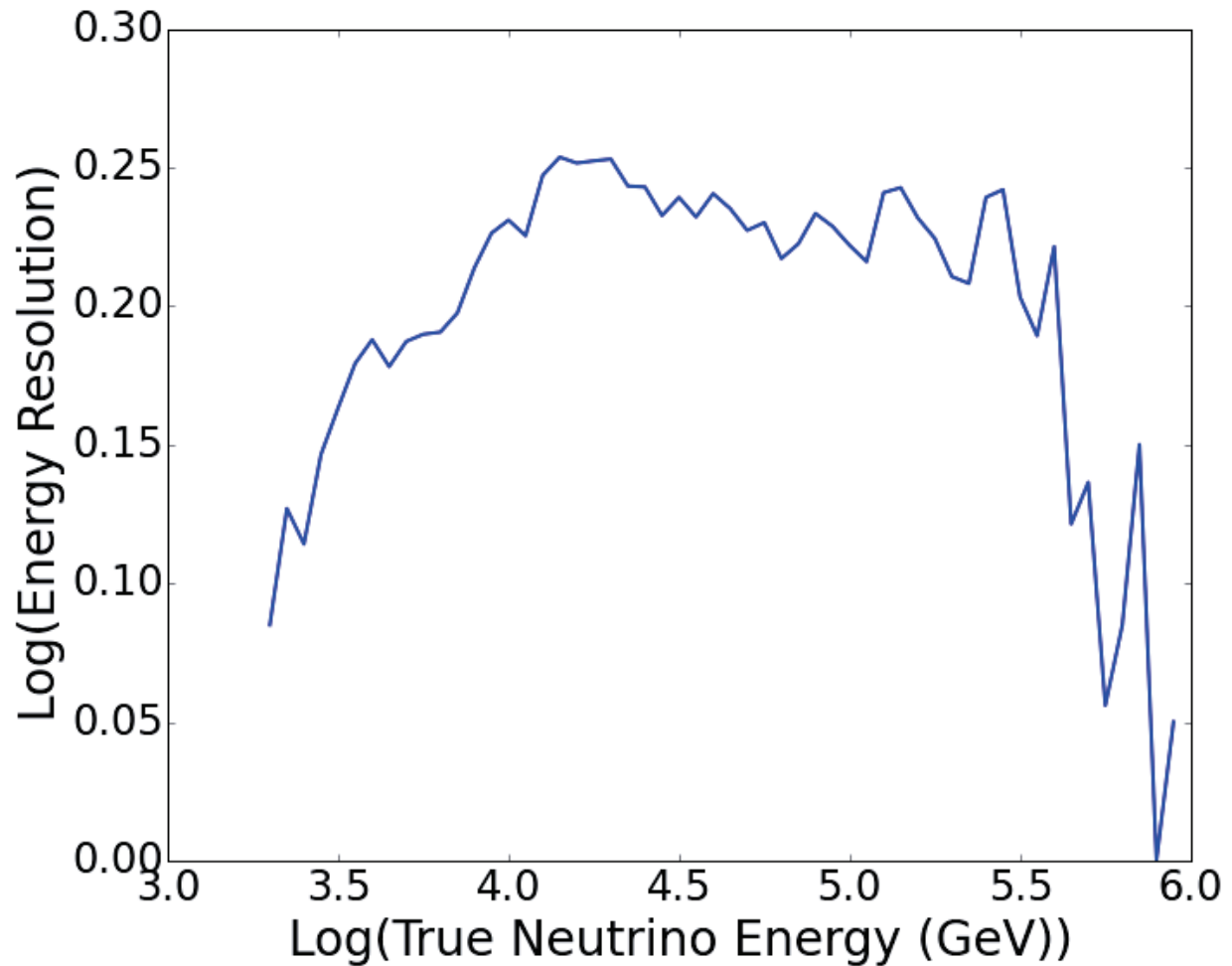


Figure 10.3: The energy resolution of ESTES as a function of neutrino energy. The resolution is around .23 in the log of the energy. This is better than what can be obtained by through-going muon energy reconstructions.

fitting a Gaussian to horizontal slices on Figure 10.4 and plotting the width parameter [99].



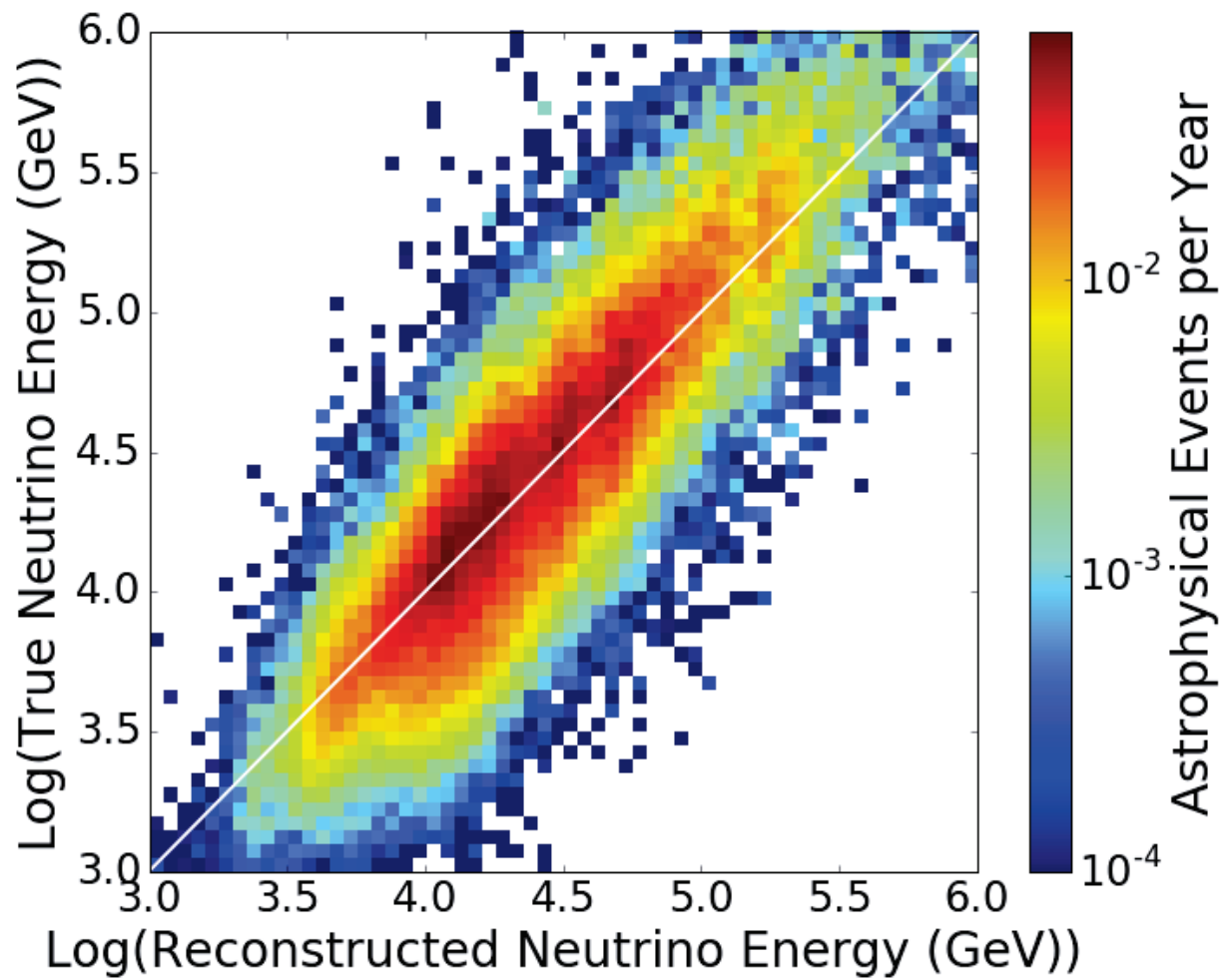


Figure 10.4: The distribution of true energy vs reconstructed energy. The positive correlation around the 1:1 line shows that the reconstruction is only slightly biased so it can be used as a direct proxy of the neutrino energy.

## 10.2 Events in the Burn Sample

Analyses in IceCube use 10% of all of the data as a validation sample for verification of results before the entire data set is used. This 10% sample is constructed by taking only runs that end with a 0. This amounts to the thesis using 15023354.7 seconds (0.47 years) of data for its burn sample, giving it roughly a half of a years worth of data to inspect and validate against. In total the burn sample contains 83 events with 31 having a zenith angle less than 85 degrees and 52 having a zenith angle greater than 80 degrees. A per year breakdown of the number of events from above and below 80 degrees is presented in Table 10.1.

	2012	2013	2014	2015	2016
<80°	4	6	5	4	10
>80°	9	13	9	9	12

Table 10.1: The number of events per year of burn sample which enter the ESTES selection in the regions above and below 80 degrees.

The events above 80 degrees are consistent with an average of 10.4 events per tenth of a year. The events below 80 degrees are consistent with an average of 4.75 events per tenth of a year for the first four years, the fifth year has 10 events, which happens by chance 1.4% assuming the number of events is a Poisson process with mean of 4.75. With only 85 events there are not enough statistics to make a diffuse fit or perform a meaningful point source analysis. However, it is still important to inspect the event’s energy distribution in interesting regions and get a feel for the event’s density in right ascension and declination.

Figure 10.5 shows the distribution of burn sample events in reconstructed energy and declination with their associated errors. The majority of the events have an energy around 10 TeV and come from near the horizon. Also depicted is the region where the atmospheric flux with self-veto applied is expected to yield less events than the astrophysical flux from the MESC analysis. There are three events which fall in this region in the burn sample. Event views and other information about these events is given in Appendix A. Figure 10.6 shows the distribution of events in Equatorial coordinates. Events below -20 degrees declination have the best astrophysical purity in the sample since most of the atmospheric background is removed. Above this, the self-veto effect is weakened and atmospheric neutrinos dominate around the horizon. Looking through the Earth, absorption in the Earth becomes relevant and the number of events again diminishes. Visual inspection for angular clustering yields no interesting coincidences.

The zenith distribution of the selections which utilize the neutrino self-veto is one of the most telling signatures of the veto’s presence. Figures 10.7 and 10.8 show the cosine zenith distribution of different atmospheric neutrino models, the astrophysical neutrino contribution from the MESC analysis, and the burn sample data. Contributions from the atmospheric muon flux are expected to be less than .5 events for

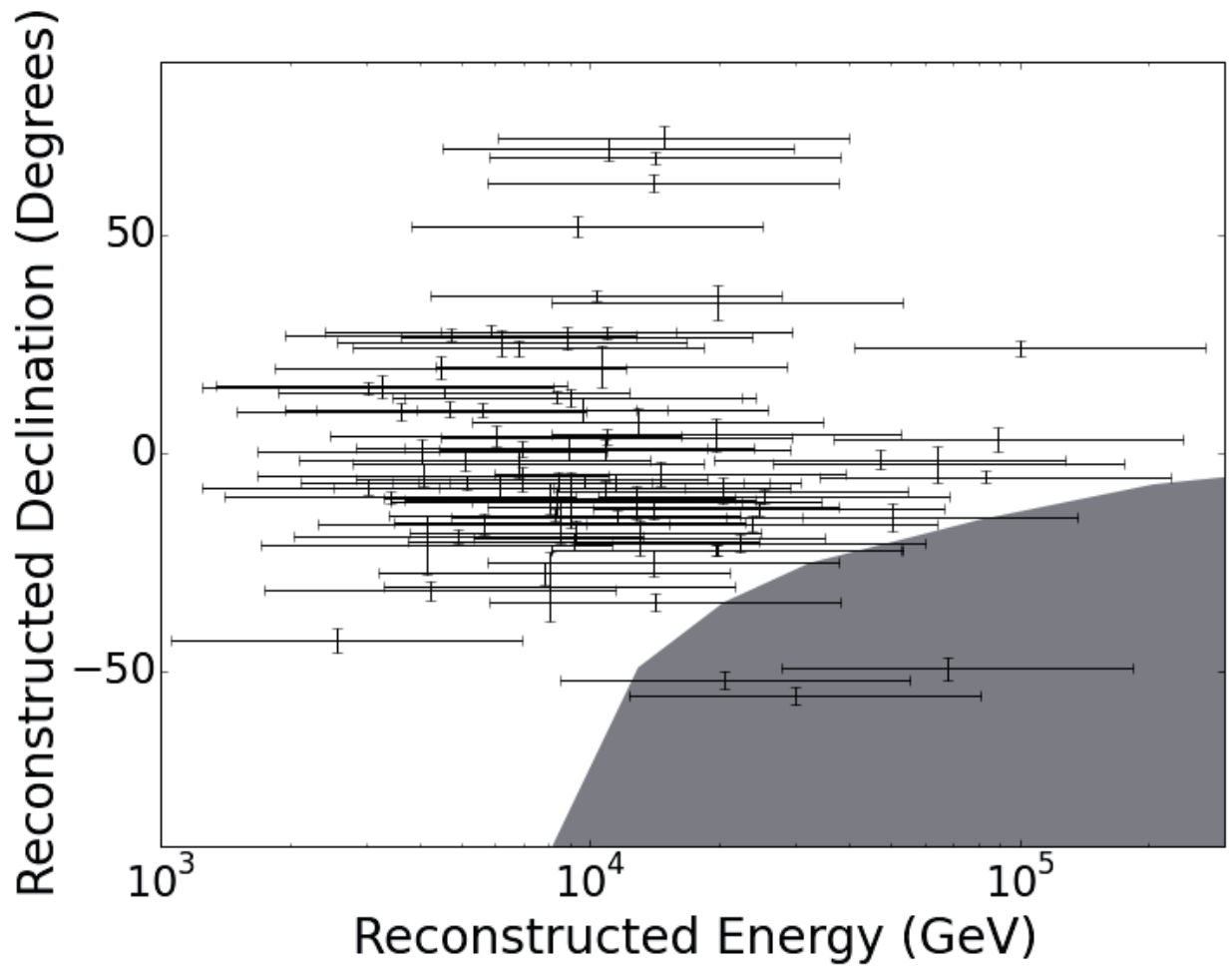


Figure 10.5: Distribution of events in reconstructed energy and declination with their associated error bars. Also included is a grey shaded region where the ratio of the astrophysical flux over the vetoed atmospheric flux is greater than 1. Events which fall into this region are likely from astrophysical neutrinos. All told there are three events which meet this criterion.

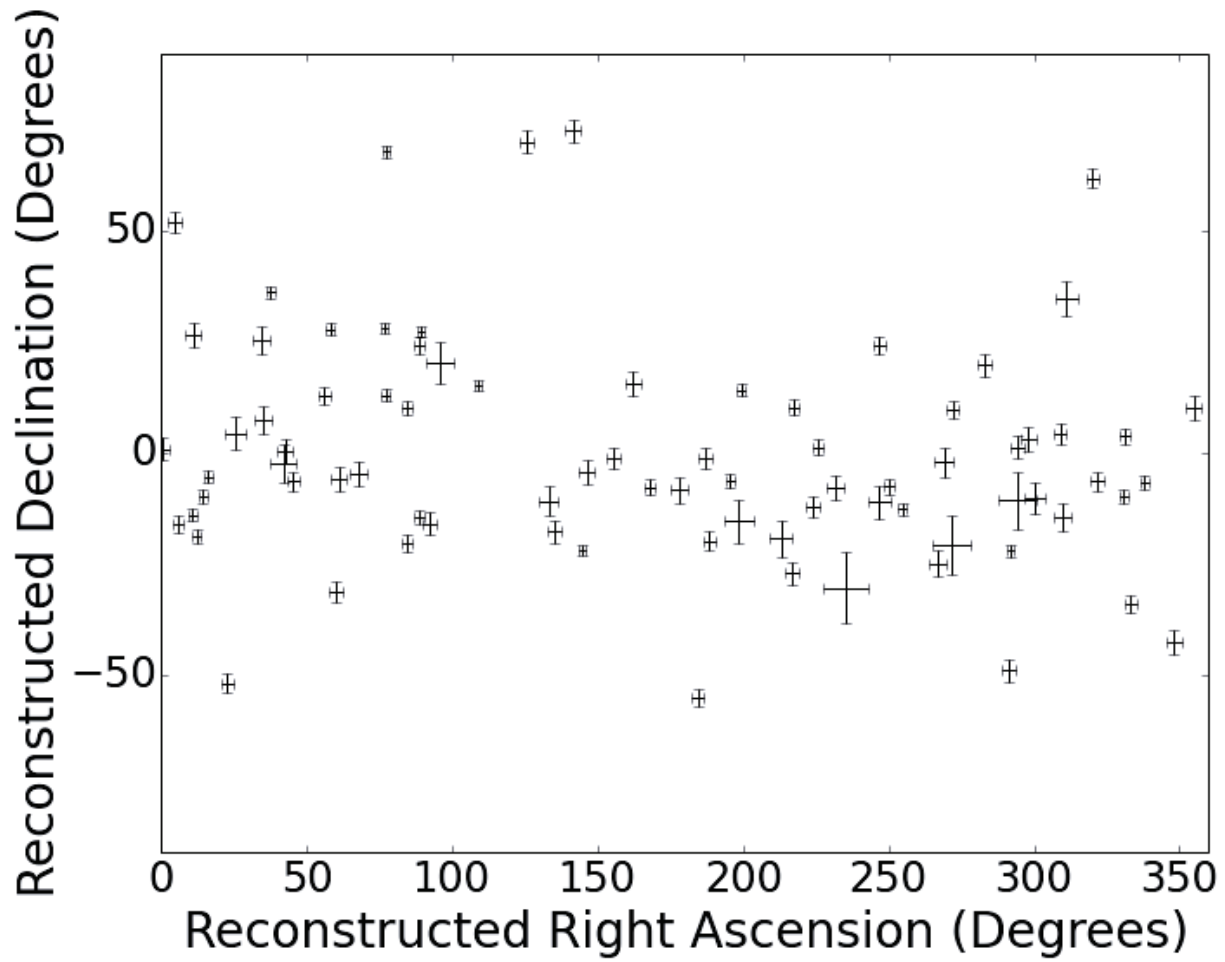


Figure 10.6: Distribution of events in reconstructed right ascension and declination with their associated error bars. The majority of the events cluster around the horizon as is expected. There is no clustering present after inspection of the event distribution.

this sample. Only a few events are present in simulation so no contribution is shown. In contrast Figure 10.9 shows the cosine zenith distribution with an unvetoes atmospheric neutrino flux. Inspecting the figures

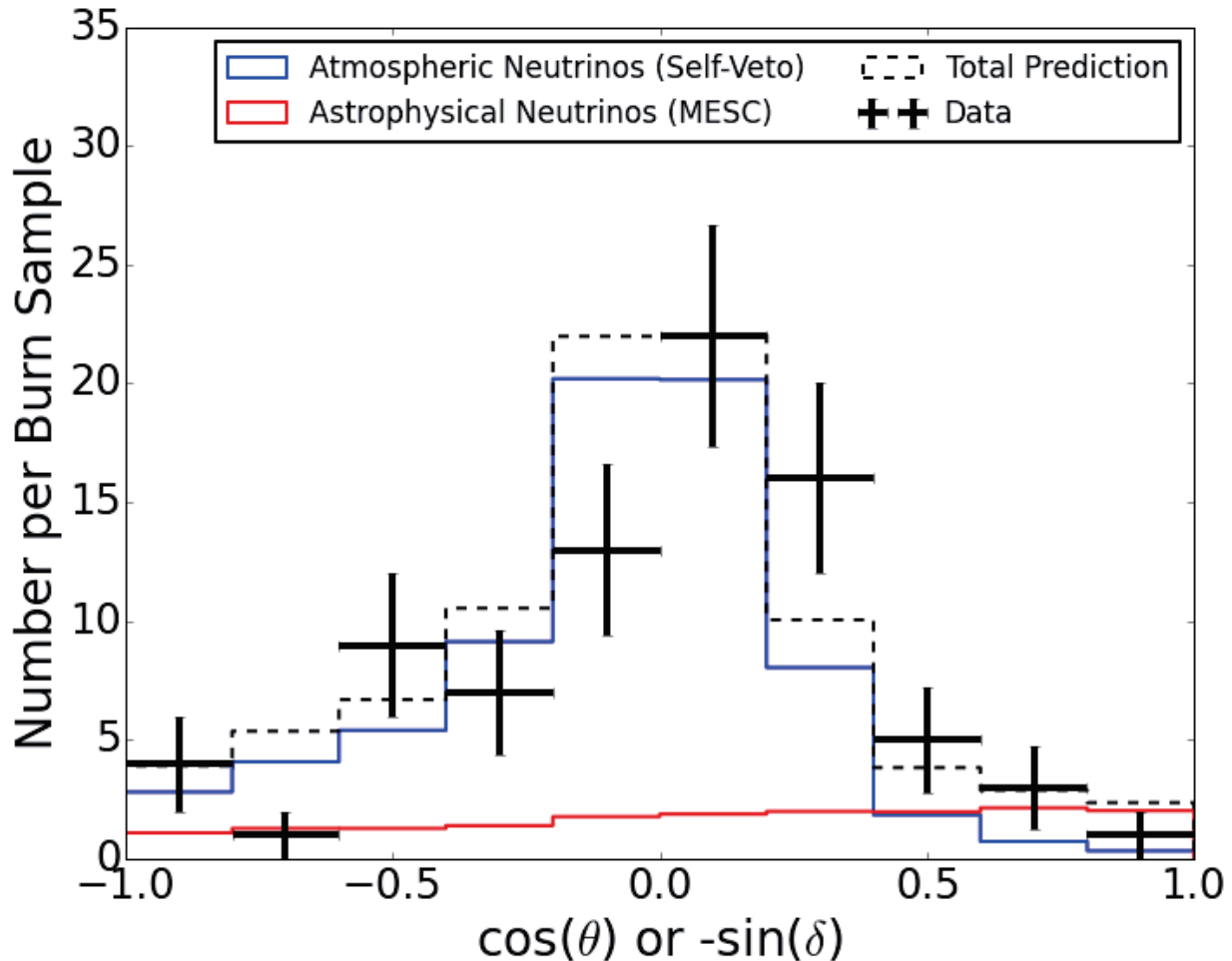


Figure 10.7: Cosine zenith distribution for the burn sample with estimates from Monte Carlo weighted to astrophysical flux measured by the MESC analysis and the vetoed atmospheric neutrino flux from the analytic parameterization. The data points agree with the Monte Carlo distribution, particularly in the region where the veto is active above a cosine zenith of 0.5.

where the self-veto is active, there is good agreement between the data and predictions from Monte Carlo. The same cannot be said about the figure where there is no self-veto applied to the neutrino flux. In this plot there is around a factor of 2 excess in the number of events predicted with respect to those observed. This excess in predicted events is evidence that the self-veto is important to describe the data well. Figures 10.10, 10.11, and 10.12 contain plots in three regions of the sky with the corresponding burn sample data

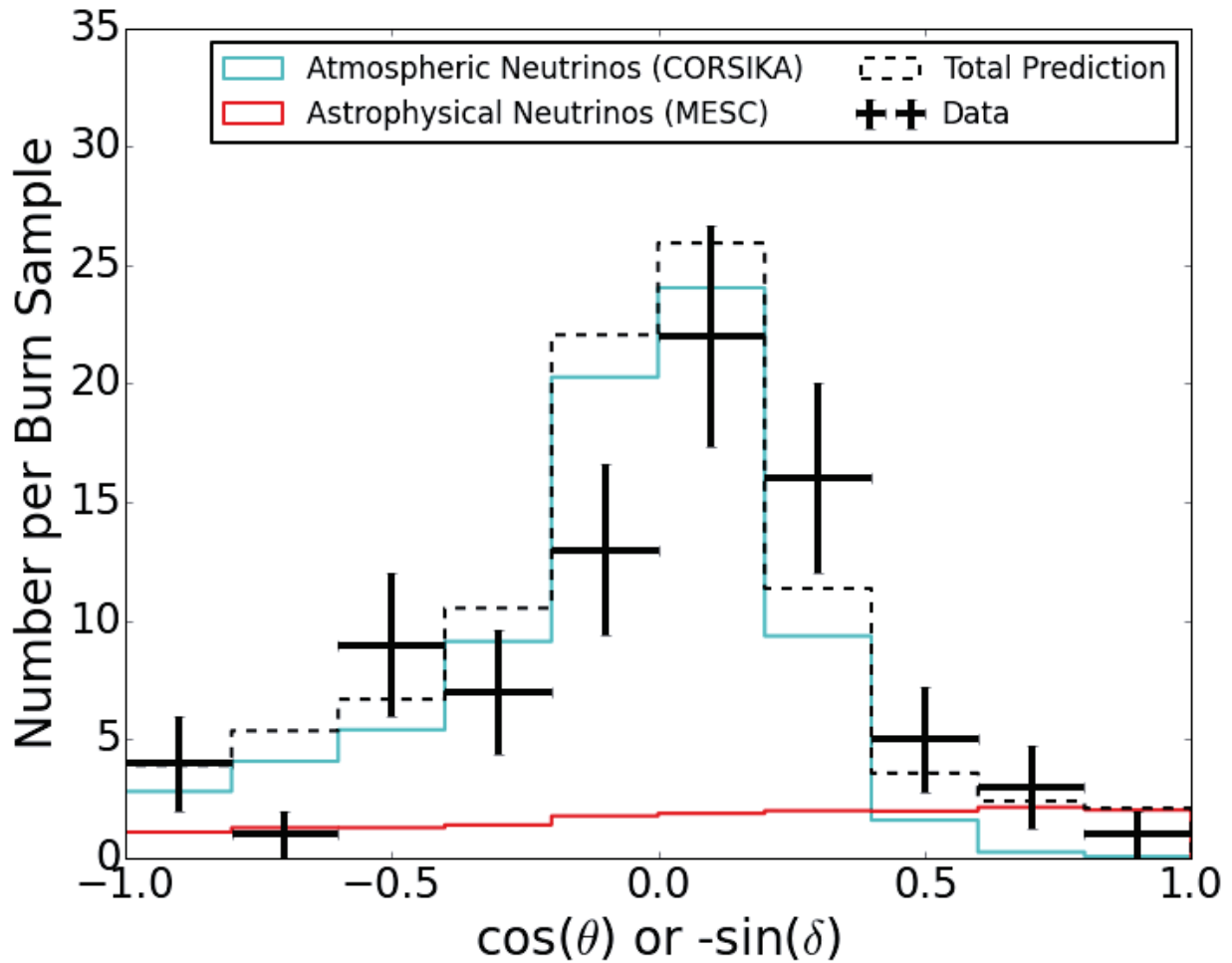


Figure 10.8: Cosine zenith distribution for the burn sample with estimates from Monte Carlo weighted to astrophysical flux measured by the MESC analysis and the vetoed atmospheric neutrino flux from CORSIKA. The data points agree with the Monte Carlo distribution, particularly in the region where the veto is active above a cosine zenith of 0.5.

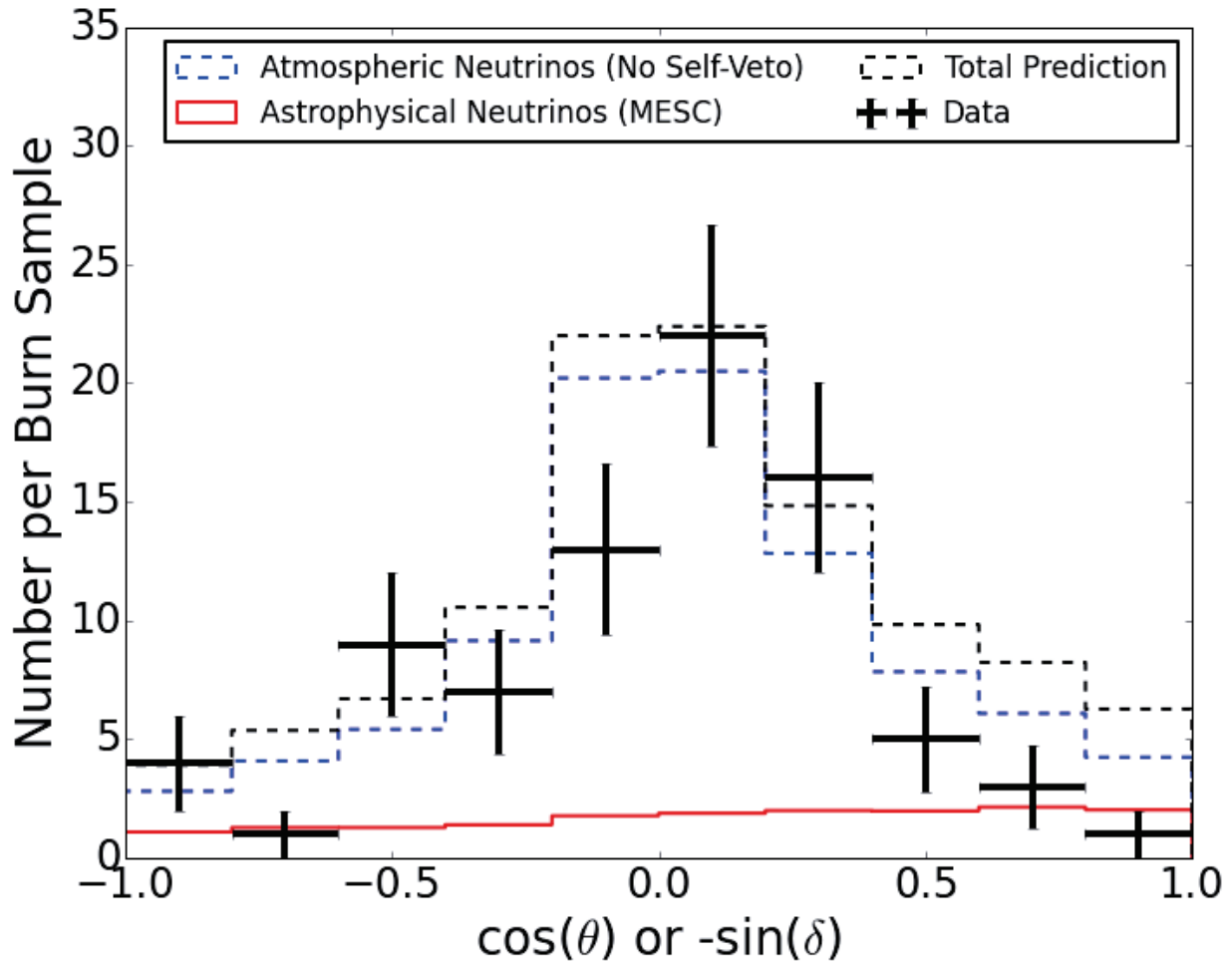


Figure 10.9: Cosine zenith distribution for the burn sample with estimates from Monte Carlo weighted to astrophysical flux measured by the MESC analysis and the atmospheric neutrino flux without the self-veto applied. The data points agree with the Monte Carlo distribution, except in the region where the veto would be active above a cosine zenith of 0.5. In this region over a factor of 2 more events are predicted than observed. This deficit shows that the neutrino self-veto is necessary to describe the data.

and predictions from simulation. Figures 10.10 and 10.11 show the contribution from atmospheric neutrinos using the analytic self-veto and CORSIKA neutrinos, respectively. In both cases the astrophysical flux from HESE provides the best match to the data points, but neither the MESC flux nor upward-going muon neutrino flux can be ruled out statistically. Both of the self-veto techniques provide good descriptions of the observed events. There are no statistically anomalous data points for either veto description. Figure 10.12

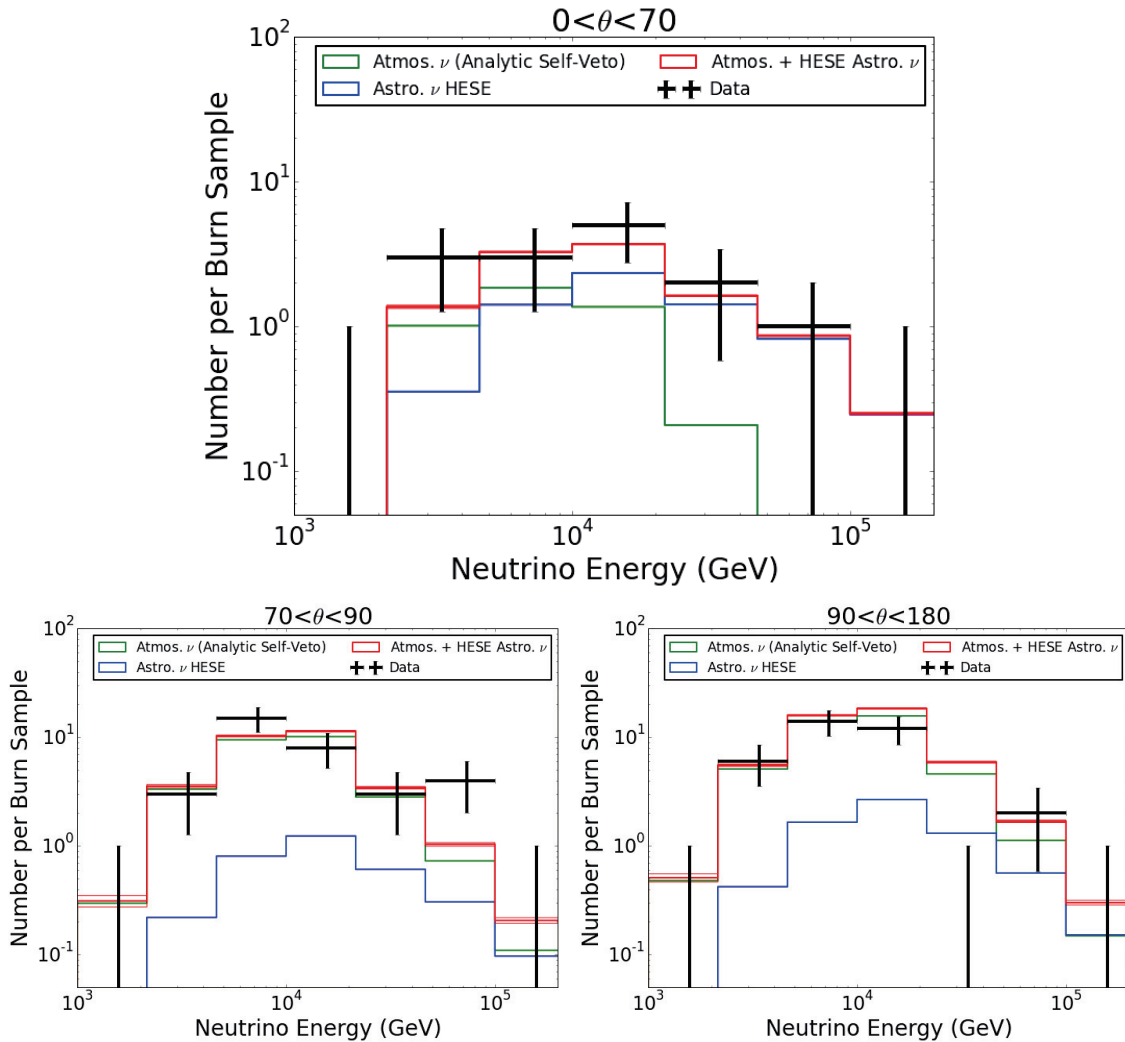


Figure 10.10: Plots of the burn sample and neutrino predictions in three slices of the sky. The largest plot on top is the region where the astrophysical neutrinos dominate, the bottom left is where slightly vetoed to unvetoed atmospheric neutrinos dominate, and the bottom right is where the unvetoed atmospheric neutrinos dominate. These plots are made with the analytic self-veto approximation.

shows the contribution of the atmospheric flux without a self-veto applied and no astrophysical neutrino flux



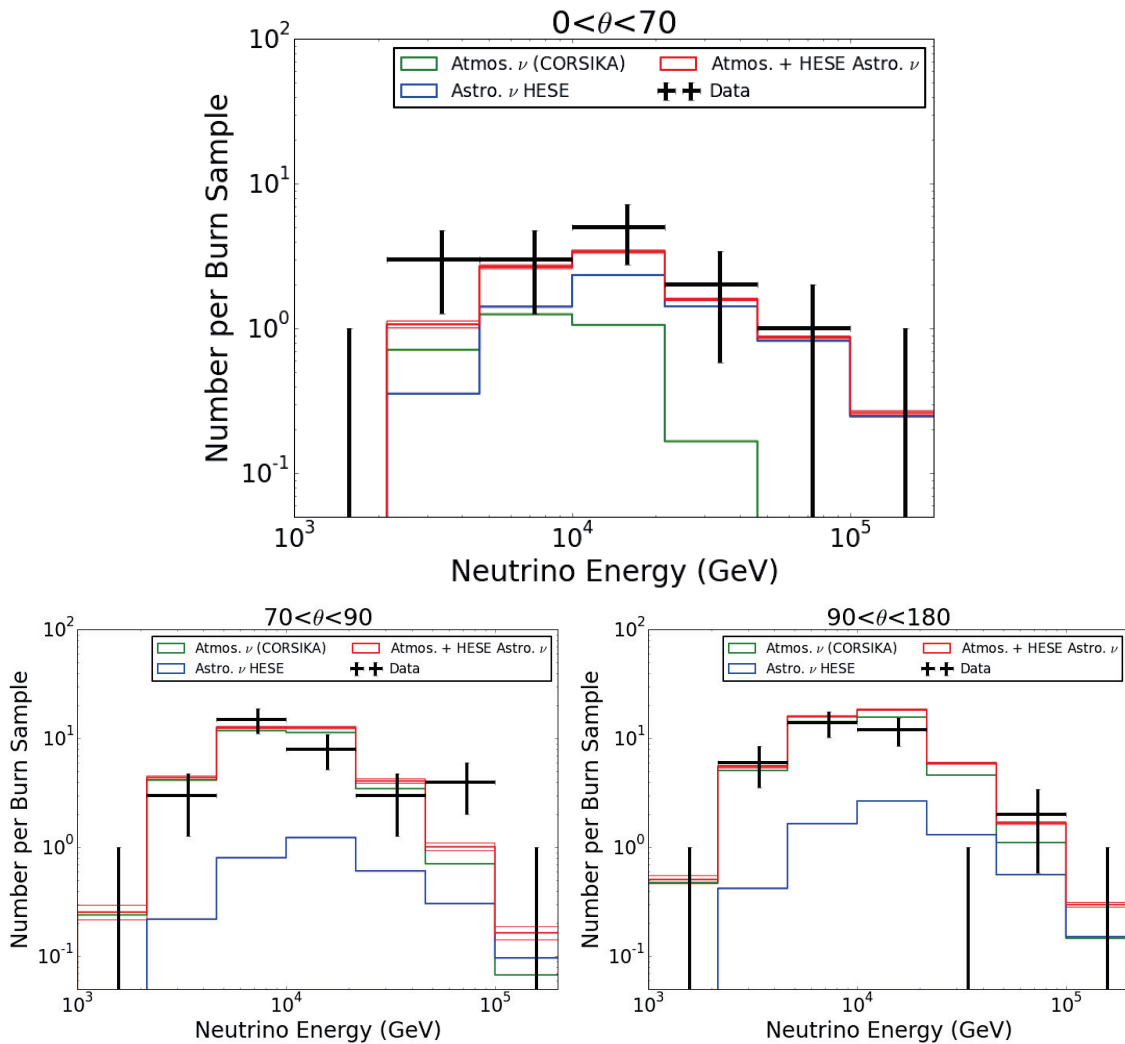


Figure 10.11: Plots of the burn sample and neutrino predictions in three slices of the sky. The largest plot on top is the region where the astrophysical neutrinos dominate, the bottom left is where slightly vetoed to unvetoed atmospheric neutrinos dominate, and the bottom right is where the unvetoed atmospheric neutrinos dominate. These plots are made with the CORSIKA neutrino self-veto approximation.

present. In this case there is a slight excess in the predicted number of events in the  $0 < \theta < 70$  plot around 10 TeV, but the excess is not statistically significant enough to reject the un-vetoed case.

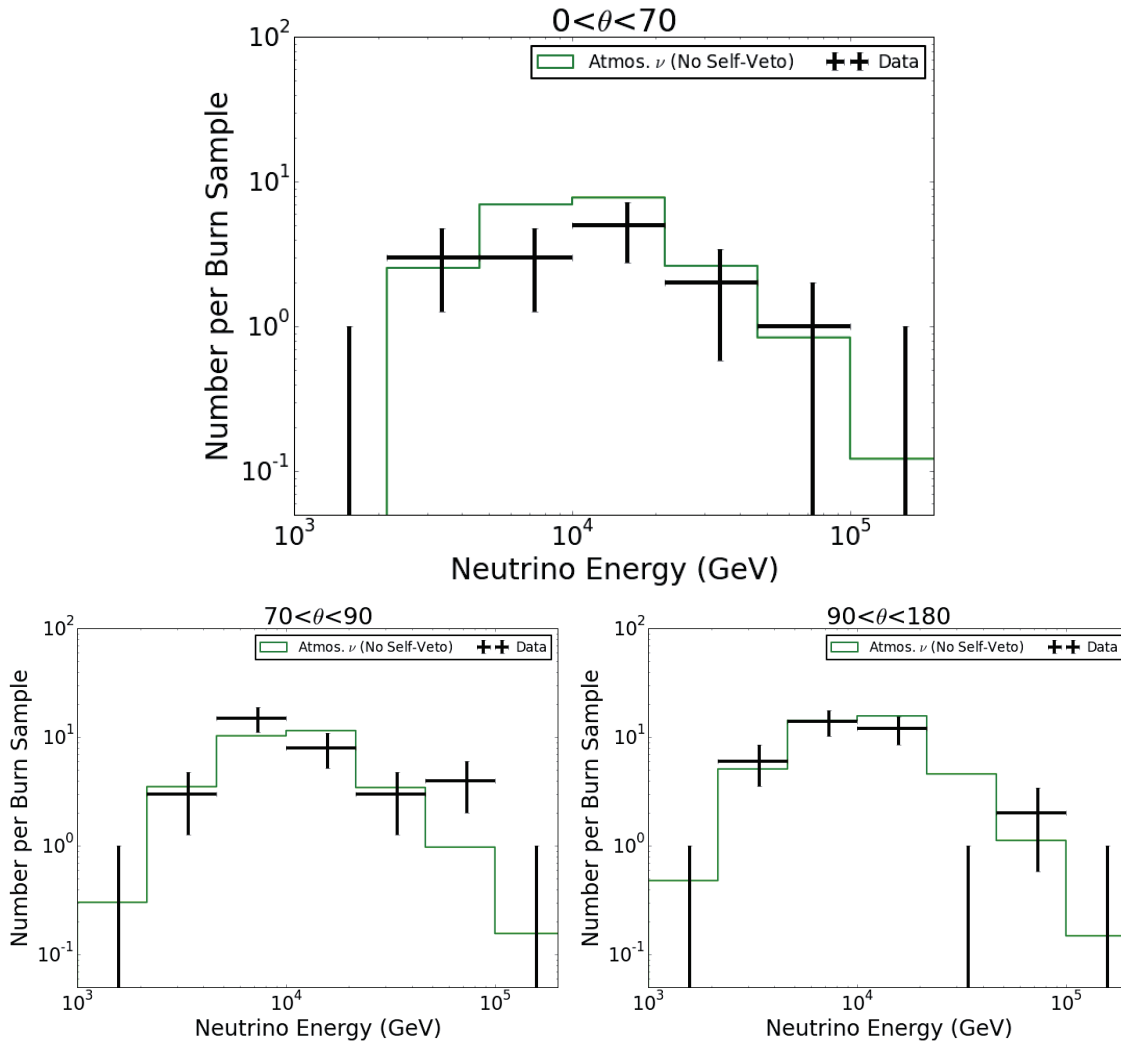


Figure 10.12: Plots of the burn sample and fit components in three slices of the sky. Here only the atmospheric contribution without a self-veto applied is shown. Only a slight difference between data and simulated prediction is present so the un-vetoed case cannot be rejected.

### 10.3 Outlook for the Full Sample

While ESTES has not been run on the entire five year sample yet, it does have a lot of potential to contribute to the community's understanding. This section will focus on the science potential of measurements of the diffuse flux and point sources.

### 10.3.1 Events From Astrophysical Fluxes

There are a number of measured astrophysical spectra from different IceCube analyses, see Section 5. Currently there is not an agreed upon value for the astrophysical spectra, so it is interesting to see what ESTES's response to these spectrum is. Figure 10.13 shows the differential and cumulative number of events per year seen in ESTES for the fluxes in Section 5. The solid lines are the best fit values for the fluxes while the bands show the range of event rates possible within the 1 sigma errors of the best fits. Because the

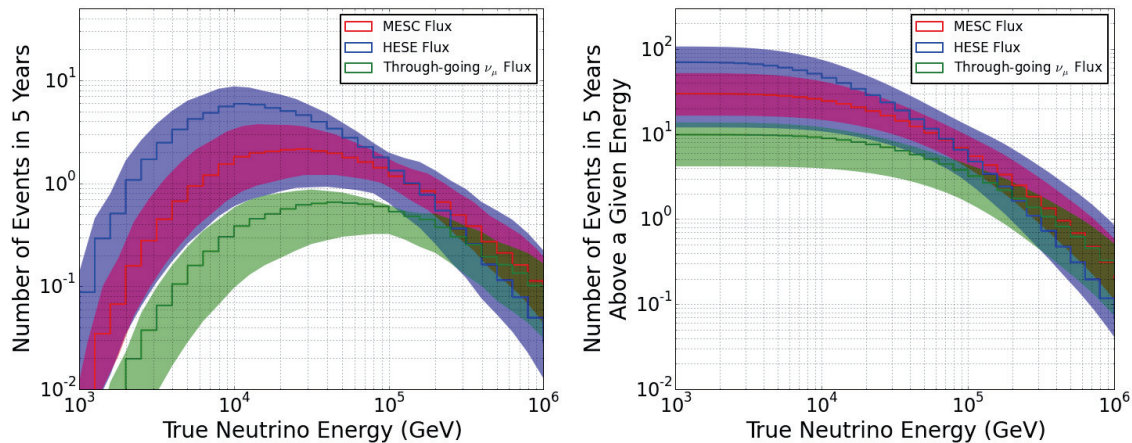


Figure 10.13: The true neutrino energy spectrum of ESTES, in the zenith range from 0 to 70 degrees, assuming the astrophysical flux measured by each analysis from Section 5. The solid lines are the best fit flux for each analysis, while the shaded regions are the possible regions of measurement for ESTES when the best fit fluxes are varied within their one sigma error contour.

measurements of the astrophysical spectrum vary from a index of approximately  $-2$  to  $-2.83$ , the options for ESTES encompass values from almost 130 events per year to 5 events in the five year sample. One interesting feature is the response of ESTES to different spectral indices. Remember the best fit for the HESE flux has a spectral index of  $-2.58 \pm 0.25$ , while the MESC flux is at  $-2.46 \pm 0.12$ , and the diffuse flux is at  $-2.13 \pm 0.13$ . This gives a greater than two sigma tension between the hardest and softest measured values.

There are a few important things to clarify about this tension. It is the upward-going muon neutrino results from above 100 TeV which tend to favor a index closer to  $-2$  while the cascade dominated samples which largely measure the astrophysical flux in the southern hemisphere and above and below 100 TeV which favor softer indices around  $-2.5$ . This leads to a few options for the tension. The first option is a north-south asymmetry to the measured fluxes. In the northern hemisphere the majority of the sources are extra-galactic and have gamma ray spectra close to  $E^{-2}$ . While the gamma ray sources are not necessarily also neutrino sources, this is an indication that the extra-galactic accelerators produce particles with a spectral index

near -2. In the southern hemisphere the galaxy is a prominent feature, including the Galactic center, and is comprised of sources with softer gamma ray indices. Another option revolves around the construction of the neutrino energy spectrum itself. Since IceCube has not resolved any sources, the diffuse flux is assumed to be comprised of a set of sources which are weakly emitting and isotropically distributed. Each of these sources has its own intrinsic flux. Each source's spectrum may possibly be a continuous power law, but could take on many forms with breaks and cutoffs, particularly if different classes of objects are contributing. Even if all the sources were emitting unbroken power law fluxes, it is important to recall that the sum of power laws with different indices is not itself a power law unless all the indices are identical. All of this is to say that it is unlikely that the neutrino flux is a single power law across all energies, just like the cosmic ray spectrum. In both the north-south anisotropy case and the varying index case ESTES offers a unique perspective.

The results from ESTES will mark the first time a selection with good angular resolution will observe the astrophysical flux below 100 TeV in the southern sky. In addition to conducting a diffuse fit which will include contributions from the Galactic Plane, ESTES will also test models of Galactic Plane emission as in the paper "Constraints on Galactic Neutrino Emission with Seven Years of IceCube Data" [111]. In this paper three models are tested, with one being ruled out. The two remaining models are the Fermi neutral pion decay map [112], and what is known as the KRA- $\gamma$  model [113]. The neutral pion decay map from Fermi should be a template for charged pions as well, and can be converted into a neutrino flux. The model known as KRA- $\gamma$  comes from the paper titled "The gamma-ray and neutrino sky: A consistent picture of Fermi-LAT, Milagro, and IceCube results" [113] which describes the results of a galactic cosmic ray transport model which predicts gamma ray and neutrino fluxes from the galaxy which can describe Fermi and Milagro data [114] simultaneously. A test of ESTES's sensitivity to each is conducted with an unbinned maximum likelihood template method which convolves the intensity of emission from the Galactic Plane models with the acceptance of ESTES (see Figure 10.14 for an example). For the Fermi neutral pion model ESTES will be sensitive to a flux times  $E^2$  of  $4.30 \times 10^{18} \text{ GeV/cm}^2 \text{ s}$ . This is larger than the  $2.97 \times 10^{18} \text{ GeV/cm}^2 \text{ s}$  sensitivity from the full sky point source search, but is still important because ESTES measures events much lower in energy than the point source search in the southern sky. For the KRA- $\gamma$  model ESTES is sensitive to a flux 65% as intense as the model. This represents an improvement over the sensitivity from the full sky point source searches result of 79%. The main difference for each analysis having an edge on different models is the morphology of the models. The Fermi neutral pion template supports more spread out emission along the plane while the KRA- $\gamma$  model favors stronger emission from the Galactic Center.

If the observed tension is from a change in the astrophysical spectrum with energy then ESTES can make a contribution there as well. Referring back to Figure 10.13 the plots show a very large difference in the number of events detected per year in the energy range below 200 TeV for each of the different spectral indices. This is largely due to ESTES being sensitive to the flux between 10 and 100 TeV, which is below

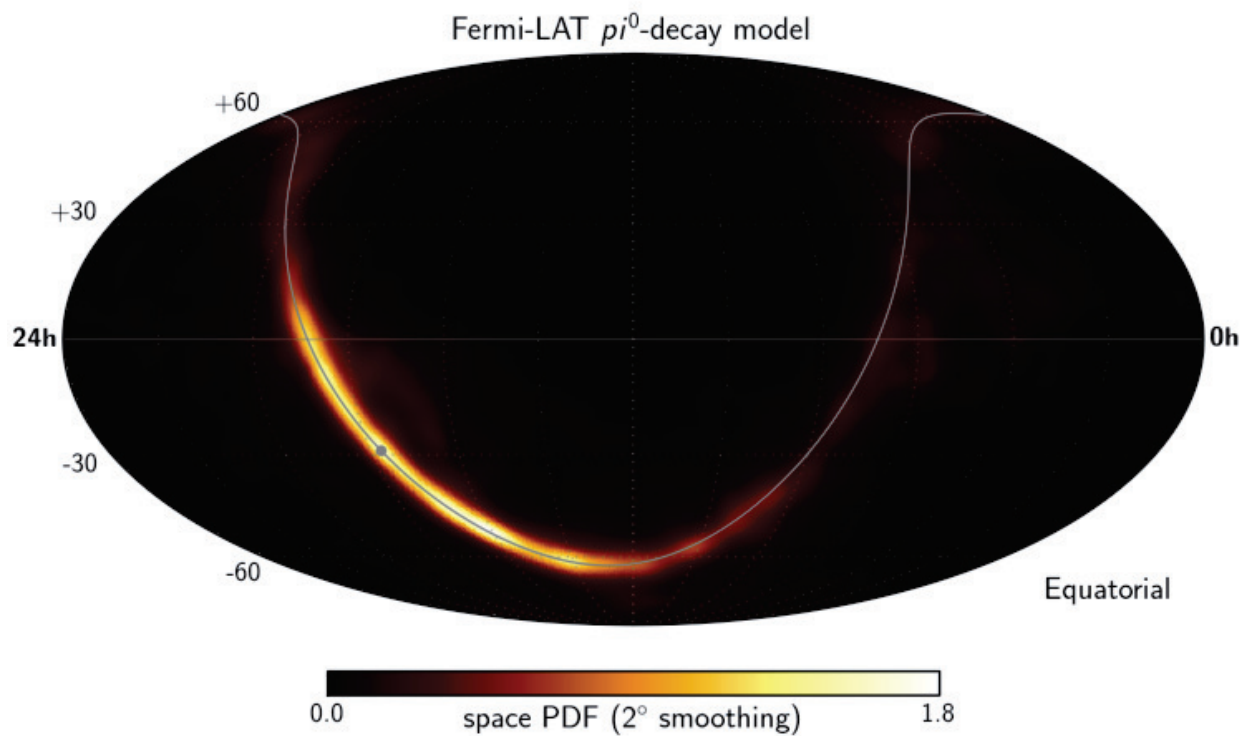


Figure 10.14: Map of the ESTES acceptance convolved with the Fermi neutral pion map. The majority of ESTES's sensitivity to this model comes near the Galactic Center, grey dot, with the peak being about 15 degrees below the Galactic Center in Equatorial coordinates.

the defined 100 TeV pivot point. Since the spectra are steeply falling, small shifts in the index lead to large shifts in the number of events detected in this lower energy range. ESTES is unique in its ability to measure astrophysical tracks in this energy range. Figure 10.15 uses simulation to predict what regions ESTES would make a measurement of the flux within 68 and 95 percent of the time assuming different analyses have measured the true value of the astrophysical spectra. In this plot the 95% contours of the upward-going muon neutrino analysis and HESE analysis do not overlap, meaning that ESTES has power to distinguish between these scenarios. The size of the contours for each flux is largely determined by the number of events

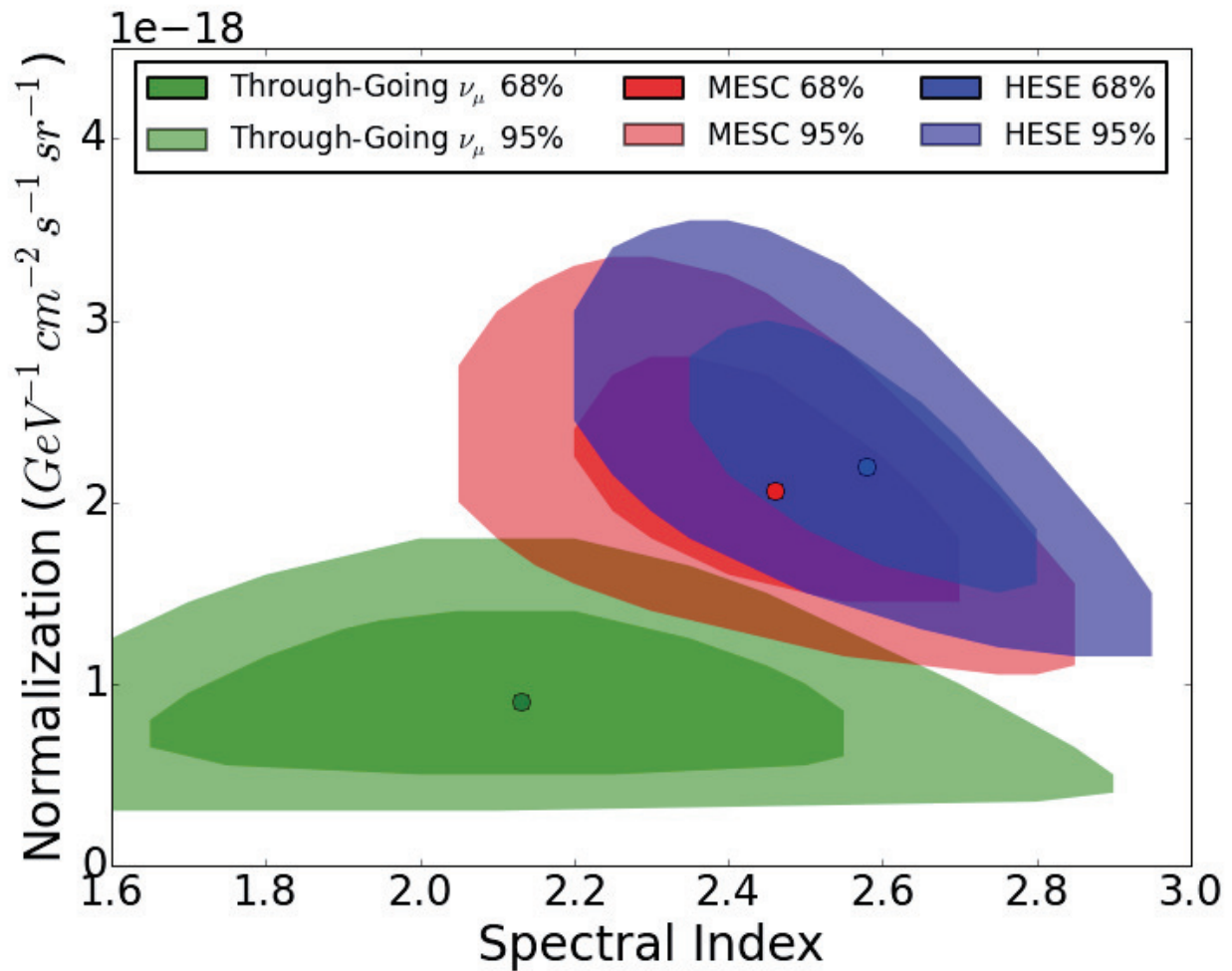


Figure 10.15: Likelihood profiles for three hypothetical astrophysical spectra as they would be detected in five years of data in ESTES. The hypothetical fluxes are either from the upward-going muons, MESC, or HESE analyses.

which are discernibly astrophysical. This can be seen by comparing the number of events expected in five years from each of the analyses' fluxes in Figure 10.15 to the numbers presented in Table 10.2.

Upward-Going $\nu_\mu$	MESC	HESE
8.4	30.0	35.3

Table 10.2: The number of astrophysical events expected in 5 years with an astrophysical probability greater than 50%.

Being able to accurately measure the astrophysical spectra from events below 100 TeV has important consequences on the classes of objects which can contribute to the flux. It is intriguing that the diffuse flux above 100 TeV is at around the Waxman-Bahcall bound [79],  $E_\nu^2 \Phi_{astro\nu} \approx 10^{-8} \text{ GeV cm}^{-2} \text{ s}^{-1} \text{ sr}^{-1}$ . This suggests that the measured flux could be connected with the production of ultra-high energy cosmic rays. If this is the case then the neutrinos are consistent with a model where ultra-high energy cosmic ray protons are produced in a calorimetric environment where all accelerated particles are guaranteed to undergo proton-proton interactions. If the unresolved neutrino sources are gamma ray sources below the current detection limit then the same cosmic rays which produce neutrinos will also produce gamma rays, albeit at a lower energies due to interactions with the extra-galactic background light. This means that a connection between the diffuse cosmic rays, neutrinos, and gamma rays could exist as is shown in Figure 10.16. At right are the diffuse cosmic rays as measured by Auger [120][116][117] with the green dotted line showing the proton contribution. The dashed blue line represents the neutrinos created assuming proton-proton interactions of the measured protons in a modeled calorimetric environment. These neutrinos match up with the measured events from IceCube shown as the black data points. The diffuse gamma rays from the proton-proton interactions are also shown as the thicker red line. Also shown are the "diffuse" gamma rays as measured by Fermi shown as the red crosses. These gamma rays are not truly diffuse as approximately 85% are from blazars [119]. The non-blazar component is shown as the red band between the data points and proton-proton gamma ray line. The ratio of the observed and predicted diffuse gamma rays gives the fraction a particular source class, represented by the modeled calorimetric environment, can contribute to the neutrino flux. Recall, that this is all under the assumption that the neutrinos are consistent with the Waxman-Bahcall bound. If the flux below 100 TeV is consistent with the measured softer  $\approx E^{-2.5}$  fluxes then the predicted proton-proton gamma rays would exceed the diffuse measurement by Fermi and could be used to place limits on the source classes which create the diffuse neutrino flux, as was originally discussed in the 2013 paper "Testing the hadronuclear origin of PeV neutrinos observed with IceCube" by Murase, Ahlers, and Lacki [121]. Since ESTES is only sensitive to the astrophysical flux below 100 TeV, its ability to differentiate between  $\approx E^{-2}$  and  $\approx E^{-2.5}$  fluxes will play an important role in determining the outcome of the discussed model. Additional, complimentary discussion can be found in "Evidence against

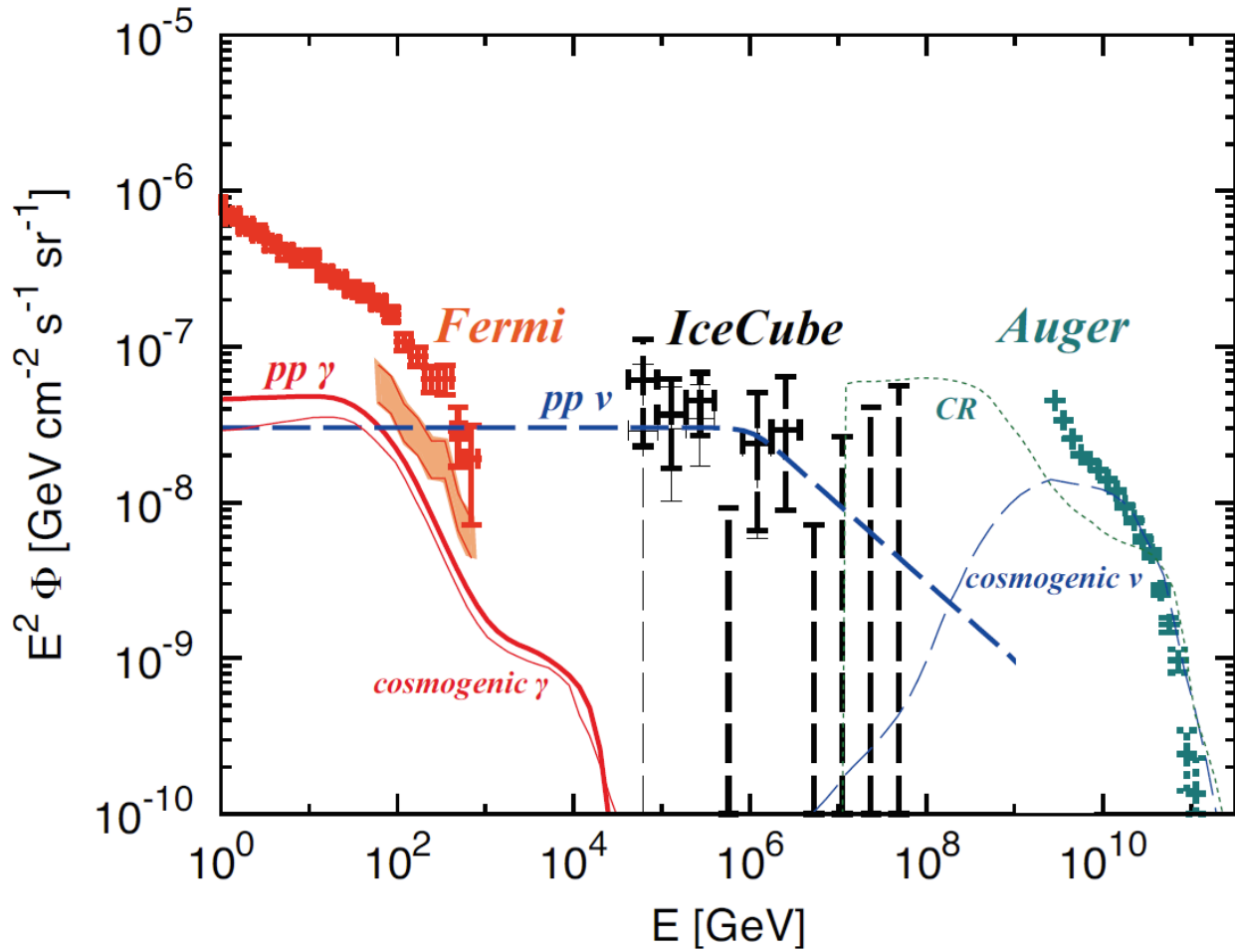


Figure 10.16: Plot from "Constraining high-energy cosmic neutrino sources: Implications and prospects" [115] showing the connection between the diffuse cosmic rays [116][117], neutrinos [70], and gamma rays [118][119] under the condition that the neutrinos are at the Waxman-Bahcall bound and are produced by proton-proton interactions in calorimetric environments. If the neutrino flux below 100 TeV is shown to have a spectrum of  $E^{-2.5}$  then the produced gamma rays would exceed the measured diffuse gamma ray flux and invalidate the model. This is already the case for starburst galaxies [54].



star-forming galaxies as the dominant source of IceCube neutrinos" by Bechtol, Ahlers, Di Mauro, Ajello, and Vandenbroucke.

### 10.3.2 Events From Atmospheric Flux Models

In addition to measuring the astrophysical flux ESTES also measures the atmospheric flux. In veto based analyses the downward-going neutrino flux is attenuated by the atmospheric self-veto, thus it is necessary to temper the flux appropriately. There are two ways to accomplish this. One way is to use the analytic approximation to the self-veto to attenuate the flux, as is described in Section 4. The other way is to simulate showers with neutrinos in CORSIKA and run them through the IceCube simulation processing, as discussed in Sections 7.1.2.2 and 7.1.3.4. The analytic method has been used by all analyses up to this point, but does make a few simplifying assumptions about the detection of muons that could lead to systematic inaccuracy. The CORSIKA option on the other hand is a full simulation of showers, so is closer to being correct as long as the hadronic and atmospheric models used are accurate. Simulation sets of both situations were processed using the ESTES selection. The model using the analytic approximation to the self-veto will be presented first followed by a comparison to the neutrinos from CORSIKA simulations.

Starting with the self-veto approximation for the atmospheric neutrino flux one gets the event rate in Figure 10.17. With this model, the atmospheric event rate peaks between 3 and 6 TeV in ESTES. The

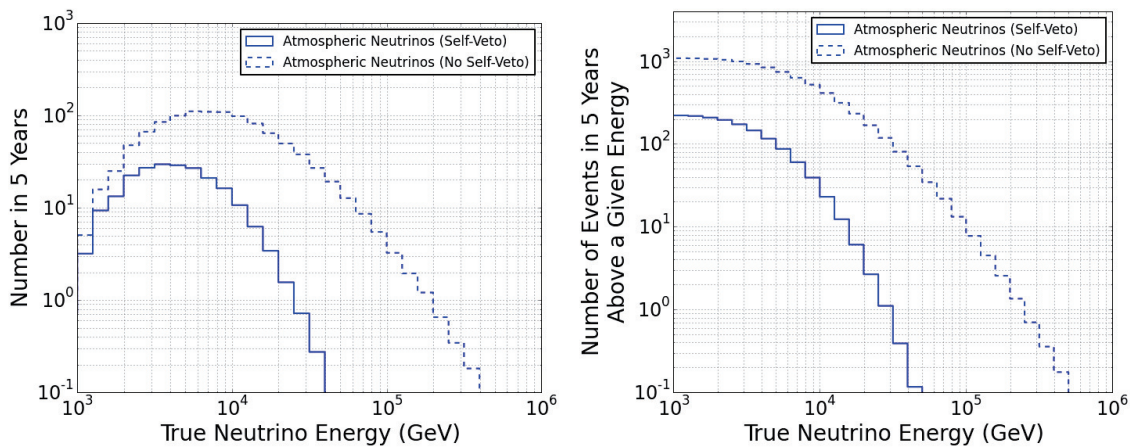


Figure 10.17: The true neutrino energy spectrum of ESTES, in the zenith range from 0 to 70 degrees, for the atmospheric flux from the self-veto approximation. This spectrum peaks before 10 TeV leaving room for the detection of the astrophysical flux above this energy. Also shown is the rate which would be present without the atmospheric self-veto. In this situation even the most abundant astrophysical neutrino fluxes would be subdominant.

effect of having no self-veto is also shown as the dashed line. If the self-veto effect was not present then

the atmospheric flux would obscure the astrophysical flux across much of the energy range for even the most abundant astrophysical fluxes. The comparison of simulating atmospheric neutrinos with the analytic approximation and the full simulation is shown in Figure 10.18. The models have a slightly different event

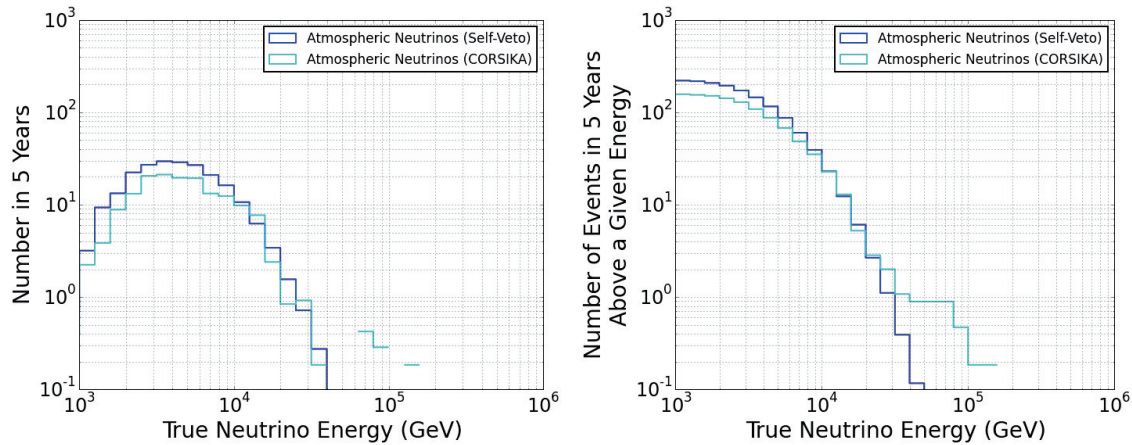


Figure 10.18: The true neutrino energy spectrum of ESTES, in the zenith angle range from 0 to 70 degrees, for the atmospheric flux from both estimates of the atmospheric neutrino flux. The models are very similar in the total number of events predicted. It should be noted that the simulation which the "Atmospheric Neutrinos (CORSIKA)" histograms are created from are test sets with limited statistics. The tails in both plots above 70 TeV are likely to be a result of the sample's small statistics.

rate as a function of neutrino energy in this zenith band for events below 10 TeV with the rate predicted from CORSIKA being about 25% lower. A total difference of 67 events in 5 years is predicted, largely coming in below 10 TeV. Figure 10.19 gives perspective on how this compares to the predicted astrophysical neutrino event rate. For this optimistic case of perfect energy reconstruction, both models have an energy region where events from the astrophysical flux are dominant. This holds if the reconstructed energy is used instead, albeit with larger binning to accommodate the resolution of the energy reconstruction, as can be seen in Figure 10.20.

Though it is slightly present in the plots above, it is important to note that there are significant changes to the neutrino self-veto as a function of zenith angle that is not obvious when viewing the expected event rates over an entire range. This is shown in Figure 10.21. There are two regions where the flux differs for these models, below and above cosine of .5. Above cosine of .5 the full simulation with CORSIKA suggests that the analytic self-veto vastly over predicts the event rate. This deviation happens in the important region where the astrophysical flux dominates and drastically affects the astrophysical purity of events in this region. Below cosine of .5 the full simulation with CORSIKA suggests that the analytic self-veto under predicts the event rate. One speculative reason for this difference comes from the way a successful veto is defined. In

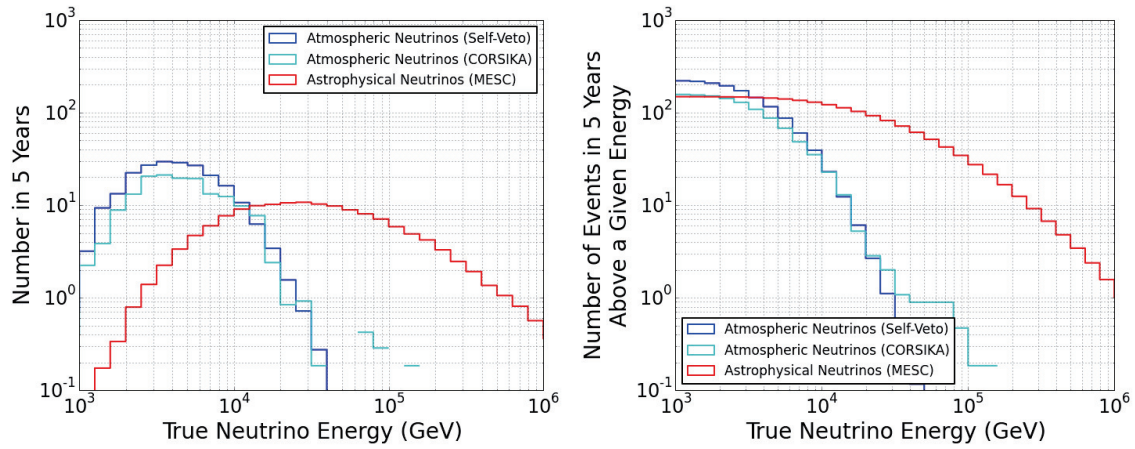


Figure 10.19: The true neutrino energy spectrum of ESTES, in the zenith range from 0 to 70 degrees, for various neutrino fluxes. The models show that a clear astrophysical signal should be detectable.

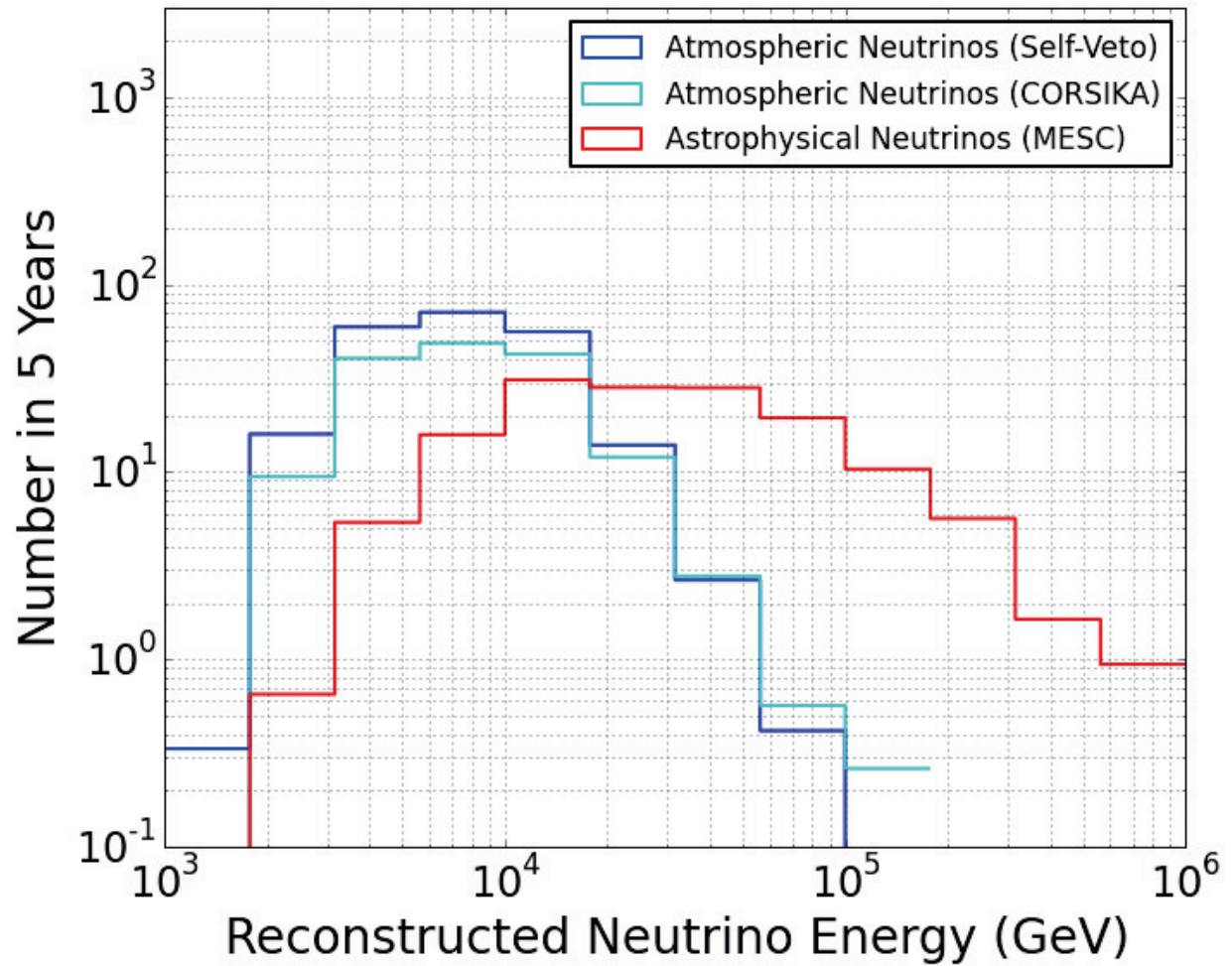


Figure 10.20: The reconstructed neutrino energy spectrum of ESTES, in the zenith range from 0 to 70 degrees, for the atmospheric flux from both estimates of the atmospheric neutrino flux and the astrophysical neutrino flux from MESC. The astrophysical flux is still dominant above 20 TeV in the reconstructed neutrino energy.

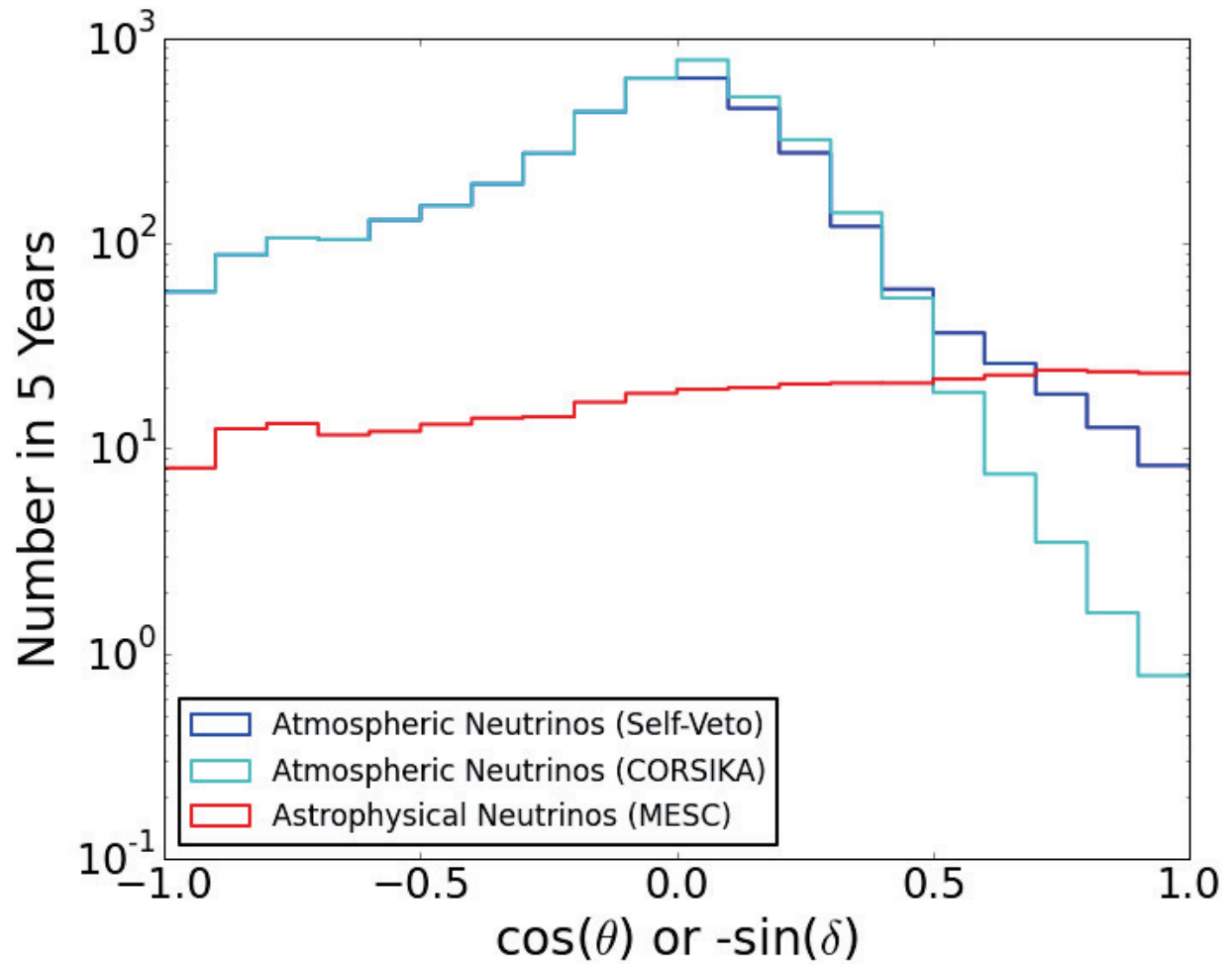


Figure 10.21: The true cosine zenith distribution of ESTES for all energies from various neutrino fluxes. In this perspective there is a large difference in the predicted event rates if the atmospheric flux is modeled with the analytic self-veto or the full CORSIKA simulation.

the analytic approach an atmospheric neutrino is vetoed if accompanying muons with a cumulative energy greater than 300 GeV reaches a depth of 1950 meters in the ice. In reality the energy and depth the veto is successful at is dependent on the location the event enters the detector. Many vertical events strike the detector above the 1950 meter mark while many horizontal events strike the detector below the 1950 meter mark. In the case that the impact position is above the 1950 meter mark the analytic veto is too conservative while for those below it is too permissive. This combined with differences in the hadronic modelling could be at play in creating the differences. Inspecting further by breaking the atmospheric neutrino rates into energy slices in the cosine distribution yields of Figure 10.22. The differences in Figure 10.21 seem to be

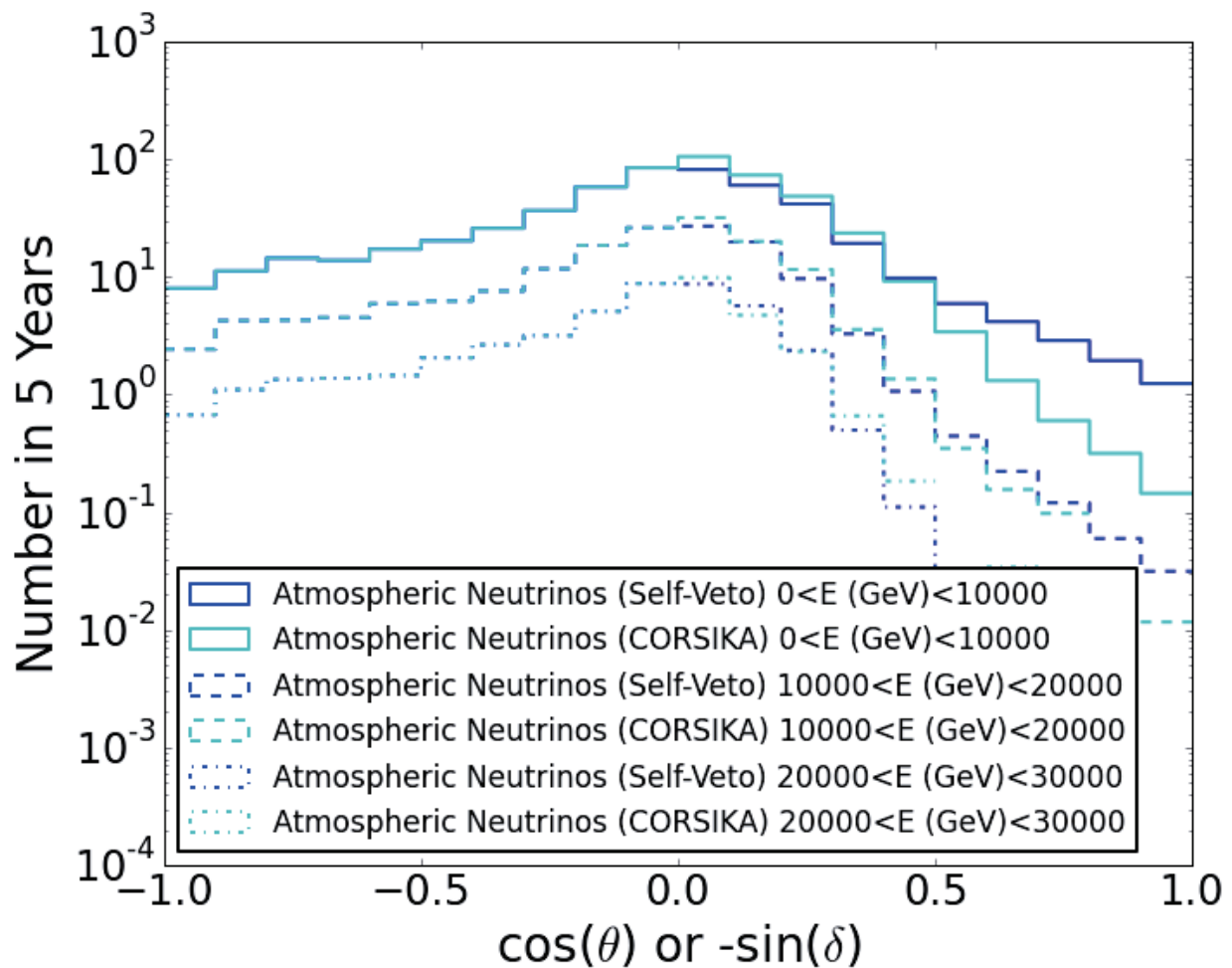


Figure 10.22: The true cosine zenith distribution of ESTES for a few slices in energy from various neutrino fluxes. In this perspective the large difference in the predicted event rates comes from the atmospheric flux below 10 TeV.

most prominent below 10 TeV, though more statistics are need for the CORSIKA neutrino simulations above 10 TeV in neutrino energy to determine the trend for event rates below  $10^{-2}$  per year.

### 10.3.3 Point Source Potential

In addition to the prospects for contributing to the understanding of the astrophysical spectrum, ESTES can also help improve IceCube’s point source sensitivity in the southern sky. Looking at the effective area plot in Figure 9.32 one can see that it is a larger selection over an energy range from 7 TeV to 200 TeV in the southern sky. However, in addition to that ESTES is also far more pure in the region due to the self-veto. In five years ESTES expects 33 background events and 8.5 signal events from a flux at the Waxman-Bahcall bound. While the signal to background ratio in this scenario is impressive, currently ESTES is signal starved. Point source searches in IceCube are conducted using the likelihood definition in Equation 10.1

$$\ell = \prod_i^{\text{allevents}} \left( \frac{n_s}{N} S(\vec{x}_i, \vec{x}_s, \sigma_i, E_i, \delta_i, \gamma) + \left(1 - \frac{n_s}{N}\right) B(\delta_i, E_i) \right) \quad (10.1)$$

where  $n_s$  is the number of signal neutrinos,  $\vec{x}_i$  is event  $i$ ’s location,  $\vec{x}_s$  is the source location,  $\sigma_i$  is the event’s angular uncertainty,  $E_i$  is the event’s reconstructed energy,  $\delta_i$  is the event’s reconstructed declination,  $\gamma$  is the spectral index of the source, and  $S$  and  $B$  are the signal and background probability distributions. The important quantity to calculate is the likelihood ratio of having signal events versus having none, as in Equation 10.2.

$$TS = 2 \log \left[ \frac{\ell(n_s, \gamma)}{\ell(n_s = 0)} \right] \quad (10.2)$$

The log of the likelihood ratio, known as a TS value, can be computed for a data set. However, for context about the probability of obtaining a TS value random ensembles from background must be obtained. For ESTES these ensembles almost always yield 0 background events, meaning the source must produce just two events for ESTES to be sensitive to it. However, these two events are almost a quarter of the 8.5 signal events ESTES expects. If such a source were emitting a quarter of the diffuse flux IceCube would have already detected the source. In this context we know that there are not any sources which are this, and ESTES is thus limited by the power of the sources themselves.

Even with the limitation, ESTES is still more sensitive than traditional searches from IceCube and ANTARES in parts of the southern hemisphere. Figure 10.23 shows ESTES’s sensitivity to a  $E^{-2}$  flux (solid red line) compared to a search using 7 years of IceCube point source data [110](dash-dotted blue line) and a combined analysis of 3 years of IceCube data and 5 years of ANTARES data [122](dashed green line). This figure shows that five years of ESTES offers the best sensitivity below a sine of declination of -0.7. While the  $E^{-2}$  scenario is generally the best case for other selections and experiments, it is important to remember that this is not the case for ESTES. Further, it is unlikely that the brightest source is emitting at  $E^{-2}$  up to the highest energies. This makes it meaningful to test scenarios where there is a cutoff. Since ESTES is

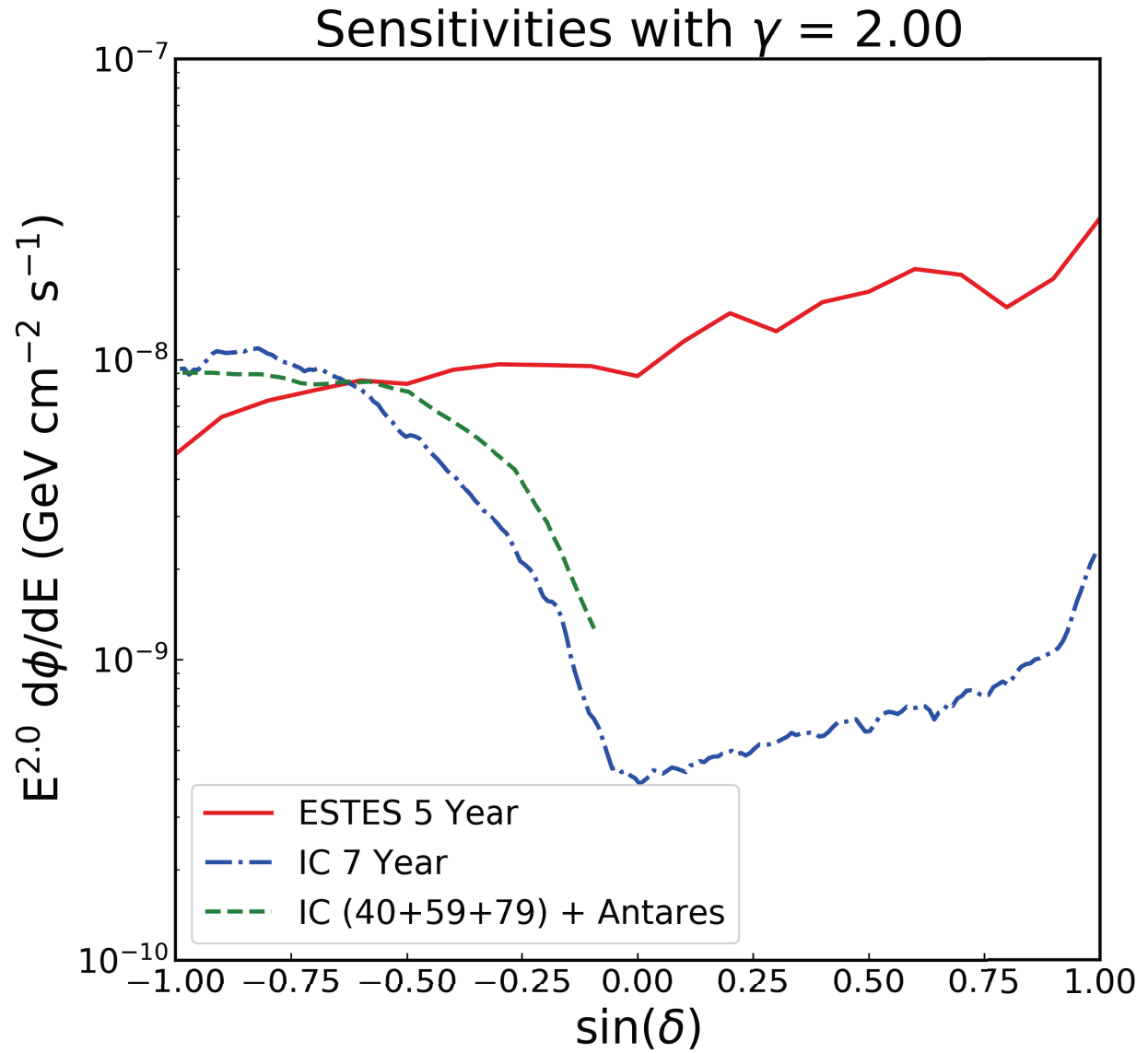


Figure 10.23: Sensitivity to  $E^{-2}$  fluxes for ESTES, 7 years of IceCube’s point source search, and a joint analysis by Antares and IceCube. ESTES is only competitive with the other selections below a sine of declination of -0.7 for this spectral index.



sensitive below 100 TeV, cutoffs above this energy do not remove many signal events from ESTES but do remove important events from other selections. This effect, as seen in Figure 10.24, leads to ESTES being two times more sensitive than existing measurements up to a sine of declination of -0.2. Another consequence

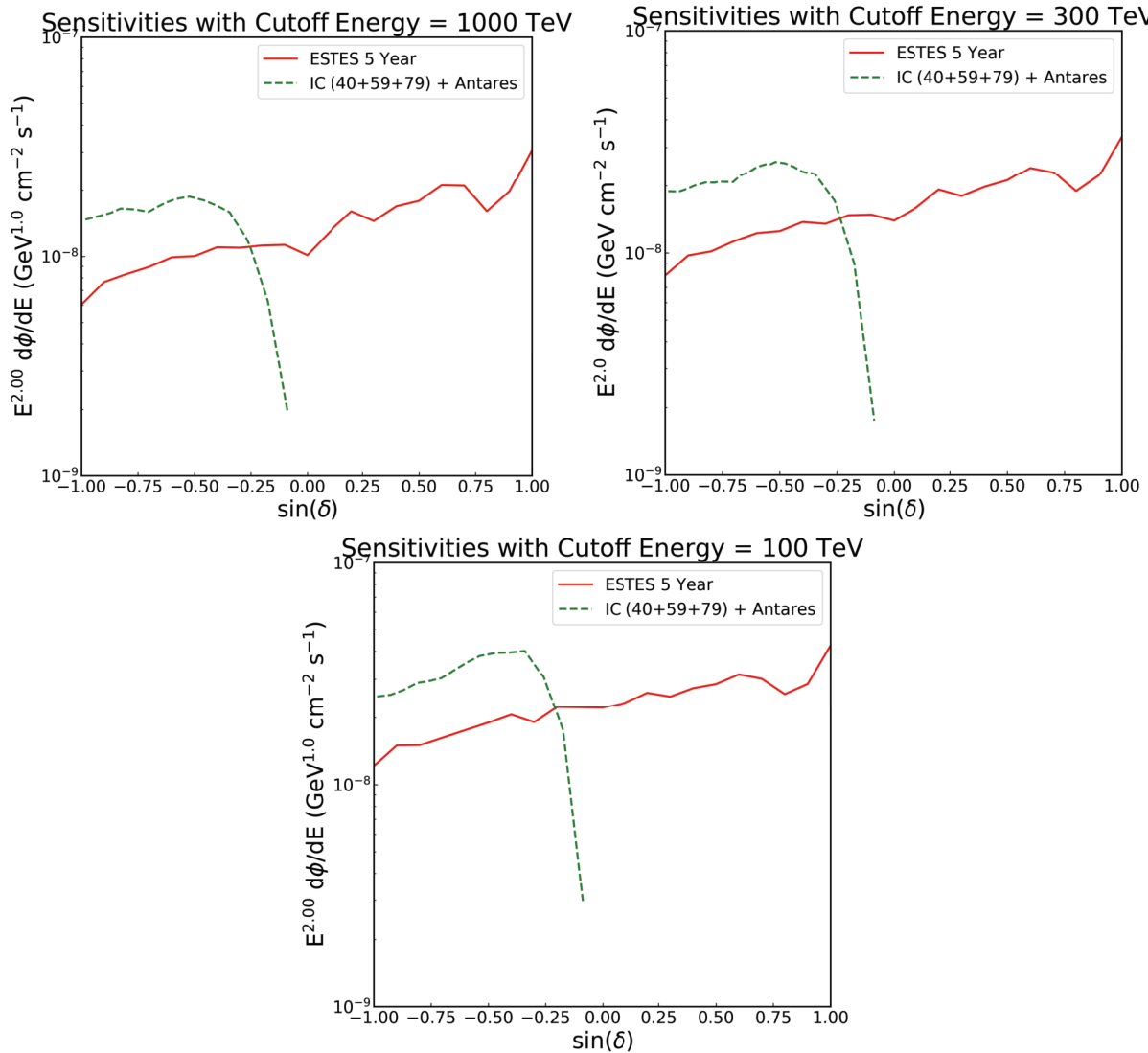


Figure 10.24: Sensitivity to  $E^{-2}$  fluxes with cutoffs for ESTES and a joint analysis by ANTARES and IceCube. ESTES is dominant over the other selection below a sine of declination of -0.2 for these scenarios. The flat portion of the ANTARES/IceCube joint analysis is dominated by ANTARES while the sharp falloff is dominated by IceCube.

of ESTES being sensitive below 100 TeV is its ability to measure softer fluxes better than harder fluxes. This

is also the opposite of most selections and leads to ESTES having the best sensitivity to these softer fluxes up to a sine of declination of -0.2, as can be seen in Figure 10.25.

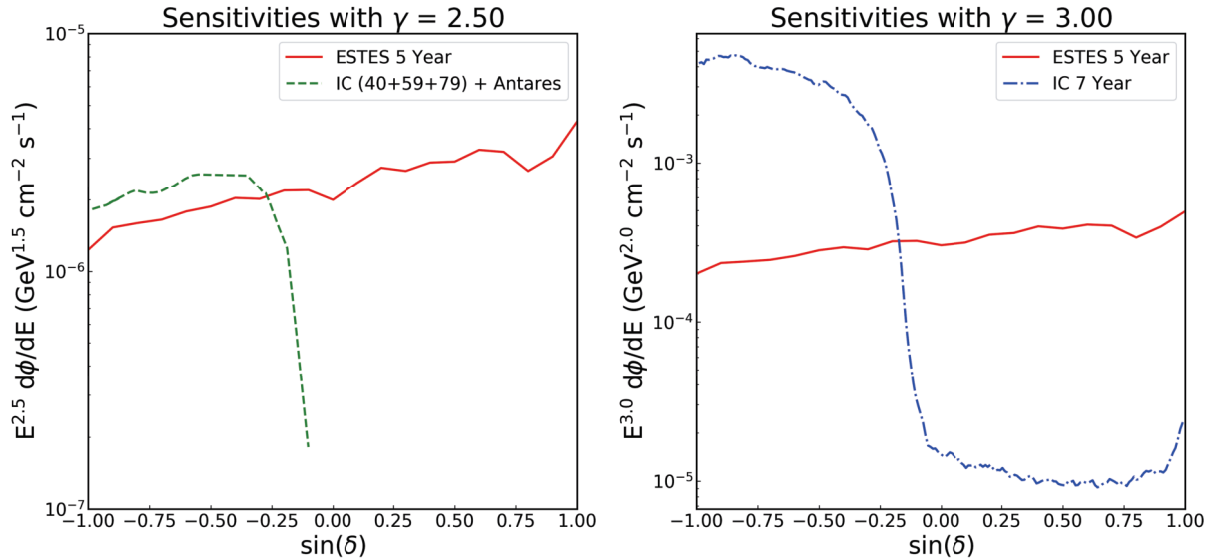


Figure 10.25: Sensitivity to  $E^{-2.5}$  and  $E^{-3}$  fluxes for ESTES, IceCube’s point source search, and a joint analysis by ANTARES and IceCube. ESTES is dominant over the other selection below a sine of declination of -0.2 for these scenarios. The flat portion of the ANTARES/IceCube joint analysis is dominated by ANTARES while the sharp falloff is dominated by IceCube. For the IceCube only search in the  $E^{-3}$  panel the poor sensitivity is due to an energy threshold above 100 TeV for events to enter the selection.

## 10.4 Conclusions

A new event selection, ESTES, has been presented and discussed. This is a new selection for finding events of astrophysical origin in archival IceCube data. Without the new techniques created for this selection these events would remain unused and unknown. ESTES is ready for use after its muon rejection power is verified. When verification is complete, ESTES will be the sole selection providing identifiable astrophysical tracks below 100 TeV and will provide some of IceCube’s most fascinating events from an astrophysical perspective. In lieu of the full data, prospects for different physics results have been discussed. ESTES can play an important role in both the discovery of or improved sensitivity to sources in the southern sky and contribute to the understanding of the astrophysical flux in the energy range from 10 to 100 TeV. Both measurements will confirm or place limits on relevant models. In particular in the case of the KRA- $\gamma$  model ESTES offers the most stringent sensitivity.

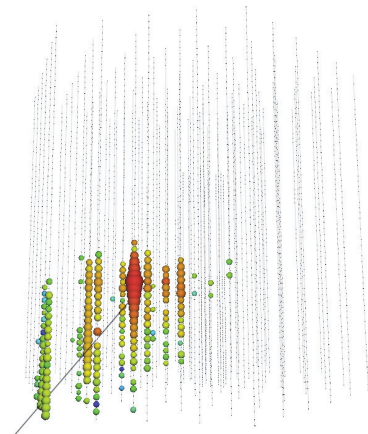
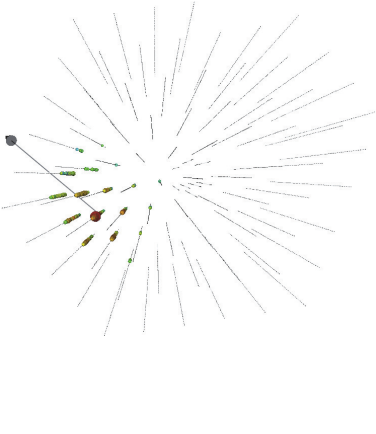
Although it was not discussed in this work, there is growing optimism about applying ESTES to cascade like events as well. This idea would take advantage of ESTES' coarse grid veto as a way to overcome some of the inherent issues with cascade angular resolution and pointing that for searches for cascades to use layer vetos. Doing this would allow more of the detector volume to be utilized in searches for cascades and would yield more astrophysical events for study.

If the strength of the neutrino sources remains below the detection threshold for ESTES then the ESTReS realtime filter offers the opportunity to detect and communicate about astrophysical neutrinos between 10 and 100 TeV in near realtime. This near realtime connection opens a new window for connections to measurements from other observatories and telescopes since the events coming from ESTReS offer the only opportunity to detect single astrophysical neutrinos in near realtime in this energy regime.

Together, ESTES and ESTReS will provide a unique window for advancing neutrino astronomy for the duration of IceCube's operation

## APPENDIX

### Interesting Observed Events

Side View	Top View	Astrophysical Probability Energy Estimate Zenith Angle $p_{miss}$ length
		<p style="text-align: center;">0.99 67.9 TeV 40.9° <math>8.7 \times 10^{-208}</math> 401 m</p>

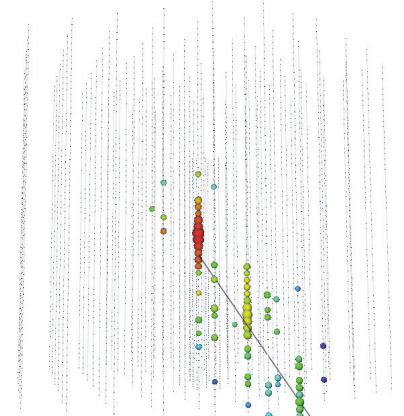
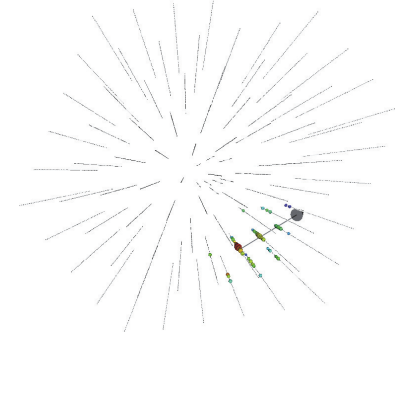
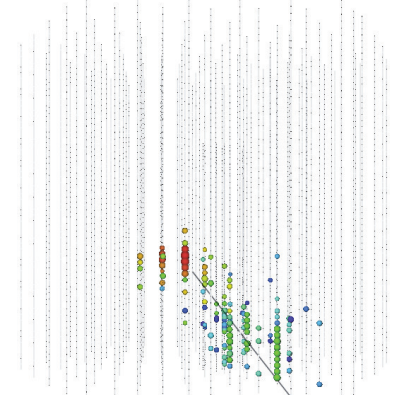
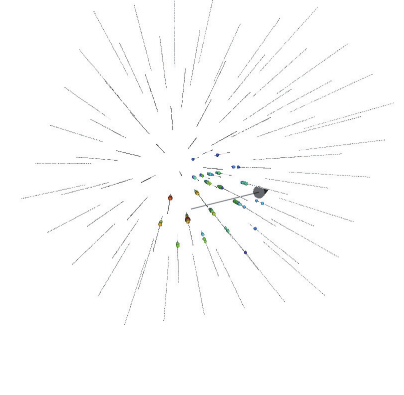
Side View	Top View	Astrophysical Probability Energy Estimate Zenith Angle $p_{miss}$ length
		0.98 30.0 TeV 34.7° $4.7 \times 10^{-29}$ 636 m
		0.98 20.6 TeV 38.1° $1.1 \times 10^{-39}$ 506 m

Table A.1: Table of the events which are likely to be astrophysical with more than 50% probability according to the best fit from the MESC selection [68]. Event views and basic information about each of the three events are provided.

## APPENDIX

### CORSIKA Modification For Faster Background Generation

#### B.1 Introduction

When estimating the background from air showers present in neutrino telescopes it is necessary to use simulations. Often the air shower simulation CORSIKA [123] is used. To accurately model the final products of an air shower, CORSIKA must track every interaction, decay, and particle present in these fabricated air showers. Since the number of secondary particles increases with energy this leads to a computation time which rises with the energy of the initial incident particle. The computation time required increases even more if rare showers are required, such as in [65].

In the specific case of [65] high energy neutrinos with no accompanying muons were the focus of study. Because neutrinos and muons are largely the decay products of secondary particles in air showers, they tend to be produced one power steeper than the cosmic ray spectrum. This makes obtaining statistics for high energy neutrinos difficult because showers which could produce a relevant neutrino often do not. Herein however, also lies an advantage. Since these neutrinos are the byproduct of secondary hadronic particles, the maximum neutrino energy obtainable in a given shower is limited by the highest energy hadronic particle. Thus, if at any point in shower development no hadron or neutrino above an energy of interest exists, then the shower being simulated is not relevant. Such showers do not need to be simulated to completion.

#### B.2 Modifications

When CORSIKA was developed in 1985 it was designed to handle primaries of all energies on contemporary systems. This meant keeping the memory footprint low was important. As such, a last in first out (LIFO) buffer was implemented. In this configuration, after the initial secondaries were produced, the most recently generated secondary was simulated next. Since new particles are always placed at the front of the buffer, the most recently generated child was simulated next. This process continues repeatedly until no new particles are added to the buffer after the simulation of an existing particle. At this point, a sibling of the previously simulated particle is simulated. Again, the generation of children repeats until no new particles are created. This process repeats until the shower completes. Effectively what is happening is the complete simulation of one branch of the shower before another begins. This completes the shower in a depth-first

manner. However, this type of shower development is not optimal for searching for the highest energy hadron since most energetic hadrons could not be simulated until nearly the end of the simulation of the shower.

Another option that exists for memory management is the first in first out (FIFO) buffer. In such a configuration, after the direct secondaries are generated, the first direct secondary would be simulated and its children placed at the end of the buffer. This continues until all the direct secondaries have been simulated. At this point the children of the direct secondaries, which are now at the front of the buffer, would be simulated and their children would be placed at the end of the buffer. This process would continue until all particles in the buffer have been simulated. A shower simulated in this way is propagated breadth-first and keeps particles in the buffer which are roughly the same number of decays/interactions after the primary particle. While this type of shower development requires more memory than a LIFO to complete the same task, it is near optimal for searching for the highest energy hadron. This is because every particle is kept at the same stage of shower development. Furthermore, high energy neutrinos appear soon after the initial interaction since it is difficult for hadrons to keep large amounts of energy through decays/interactions.

The only way to make the process of finding these neutrinos faster is to first simulate the hadrons which can create a neutrino above threshold. This can be done simply by operating the buffer as a dual ended insert and single ended removal buffer, making it a hybrid between the FIFO and LIFO. By putting particles which are above threshold at the front of the buffer and particles which are below threshold at the end of the buffer the relevant hadrons are inspected first while the rest of the shower is held. If a neutrino above threshold is produced, then the full shower can be completed. In this way only the necessary computations are completed to find out if the shower is relevant or not.

A version of CORSIKA with the implementation of the hybrid buffer and a threshold energy was the final outcome of the modifications. The threshold works by stopping showers and starting the next if no particles above the energy threshold are in the buffer and no neutrino above threshold has been created. Showers which are stopped save the primary particle's information to the output file, while fully propagated showers appear as normal output. This modification has been submitted to and accepted by the CORSIKA maintainers. It will appear in the next major release of CORSIKA.

### B.3 Performance

By stopping showers once they have crossed a threshold energy for neutrino production and saving their full output only if they possess a relevant neutrino we improve the run time and file size requirements of our simulation. Since the reduction truncates events and does not change the underlying algorithms, the savings are proportional to the amount of truncation achieved. This can be seen in Figure B.1 on top of a minimum floor value.

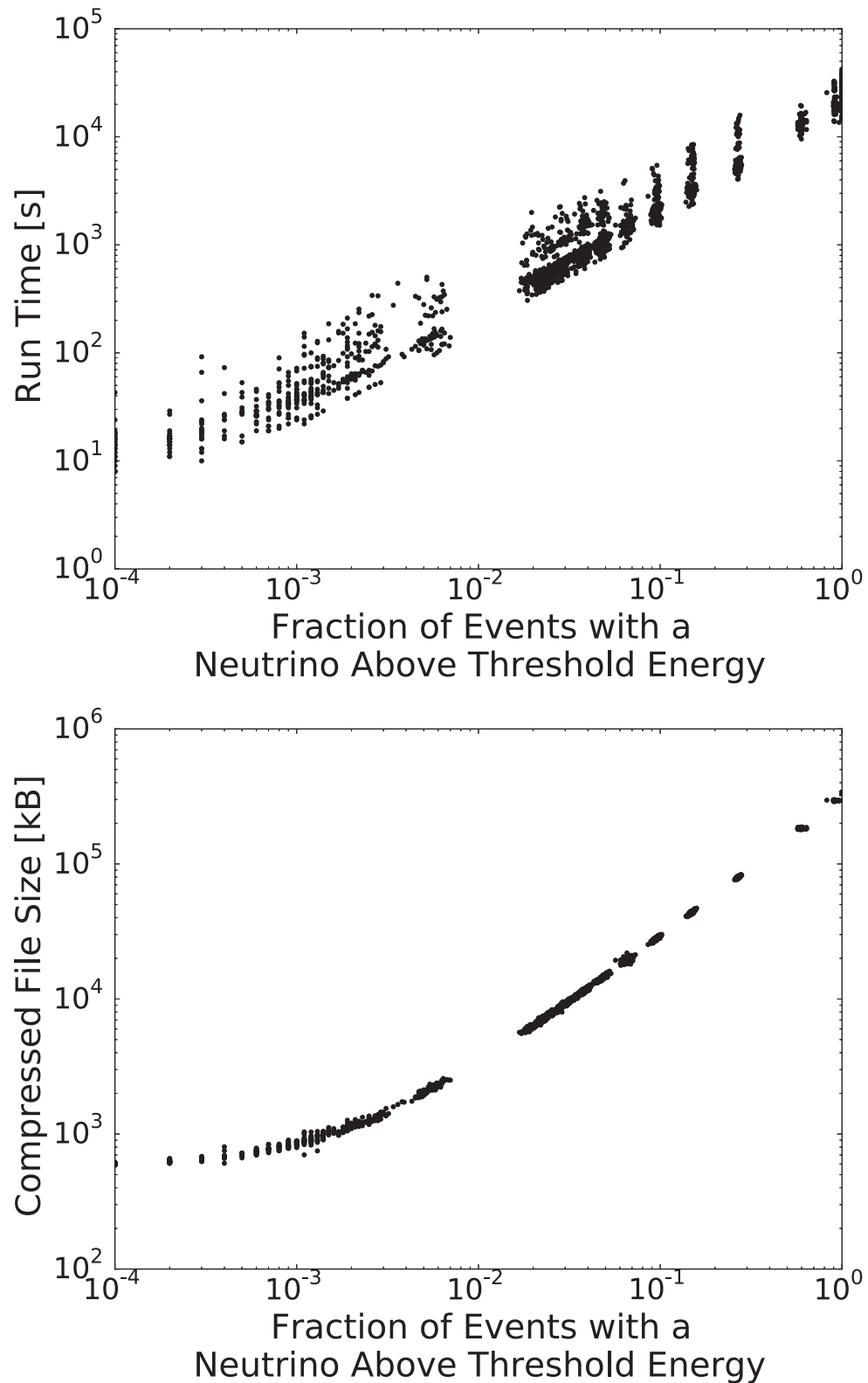


Figure B.1: The file size (top) and run time (bottom) as a function of the fraction of events above a threshold energy. Both show a power law dependence with an increasing fraction of events on top of a minimum floor value to run and save basic information when no events meet the criterion.



## B.4 Applications

This modification was first used to obtain statistics at high neutrino energy for [65]. Here, a data set of showers with neutrinos above 100 TeV allowed a model fit of suppressed atmospheric neutrino sources as well as a confirmation of the conventional atmospheric neutrino veto from [32].

One detail about neutrino vetos that was not in the scope of [65] is the question of what primaries create neutrinos which are not accompanied by enough muon energy at depth to consider them vetoed. This question is particularly relevant for surface vetos of neutrinos since it gives the relevant energy of primaries one must be able to reliably detect at the surface to reject the background of atmospheric neutrinos [67] [124]. To do this requires a connection between a neutrino and its parent primary, thus the question must be answered using Monte Carlo. Using the modification, a simulation sample was produced with a neutrino energy threshold of 50 TeV and the SIBYLL 2.1 interaction model [125]. From this data, the cumulative response to a given neutrino energy from possible parent primary types and energies was calculated assuming the composition model of [126] and is shown in the plots of Figure B.2.

These plots show that most of the contribution to neutrinos from 50-55 TeV comes from hydrogen primaries between 1-2 PeV. Additionally plotted is the fraction of neutrinos which have less than 300 GeV of accompanying muons (the passing fraction). For nearly vertical events, the largest contribution comes from neutrinos which take nearly all their parent's energy. As the zenith angle increases the muon energy decreases due to increased overburden leading to more events from higher energy primaries contributing to the passing fraction.

Another interesting potential use for these simulations is to determine the significance of events with a contained vertex from IceCube's high energy starting event search [70]. In the most recently released starting event data [127] a very vertical muon neutrino was found. This event starts after passing through more than 10 layers of DOMs and deposits 400 TeV of energy in the detector. Because of energy and zenith only charmed decays could potentially produce this event. Producing a target simulation with the modification and the DPMJET II.5 [128] hadronic model a background of one event per 391 years was found to be accompanied by a muon bundle with less than 300 GeV of total energy. This gives the event a conservative estimate of a  $3\sigma$  deviation from background since DPMJET II.5 is known to exceed the limits on charmed atmospheric muons and neutrinos [129] [130].

## B.5 Conclusion

Modifications to CORSIKA's memory management were made which make "breadth-first" shower propagation possible. With this it is possible to stop showers when particles in the shower have dropped below a threshold energy. In the case of this modification neutrinos were the focus, and a neutrino energy threshold

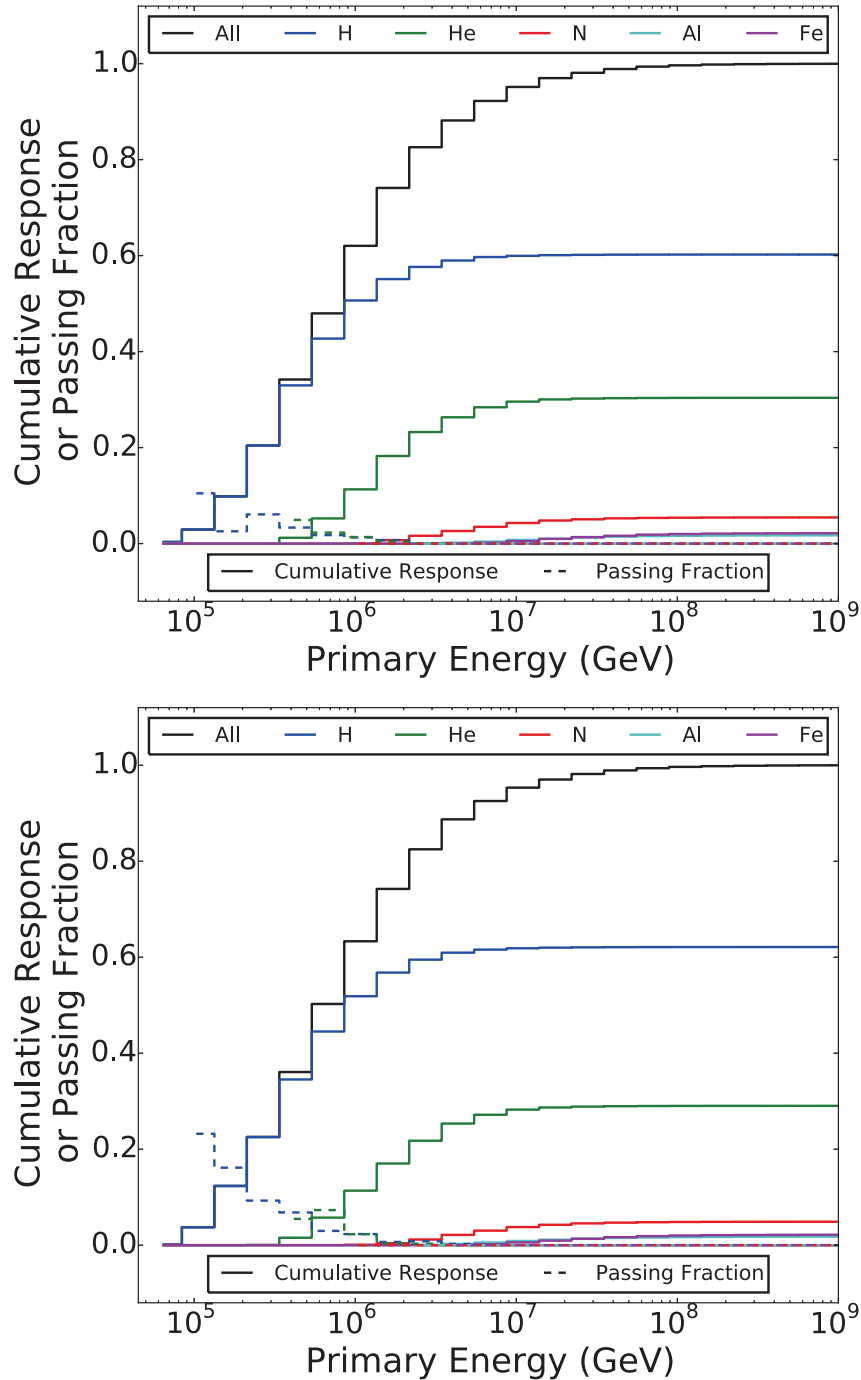


Figure B.2: The cumulative response(solid) and passing fraction(dashed) of 50 to 55 TeV neutrinos from various primaries are presented for two different zenith bands,  $1 < \cos(\theta) < .8$  (top) and  $.8 < \cos(\theta) < .6$  (bottom). The cumulative response shows how much a given primary type and energy contributes to the flux of neutrinos between 50 and 55 TeV in the zenith band. The passing fraction shows how often a shower of a given type and energy has a neutrino between 50 and 55 TeV in the zenith band but less than 1 TeV of muons at the depth of IceCube. The largest contribution to the passing fraction always comes from primaries near the neutrino energy.

was also implemented. The modified code will be available for use in the next public release of CORSIKA. Already this modification has assisted in determining the significance of a starting event from IceCube's high energy starting event sample and can play a role in determining the backgrounds for a possible surface veto above IceCube.

## APPENDIX

### The pDOM DAQ

This appendix describes a project completed for this thesis to redesign the DAQ of the DOM. This project was a sub project of what is known as the pDOM or prototype DOM which was a complete overhaul of the DOM's electronics from the original design. The intended sampling speed was 300 MHz, but was never achieved with this design. A single implementation of this design can be run at 200 MHz. In order to achieve this a triple implementation of the system designed below was run in parallel at 100MHz and gave the desired 300 MHz. This 300 MHz system was not implemented by me so I take no credit beyond the initial system.

#### C.1 Description of the DAQ System

The DAQ system was constructed of three components, a Field Programmable Gate Array (FPGA) embedded in a test kit, a Analog to Digital Converter (ADC), and a high speed bridge to connect them, shown in Figure C.1. All of the logic to store the data from the ADC was implemented on the FPGA. The logic of all processes on the FPGA was implemented as state machines to make the design modular, reproducible, and optimized.

The FPGA performs a few operations continuously that are vital to its operation. A clock signal is derived off of a 148.5 MHz oscillator included on the test kit after being fed through a phase locked loop (PLL) which converts the signal to a 200.0625 MHz clock and feeds it off the board via SubMiniature version A (SMA) cable, highlighted in blue in Figure C.2, to the clock input of the ADC, as can be seen in the cable connecting the FPGA and ADC at the bottom of Figure C.1. The ADC then uses this clock to sample incoming signals and feeds the sampled values and state of the sample clock back to the ADC via the HSMC (High Speed Mezzanine Card) bridge. The clock and data are then sampled by a double data rate module and aligned to each other by a PLL. It is important to note that the bits of each sample are interleaved at this point and must be de-interleaved to properly recover the sample. The clock that is derived at this point is the clock which controls all other operations of the FPGA.

The moment the FPGA program is loaded a local counter begins iterating up from 0 to indicate the local time for the digitizer system. The counter is 48 bits in length and has a rollover approximately every 1407374

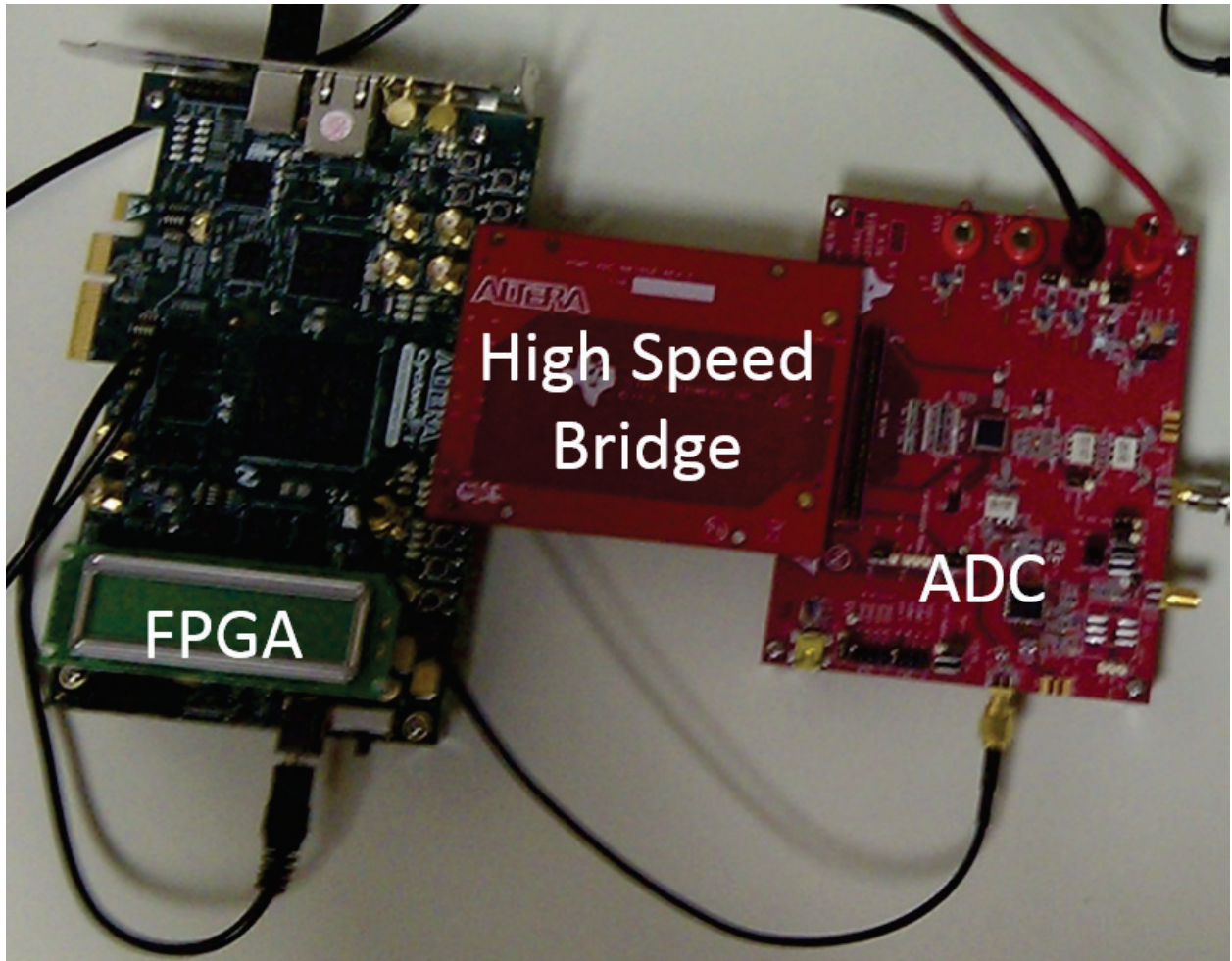


Figure C.1

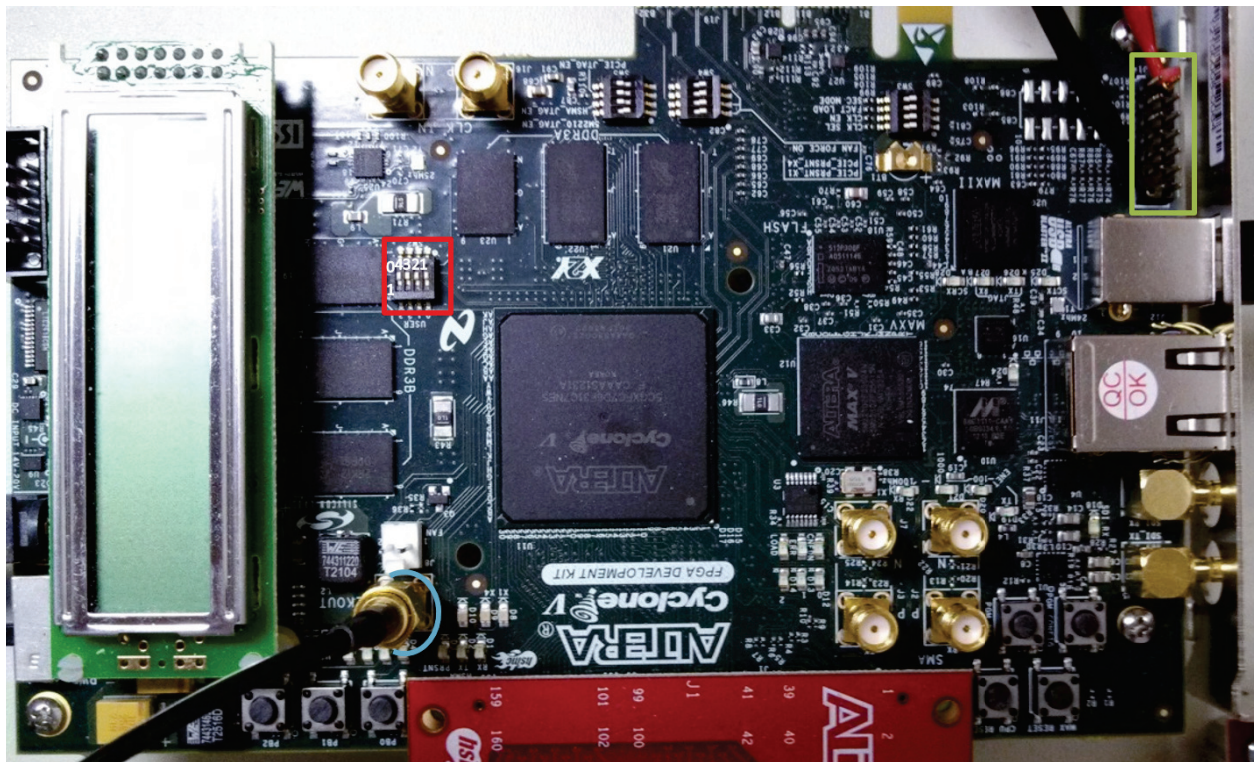


Figure C.2

seconds or  $\sim 16$  days at a clock speed of 200 MHz. When the FPGA program is loaded to the firmware it is automatically sitting in it's home state where nothing will happen. The program will operate a check on the state of a set of switches, boxed in red in Figure C.2, on the board during each clock cycle. This is done by storing a list of the switch values from the previous clock cycle and a list of the current switch values. This list would be 0,0,0,0 when all the switches are in their off positions. When one of the switches is changed, the new configuration is checked for a match against sets that correspond to normal data taking, baseline measurement, and forced data taking. This is implemented in a case statement and can be thought of as the state machine in Figure C.3. The activation of one of these modes allows the FPGA to begin executing the

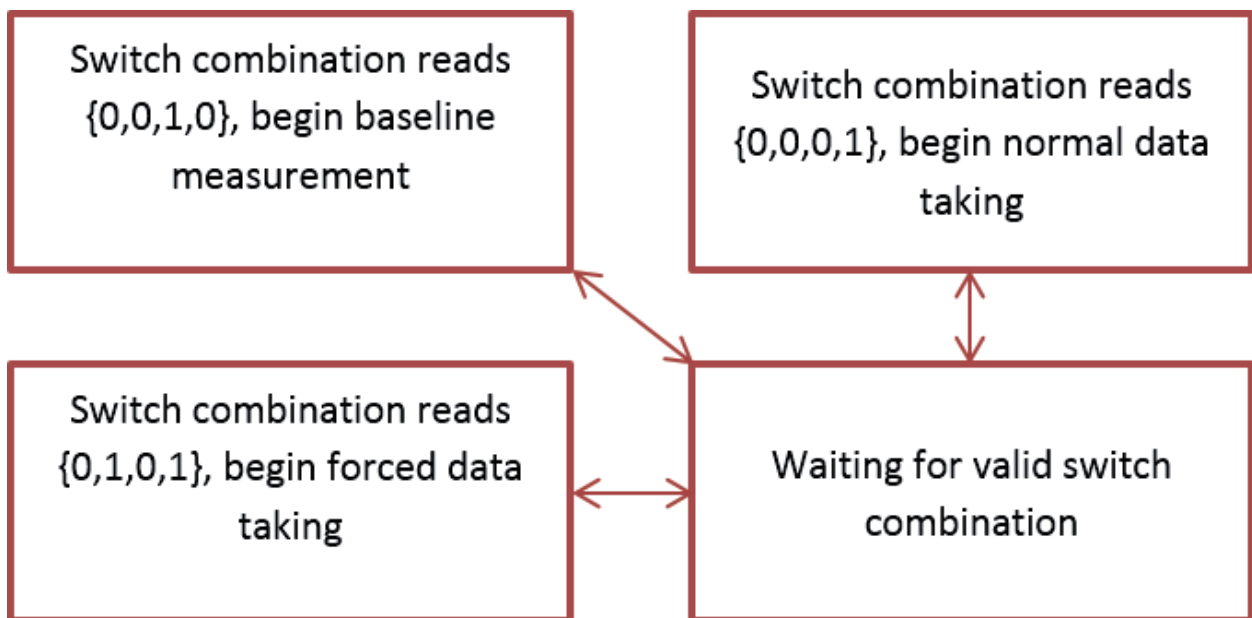


Figure C.3

corresponding acquisition code.

The simplest of the acquisition codes is the baseline taking case. It's operation can be found in the flow diagram below, Figure C.4. One should note that in the states do not always go in strict binary order, but do always increase. This is because one can save on time by not iterating a counter variable at the completion of each state but instead by using the change of existing signals to indicate a change in the state. The result of the state machine is the storage of two pieces of information, one that indicates if the baseline, or zero voltage value, needs to be shifted up or down for the subsequently taken data and one that stores how much of a shift needs to be performed. The act of shifting the data is never performed on the FGPA to save time during clock cycles. Instead the shift is performed on the thresholds only and is passed off the board as part of a header that gives other information about saved events.

The normal and forced data taking modes are actually the same set of case statements with different sub case statements that perform operations depending on the state of the forced trigger flag, 0=not a forced trigger, 1=forced trigger. The activation of the normal or forced mode also starts a scaler counter, this counter checks on every clock cycle if the incoming data is above a scaler threshold, which can be set independent of the normal threshold. If the threshold is exceeded the scaler counter is incremented by one. Every  $2^{18}$  clock cycles ( every millisecond) the value of the scaler counter is pushed to the a processor for recording and then reset to 0. The processor is set up to directly read the output of the scaler counter and buffers which contain waveforms and header information for those waveforms. As a result there are some communications which go between the FPGA and processor that become necessary. The extent of the purpose of these communications is to start and stop data acquisition so the processor's buffers don't overflow and subsequently lose data before they are emptied. This is a difficult problem to overcome because the processor is running at a maximum speed of 100 MHz and therefore can only pull one sample off a storage array for every two written into it. As a result the DAQ must stop data acquisition and drain the buffers when using the processor. More about this will be discussed after describing the flow of the data acquisition. The main goal of the data acquisition system is to have a buffer of the past N events and inspect the most recent for passing of a threshold. When this is true the buffer, which includes the above threshold point, begins being saved in a waveform buffer until the incoming data has gone below threshold for a specified amount of them. At this point a header with the event time, event length, forced trigger info, and baseline adjustment parameters is saved while new data is analyzed. This system is visualized in Figure C.4 and the state diagram is in Figure C.5. The data acquisition states are designed to have no deadtime when operating without the slow processor, writing to the waveform buffer happens on every clock cycle and writing to the waveform header buffer occurs after an event has finished simultaneously with a new event being looked for.

## C.2 Data Taking Setup for the DAQ System

The system was validated with a simple experimental setup which involved a light pulse generator, labotamized DOM, and the setup of the test DAQ. The configuration is shown in Figure C.6. The DAQ system was switched into the forced data taking mode and began generating pulses every second. These pulses triggered a pulsed laser which fed into a light diffuser. The light diffuser cut down the number of photons which were subsequently led to a DOM in a light tight box via a fiber optic cable. Just before the photons left the cable a second diffuse was used. The number of photons was tuned such that either 0, 1, or on rare occasion 2 photons were recorded with each pulse of the laser. The DOM was modified such that only the high voltage and coupling transformer were left. The DAQ was attached directly to the cable coming from coupling transformer. In this way the response of the system to single PEs was inspected. An example waveform with charge of 1 PE is shown in Figure C.7.



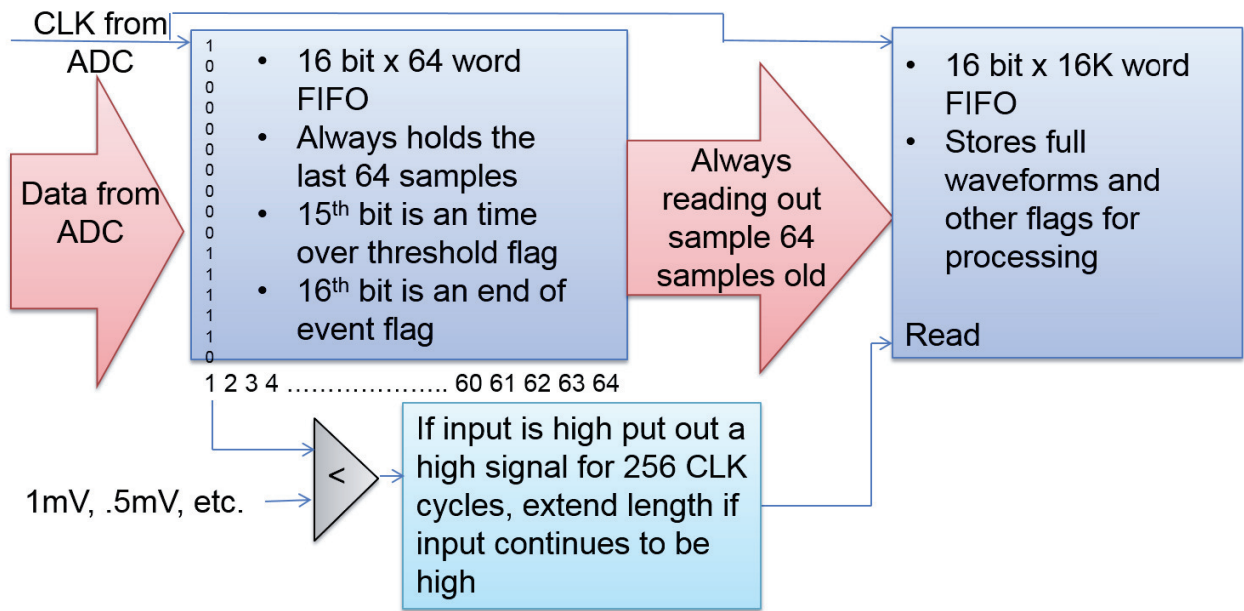


Figure C.4

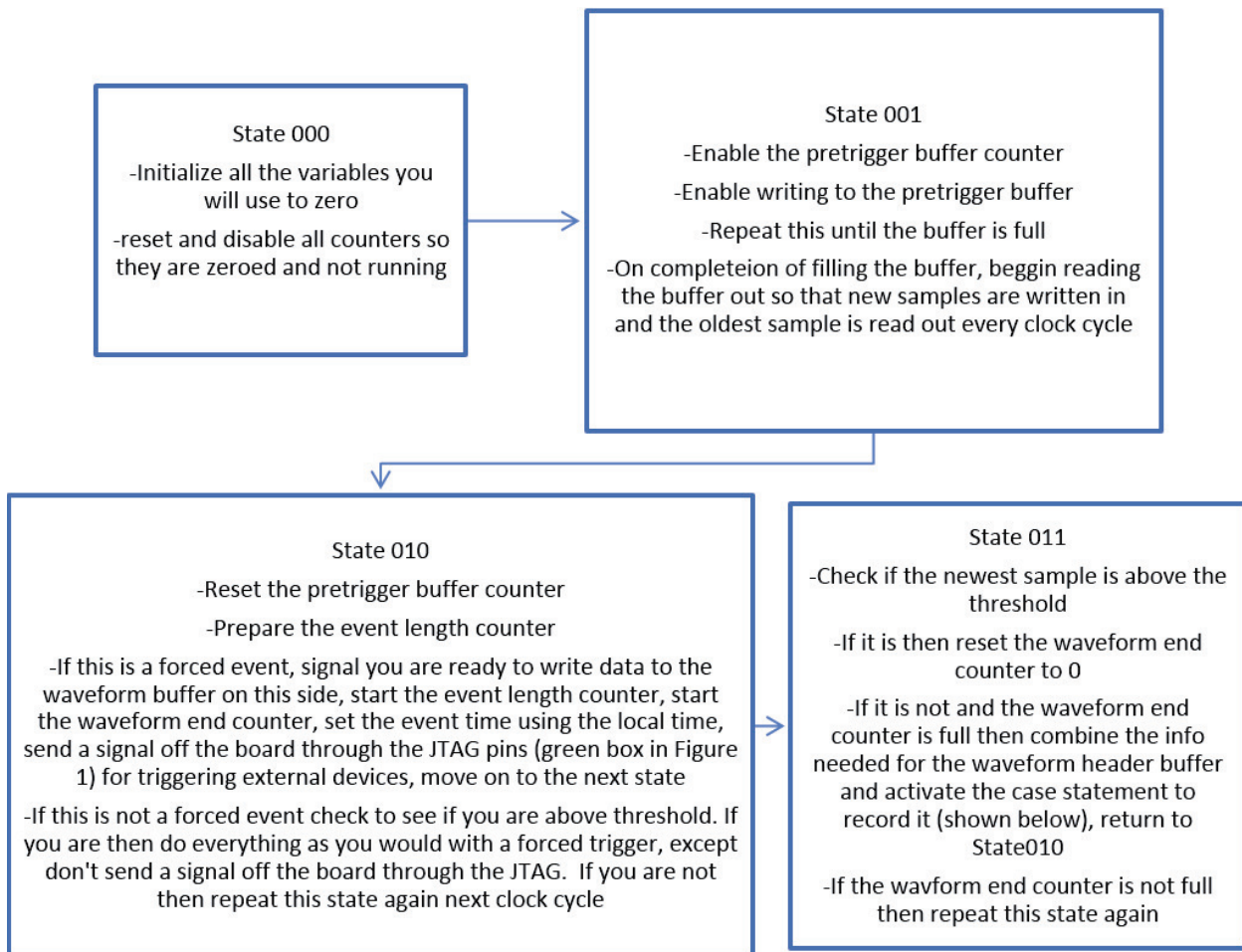


Figure C.5

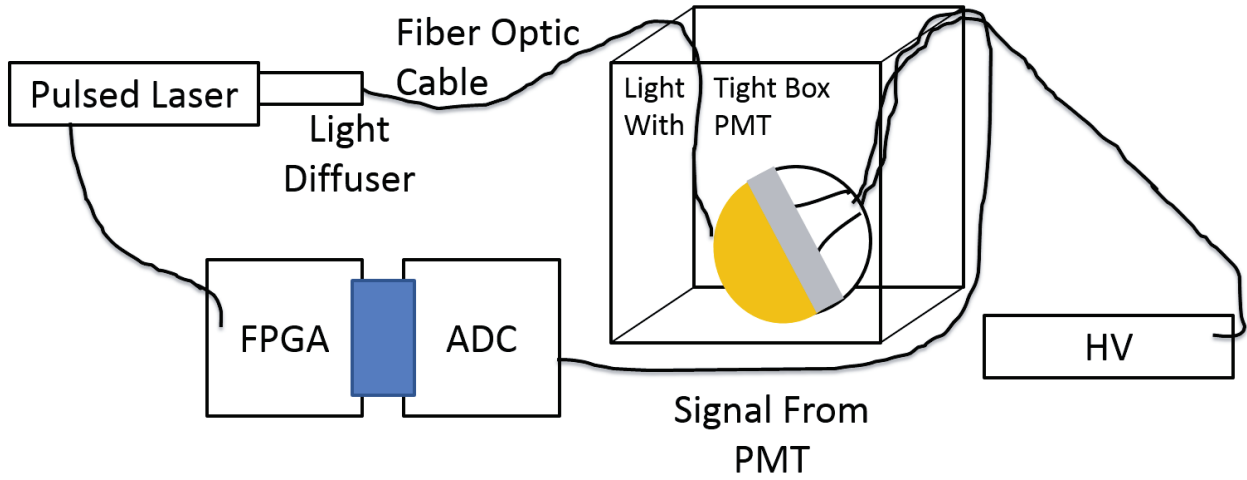


Figure C.6

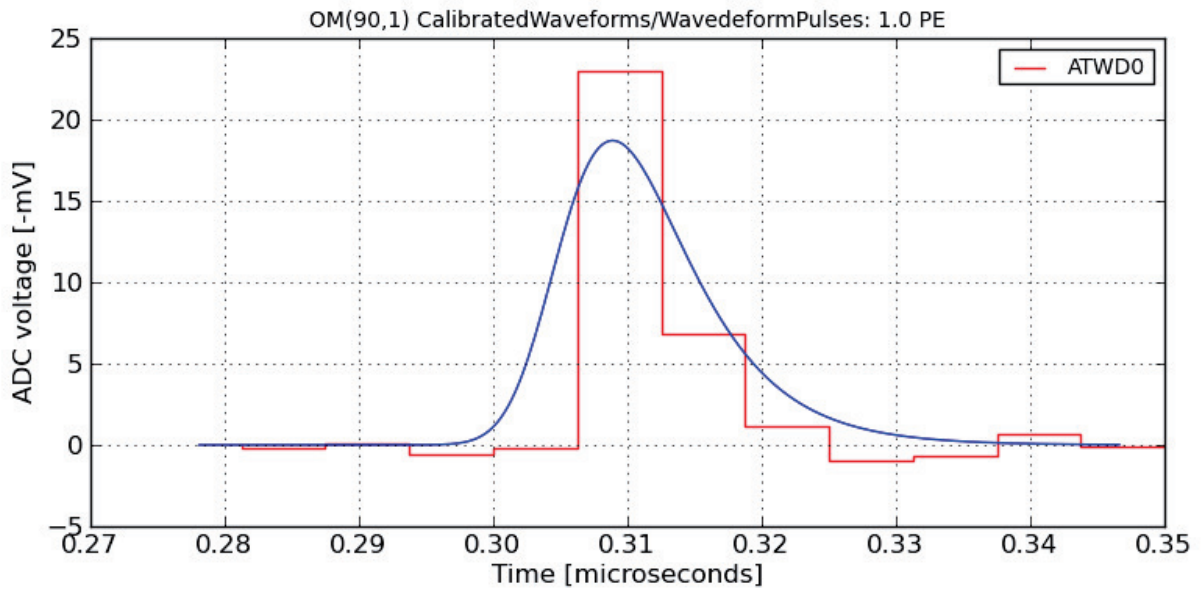


Figure C.7

### C.3 Results of Data Taking With the DAQ System

The interesting quantities for the system to measure are the charge of the single PE events and their time delay. Both should be close to what the measured IceCube values are. Figure C.8 shows a histogram of the charge of a collection of events and their corresponding time delay from the PMT transit. The charge

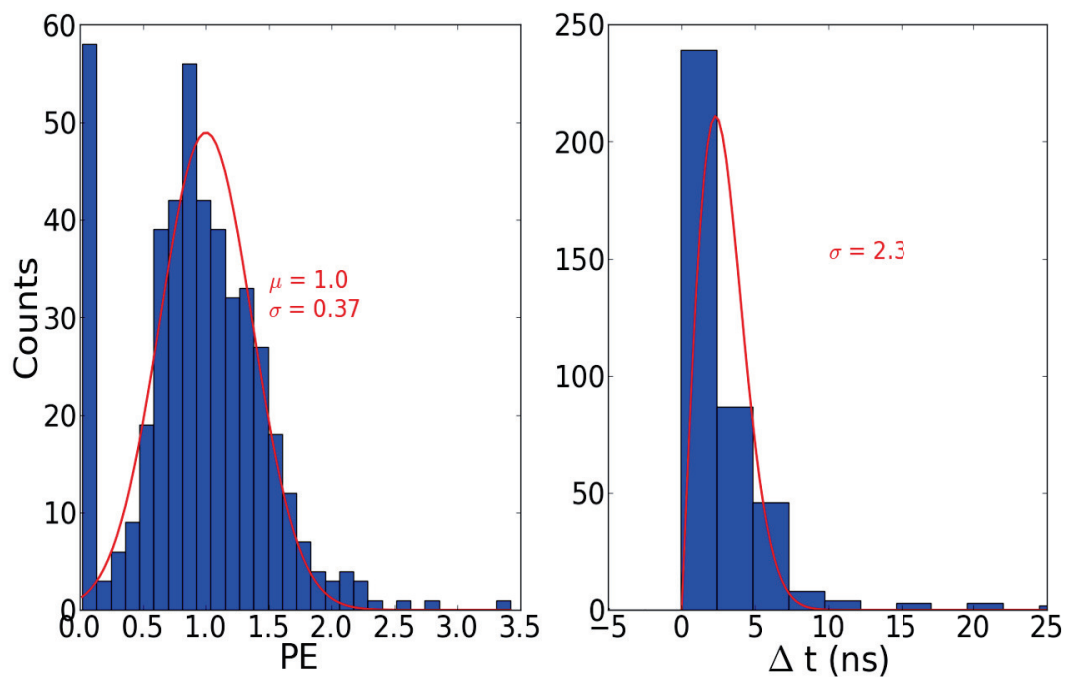


Figure C.8

histogram at left is fit to a Gaussian, with 0 values ignored, to determine the mean and standard deviation. A mean charge of 1 is obtained with a standard deviation of .37. This agrees with the values measured in IceCube. The timing distribution on the right has an average width of 2.3 ns which is in line with the 3 ns value commonly quoted for IceCube's PMTs.

## APPENDIX

### LIST OF REFERENCES

- [1] Charles-Augustin de Coulomb. Troisième mémoire sur l'électricité et le magnétisme. *Histoire de l'Académie Royale des Sciences*, 1785.
- [2] Marie Curie. *Recherches sur les substances radioactives*. Gauthier-Villars, 1904.
- [3] V. F. Hess. Ältere Beobachtungen der durchdringenden Strahlung bei sieben Freiballonfahrten. *Physikalische Zeitschrift*, 13:1084–1091, November 1912.
- [4] James J Beatty and Stefan Westerhoff. The highest-energy cosmic rays. *Annual Review of Nuclear and Particle Science*, 59:319–345, 2009. URL: <http://www.annualreviews.org/doi/abs/10.1146/annurev.nucl.58.110707.171154>.
- [5] C. Patrignani et al. Review of Particle Physics. *Chin. Phys.*, C40(10):100001, 2016. doi:10.1088/1674-1137/40/10/100001.
- [6] Juerg Beringer, J-F Arguin, RM Barnett, K Copic, O Dahl, DE Groom, C-J Lin, J Lys, H Murayama, CG Wohl, et al. Review of particle physics particle data group. *Physical Review D (Particles, Fields, Gravitation and Cosmology)*, 86(1), 2012. URL: <http://pdg.lbl.gov/>.
- [7] Emiliano Mocchiutti. Direct detection of cosmic rays: through a new era of precision measurements of particle fluxes. *Nuclear Physics B-Proceedings Supplements*, 256:161–172, 2014. URL: <https://arxiv.org/abs/1407.1143>.
- [8] Vitalii Lazarevich Ginzburg and SI Syrovatsky. Origin of cosmic rays. *Progress of Theoretical Physics Supplement*, 20:1–83, 1961. URL: <http://iopscience.iop.org/article/10.1070/PU1966v009n02ABEH002871>.
- [9] Satyendra Thoudam, JP Rachen, A van Vliet, A Achterberg, S Buitink, H Falcke, and JR Hörandel. Cosmic-ray energy spectrum and composition up to the ankle: the case for a second galactic component. *Astronomy & Astrophysics*, 595:A33, 2016. URL: <https://arxiv.org/abs/1605.03111>.
- [10] High Resolution Fly's Eye Collaboration, RU Abbasi, T Abu-Zayyad, M Allen, JF Amman, G Archbold, K Belov, JW Belz, SY Ben Zvi, DR Bergman, et al. First observation of the greisen-zatsepinkuzmin suppression. *Physical Review Letters*, 100(10):101101, 2008. URL: <https://arxiv.org/abs/astro-ph/0703099>.
- [11] Tareq Abu-Zayyad, R Aida, M Allen, R Anderson, R Azuma, E Barcikowski, JW Belz, DR Bergman, SA Blake, R Cady, et al. The cosmic-ray energy spectrum observed with the surface detector of the telescope array experiment. *The Astrophysical Journal Letters*, 768(1):L1, 2013. URL: <https://arxiv.org/abs/1205.5067>.

- [12] P Abreu, M Aglietta, EJ Ahn, IFM Albuquerque, D Allard, I Allekotte, J Allen, P Allison, J Alvarez Castillo, J Alvarez-Muñiz, et al. The pierre auger observatory ii: Studies of cosmic ray composition and hadronic interaction models. *arXiv preprint arXiv:1107.4804*, 2011. URL: <https://arxiv.org/abs/1107.4804>.
- [13] Francis Halzen and Dan Hooper. High-energy neutrino astronomy: the cosmic ray connection. *Reports on Progress in Physics*, 65(7):1025, 2002. URL: <https://arxiv.org/abs/astro-ph/0204527>.
- [14] AM Hillas. The origin of ultra-high-energy cosmic rays. *Annual Review of Astronomy and Astrophysics*, 22:425–444, 1984. URL: <http://www.annualreviews.org/doi/abs/10.1146/annurev.aa.22.090184.002233>.
- [15] Hillas plot. URL: <http://rsta.royalsocietypublishing.org/content/roypta/366/1884/4417/F2.large.jpg>.
- [16] Wikimedia Commons. *Gamma rays mean free path*. 2014. URL: [https://commons.wikimedia.org/wiki/File:Gamma\\_ray\\_mean\\_free\\_path.png](https://commons.wikimedia.org/wiki/File:Gamma_ray_mean_free_path.png).
- [17] Charles D Dermer. Best-bet astrophysical neutrino sources. In *Journal of Physics: Conference Series*, volume 60, page 8. IOP Publishing, 2007. URL: <https://arxiv.org/abs/astro-ph/0611191>.
- [18] Thomas K Gaisser, Ralph Engel, and Elisa Resconi. *Cosmic rays and particle physics*. Cambridge University Press, 2016. URL: <http://alpha.sinp.msu.ru/~panov/Gaisser1990.pdf>.
- [19] ENRICO Fermi. On the origin of the cosmic radiation. *Phys. Rev.*, 75:1169–1174, Apr 1949. URL: <http://link.aps.org/doi/10.1103/PhysRev.75.1169>, doi:10.1103/PhysRev.75.1169.
- [20] Yves A Gallant. Particle acceleration at relativistic shocks. In *Relativistic flows in Astrophysics*, pages 24–40. Springer, 2002. URL: <https://arxiv.org/abs/astro-ph/0201243>.
- [21] Michal Ostrowski. Energetic particle acceleration in shear layers. *arXiv preprint astro-ph/9911091*, 1999. URL: <https://arxiv.org/abs/astro-ph/9911091>.
- [22] P. Goldreich and W. H. Julian. Pulsar Electrodynamics. *Astrophysical Journal*, 157:869, August 1969. doi:10.1086/150119.
- [23] John N Bahcall, Neta A Bahcall, and Giora Shaviv. Present status of the theoretical predictions for the cl 37 solar-neutrino experiment. *Physical Review Letters*, 20(21):1209, 1968. URL: <https://journals.aps.org/prl/abstract/10.1103/PhysRevLett.20.1209>.
- [24] V. Radeka R. Davis Jr., J. C. Evans and L. C. Rogers. Report on the brookhaven solar neutrino. *Proceeding Symposium Neutrino, Balatonfured, Hungary*, 1972. URL: <https://digital.library.unt.edu/ark:/67531/metadc1028894/>.
- [25] K. S. Hirata, T. Kajita, T. Kifune, K. Kihara, M. Nakahata, K. Nakamura, S. Ohara, Y. Oyama, N. Sato, M. Takita, Y. Totsuka, Y. Yaginuma, M. Mori, A. Suzuki, K. Takahashi, T. Tanimori, M. Yamada, M. Koshiba, T. Suda, K. Miyano, H. Miyata, H. Takei, K. Kaneyuki, H. Nagashima, Y. Suzuki, E. W. Beier, L. R. Feldscher, E. D. Frank, W. Frati, S. B. Kim, A. K. Mann, F. M. Newcomer, R. Van Berg, and W. Zhang. Observation of  $^8\text{B}$  solar neutrinos in the kamiokande-ii detector. *Phys. Rev. Lett.*, 63:16–19, Jul 1989. URL: <https://link.aps.org/doi/10.1103/PhysRevLett.63.16>, doi:10.1103/PhysRevLett.63.16.

- [26] John F Beacom, Nicole F Bell, Dan Hooper, Sandip Pakvasa, and Thomas J Weiler. Measuring flavor ratios of high-energy astrophysical neutrinos. *Physical Review D*, 68(9):093005, 2003. URL: <https://arxiv.org/abs/hep-ph/0307025>.
- [27] H Athar, M Jezabek, and O Yasuda. Effects of neutrino mixing on high-energy cosmic neutrino flux. *Physical Review D*, 62(10):103007, 2000. URL: <https://arxiv.org/abs/hep-ph/0005104>.
- [28] Joseph A Formaggio and GP Zeller. From  $\nu_e$  to  $\bar{\nu}_e$ : Neutrino cross sections across energy scales. *Reviews of Modern Physics*, 84(3):1307, 2012. URL: <https://arxiv.org/abs/1305.7513>.
- [29] Jakob Van Santen. *Neutrino Interactions in IceCube above 1 TeV*. PhD thesis, University of Wisconsin Physics Department, 2014. URL: <https://inspirehep.net/record/1339582/references>.
- [30] Bernhard Voigt. *Sensitivity of the IceCube detector for ultra-high energy electron-neutrino events*. PhD thesis, Humboldt-Universität zu Berlin, Mathematisch-Naturwissenschaftliche Fakultät I, 2008. URL: <https://edoc.hu-berlin.de/handle/18452/16502>.
- [31] Raj Gandhi, Chris Quigg, Mary Hall Reno, and Ina Sarcevic. Ultrahigh-energy neutrino interactions. *Astroparticle Physics*, 5(2):81–110, 1996. URL: <https://arxiv.org/abs/hep-ph/9512364>.
- [32] Stefan Schönert, Thomas K Gaisser, Elisa Resconi, and Olaf Schulz. Vetoing atmospheric neutrinos in a high energy neutrino telescope. *Physical Review D*, 79(4):043009, 2009. URL: <https://arxiv.org/abs/0812.4308>.
- [33] Anatoli Fedynitch, Ralph Engel, Thomas K Gaisser, Felix Riehn, and Todor Stanev. Calculation of conventional and prompt lepton fluxes at very high energy. In *EPJ Web of Conferences*, volume 99, page 08001. EDP Sciences, 2015. URL: <https://arxiv.org/abs/1503.00544>.
- [34] Francis Halzen and Logan Wille. Upper limit on forward charm contribution to atmospheric neutrino flux. *arXiv preprint arXiv:1601.03044*, 2016. URL: <https://arxiv.org/abs/1601.03044>.
- [35] Rikard Enberg. Neutrinos from charm production in the atmosphere. In *AIP Conference Proceedings*, volume 1630, pages 44–49. AIP, 2014. URL: <https://arxiv.org/abs/1402.0880>.
- [36] Rhorry Gauld, Juan Rojo, Luca Rottoli, Subir Sarkar, and Jim Talbert. The prompt atmospheric neutrino flux in the light of lhcb. *Journal of High Energy Physics*, 2016(2):130, 2016. URL: <https://arxiv.org/abs/1511.06346>.
- [37] MG Aartsen, K Abraham, M Ackermann, Joe Adams, JA Aguilar, M Ahlers, M Ahrens, D Altmann, K Andeen, T Anderson, et al. Observation and characterization of a cosmic muon neutrino flux from the northern hemisphere using six years of icecube data. *The Astrophysical Journal*, 833(1):3, 2016. URL: <https://arxiv.org/abs/1607.08006>.
- [38] Markus Ahlers, Yang Bai, Vernon Barger, and Ran Lu. Galactic neutrinos in the tev to pev range. *Physical Review D*, 93(1):013009, 2016. URL: <https://arxiv.org/abs/1505.03156>.
- [39] Walter Baade and Fritz Zwicky. On super-novae. *Proceedings of the National Academy of Sciences*, 20(5):254–259, 1934. URL: <https://authors.library.caltech.edu/5688/1/ZWIpnas39a.pdf>.
- [40] Kurt W Weiler and N Panagia. Are crab-type supernova remnants (plerions) short-lived? *Astronomy and Astrophysics*, 70:419, 1978. URL: <http://adsabs.harvard.edu/abs/1978A%26A...70..419W>.
- [41] D. Backer, S. Kulkarni, C. Heiles, M. Davis, and M. Goss. Millisecond Pulsar in 4C 21.53. *IAU Circulars*, 3743:2, November 1982.

- [42] Ke Fang, Kumiko Kotera, and Angela V Olinto. Newly born pulsars as sources of ultrahigh energy cosmic rays. *The Astrophysical Journal*, 750(2):118, 2012. URL: <https://arxiv.org/abs/1201.5197>.
- [43] Kevin Schawinski, Stephen Justham, Christian Wolf, Philipp Podsiadlowski, Mark Sullivan, Katrien C Steenbrugge, Tony Bell, Hermann-Josef Röser, Emma S Walker, Pierre Astier, et al. Supernova shock breakout from a red supergiant. *Science*, 321(5886):223–226, 2008. URL: <https://arxiv.org/abs/0803.3596>.
- [44] K Koyama, V Gotthelf, and U I-lwangi. Evidence for shock acceleration of high-energy electrons in the. *Nature*, 378:16, 1995. URL: <https://www.nature.com/articles/378255a0>.
- [45] LO’C Drury, FA Aharonian, and HJ Völk. The gamma-ray visibility of supernova remnants. a test of cosmic ray origin. *Astronomy and Astrophysics*, 287:959–971, 1994. URL: <https://arxiv.org/abs/astro-ph/9305037>.
- [46] Hugo R Christiansen, Mariana Orellana, and Gustavo E Romero. High-energy neutrino emission from x-ray binaries. *Physical Review D*, 73(6):063012, 2006. URL: <https://arxiv.org/abs/astro-ph/0509214>.
- [47] Malcolm S Longair. *High energy astrophysics*. cambridge university Press, 2011. URL: [http://alpha.sinp.msu.ru/~panov/LibBooks/CR/1556\\_\\_legalreads.com.pdf](http://alpha.sinp.msu.ru/~panov/LibBooks/CR/1556__legalreads.com.pdf).
- [48] Armen Atoyan and Charles D Dermer. High-energy neutrinos from photomeson processes in blazars. *Physical Review Letters*, 87(22):221102, 2001. URL: <https://arxiv.org/abs/astro-ph/0108053>.
- [49] RJ Protheroe. High energy neutrinos from blazars. *arXiv preprint astro-ph/9607165*, 1996. URL: <https://arxiv.org/abs/astro-ph/9607165>.
- [50] Charles D Dermer, Enrico Ramirez-Ruiz, and Truong Le. Correlation of photon and neutrino fluxes in blazars and gamma-ray bursts. *The Astrophysical Journal Letters*, 664(2):L67, 2007. URL: <http://iopscience.iop.org/article/10.1086/520638>.
- [51] Dafne Guetta, D Hooper, J Alvarez-Muniz, F Halzen, and E Reuveni. Neutrinos from individual gamma-ray bursts in the batse catalog. *Astroparticle Physics*, 20(4):429–455, 2004. URL: <https://arxiv.org/abs/astro-ph/0302524>.
- [52] Ph Podsiadlowski, PA Mazzali, K Nomoto, D Lazzati, and E Cappellaro. The rates of hypernovae and gamma-ray bursts: implications for their progenitors. *The Astrophysical Journal Letters*, 607(1):L17, 2004. URL: <https://arxiv.org/abs/astro-ph/0403399>.
- [53] FW Stecker. Upper limits to fluxes of neutrinos and gamma-rays from starburst galaxies. In *Journal of Physics: Conference Series*, volume 60, page 215. IOP Publishing, 2007. URL: <https://arxiv.org/abs/astro-ph/0610208>.
- [54] Keith Bechtol, Markus Ahlers, Mattia Di Mauro, Marco Ajello, and Justin Vandenbroucke. Evidence against star-forming galaxies as the dominant source of icecube neutrinos. *The Astrophysical Journal*, 836(1):47, 2017. URL: <https://arxiv.org/abs/1511.00688>.
- [55] Kenneth Greisen. End to the cosmic-ray spectrum? *Physical Review Letters*, 16(17):748, 1966. URL: <https://journals.aps.org/prl/abstract/10.1103/PhysRevLett.16.748>.
- [56] Georgi T Zatsepin and Vadem A Kuz’min. Upper limit of the spectrum of cosmic rays. *JETP Lett.(USSR)(Engl. Transl.)*, 4, 1966. URL: <http://inspirehep.net/record/49999?ln=en>.



- [57] VS Beresinsky and GT Zatsepin. Cosmic rays at ultra high energies (neutrino?). *Physics Letters B*, 28(6):423–424, 1969. URL: <http://www.sciencedirect.com/science/article/pii/0370269369903414>.
- [58] David Seckel. In-ice radio detection of gzk neutrinos. In *AIP Conference Proceedings*, volume 579, pages 196–203. AIP, 2001. URL: <https://arxiv.org/abs/astro-ph/0103300>.
- [59] Florian Scheck. Muon physics. *Physics Reports*, 44(4):187–248, 1978. URL: <https://www.sciencedirect.com/science/article/pii/0370157378900145>.
- [60] J-H Koehne, Katharina Frantzen, Martin Schmitz, Tomasz Fuchs, Wolfgang Rhode, Dmitry Chirkin, and J Becker Tjus. Proposal: A tool for propagation of charged leptons. *Computer Physics Communications*, 184(9):2070–2090, 2013. URL: <http://linkinghub.elsevier.com/retrieve/pii/S0010465513001355>.
- [61] John David Jackson. *Classical electrodynamics*. John Wiley & Sons, 2007. URL: <http://www.thp.uni-koeln.de/alexal/pdf/electrodynamics.pdf>.
- [62] Rasha Abbasi, Yasser Abdou, T Abu-Zayyad, J Adams, JA Aguilar, M Ahlers, K Andeen, J Auffenberg, X Bai, M Baker, et al. Calibration and characterization of the icecube photomultiplier tube. *Nuclear Instruments and Methods in Physics Research Section A: Accelerators, Spectrometers, Detectors and Associated Equipment*, 618(1):139–152, 2010. URL: <https://arxiv.org/abs/1002.2442>.
- [63] Sven. *24 GeV e- on Fe*. URL: <https://www.mpp.mpg.de/~menke/elss/pic3.shtml>.
- [64] Leif Rädcl and Christopher Wiebusch. Calculation of the cherenkov light yield from electromagnetic cascades in ice with geant4. *Astroparticle Physics*, 44:102–113, 2013. URL: <https://arxiv.org/abs/1210.5140>.
- [65] Thomas K Gaisser, Kyle Jero, Albrecht Karle, and Jakob van Santen. Generalized self-veto probability for atmospheric neutrinos. *Physical Review D*, 90(2):023009, 2014. URL: <https://arxiv.org/abs/1405.0525>.
- [66] JW Elbert. Proceedings of the dumand summer workshop, la jolla, california, 1978. 1979. URL: [https://www.researchgate.net/publication/4716588\\_DUMAND\\_Summer\\_Workshop\\_University\\_of\\_California\\_La\\_Jolla\\_Calif\\_July\\_24-September\\_2\\_1978\\_Proceedings\\_Volume\\_1\\_-\\_Array\\_studies](https://www.researchgate.net/publication/4716588_DUMAND_Summer_Workshop_University_of_California_La_Jolla_Calif_July_24-September_2_1978_Proceedings_Volume_1_-_Array_studies).
- [67] Kyle Jero and Delia Tosi. IceTop as Veto for IceCube. In *Proceedings, 34th International Cosmic Ray Conference (ICRC 2015)*, 2015. URL: [http://pos.sissa.it/archive/conferences/236/1086/ICRC2015\\_1086.pdf](http://pos.sissa.it/archive/conferences/236/1086/ICRC2015_1086.pdf).
- [68] MG Aartsen, M Ackermann, J Adams, JA Aguilar, M Ahlers, M Ahrens, D Altmann, T Anderson, C Argüelles, TC Arlen, et al. Atmospheric and astrophysical neutrinos above 1 tev interacting in icecube. *Physical Review D*, 91(2):022001, 2015. URL: <https://arxiv.org/abs/1410.1749>.
- [69] MG Aartsen, R Abbasi, Yasser Abdou, M Ackermann, J Adams, JA Aguilar, M Ahlers, D Altmann, J Auffenberg, X Bai, et al. First observation of pev-energy neutrinos with icecube. *Physical review letters*, 111(2):021103, 2013. URL: <https://arxiv.org/abs/1304.5356>.
- [70] MG Aartsen, M Ackermann, J Adams, JA Aguilar, M Ahlers, M Ahrens, D Altmann, T Anderson, C Argüelles, TC Arlen, et al. Observation of high-energy astrophysical neutrinos in three years of icecube data. *Physical review letters*, 113(10):101101, 2014. URL: <https://arxiv.org/abs/1405.5303>.

- [71] N Whitehorn and C Kopper. High-energy starting track event search, 2012. URL: [https://wiki.icecube.wisc.edu/index.php/High-Energy\\_Starting\\_Track\\_Event\\_Search](https://wiki.icecube.wisc.edu/index.php/High-Energy_Starting_Track_Event_Search).
- [72] C Kopper. Observation of astrophysical neutrinos in six years of icecube data. *Proceeding of Science, ICRC*, 2017. URL: <https://arxiv.org/abs/1607.08006>.
- [73] J Van Santen. Neutrino-level event selection. URL: <http://icecube.wisc.edu/~jvansanten/docs/analysis/level4/index.html>.
- [74] C Haack, L Radel, and S Schoenen. Multi-year diffuse muon neutrino analysis, 2014. URL: <http://icecube.wisc.edu/~lraedel/html/>.
- [75] MG Aartsen, K Abraham, M Ackermann, J Adams, JA Aguilar, M Ahlers, M Ahrens, D Altmann, T Anderson, M Archinger, et al. Evidence for astrophysical muon neutrinos from the northern sky with icecube. *Physical review letters*, 115(8):081102, 2015. URL: <https://arxiv.org/abs/1507.04005>.
- [76] A Schukraft. Icecube diffuse event selection, 2012. URL: <https://web.physik.rwth-aachen.de/~icecubemgr/?n=IceCube.Diffuse-EventSelection>.
- [77] MG Aartsen, R Abbasi, M Ackermann, J Adams, JA Aguilar, M Ahlers, D Altmann, C Argüelles, TC Arlen, J Auffenberg, et al. Search for a diffuse flux of astrophysical muon neutrinos with the icecube 59-string configuration. *Physical Review D*, 89(6):062007, 2014. URL: <https://arxiv.org/abs/1311.7048>.
- [78] Rasha Abbasi, Yasser Abdou, M Ackermann, J Adams, JA Aguilar, M Ahlers, D Altmann, K Andeen, J Auffenberg, X Bai, et al. An improved method for measuring muon energy using the truncated mean of  $dE/dx$ . *Nuclear Instruments and Methods in Physics Research Section A: Accelerators, Spectrometers, Detectors and Associated Equipment*, 703:190–198, 2013. URL: <https://arxiv.org/abs/1208.3430>.
- [79] Eli Waxman and John Bahcall. High energy neutrinos from astrophysical sources: An upper bound. *Physical Review D*, 59(2):023002, 1998. URL: <https://arxiv.org/abs/hep-ph/9807282>.
- [80] Rasha Abbasi, Yasser Abdou, T Abu-Zayyad, M Ackermann, J Adams, JA Aguilar, M Ahlers, MM Allen, D Altmann, K Andeen, et al. The design and performance of icecube deepcore. *Astroparticle physics*, 35(10):615–624, 2012. URL: <https://arxiv.org/abs/1109.6096>.
- [81] MG Aartsen, M Ackermann, J Adams, JA Aguilar, M Ahlers, M Ahrens, D Altmann, K Andeen, T Anderson, I Anseau, et al. The icecube neutrino observatory: Instrumentation and online systems. *arXiv preprint arXiv:1612.05093*, 2016. URL: <https://arxiv.org/abs/1612.05093>.
- [82] Rasha Abbasi, Markus Ackermann, John Adams, Markus Ahlers, J Ahrens, K Andeen, Jan Auffenberg, Xinhua Bai, Michael Baker, SW Barwick, et al. The icecube data acquisition system: Signal capture, digitization, and timestamping. *Nuclear Instruments and Methods in Physics Research Section A: Accelerators, Spectrometers, Detectors and Associated Equipment*, 601(3):294–316, 2009. URL: <https://arxiv.org/abs/0810.4930>.
- [83] IceCube-Gen Collaboration, MG Aartsen, M Ackermann, J Adams, JA Aguilar, M Ahlers, M Ahrens, D Altmann, T Anderson, G Anton, et al. Icecube-gen2: a vision for the future of neutrino astronomy in antarctica. *arXiv preprint arXiv:1412.5106*, 2014. URL: <https://arxiv.org/abs/1412.5106>.
- [84] T Glusenkamp. Muon filter proposal ic86-2012, 2012. URL: [https://docushare.icecube.wisc.edu/dsweb/Get/Document-59906/MuonFilter2012\\_v3\\_with\\_addendum.pdf](https://docushare.icecube.wisc.edu/dsweb/Get/Document-59906/MuonFilter2012_v3_with_addendum.pdf).

- [85] R Strom, A Hallgren, M Bissok, and D Boersma. Fullskystarting and minbias online filters proposal for ic86, 2012 season, 2011. URL: [https://docushare.icecube.wisc.edu/dsweb/Get/Document-59354/FSS\\_MinBias\\_TFT2012.pdf](https://docushare.icecube.wisc.edu/dsweb/Get/Document-59354/FSS_MinBias_TFT2012.pdf).
- [86] MG Aartsen, R Abbasi, Yasser Abdou, M Ackermann, J Adams, JA Aguilar, M Ahlers, D Altmann, J Auffenberg, X Bai, et al. Measurement of south pole ice transparency with the icecube led calibration system. *Nuclear Instruments and Methods in Physics Research Section A: Accelerators, Spectrometers, Detectors and Associated Equipment*, 711:73–89, 2013. URL: <https://arxiv.org/abs/1301.5361>.
- [87] IceCube Collaboration et al. Study of south pole ice transparency with icecube flashers. In *Proceedings of the 32nd International Cosmic Ray Conference, Beijing, China 2011*, 2011. URL: <https://arxiv.org/abs/1301.5361>.
- [88] Dmitry Chirkin. Evidence of optical anisotropy of the south pole ice. In *33rd International Cosmic Ray Conference, The Astroparticle Physics Conference*, 2013. URL: <https://arxiv.org/abs/1309.7010>.
- [89] Markus Ackermann, J Ahrens, X Bai, M Bartelt, SW Barwick, RC Bay, T Becka, JK Becker, K-H Becker, P Berghaus, et al. Optical properties of deep glacial ice at the south pole. *Journal of Geophysical Research: Atmospheres*, 111(D13), 2006. URL: <http://onlinelibrary.wiley.com/doi/10.1029/2005JD006687/abstract>.
- [90] Gustav Mie. Beiträge zur optik trüber medien, speziell kolloidaler metallösungen. *Annalen der physik*, 330(3):377–445, 1908.
- [91] Louis G Henyey and Jesse Leonard Greenstein. Diffuse radiation in the galaxy. *The Astrophysical Journal*, 93:70–83, 1941. URL: <http://adsabs.harvard.edu/doi/10.1086/144246>.
- [92] Pingyu Liu. A new phase function approximating to mie scattering for radiative transport equations. *Physics in Medicine and Biology*, 39(6):1025, 1994. URL: <http://iopscience.iop.org/article/10.1088/0031-9155/39/6/008/meta>.
- [93] D. Heck, J. Knapp, J. N. Capdevielle, G. Schatz, and T. Thouw. *CORSIKA: a Monte Carlo code to simulate extensive air showers*. February 1998.
- [94] G Carminati, M Bazzotti, A Margiotta, and M Spurio. Atmospheric muons from parametric formulas: a fast generator for neutrino telescopes (mupage). *Computer Physics Communications*, 179(12):915–923, 2008. URL: <https://arxiv.org/abs/0802.0562>.
- [95] Frederick J Gilman and Sun Hong Rhie. Calculation of exclusive decay modes of the tau. *Physical Review D*, 31(5):1066, 1985. URL: <http://www.slac.stanford.edu/cgi-wrap/getdoc/slac-pub-3444.pdf>.
- [96] Sea Agostinelli, John Allison, K al Amako, J Apostolakis, H Araujo, P Arce, M Asai, D Axen, S Banerjee, G Barrand, et al. Geant4 simulation toolkit. *Nuclear instruments and methods in physics research section A: Accelerators, Spectrometers, Detectors and Associated Equipment*, 506(3):250–303, 2003. URL: <http://www.sciencedirect.com/science/article/pii/S0168900203013688?via%3Dihub>.
- [97] Christopher Henrik Viktor Wiebusch. *The detection of faint light in deep underwater neutrino telescopes*. PhD thesis, Physikalische Inst., 1995. URL: <https://web.physik.rwth-aachen.de/~wiebusch/Publications/Various/phd.pdf>.

- [98] Dirk Pandel. Bestimmung von wasser-und detektorparametern und rekonstruktion von myonen bis 100 tev mit dem baikal-neutrino-teleskop nt-72. *Humboldt-Universitaet Berlin*, 1996. URL: <https://docushare.icecube.wisc.edu/dsweb/ServicesLib/Document-74814/Comments>.
- [99] MG Aartsen, R Abbasi, M Ackermann, J Adams, JA Aguilar, M Ahlers, D Altmann, C Argüelles, J Auffenberg, X Bai, et al. Energy reconstruction methods in the icecube neutrino telescope. *Journal of Instrumentation*, 9(03):P03009, 2014. URL: <https://arxiv.org/abs/1311.4767>.
- [100] Patrick Hallen. *On the Measurement of High-Energy Tau Neutrinos with IceCube*. PhD thesis, Master thesis, 2013. URL: [https://www.institut3b.physik.rwth-aachen.de/global/show\\_document.asp?id=aaaaaaaaaapwhzq](https://www.institut3b.physik.rwth-aachen.de/global/show_document.asp?id=aaaaaaaaaapwhzq).
- [101] David G Luenberger, Yinyu Ye, et al. *Linear and nonlinear programming*, volume 2. Springer, 1984. URL: <http://www.springer.com/us/book/9783319188416>.
- [102] G I Angelis, A J Reader, F A Kotasidis, W R Lionheart, and J C Matthews. The performance of monotonic and new non-monotonic gradient ascent reconstruction algorithms for high-resolution neuroreceptor pet imaging. *Physics in Medicine and Biology*, 56(13):3895, 2011. URL: <http://stacks.iop.org/0031-9155/56/i=13/a=010>.
- [103] Roger Fletcher. *Practical methods of optimization*. John Wiley & Sons, 2013. URL: <http://www.wiley.com/WileyCDA/WileyTitle/productCd-0471494631.html>.
- [104] Erkan U Mumcuoglu, Richard Leahy, Simon R Cherry, and Zhenyu Zhou. Fast gradient-based methods for bayesian reconstruction of transmission and emission pet images. *IEEE transactions on Medical Imaging*, 13(4):687–701, 1994. URL: <http://ieeexplore.ieee.org/document/363099/>.
- [105] David Altmann. Studies for millipede, 2013. URL: [https://wiki.icecube.wisc.edu/index.php/Studies\\_for\\_Millipede](https://wiki.icecube.wisc.edu/index.php/Studies_for_Millipede).
- [106] Sebastian Euler, David Altmann, and Rickard Ström. Low-energy point source searches with icecube. In *EPJ Web of Conferences*, volume 116, page 04004. EDP Sciences, 2016. URL: [https://www.epj-conferences.org/articles/epjconf/abs/2016/11/epjconf-VLVnT2015\\_04004/epjconf-VLVnT2015\\_04004.html](https://www.epj-conferences.org/articles/epjconf/abs/2016/11/epjconf-VLVnT2015_04004/epjconf-VLVnT2015_04004.html).
- [107] Dimitri P Solomatine and Durga L Shrestha. Adaboost. rt: a boosting algorithm for regression problems. In *Neural Networks, 2004. Proceedings. 2004 IEEE International Joint Conference on*, volume 2, pages 1163–1168. IEEE, 2004. URL: <http://ieeexplore.ieee.org/document/1380102/>.
- [108] Mike Richman. pybdt user manual, 2017. URL: [http://software.icecube.wisc.edu/documentation/projects/pybdt/man\\_index.html](http://software.icecube.wisc.edu/documentation/projects/pybdt/man_index.html).
- [109] Azadeh Keivani, Hugo Ayala, and James DeLaunay. Astrophysical multimessenger observatory network (AMON): Science, infrastructure, and status. *arXiv preprint arXiv:1708.04724*, 2017. URL: <https://arxiv.org/pdf/1708.04724>.
- [110] MG Aartsen, K Abraham, M Ackermann, J Adams, JA Aguilar, M Ahlers, M Ahrens, D Altmann, K Andeen, T Anderson, et al. All-sky search for time-integrated neutrino emission from astrophysical sources with 7 yr of icecube data. *The Astrophysical Journal*, 835(2):151, 2017. URL: <https://arxiv.org/abs/1609.04981>.
- [111] MG Aartsen, M Ackermann, J Adams, JA Aguilar, M Ahlers, M Ahrens, I Al Samarai, D Altmann, K Andeen, T Anderson, et al. Constraints on galactic neutrino emission with seven years of icecube data. *arXiv preprint arXiv:1707.03416*, 2017. URL: <https://arxiv.org/abs/1707.03416>.

- [112] Markus Ackermann, Marco Ajello, A Albert, A Allafort, WB Atwood, Magnus Axelsson, Luca Baldini, J Ballet, Guido Barbiellini, D Bastieri, et al. The fermi large area telescope on orbit: event classification, instrument response functions, and calibration. *The Astrophysical Journal Supplement Series*, 203(1):4, 2012. URL: <https://arxiv.org/abs/1206.1896>.
- [113] Daniele Gaggero, Dario Grasso, Antonio Marinelli, Alfredo Urbano, and Mauro Valli. The gamma-ray and neutrino sky: A consistent picture of fermi-lat, milagro, and icecube results. *The Astrophysical Journal Letters*, 815(2):L25, 2015. URL: <https://arxiv.org/abs/1504.00227>.
- [114] AA Abdo, B Allen, T Aune, D Berley, E Blaufuss, S Casanova, C Chen, BL Dingus, RW Ellsworth, L Fleysner, et al. A measurement of the spatial distribution of diffuse tev gamma-ray emission from the galactic plane with milagro. *The Astrophysical Journal*, 688(2):1078, 2008. URL: <https://arxiv.org/abs/0805.0417>.
- [115] Kohta Murase and Eli Waxman. Constraining high-energy cosmic neutrino sources: implications and prospects. *Physical Review D*, 94(10):103006, 2016. URL: <https://arxiv.org/abs/1607.01601>.
- [116] Alexander Aab, Pedro Abreu, Marco Aglietta, Eun-Joo Ahn, Imen Al Samarai, Ivone Albuquerque, Ingomar Allekotte, Patrick Allison, Alejandro Almela, Jesus Alvarez Castillo, et al. Measurement of the cosmic ray spectrum above  $4 \times 10^{18}$  ev using inclined events detected with the pierre auger observatory. *arXiv preprint arXiv:1503.07786*, 2015. URL: <https://arxiv.org/abs/1503.07786>.
- [117] Auger Collaboration Pierre, Abreu Pedro, Aglietta Marco, Ahn Eun-Joo, Al Samarai Imen, Albuquerque Ivone, Allekotte Ingomar, Allison Patrick, Almela Alejandro, Alvarez Castillo Jesus, et al. The pierre auger observatory: Contributions to the 34th international cosmic ray conference (icrc 2015). *POS PROCEEDINGS OF SCIENCE*, 2015. URL: <https://arxiv.org/abs/1509.03732>.
- [118] M Ackermann, M Ajello, A Albert, WB Atwood, L Baldini, J Ballet, G Barbiellini, D Bastieri, K Bechtol, R Bellazzini, et al. Resolving the extragalactic  $\gamma$ -ray background above 50 gev with the fermi large area telescope. *Physical review letters*, 116(15):151105, 2016. URL: <https://arxiv.org/abs/1511.00693>.
- [119] Mariangela Lisanti, Siddharth Mishra-Sharma, Lina Necib, and Benjamin R Safdi. Deciphering contributions to the extragalactic gamma-ray background from 2 gev to 2 tev. *The Astrophysical Journal*, 832(2):117, 2016. URL: <https://arxiv.org/abs/1606.04101>.
- [120] Auger Collaboration et al. The pierre auger project design report. *Nov. 1996, Revised Mar. 1997) p*, 21, 1997. URL: <http://inspirehep.net/record/416403?ln=en>.
- [121] Kohta Murase, Markus Ahlers, and Brian C Lacki. Testing the hadronuclear origin of pev neutrinos observed with icecube. *Physical Review D*, 88(12):121301, 2013. URL: <https://arxiv.org/abs/1306.3417>.
- [122] S Adrián-Martínez, A Albert, Michel André, G Anton, M Ardid, J-J Aubert, B Baret, J Barrios-Martí, S Basa, V Bertin, et al. The first combined search for neutrino point-sources in the southern hemisphere with the antares and icecube neutrino telescopes. *The Astrophysical Journal*, 823(1):65, 2016. URL: <https://arxiv.org/abs/1511.02149>.
- [123] D. Heck et al. CORSIKA: A Monte Carlo Code to Simulate Extensive Air Showers. *Forschungszentrum Karlsruhe Technik und Umwelt Wissenschaftliche Berichte*, FZKA 6010, 1998. URL: [https://web.ikp.kit.edu/corsika/physics\\_description/corsika\\_phys.pdf](https://web.ikp.kit.edu/corsika/physics_description/corsika_phys.pdf).

- [124] Sebastian Euler, Javier Gonzalez, and B. Roberts. Simulation Studies for a Surface Veto Array to Identify Astrophysical Neutrinos at the South Pole. In *Proceedings, 34th International Cosmic Ray Conference (ICRC 2015)*, 2015. URL: [http://pos.sissa.it/archive/conferences/236/1070/ICRC2015\\_1070.pdf](http://pos.sissa.it/archive/conferences/236/1070/ICRC2015_1070.pdf).
- [125] Eun-Joo Ahn, Ralph Engel, Thomas K. Gaisser, Paolo Lipari, and Todor Stanev. Cosmic ray interaction event generator sibyll 2.1. *Phys. Rev. D*, 80:094003, Nov 2009. URL: <http://link.aps.org/doi/10.1103/PhysRevD.80.094003>, doi:10.1103/PhysRevD.80.094003.
- [126] Thomas K. Gaisser. Spectrum of cosmic-ray nucleons, kaon production, and the atmospheric muon charge ratio. *Astroparticle Physics*, 35(12):801 – 806, 2012. URL: <http://www.sciencedirect.com/science/article/pii/S0927650512000497>, doi:<http://dx.doi.org/10.1016/j.astropartphys.2012.02.010>.
- [127] C. Kopper, W. Giang, and N. Kurahashi for the IceCube Collaboration. Observation of Astrophysical Neutrinos in Four Years of IceCube Data. In *Proceedings, 34th International Cosmic Ray Conference (ICRC 2015)*, 2015. URL: <https://arxiv.org/abs/1510.05223>, arXiv:1510.05223.
- [128] J. Ranft. New features in dpmjet version ii.5. *ArXiv High Energy Physics - Phenomenology e-prints*, 1999. URL: <https://arxiv.org/abs/hep-ph/9911213>, arXiv:hep-ph/9911213.
- [129] M. G. Aartsen, R. Abbasi, M. Ackermann, J. Adams, J. A. Aguilar, M. Ahlers, D. Altmann, C. Argüelles, T. C. Arlen, J. Auffenberg, et al. Search for a diffuse flux of astrophysical muon neutrinos with the icecube 59-string configuration. *Phys. Rev. D.*, 89:062007, 2014. doi:10.1103/PhysRevD.89.062007.
- [130] A. Fedynitch, R. Engel, T. K. Gaisser, F. Riehn, and T. Stanev. Calculation of conventional and prompt lepton fluxes at very high energy. In *European Physical Journal Web of Conferences*, volume 99 of *European Physical Journal Web of Conferences*, page 08001, 2015. arXiv:1503.00544, doi:10.1051/epjconf/20159908001.